Dissertation

submitted to the

Combined Faculties for the Natural Sciences and for Mathematics

of the Ruperto-Carola University of Heidelberg, Germany

for the degree of

Doctor of Natural Sciences

Xinguang Cui, Mech. Eng.

from Heilongjiang Province, China

Oral examination: June 15, 2012

CFD Study of the Flow Field and Particle Dispersion and Deposition in the Upper Human Respiratory System

Supervisors: Prof. Dr. rer. nat. Eva Gutheil
Prof. Dr. med. Ingo Baumann

Abstract

Air taking particles into the human body through breathing has two ways of affecting human health. On one hand, there are significant toxic particles in the environment. When they enter into the human body, they may cause different kinds of diseases such as heart disease and respiratory diseases; even death can be caused, in particular by the particles smaller than 2.5 µm. On other hand, particle deposition in the human respiratory system also has positive effects on human health, with controlled particles inhaled into the human body. Aerosol drug therapy, which delivers the drug mainly through nasal or oral airway to the lung or some other location of the respiratory tract, has become a popular way to treat different diseases such as asthma and chronic obstructive pulmonary disease, due to the advantage of smaller dosages, minimal systemic adverse effects and rapid response. In this case, it is desired that the drug penetrates deep into the lung, that is where the disease occurs. The typical size of these particles ranges from 1 to 5 µm. It is expected that such drugs can be controlled to reach special locations such as the position of tumor so that the drug is efficiently positioned and side effects are minimized. An improved understanding of the process includes the knowledge of properties of the airflow field and particle deposition, and how the gas field influences particle transport.

In the present work, which studies the airflow field and particle dispersion and deposition in the human upper respiratory system, four different geometries have been adopted including the constricted tube, the mouth-throat based on cast, the mouth-throat based on computed tomography (CT) scans and the nasal cavity based on CT scans. NeuRa2 is used to build the surface grid, and Ansys ICEM-CFD 11.0 is used to generate volume grids. One-way and two-way coupling have been used in the present work considering different particle volume fraction. Three-dimensional incompressible Navier-Stokes (N-S) equations are used to depict the airflow field. Large eddy simulation (LES) is used to treat turbulence, and the Smagorinsky sub-grid scale (SGS) model as well as the dynamical Smagorinksy sub-grid model are adopted. Assuming a large particle-to-air density ratio, negligible particle rotation, no inter-particle collision, and drag force as the dominant point force, Lagrangian equations are used to describe particle motion. In the case of sub-micron particles, the Brownian force is also adopted. To solve these equations, the software platform of OpenFOAM 1.5 is used, and new solvers, which can solve the airflow field with LES and particle motion using a Lagrangian formulation, are reconstructed. Depending on the volume fraction, one way or two-way coupling is adopted without or with considering the particle momentum to the gas phase.

First, the velocity at the centerline and velocity profiles at different cross sections downstream the glottis in the constricted tube are compared with numerical results and experimental data, in particular with Reynolds Averaged Navier-Stokes equations (RANS)/low Reynolds number (LRN) $k - \omega$ model. It is demonstrated that the present methodology can predict the laminar-transitional-turbulent airflow in the constricted tube and improve the prediction of transitional airflow, which sets the basis for further studies of the airflow field in the cast-based mouth throat model, CT-based mouth-throat and CT-based nasal cavity.

The airflow fields at three different inspiration flow rates in the cast-based mouth-throat are simulated for the steady inspiration airflow rate. The numerical results show that the unsteady airflow field is quite different from the mean airflow field, in particular the vortices distribution. Mono-disperse particles are tracked in the cast-based mouth throat at first. Numerical simulation shows that particle deposition is related to the particle size, particle release position and inspiration airflow rate as well as geometrical properties. The turbulence and recirculation zone has great influence on the particle transport. In addition, the poly-disperse particles, which are measured from dry power inhaler (DPI), are simulated. Two-way coupling is adopted when the injection drug dose from the inhaler, which is closer to reality, is adopted, otherwise one-way coupling is used. Poly-disperse particle deposition shows different properties compared to the mono-disperse particle. Thus, it is necessary to adopt poly-disperse particle distribution and two-way coupling when the injection dose used in the clinical treatment is adopted.

To study the airflow field under an unsteady inspiration flow rate, a numerical simulation is conducted in the cast-based mouth-throat considering the inspiration flow phase and neglecting the expiration phase. The investigation shows that the airflow field has a significant correlation with the inspiration flow rate and the stage that the inspiration locates at the accelerating phase or decelerating phase. For the same inspiration flow rate, at the accelerating phase, the airflow displays closer to the laminar. In contrast, the airflow at the decelerating phase displays closer to turbulence.

To analyze the influence of geometrical properties on particle deposition, numerical simulations are implemented for the airflow field and particle motion in the CT-based mouth-throat. It is found that the airflow field in the CT-based mouth throat is very different from the airflow field in the cast-based mouth-throat. For instance, the maximum velocity appears at the tip of the soft palate and no laryngeal jet is observed in the CT-based mouth-throat. Although the velocity contour is similar in both mean and instant airflow fields, the airflow field has a very complex vortex field with high spacial and temporal dynamics. 2 μm particles can go through the pharynx, deposit in the trachea, or go further into the pulmonary region.

To investigate the properties of airflow in the nasal cavity, a geometrical model of nasal cavity based on CT scans has been constructed and the airflow field is simulated. The numerical results show that the air pass through the nasal cavity mainly via the main nasal passage and little air can reach the tips of meatuses and olfactory region.

Keywords: human upper respiratory system, large eddy simulation, airflow, particle dispersion and deposition

Zusammenfassung

Das Einatmen von Partikeln in den menschlichen Körper hat zwei verschiedene Aspekte im Hinblick auf die Gesundheit des Menschen. Einerseits existieren schädliche Partikel wie beispielsweise Feinstaub in der Umwelt, der nach Eintreten in den menschlichen Körper Krankheiten wie Herzerkrankungen und Erkrankungen der Atemwege auslösen kann, und der sogar zum Tod führen kann. Hier sind insbesondere Partikel, die kleiner als 2,5 µm sind, relevant. Andererseits ist es in der medizinischen Therapie einiger Atemwegerkrankungen wünschenswert, gezielt Partikel den Atemwegen zuzuführen. Die medikamentöse Aerosol-Therapie, bei der das Medikament durch den nasalen oder oralen Atemweg in die Lunge oder einen anderen Ort des Atemtrakts gebracht wird, wird gern verwendet, um Krankheiten wie z.B. Asthma oder chronisch obstruktive Lungenerkrankungen zu behandeln. Diese Therapie hat den Vorteil der kleinen Dosierung, der minimalen systemischen Nebenwirkungen und der schnellen Wirkung. Das Medikament soll hier tief in die Lunge, in der die Krankheit auftritt, eindringen. Die typische Größe dieser Partikel liegt im Bereich von 1 bis 5 µm. Fokus ist die gezielte Steuerung des Medikaments in spezielle Regionen wie beispielsweise zu einer Tumorposition, sodass Nebenwirkungen durch Ablagerung in anderen Regionen vermieden werden. Ein verbessertes Verständnis des Gesamtprozesses beinhaltet die Kenntnis der charakteristischen Luftströmung und des Partikeltransports sowie deren gegenseitige Beeinflussung.

In der vorliegenden Arbeit, in der die Luftströmung sowie die Partikelverteilung und -ablagerung in den menschlichen oberen Atemwegen untersucht werden, werden vier verschiedene Geometrien verwendet: die verengte Luftröhre, das auf einem Gussstück basierende Mund-Rachen-Modell, das auf Computertomographie (CT) basierende Mund-Rachen-Modell und das auf CT-Skans basierende Nasenhöhlen-Modell. Die Software NeuRa2 wird zur Generierung des numerischen Oberflächengitters verwendet und ANSYS ICEM CFD-11.0, um Volumengitter zu erzeugen. Ein-Weg- und Zwei-Wege-Kopplung zwischen der Gasphase und den Partikeln werden in der Arbeit in Abhängigkeit verschiedener Partikelvolumenanteile angewendet. Dreidimensionale inkompressible Navier-Stokes (N-S) Gleichungen werden zur Beschreibung der Luftströmung verwendet. Large Eddy Simulation (LES) wird zur Modellierung der turbulenten Strömung herangezogen, und das Smagorinsky Feinskalen-Modell sowie das dynamische Smagorinsky Modell dienen der Beschreibung der kleinen turbulenten Skalen. Unter der Annahme eines großen Partikel-Luft Dichteverhältnisses, der Vernachlässigbarkeit der Partikelrotation und der Kollision zwischen den Partikeln sowie der Annahme, dass die Trägheitskraft die Partikelbewegung dominiert, werde Lagrange-Gleichungen herangezogen, um die Bewegung der Partikel zu modellieren. Im Falle von Partikeln, die kleiner als ein Mikrometer sind, wird die Brownsche Kraft zusätzlich berücksichtigt. Zur Lösung der Gleichungen wird die Software-Plattform OpenFOAM 1.5 benutzt, für die neue Solver entwickelt werden, die die Luftströmung mit LES und die Teilchenbewegung mit Hilfe einer Lagrange-Formulierung lösen können. Abhängig von der Partikelbeladung wird Ein-Weg- oder Zwei-Wege-Kopplung mit oder ohne Berücksichtigung des Einflusses des Partikelimpulses auf die Gasphase verwendet.

Zunächst wird die Luftgeschwindigkeit an der Mittellinie und in unterschiedlichen Querschnitten stromabwärts der Glottis in der verengten Luftröhre mit numerischen Ergebnissen und experimentellen Daten aus der Literatur verglichen, hier wird ein Modell der Reynolds-gemittelten Navier-Stokes-Gleichungen (RANS) bei niedriger Reynolds-Zahl, das $k - \omega$ Modell, verwendet. Die hier verwendete Methode verbessert die vorliegenden Literaturergebnisse, sodass sie die Basis für weitere Berechnungen in den verbleibenden Geometrien bildet.

Die Luftströmung wird im Gussstück-basierten Mund-Rachen-Modell für drei verschiedene Inhalationsgeschwindigkeiten simuliert. Die numerischen Ergebnisse zeigen, dass das Geschwindigkeitsfeld der instationären Luftströmung sehr stark vom mittleren Geschwindigkeitsfeld abweicht, dies gilt insbesondere für das Auftreten von Wirbeln. Die numerische Simulation zeigt, dass die Partikelablagerung von der Partikelgröße, ihrer Ausgangsposition, der Inhalationsgeschwindigkeit sowie von der Geometrie abhängt. Turbulenz und Existenz von Rezirkulationszonen haben ebenfalls großen Einfluss auf den Partikeltransport. Eine polydisperse Partikelverteilung, die aus Messungen an einem Trockenpulver-Inhalator zur Verfügung steht, wird ebenfalls zur Simulation herangezogen. In diesem Fall wird Zwei-Wege-Kopplung verwendet. Polydisperse Partikelablagerung zeigt im Vergleich zur monodispersen Partikelablagerung stark unterschiedliche Charakteristika. Deshalb ist es notwendig, polydisperse Partikelverteilung und Zwei-Wege-Kopplung zu verwenden, wenn die reale medikamentöse Dosis eines Hubs berücksichtigt wird, die bei der klinischen Behandlung Anwendung findet.

Um das Strömungsfeld bei einer realistischeren zeitabhängigen Inhalation zu untersuchen, wird eine numerische Simulation für das Gussstück-basierte Mund-Rachen-Modell unter den gleichen Bedingungen durchgeführt. Die Untersuchung zeigt, dass das Strömungsfeld signifikant verschieden ist in der beschleunigenden und der verlangsamenden Phase der Inhalation: In der Beschleunigungsphase ist die Luftströmung laminar während sie in der verlangsamenden Phase eher turbulent ist.

Zur Untersuchung des Einflusses geometrischer Eigenschaften auf die Partikelablagerung werden numerische Simulationen für das CT-basierte Mund-Rachen-Modell durchgeführt. Im Ergebnis ist das Strömungsfeld im CT-basierten Mund-Rachen-Modell sehr verschieden von dem im Gussstück-basierten Mund-Rachen-Modell. Obwohl das Geschwindigkeitsfeld sowohl im mittleren als auch im zeitabhängigen Fall ähnlich ist, hat das Strömungsfeld ein sehr kompliziertes Wirbelfeld mit hoher räumlicher und zeitlicher Dynamik. Partikel der Größe 2 μm können den Pharynx passieren, sich in der Luftröhre ablagern oder weiter in die Lungenregion vordringen.

Um die Eigenschaften des Geschwindigkeitsfelds in der Nasenhöhle zu untersuchen, wurde ein geometrisches Modell der Nasenhöhle aus CT-Skans konstruiert. Die numerischen Ergebnisse zeigen, dass die Luft durch die Hauptluft-Passage der Nasenhöhle fließt und nur wenig Luft die Spitzen der Nasengänge und der olfaktorischen Region erreicht.

Schlüsselwörter: Menschliche obere Atemwege, Large Eddy Simulation, Luftstrom, Partikeldispersion und -ablagerung

Contents

List of Tables

List of Figures

1. Introduction

1.1 Motivation

It is common for people to observe particles in the air and feel air entering into human bodies through breathing. But it is possible that few people notice that air takes particle into human body through breathing. As common events, the particle entering into human body with air has two ways to influence human health. On one hand, the toxic particles in the environment, going into human body definitely influences the health negatively. It may induce different kinds of diseases such as heart disease and respiratory disease, even death [1]. As it was reported, the particulate matter pollution was estimated to cause 200,000 deaths per year in Europe [1]. In particular, particles in the size range less than 2.5 μm [2] can reach the lung and enter into the circulation of blood via the lung. The study of the toxic particle transport and deposition in the human respiratory system will benefit human health, in particular, for the person exposed to the toxic particles in the work location or live environment [3].

As mentioned above, there is also another aspect which can benefit human health by controlling particles that enter human body. Aerosol drug therapy, which mainly delivers the drug through nasal airway or oral airway to the lung or other location of the respiratory tract [4], has become a popular way to treat different diseases such as asthma and chronic obstructive pulmonary disease (COPD) due to the advantage of smaller dose, minimal systemic adverse effects and rapid response [5]. In this case, in contrast, people prefer that the drug can go deep inside of the lung where the diseases occur. The diameter of the particle usually ranges from 1 to 5 μm [6]. It is expected that more drugs may be controlled to reach specific location such as the position of tumor so that it can save the drug and decrease the side effect significantly [4, 7]. One important issue in the aerosol drug therapy is that particle size influences the particle deposition [6]. Aerosol drug with larger size than, i.e. 5 μm is harder to reach the deep region of the lung. In fact, only $10 - 20\%$ of aerosol drug can go into the deep location of the lung [6]. Other drugs deposit on the device, mouth-cavity or oropharynx depending on the device and drug formation [6]. It is of great importance to enhance the efficiency of aerosol drug to save dose and decrease the side-effects.

Hence, it is very important to study the particle transport and deposition in the human respiratory system concerning the environment and aerosol drug delivery. More understanding of the influence of the respiratory flow rate, particle size and geometric properties on the particle transport and deposition will definitely improve the development of the aerosol drug therapy, and prevention and cure of toxic particles in the environment.

1.2 Human Respiratory System

In this section, the human respiratory system is explained in order to set basis of understanding the influence of toxic particles in the environment on the human health and the aerosol drug therapy in the beginning.

It is known that air is the necessary material for human beings to sustain human life and it enters into human body through human respiratory system by breathing. Human respiratory system is an essential system to keep normal human metabolic processes through exchanging air between body and environment [8]. In this section, the structure and the breathing mechanism will be presented.

1.2.1 Geometrical Structures

The respiratory system mainly consists of two parts from the view of function. It can be divided into the respiratory zone and conducting zone, seen in Fig. 1.1 [7]. The conducting zone consists of 0 generation to 16 generation (G), and the respiratory zone consists of generations 17 to 23. The O_2 - CO_2 gas exchange takes place in the generation 13 [7]. From the view point of numerical modeling [9], it can be divided into the extra-thoracic region, tracheo-bronchial region (TB), and the alveolar region [10]. The TB and alveolar region can be attributed to intrathoracic region [11]. The extrathoracic region [10], the human upper respiratory system, consists of nasal cavity, oral cavity, pharynx, larynx and trachea seen in Fig. 1.2. It is the main component of the respiratory tract and it is the first barrier for the particle entering into human body [12]. Most of aerosol drugs cannot go into the deep location because of its filtering function [6].

On the surface of the respiratory airways, there is a mucus layer overlayed by fine hairs, cilia, and the oscillatory movement of the cilia propelling the muscle layer may capture inhaled particles [9]. In reality, the surface of trachea is not even as in the configuration model used for numerical simulation. There are cartilaginous rings in the trachea and upper bronchi to stabilize the airway, which produces the uneven surface [9]. These properties of respiratory tract may influence properties of the air flow and particle deposition [13, 14] in the respiratory tract.

1.2.2 Breathing Mechanism

Between human body and environment, the gas exchange process is called respiration [15]. It is necessary activity for body metabolism to take in O_2 from the atmosphere, and expel out CO_2 which is produced by body metabolism [15]. Breathing is an involuntary process and is carried out unconsciously, which is controlled by the nervous system, the respiratory center of the brain and respiratory muscles [16]. The respiratory center is divided further into two parts namely, the inspiration and the expiratory centers, which involve two movements namely, inspiration and expiration following one after the other [17]. In addition to the respiratory center, there is another center called pneumotaxic center in the medulla oblongata,

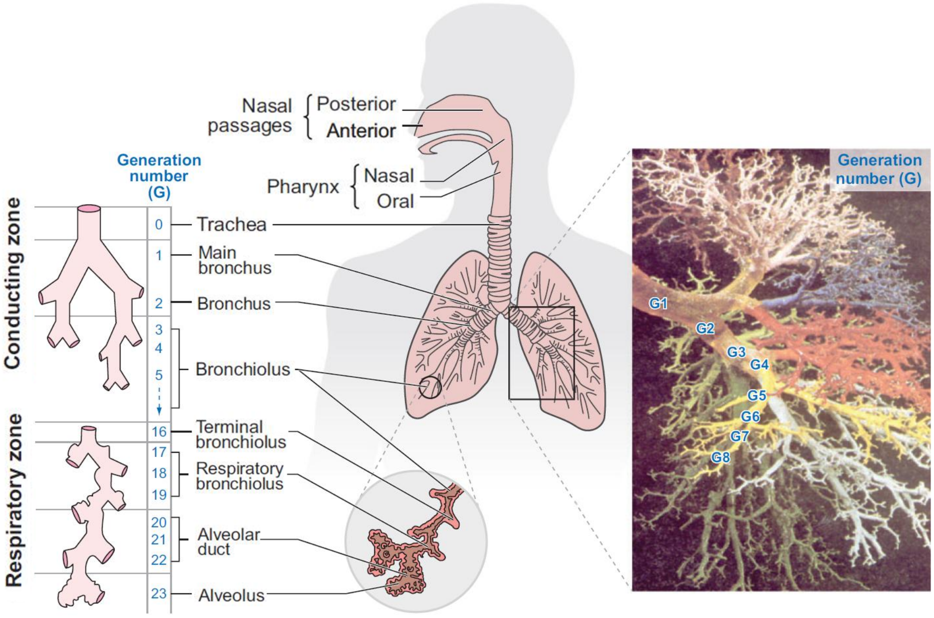

Fig. 1.1: Schematics of human respiratory system [7].

which ensures rhythmic breathing. In the process of inspiration, the pneumotaxic center received impulses from the inspiratory center and it responds to it by sending impulses to the expiratory center. Then, it restrains further inspiration and starts the process of expiration. Thus, the respiratory center together with the pneumotaxic center make the respiration a rhythmic process [17].

In the process of respiration, pressure plays an important role in the mechanism of breathing [8]. Three pressures are particularly important in breathing, which are atmospheric, intrapleural, and intrapulmonic pressure. Atmospheric pressure is the pressure of the external environment out of human body [8]. The intrapulmonic pressure is the pressure within the lung, which cause the lung to inflate during inhalation and deflate during exhalation. In the process of inspiration, the respiratory muscles contract and expand the chest cavity, reducing the intrapulmonic pressure and drawing atmospheric air in. In contrast, in the process of expiration, the respiratory muscles relax and the intrapulmonic pressure increases above atmospheric pressure. The intrapleural pressure is the pressure within the potential pleural space between the parietal and visceral pleura (the membranes surrounding the lung). It is called a potential space because there should be no real space between the membranes. Usually, the intrapleural pressure is slightly below atmospheric pressure, referred to as negative pressure [8].

Under the function of pressure, breathing is conducted through nose and/or mouth. Air passes through nasal passages/mouth cavity, pharynx, larynx, trachea, main bronchi, smaller bronchial tubules, bronchioles, and finally into alveolus [19]. The alveoli are surrounded by the extensive network of blood vessels called capillaries. The exchange of oxygen in air with carbon dioxide in the blood occurs across the walls of alveolus of lung [19]. Afterwards, this

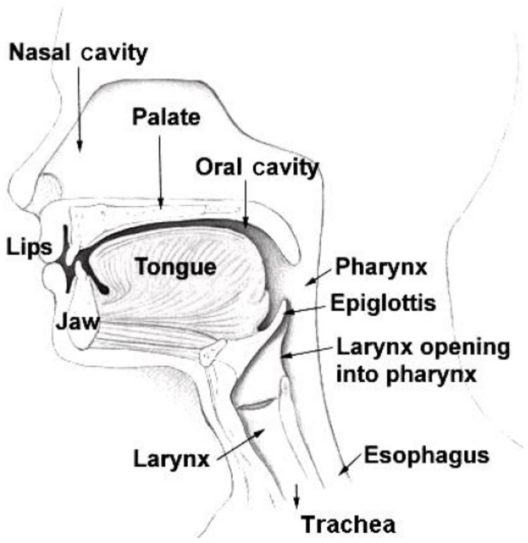

Fig. 1.2: Schematic representation of the extra-thoracic (upper) airway [10, 18].

oxygen enriched blood flows out through capillaries and feeds oxygen to the cells through circulatory system. Cells in the tissues of body require oxygen for cellular respiration and need to expel out the carbon dioxide, so the blood is carried throughout the body to exchange oxygen and carbon dioxide with the body's tissues [19]. The whole respiration procedure is also the process of particle entering into human body. It is also found that the inspiration and expiration process influence the aerosol drug efficiency [13, 20, 21].

1.3 Respiratory Particles

Particles entering into human body may come from different sources such as the exhaust of vehicles, volcano, smoking and aerosol drug [22]. Some of them are large enough for us to observe and others are so small that they can only be detected through an electron microscope [22]. Anthropogenic aerosols, which are made by human activities, have been accounted for about 10% of the total amount of aerosols in the atmosphere [23]. The particle transport and deposition in the human respiratory can take both of the negative and positive effects. The physical properties, in particular the particle size, are important factors to influence particle transport and deposition in respiratory tract [7]. So, in this section, the particle size categories and the influence of huamn heath of the inhaled particles are presented.

1.3.1 Inhaled Particle Size Categories

Before it discusses the influence of the inhaled particles on health for both of the toxic particles and aerosol drug therapy, it is better to introduce the particle classification based on size so that there is an overview of the particles which are introduced later.

The categorization with respect to size is the most common way to classify particles, referred to as fractions [22]. There are a lot of definitions of particle size due to the fact that particles are often non-spherical shape. Among them, the aerodynamic diameter is used most widely. In reality, the particle is non-sphere. The aerodynamic diameter is an expression of a particle's aerodynamic behavior as if it were a perfect sphere with unit-density and diameter equal to the aerodynamic diameter. For instance, a particle with an aerodynamic diameter of 10 μm means that it moves in the gas like a sphere of unit density (kg/m^3) with 10 μm. The diameter of particulate matter can range from less than 10 nm to more than 10 μm. The aerodynamic diameter of particles, which is less than 10 μm, is denoted PM_{10}; and which is less than 2.5 μm, is denoted by $PM_{2.5}$ [24]. Particles under 1 μm called sub-micron particles are denoted as PM_1. All of particles whose sizes are below 10 nm, down to the size of individual molecules are categorized as ultrafine particles [2].

These definitions are the formal way to characterize particles. Up to the context, it is possible to adopt alternative definitions. In some specialized settings, each fraction may exclude the fractions of lesser scale, so that PM_{10} excludes particles in a smaller size range, e.g. $PM_{2.5}$, usually reported separately in the same work. Such a case is sometimes emphasized with the different notation, e.g. PM_{10} - $PM_{2.5}$ [2]. The small particles, which are less than 10 μm in diameter pose the greatest problems, because they can go deep into your lung, and some may even get into the blood stream, in particular, the finer particles with diameter less than 2.5 μm ($PM_{2.5}$). These particles can enter indoors and travel large distance in the air. They are small enough to go through the defensive of the nose hairs and deposit on the different sites of respiratory tract such as throat and penetrate deep into the lung. Moreover, they do not stop in this region. They can pass from the lung into the blood supply and then be carried out throughout human body [3]. In contrast, in the aerosol drug therapy, people hope that more drug can go into the deep of lung so that the diameter of aerosol drug is usually between 1 to 5 μm [6]. More details on the health effects of particles are discussed in the next section.

1.3.2 Health Effects of Inhaled Particles

As aforementioned, the particle transport and deposition in the human breathing system, has two ways to influence on the human health. First, the increasing amount of fine particles in the air are related to health hazards such as lung cancer [7, 25, 26]. In contrast, the aerosol drug therapy has become a popular way to treat different kinds of lung diseases, and then benefit human health. The investigations have been implemented significantly on the particle transport and deposition in the regard of toxic particle in the environment and aerosol drug delivery [3, 7, 27].

1.3.2.1 Toxic Particles in the Air

As mentioned, the toxic particles broadly range from micrometer to nanometer. Particulate matter comes from many sources. Generally, any activity which involves burning of materials or any dust generating activities are sources of particulate matter [3]. Some sources are natural, such as volcanoes and water mist. In contrast, human's activities create huge quantities of particulate matter in the regulated way, such as smoke stacks at factories, power plants and auto paint shops, and unregulated way such as burning coal in the winter and exhaust from cars. Toxic particulate matter in the air involve oxides of nitrogen, carbon monoxide, sulfur dioxide, ozone and many hazardous hydrocarbons and metal compounds [3]. These toxic particles cause illness leading to increasing use of medication, hospitalization and even premature death [3]. It was first reported in the 1970's that the large number of deaths and other health problems were demonstrated to be associated with particulate pollution [28] and has been reproduced many times since then. Particulate matter pollution is estimated to cause 200,000 deaths per year in Europe [1]. In the epidemiological studies conducted over the past ten years, a very consistent quantitative picture has emerged between the levels of air pollution and increase in morbidity and mortality [29].

As mentioned in last section, fine particles' pollution especially particles less than 2.5 μm pose the greatest risk to health because it can suspend in the air up to days and they can deposit deep into the lung, with increased respiratory symptoms, such as irritation of the airways, coughing, difficulty in breathing, decreased lung function, aggravation of lung disease, causing asthma attacks and acute bronchitis, an irregular heartbeat, nonfatal heart attacks and premature death in people with pre-existing heart or lung diseases [30]. In contrast to other pollutant particles, the health impact of these particles is so significant that they alone are usually considered as a surrogate for health effect [3]. Moreover, the older adults, individuals with heart or lung diseases, and children are more likely to be affected by micrometer particles exposure due to their particular body conditions [31].

1.3.2.2 Aerosol Drug Therapy

The lung has served as a route of drug administration for thousands of years. The origin of inhaled therapies can be dated back 4,000 years ago to India [29]. But, the aerosol drug therapy has been playing an important role in the medical treatment since 1950's [32]. Aerosol drug therapy is a kind of topical treatment with the aerosol drugs via air delivered by a suitable device, which is inhaled and absorbed by patient through lung [33].

Aerosol drugs are applied broadly in circumstances, which require rapid absorption and local effects of drug. It is most commonly used in asthmatic conditions or specific lung conditions that cause difficulty in breathing [4]. Generally, aerosol drug therapy is a safe approach, as long as the health care provider or client is well educated to use it. It is constrained in the condition that the airway is completely blocked [4]. Successful aerosol drug therapy depends on the systematical work of patient condition, drug device and drug formation [33].

Aerosol Drug Devices Today, the devices applying clinical treatment can be commonly classified in three types: metered dose inhaler (MDI), dry powder inhaler (DPI), and nebulizer. The nebulizers consist of two types, namely, jet nebulizer and ultrasonic nebulizer [34].

Metered dose inhaler is one of the most commonly used medical devices in the clinical application. The micronised form of the drug is put in a propellant under pressure with surfactant. As the device is actuated, the propellant becomes exposed to atmospheric pressure leading to aerosolization of the drug. The fraction of drug to the deep site of the lung only ranges from 5% to 15% usually [35]. To overcome the major problem related to the coordination, a valved holding chamber may be used as supporting device to the MDI. In addition, it is also helpful for the patients unable to hold breathing. With the help of spacer devices using MDI, the inhaled aerosol particle size are reduced because larger particles incline to deposit on the chamber walls/valves. At the same time, it also decreases the particle velocity, which leads to smaller particle inertia, an then it produces less upper airway deposition. DPI is the second kind of inhalers which includes pharmacologically active powder as an aggregate of fine mironised particles in one inhalation chamber. The aggregates are transferred into aerosol particles by inspiration air flow generated by the patients themselves through the inhaler, which excludes the problem of coordination between the drug delivery and inspiration initiation. But, at the same time, it limits the application in the treatment of patients unable to produce high inspiration flow rates. Compared with MDI, the advantage of DPI is lack of the requirement of propellant and there are usually 9% to 30% drug delivered to the site of action by using DPIs, which varies among different commercial products [36]. Two types of nebulisers, mentioned above have different functions, but significant common features. Same as DPI, the nebulisers have no propellant either. So, it does not require patient coordination and has the ability to transport high doses of a particular drug during a short time such as acute exacerbations of obstructive airway diseases in emergency [34]. More details on the drug delivery device can be found in [6, 29, 34]. The characteristics and comparison of the inhalers are conducted in [29, 34], and they are shown in Tab. 1.1. Through the comparison, it is easy to find that MDI and DPI delivery systems should be the first clinical choices due to their convenience and less cost for patients with obstructive airway disease. If the patient is not able to demonstrate acceptable hand breath coordination and whenever pharyngeal

Tab. 1.1: Characteristics of aerosol generators [34].

	MDI	DPI	Nebuliser
Technique of generation of aerosol	Propellant based	Patient driven flow	Bernoulli's principle
Particle size	1 - 10 µm	1 - 10 µm	Variable
Drug deposition	5 - 10%	9 - 30%	2 - 10%
Oropharygeal deposition	Significant	Variable	Insignificant
Patient coordination	Required	Not applicable	Not required
Breath hold	Required	Not required	Not required
Patient generation of flow	Not required	Required	Not required
Amount of drug	Small doses only	Small doses only	Large doses possible
Contamination	No	No	Possible
Use for chronic therapy	Yes	Yes	Rarely
Use for emergency management	No	No	Yes
Use for intubated patients	Preferred	No	Second choice
Cost	Cheap	Cheap	Expensive

deposition is a concern, a valved holding chamber should be adopted together with the MDI. In the situation of a high drug dose or large volume requirement, the nebulizer may be one suitable candidate. A nebulizer may also be considered on condition that only the drug in solution formulation is available or MDI/DPI does not work effectively. In addition, the patient preference should also be considered when an aerosol delivery device is chosen. In fact, there is a guideline from the 1997 National Asthma Education and Prevention Program [37] to recommend age limits to ensure effective clinical application. Anyway, when the inhaler is used in the treatment, the application needs to be evaluated properly in order to choose optimal technique, and assure that patient is able to use the device correctly [6].

Host Factors Host factors play critical roles in the aerosol drug delivery. The host factors include the conditions related to the ventilatory and the airway status of the patients [34]. Four sides of ventilatory factors have been shown to be important, i.e. inspired volume, inspiratory time, breath-hold duration, and timing of aerosol delivery during inspiration. Inspiration volume is very important in the process of aerosol drug delivery. Increasing inhalation volume has more ability to carry particles further into lung. So, patients are suggested to take a deep breathing under the actuation of aerosol drug devices. At the same time, they are also advised to exhale to functional residual capacity before initial inspiration. However, it is not recommended to force exhalation to residual volume before inhalation since this may let some airways collapse temporarily, and then reduce drug delivery efficiency. In addition, holding breath is very important to maximize the aerosol drug delivery efficiency including increasing the penetration and particle deposition in the lung. However, the duration which the breath should be held has been debated. It was reported by Newman, et al. [38] that a four-second holding is extremely helpful in the improvement of aerosol drug delivery while a longer duration may not be helpful. But, the mechanism of increased penetration of aerosol particles is not fully understood. Among the airway factors, the status of the airways and the lung pathology has no influence on the total amount of drug to the airways but it definitely influences the fraction of dose arriving at the desired site. Investigations have also shown that increasing airway resistance, which is seen in patients with obstructive airway disease, make the aerosol particles predominantly deposit in the proximal locations [39, 40]. However, these problems have been overcome with certain techniques of improving aerosol drug delivery to the circumferential locations within the airways. The patient inspiration rates, the timing of inhalation, and the breath-holding duration can be suitably changed to increase the aerosol fraction going into the lung at the ideal locations [34].

Aerosol Drug Formation Nowadays, most of the aerosol drugs applied in medical treatment is to cure obstructive airway diseases. In Tab. 1.2, different kinds of drugs related to dosages and the type of aerosol devices available for each kind of drug [34] are listed. In addition, there are some antibiotics and mucolytic agents available in the aerosol therapy as well [34]. Although there are different commercial products available, the lung deposition is usually 10 - 20% for most aerosol drug devices [41–43]. The rest of the aerosol drug deposits in

Tab. 1.2: Properties of aerosol drug formation [29].

Drug	Type of aerosol generator	Dose
Salbutamol	MDI	100 - 200 µg, 4 - 6 times/day
Salbutamol Sulphate	DPI	200 - 400 µg, qid
Salbutamol Sulphate	Solution for nebuliser	2.5 - 5 mg
Terbutaline Sulphate	MDI	250 - 500 µg, qid
Terbutaline Sulphate	Solution for nebuliser	10 - 20 mg
Smalmetrol Xinafoate	MDI	50 µg, bid
Smalmetrol Xinafoate	DPI	50 µg, bid
Formoterol Fumarate	MDI	12 - 24 µg, bid
Formoterol Fumarate	DPI	12 - 24 µg, bid
Ipratropium Bromide	MDI	20 - 40 µg, qid
Ipratropium Bromide	DPI	20 - 40 µg, qid
Ipratropium Bromide	Solution for nebuliser	100 - 500 µg
Tiotropium	DPI	18 µg/day
Sodium Cromoglycate	MDI	5 mg, qid
Sodium Cromoglycate	DPI	20 mg, qid
Sodium Cromoglycate	Solution for nebuliser	20 mg, qid
Beclomethasone Dipropionate	MDI	100 - 400 µg, 2 - 4 times/day
Beclomethasone Dipropionate	DPI	200 - 400 µg, 2 - 4 times/day
Budesonide	MDI	100 - 400 µg, bid
Budesonide	DPI	200 - 400 µg, bid
Fluticasone propionate	MDI	100 - 1000 µg, bid
Fluticasone propionate	DPI	100 - 1000 µg, bid

the oropharynx, the device, the exhaled breath, and the environment [6]. It is very important to emphasize that different types of aerosol devices do not have the same total dose injection such as a nebulizer and an MDI. Taking an example of using albuterol, a typical MDI total dose is about 200 µg, whereas a typical nebulizer total dose is 2.5 mg [34]. More drugs reach the lung in condition of same delivery efficiency using a MDI than a nebulizer. Although in the clinical application, it is recognized that nebulizer is more effective, several studies show that MDI can be as effective as nebulizer when the number of actuation is increased with a MDI [44].

Aerosol drug formation size plays an important role in lung deposition, along with particle velocity and settling time [45]. As particle size exceeds above 3 µm, there is a shift in aerosol deposition from the periphery to the conducting airways. Oropharyngeal deposition also increases as particle sizes increase above 6 µm. Exhaled loss is high with very small particles of 1 µm or less. These data support the view that particle sizes of 1 - 5 µm are best for reaching the lung periphery, while 5 - 10 µm particles deposit preferentially in the conducting airways. Aerosol devices in clinical use produce poly-disperse particle size, meaning that there are variations in sizes of the aerosol. A measure that can be useful in describing a poly-disperse aerosol is the mass median diameter (MMD) defined as the particle size, which is in the range of the micrometer, above and below which 50% of the mass of the particles is contained. This is the particle size that evenly divides the mass, or amount of the drug in the particle size distribution. This is usually given as the mass median aerodynamic diameter, or MMAD, due to the way that particle sizes are measured [6].

1.4 Research Objectives

From the introduction, it can be recognized that the topic is really interesting and it will benefit human health with its development. All of the applications in this field cannot go ahead unless the characteristics of the gas field, and particle transport and deposition are understood, and how the gas field influences particle transport. Although, a lot of contribution has been made by other researchers [7, 9] and there is a significant literature [7, 9] available on the flow field in the oral airway and on the physics of particle deposition through numerical simulations and experimental measurements, some questions still need to be answered, such as the unsteady flow field in the respiratory tract. For instance,it is known that the turbulence increases the particle deposition in the trachea, but few explanations are given to the phenomena. In addition, although the secondary flow, which is the flow in the plan vertical to the main flow direction, has been seen, the unsteady dynamics of the flow field is not investigated. Recently, researchers have started to notice the CT-based mouth-throat model, which is more close to the realistic anatomic structure, influence on the drug deposition [21, 46], but most studies still assume mono-disperse particles and little research has been developed on the poly-disperse particles except Longest's group [47]. In addition, little numerical modeling considers the realistic drug dose at one actuation.

In the thesis, computational fluid dynamics (CFD) method is adopted since it has the advantages of noninvasive, high-resolution, cost-effective, and safe modeling of air flow patterns, particle transport, particle deposition, and particle mass penetration into the lung tissue [9]. In the present work, large eddy simulation (LES) together with Lagrangian equations is used to analyze the particle transport in the human upper respiratory. LES predicts large-scale vortex directly and model the small vortices with sub-grid scale model. It has been acknowledged as a powerful method to capture the turbulent structure and simulate the laminar-transitional-turbulent flow [46]. Lagrangian method tracks the particle trajectory separately and it is suitable to track the micron particles in the dilute two-phase flows [9]. More attention is paid to the study of unsteady flow characteristics in a cast-based and CT-based mouth-throat. The particle transport in the turbulent flow region has been studied using one-way coupling. In addition, the realistic drug injection is adopted as well with two-way coupling. The thesis is organized as follows: In chapter 2, the state of the art is presented to give the overview of the research status. Afterwards, the governing equations and physical models are described in the chapter 3 to set the physical understanding of the topic. The numerical methods for solving the gas phase and particle motion, and the solvers construction are addressed in the chapter 4. In chapter 5, the numerical results will be presented, which includes the flow field in a constricted tube, flow field and particle transport in a cast-based mouth-throat, flow field and particle transport in a CT-based mouth-throat, the flow field in the cast-based mouth-throat under unsteady inspiration flow rate and the flow field in a CT-based nasal cavity. In the last chapter, conclusions and perspectives are presented.

2. State of the Art

Concerning the influence of particle transport in the respiratory system on human health, there is significant literature developed by fluid researchers through three approaches commonly, i.e. experimental methods [48–51], numerical methods [13, 20, 52–59] and empirical formula based on experimental data [60–64]. The properties of the airflow field, and particle transport and deposition, in particular the efficiency of particle deposition are investigated broadly to improve the drug delivery efficiency and validity. As the pages limit, it is impossible to give an entire literature review including all of the research issues in this area during past decades. More attentions will be paid to the research related to numerical simulations in the upper airway region because present thesis focuses on this field.

In this chapter, the geometry models used in the numerical simulation and some in experimental investigations, numerical methods for the two-phase flows in the respiratory system, the recent achievements related to airflow field, particle transport and deposition in the extra-thoracic region, and intra-thoracic region are presented.

2.1 Geometrical Models

A suitable configuration is the first step towards experimental or numerical study of the air flow and particle transport. In this section, geometry models of extra-thoracic region and intra-thoracic region (tracheobronchial region and alveolar region) including the idealized models and image-based models, which are closer to the realistic anatomical structures, are described.

2.1.1 Geometry Construction Method

In the early studies, most of the work is conducted on the simplified geometry model of the respiratory system [65–71], which is based on the cast, literature, observation or medical images. Even today, there are still a lot of studies based on these geometrical models [72, 73]. Although it is known that the speciality of airway geometry has a major influence on the local airflow structures and the particle deposition pattern, the simplified geometry models can adequately fulfill the requirement for the estimation of global deposition values [7]. The simplified models keep the common properties of the configurations of respiratory system, which have the advantages of studying common properties in theory. But at the same time, it cannot reflect the individual character of patients. So, it is not suitable to provide precise information for the clinical treatment.

From the view of clinical treatment, it is very important to study the airflow field and particle deposition and dispersion in the more realistic models, namely patient-specific model. It is expected that one day the patient-specific modeling will be applied into relevant problems in the biomedical engineering. It would gain quantitative results and valuable physical insight in finding optimal medical treatment [7]. There is one modern way to construct the configuration from the medical images, i.e. computed tomography (CT) and magnetic resonance imaging (MRI) scans [46, 55, 74]. The configuration built on this way is closer to configuration of the realistic respiratory system.

CT scans are able to outline bone inside the body accurately and they are suitable for lung and chest imaging, and cancer detection [9]. In contrast, MRI scans can highlight different tissues through changing the contrast of the image. Thus, it may have advantage of estimating wall thickness [9]. However, the cost of CT scans are less than MRI scans and it is more used in the examination of lung and CT scans are more used in the lung examination. Therefore, many geometrical models are constructed based on CT scans [9].

There is a generic procedure to generate the configuration based on CT or MRI scans. At first, the CT or MRI images of interested portion of human body with the file format of "DiCom", are obtained from a radiologist or surgeon. Then, the medical scans are imported into image processing software such as Amira [75], Mimics [76], Simpleware [77] and NeuRA2 [78]. These images may be undergone the process of preparation, segmentation, surface mesh generation and optimization [46, 55, 74, 79–82]. With this methodology, the complex geometrical models of entire lung and pulmonary branches can be generated, as shown in Figs. 2.1 and 2.2. The geometrical models are exported with ".stl" file and imported into the volume mesh generation software. The volume mesh will be generated and exported into the CFD software to simulate the two-phase flows.

Although the 3D geometry model close to the realistic anatomical structures based on medical images has been applied in the numerical studies, the construction of 3D geometrical

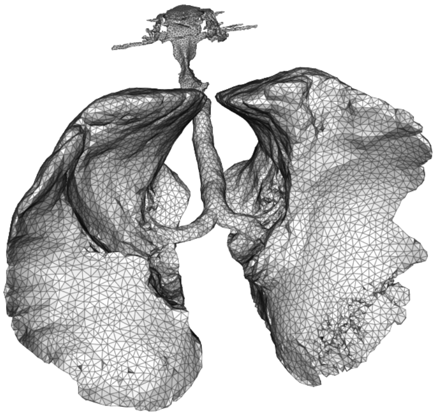

Fig. 2.1: Entire respiratory airways from the mouth to lung using NeuRA2 [78].

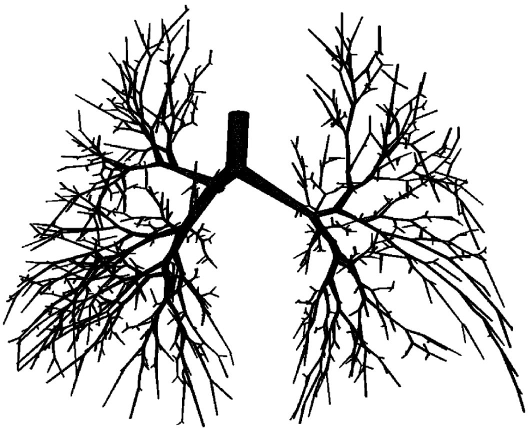

Fig. 2.2: Pulmonary branches with 17 generations including 1453 bronchi [83].

model for whole respiratory tract based on medical images, and its application in numerical simulations, are still impractical due to the following obstacles [9]:

(a) At present, the resolution of CT/MRI is not high enough after the 6^{th} or 8^{th} generation of the branches.

(b) There are 23 generations in the lung and 223 airways in total, together with millions of alveoli.

(c) The geometry of the respiratory tract depends on the time, in particular, the alveoli.

(d) The lung morphology is different among all of the patients.

(e) The cost of exact patient-specific modeling is still too high.

In the above paragraphs, the geometrical models used in the numerical simulation are discussed. As experimental investigation of the airflow and particle transport in the human respiratory system is not the concentration of the present work, only the modern technique to generate the experimental model is introduced because it is much close to the modern technique to create the numerical geometrical models. With the appearance of rapid prototyper, it is possible to create experimental model based on CT scans, computer aided design (CAD) technique and manufacturing technique of prototyper [9]. For instance, seven geometries based on MRI scans, which are chosen from 80 sets of patients scans, have been created by Grgic et al. [50] to study the inter-subject and intra-subject particle deposition; a replica of nasal airway based on CT scans using rapid prototyping is created by Kim et al. [82] to study the airflow with PIV method. The nasal airway includes nasal cavities, larynx, trachea, and 2 generations of bronchi.

In summary, the modern technique to construct the numerical and experimental respiratory airway models based on medical images using image-processing, CAD and manufacturing technique of prototyper (experimental model) has become a popular way. It will be more and more applied in the numerical and experimental investigations of airflow and particle transport in the human respiratory system. Thus, a CT-based mouth-throat model is constructed in present work and it is used for the numerical simulation of airflow and particle transport in the human upper respiratory system.

2.1.2 Extra-Thoracic Region

As it is introduced, the extra-thoracic region is the first barrier for particle entering into human body. Aerosol drug deposition in this region has important implications in drug delivery efficiency. In the research, it can generally be classified in oral airway and nasal airway. It also includes some generations of bronchial branches after the trachea frequently [59, 84, 85]. This kind of geometries are also presented together with the oral and nasal airways in this section.

One challenge in studying particle transport in this portion of respiratory tract is the geometry complexity. The complexity of the extra-thoracic airway includes the bends, sudden cross-sectional area change [10, 86], which induce turbulence and aerosol drug deposition. Due to the complexity, there are several simplified geometric models of mouth-throat used in the literature [20, 48, 49, 67, 69, 71, 87, 88].

Among them, Cheng et al. [48] produced a human airway cast including oral cavity pharynx, larynx, trachea, and 3 generations of bronchi to study the particle deposition in the oral airway in 1999. Of the cast, the oral portion was modeled from the dental impression of a human volunteer, whereas the other portions of the cast were made from a cadaver. The cast is produced using the production of silicone rubber and filling wax [48].

To study the filtering function of oral airway and to avoid large error produced by over-simplified geometry model [48, 65], a simplified mouth-throat with variable circular cross-sections is produced by Kleinstreuer and his colleagues [89]. It is based on the dimensions of the cast provided by Cheng et al. [48], which includes the position of cross sections and hydraulic diameters. The region from mouth-cavity to the larynx is modeled as a curved tube close to 180° as suggested by Cheng et al. [48]. There are also some other variations to the cast including addition of mouth-inlet tube of 2 cm diameter and a modification of soft palate [89]. A series of research work [20, 59, 84, 86, 89–96] have been done on this geometry model by the group. The results related to the geometry are cast-based mouth-throat model in the section 2.3.1.

Another very popular ideal mouth-throat is built by Stapleton et al. [71] to study particle deposition in the human upper airway. It has been adopted widely in the experimental and numerical studies [14, 50, 57, 82, 85, 97–101] since its creation. It is constructed on the information from literature [102–105], CT scans of patients, MRI scans [71], and direct observation of living subjects [71], as shown in Fig. 2.3 [97]. The obvious differences between this configuration and the one built by Kleinstreuer et al. [89] is that the cross-section of the geometry is not circular and it is closer to the realistic upper airway because it includes more information of anatomical structure. In addition, the pharynx is an elliptical cylinder [71].

Jayaraju et al. [46] also built a simplified geometrical model of human upper airway based on the CT scans in the study of evaluating turbulent modeling methods [88] and the airflow field in the upper airway with the tracheal stenosis [106]. The main simplification of the geometrical model is that the left and right sides of configuration are planes, which is not realistic profile. To identify the influence of geometrical model on the airflow field and particle transport, four different geometrical modes of upper airway are adopted by Xi et al. [74]. One of the geometrical model is closer to the realistic anatomical structure, which is built based on CT scans in the portion of trachea and based on cast [48] in the portion of oral cavity. Other three geometrical models are simplified models, which are gained by using elliptic cross section, circular cross-section with the hydraulic diameter based on cast and circular cross-sections with equal diameters correspondingly.

In addition to the image-based geometrical model created by Xi et al. [74], there are other image-based geometrical models in the research [21, 46, 50, 53, 82, 107, 108]. As mentioned in the last section, the geometrical model built on CT or MRI scans is much closer to the realistic anatomical geometry of respiratory tract in aspects of the profile and topology. But most of the models have some simplification in the portion before tongue. For example, in the geometrical model of human upper airway built by Xi et al. [74] based on CT scans, the

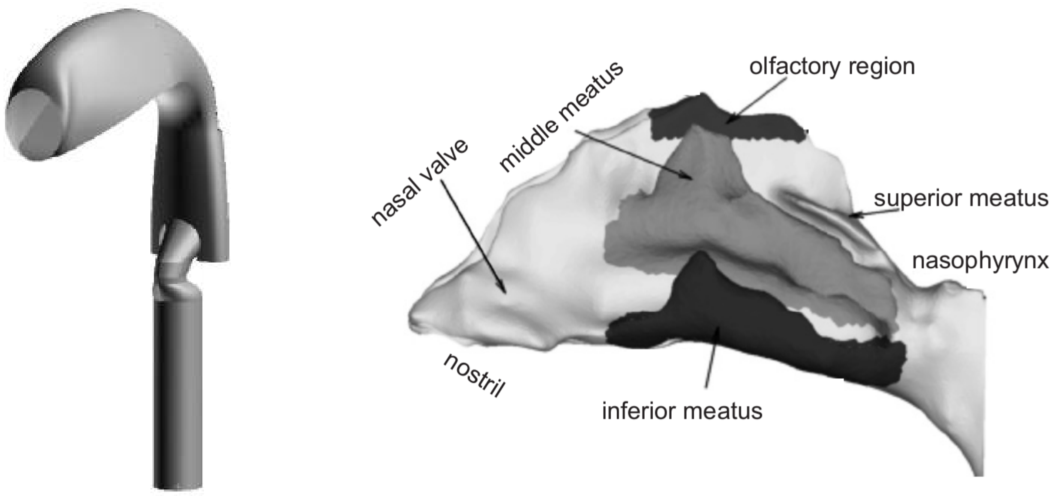

Fig. 2.3: Three-dimensional view of an idealized oral airway model [97] (left) and a nasal airway [79] (right) based on CT scans.

oral inlet is simplified with a circular tube. Takano et al. [21] built an oral airway based on MRI scans, which kept the properties of rough surface of the upper airway, but it does not demonstrate profile of the oral cavity before the portion of the tongue. In the extra-thoracic airway built by Jayaraju et al. [46], the portion of tongue and lips have been considered, but it seems that the angle of lips is not in accordance with the realistic situation. To study the laryngeal jet and intra-thoracic air flow, one geometry model of human upper system was created by Lin et al. [53]. This geometrical model includes the oral airway and 5 generations of bronchial branches. A circular tube is put at the mouth piece with a circular tube as well.

In addition to investigations of the oral airway, recently more researchers started to pay attention on the investigation in the nasal airway due to its ability to deliver systematical drug. The nasal cavity is very complex, which includes three different meatuses in the main airway region seen in Fig. 2.3 [79]. In addition, there are many passages to connect the nasal cavity and sinuses. As the author's best knowledge, there is no simplified geometrical model of nasal airway and most of them are built based on medical images [82, 109–115]. Some of them do not consider the nasopharynx or assume the nasopharynx as a tube. For instance, Shi et al. [79, 114, 116] created a nasal cavity on CT scans. Two tubes are added to nostril and one tube is used to model the nasopharynx.

In this project, a simplified mouth-throat model is constructed based on the dimensions of cast [48, 89], a more realistic mouth-throat model based on CT scans, and a nasal cavity based on CT scans as well. These geometries will be addressed in detail in Chapter 5.

2.1.3 Intrathoracic Region

During the past decades, a series of models of pulmonary branches have been adopted by researchers to study the respiratory airflow and particle transport. These studies either assumed the respiratory airways as symmetric bifurcation airways [117–125] or considered them as asymmetric airways [13, 55, 126–131]. Most of these geometrical models are based on Weibel Type A model [132]. The Weibel model has 23 generations with the assumption that each parent generation of lung branches is divided into two identical daughter generations symmetrically [9, 55]. However, this assumption does not match with the reality, even the equivalent diameters and length of individual tubes [18]. Moreover, the configuration is for normal adult lungs so that child and adult patients with asthma or other pulmonary diseases may have different features with the different geometrical models. Thus, various improvements and extensions [18, 133–136] are proposed for the geometrical model. Recently, following the Weibel Type A model, Kleinstreuer et al. [137] constructed a tracheobronchial model to study the air particle flow. The computational results are evaluated to be consistent with the experimental data.

However, the actual anatomical human bronchial airways display irregular features, and thus these regular airway models may not reflect the realistic properties of the human lung and then influence the precise prediction of the airflow field and particle motion in the lung. More realistic geometrical models [138–146] have been reported. Nowak et al. [147] and Cebral et al. [148] characterize one bronchial airway from generation 0 to generation 4 (G0 - G4) with CT scans. Van Ertbruggen et al. [149] created a geometry model for seven generations based on the morphometrical data created by Horsfield et al. in 1971 [134]. A 17 generations of human respiratory tract, which is the abstracted topological graphical data from anatomical model by Schmidt et al. [144], was adopted by Gemci et al. [83] to study the airflow in the human respiratory system. It includes a maximum 17 generations of the total 26 generations of the human tracheobronchial airways with 1453 bronchi [83]. Nonetheless, as long as restrictions on computer (and laboratory) resources prevail, simplified modeling approaches are necessary [9].

The alveolar sac appears from G20 of the bronchial trees at the end of alveolate duct in the Weibel's model [133]. At present, several kinds of idealized models have been applied in the investigations of acinar flow. These geometric models consist of a two dimensional (2D) long central channels surrounded by circular alveoli [150–152], a 2D multi-generation alveolate bifurcations [153, 154], a three-dimenisonal (3D) straight tube with hemispherical alveoli [155–157], 3D alveolate bends [158] and 3D alveolate bifurcations [159]. In these geometry models, the alveolar sacs are different. The circular alveolar sac is adopted by Tsuda et al. [160], and the sharp-edged polygon-cell was used by Darquenne et al. [26, 154].

2.2 Mathematical Methods

It is well known that the toxic particle motion and aerosol drug delivery in the human respiratory system are the phenomena of two-phase flows that involve micron and nanoparticles. In this section, the mathematical methods are discussed considering the methods to solve the two phase flows in the human respiratory system including both of the particle phase and gas phase.

2.2.1 Particle Phase

At present, there are basically two different approaches in the analysis of the phenomenon of particles dispersed in the air flow in the respiratory system such as Euler-Lagrange method [7] and Euler-Euler method [21]. In the Euler-Lagrange method, a particle trajectory is calculated by solving equations of the motion for each particle in the Lagrangian approach [21, 46, 73, 86, 161]. On the other hand, in the Euler-Euler approach, a particle concentration distribution of the carrier fluid is calculated [162–164].

In this research field, the Euler-Lagrange method is adopted mainly to solve the micro-particle and sub-micron particles and usually only drag force is adopted although there are different drag models [20, 46, 67]. Researchers also start to consider the influence of Brownian force on the sub-micron particle trajectories [67, 165]. There are different ways to couple the gas phase and particle phase. The commonly used and simplest way is one-way coupling, which only considers the influence of gas phase on the particle phase through the gas velocity [166]. The second one is the two-way coupling. In this way, the gas phase modifies the behavior of particle phase, which in return modifies the gas behavior of the airflow field because the micron turbulence is created in the interaction process. If particle volume density is large enough, the two-way coupling should be considered. Furthermore, if the particle volume density is so large that collisions among particles happen, the four-way coupling should be adopted.

Nowadays, most of numerical simulations adopt the one-way coupling and neglect the influence of the particle on the airflow field and interactions between particles due to low particle-loading. In this coupling way, it doesn't consider the injection mass from the inhaler in the clinical treatment. For instance, in this kind of coupling way, the properties of injected particles are particle diameter $d_p = 5$ µm, particle density $\rho_p = 1000$ kg/m^3 and particle number $N_p = 10,000$ [86]. Then the total injection mass is 0.65 μg. But in fact, in medical treatment, one actuation from inhaler, i.e. DPI, is usually 200 µg [6, 34]. Thus, the particle-loading is large enough for particles to influence the airflow. To consider the drug dose from the inhaler in the clinical treatment, it is necessary to apply the two-way coupling. In this case, the particle number can reach 10^{11}, therefore it is impossible to track each particle and it is necessary to adopt parcel method [166]. The parcel method assumes that there are more particles in one parcel with the same physical properties such as diameter and velocity [166]. If there are more particles, the volume fraction will become large, then it may be necessary to consider the influence of particle momentum on the airflow field at least, which means that two-way coupling should be adopted [166, 167]. At present one-way and two-way coupling are taken into account due to the low-loading particles in the air.

The Euler-Euler method is usually adopted to solve the nanoparticle diffusion in the gas flow in the respiratory system. Neglecting particle coagulation, surface growth, nucleation, and external forces, the standard convection-diffusion equation can be used to depict the transport of quasi-spherical nanoparticles under the Brownian force [7, 168]. More details on the method can be referenced in [7, 9, 168] since it is not main work of the thesis.

2.2.2 Gas Phase

One challenge in the numerical simulation of airflow field in the respiratory system is that the flow ranges from laminar, transitional and turbulent within the respiratory system, which requires the method not only to capture laminar flows, but also transitional and turbulent flow structures [9, 86, 88]. Nowadays, there are several approaches available in analysis of the laminar-transitional-turbulent flow in the human respiratory system such as direct numerical simulation (DNS) [53], large eddy simulation (LES) [55, 85, 88], Reynolds-averaged equations [46, 57, 70, 71, 161], detached eddy simulation (DES) [88] and Lattice Boltzmann method (LBM) [169]. Presently, little work has been developed with DNS because it requires huge amount of grid nodes, which can be estimated as $Re^{\frac{9}{4}}$ [10], which takes huge time and computer memory to conduct the computation.

RANS solves the averaged flow variables directly and model the turbulent effects through Reynolds averaged stress tensor [170]. There are two different ways to model the Reynolds stress, i.e. eddy viscosity model and Reynolds stress model [170]. Eddy viscosity models are based on the assumption that turbulent mixing, analogous to molecular mixing, is governed by an effective viscosity, the eddy viscosity [170, 171]. The turbulent effects are lumped to the eddy viscosity and Reynolds stress are expressed with it. In Reynolds stress model, the eddy viscosity is discarded and the Reynolds stresses are directly computed [170, 171]. The exact Reynolds stress transport equation is used account for the directional effects of the Reynolds stress [170]. Among plenty of turbulence models Two-equation models are popular, because it accounts for history effects like convection and diffusion of turbulent energy with the transport equations of turbulence variables [170, 171].

Two-equation models include two extra transport equations to describe the turbulent properties of the flow such as the transport equations of kinetic turbulent energy k and dissipation ϵ or specific turbulent dissipation ω [172]. $k - \epsilon$ model includes transport equations of kinetic turbulent energy, k, and turbulent dissipation, ϵ. k determines the energy in the turbulence and ϵ determines the turbulence scale [171]. It is suitable for simulating the flow with small pressure gradient [171], while it cannot accurately predict the flow containing large adverse pressure gradient [171]. The RNG $k - \epsilon$ model is developed using re-normalization group (RNG) methods by Yakhot et al. [173] to re-normalize the Navier-Stokes equations, which is to account for the effects of smaller scales of motion. In the contrast to the standard $k - \epsilon$ model, the RNG $k - \epsilon$ model uses the RNG approach to derive a turbulence model with a modified form of the ϵ equation aiming to account for the different scales of motion through changes to the production term. The $k - \omega$ model is another kind of the most commonly used two-equation turbulence models including the transport equations of kinetic turbulent energy k and specific turbulent dissipation ω [172]. Usually, $k - \epsilon$ model is good at simulating the free stream region and $k - \omega$ is robust in the near wall region [174]. Menter $k - \omega$ model [174] has combined the original $k - \omega$ model and $k - \epsilon$ model and keep both of the advantages of them. Shear stress transport (SST) $k - \omega$ model is improved based on the Menter $k - \omega$ model with the ability to account for the transport of the principal turbulent shear stress in the adverse pressure gradient boundary layers. In addition, low Reynolds number (LRN) turbulence models are created based on the $k - \epsilon$ or $k - \omega$ models such as the LRN $k - \epsilon$ model by Radmehr et al. [175, 176] and LRN $k - \omega$ model by [170] to simulate the viscous sub-layers.

Most of the previous work in this field use the RANS method to simulate the flow field, e.g. [20, 46, 50, 54, 71, 86, 90, 161, 165, 168]. Among these work, in 2001, Stapleton et al. [71] adopted the $k - \epsilon$ model to simulate the flow field using a Lagrangian tracking method coupled with the eddy interaction model to simulate the fluid-particle in a simplified mouth-throat model. It is observed that the model failed to predict the flow field in the relatively high flow rate and it is not suitable for the accurate prediction of particle deposition [71]. Four different turbulent models such as low Reynolds number (LRN) $k - \epsilon$ model [176], renormalization group (RNG) $k - \epsilon$ model [177], Menter $k-\omega$ model [178] and LRN $k - \omega$ [170], are used by Zhang et al. [90] to simulate the internal flow field in two different test conduits with local constrictions. The LRN $k - \omega$ model is identified to be more suitable to simulate the laminar-transitional-turbulent flow in the constricted tube [90]. The LRN $k - \omega$ model is widely used in numerical simulations of the flow field in the respiratory system [54, 84, 86, 161]. In addition, shear-stress transport (SST) $k - \omega$ model [46, 179] is proved to predict the transitional flow accurately [46]. The RANS model is suitable for fully developed turbulence, but it may be inappropriate for particle transport in the region with complex flow such as upper respiratory tract [88].

Recently, the prediction of particle deposition has been implemented more and more with large eddy simulation (LES). LES predicts the large scale flow structures by solving the filtered Navier-Stokes equations and modeling unresolved vortices with subgrid scale model. Thus, it is expected to have more accuracies than RANS method [180]. Luo et al. [56] used LES to simulate the flow in a single asymmetric bifurcation model and a constricted tube. It was demonstrated that LES predicts the transitional flow in the constricted tube better than the LRN $k - \epsilon$ model. Jin et al. [85] simulated the flow and micro-particle deposition in a three-dimensional geometric model of human upper respiratory tract. It is found that turbulent dispersion plays an important role in the particle deposition for the particles with small Stokes number. It is observed that particles with the diameter of 1 μm not only deposit on the opposite wall but also on the side wall. Jayaraju et al. [88] simulated the fluid flow in a human mouth-throat model under normal breathing condition (30 L/min) alternatively using RANS $k - \omega$ (without near-wall corrections), detached eddy simulation (DES), and LES methods. DES is a method based on RANS and LES, which is switched from a RANS model to a subgrid scale model in regions of grid fine enough for LES calculations [181]. Through comparison with existing experimental data in situations below 5 μm and larger particles, it is found [88] that for the medication aerosols inhaled at a steady flow rate of 30 L/min, LES and DES provide more accurate results than the RANS $k - \omega$ model in predicting particle deposition. Also, both the LRN $k - \omega$ and shear-stress transport (SST) $k-\omega$ model have been evaluated for the flow field in the constricted tube through comparison with experimental data and other RANS models, and these models are frequently used in the numerical simulation of particles transport and deposition in the respiratory system as mentioned above. However, no comparison has been made for the numerical results using LRN $k - \omega$, SST $k - \omega$ and LES [9] in the constricted tube. In present work, LES is adopted and the validation of the methodology with LES is performed through the comparison of flow field in the constricted tube with RANS/LRN $k - \omega$ model and RANS/SST $k - \omega$ model.

Until now, the governing equations have been solved with commercial software such as KIVA [182], FLUENT [168, 183] and CFX [20, 183]. Sometimes, it is accompanied with the user-defined program in C or FORTRAN. Little work has been done through in-house program, such as finite volume method (FVM) [21]. In the present work, the open source program platform of OpenFOAM 1.5 [184] is adopted due to its powerful ability to compute flow field and its possibility to adopt models defined by user. More details about OpenFOAM will be introduced in the Chapter 4.

2.3 Airflow and Particle Transport in the Human Respiratory System

Understanding of airflow structures in the human respiratory system underlines the basis for analyzing particle transport and deposition. The flow structure in the respiratory has been reviewed in the literature [7, 9, 118]. Historically, the research of aerosol dynamics in the lung were mainly related to toxic particulate matter deposition and its implications of negative health influence. The rapidly growing interest in aerosol drug therapy caused a shift in the application [7, 27]. Depending on interpretation of computational and experimental inhalation investigations, toxic particle deposition results can appear as therapeutic drug-aerosol targeting outcome due to the relationship between them [185]. So, the scientific investigation will benefit them [7].

2.3.1 Airflow and Particle Transport in the Extra-Thoracic Region

In this section, investigations on the flow field and particle transport in the extra-thoracic region are explained. Special attention is paid to the micro-particle transport and deposition in the oral airway. A simplified overview is given to the issues related to nanoparticle motion in the oral airway and particle transport in the nasal airway since it is not main part of the thesis.

2.3.1.1 Properties of the Airflow

The flow field in the respiratory system has been investigated significantly through experimental and numerical methods. The main features of the time-averaged flow field in a simplified oral airway based on cast have been identified by Zhang et al. [86]. They included the recirculation zones after the mouth cavity, the soft palate and glottis, and the laryngeal jet. The flow structure shows very different properties with different geometrical topology. In the numerical results of Zhang et al. [86], no turbulence is found at an inspiration flow rate of 15 L/min, but there is turbulence observed in the numerical simulation of Jayaraju et al. [46] at the same flow rate. It was argued that the geometry used by Zhang et al. [86] is simplified, whereas Jayaraju et al. [46] presented and discussed a more realistic extra-thoracic airway based on CT scans. It is also interesting that the turbulence onset was observed in the experimental study referenced by Stapleton et al. [71] in the tracheal cast when the flow rate is more than 3 L/min.

Due to glottal contribution, a laryngeal jet is generated after the glottis in the trachea and the geometrical influence can also be observed in the larynx. As emphasized by Xi et al. [186], the orientation between the larynx and the trachea in a simplified laryngeal-tracheobronchial model has great influence on the laryngeal jet within the trachea so that the laryngeal jet has different profiles. For instance, a laryngeal jet located in the center of the trachea without impinging on the wall is studied in the numerical simulation of Zhang et al. [86]. They investigated a circular idealized mouth-throat, which includes the circular larynx and straight trachea [86]. However, several other studies are in contrast to these findings. The study of Jayaraju et al. [88] shows the laryngeal jet to impinge on the front side of the trachea in a simplified mouth-throat model with forward-sloped larynx and straight trachea configuration. Xi et al. [186] found that the laryngeal jet is skewed towards the right side of the trachea. They used an approximate model of the upper tracheobronchial airways with a forward-sloped larynx and rearward-sloped trachea. The result is in agreement with the *in vitro* experiments of Corcoran and Chigier [187]. Recently, Lin et al. [53] found a laryngeal jet to approach the back of the trachea in a patient-specific airway model with rearward-sloped larynx and a straight trachea. In fact, not only the orientation of the larynx and trachea influences the entrance of the laryngeal jet, but also the shape of glottal aperture affects the laryngeal jet and reverse flow pattern. Brouns et al. [188] studied the influence of the shape and cross-section area on the flow structure with circular, triangular, and elliptical glottal aperture in an idealized mouth-throat model. It was found that the triangular glottal aperture shifted the laryngeal jet in the direction of posterior wall, and there were two pairs of counter-rotating secondary vortices corresponding to one pair in the cases of circular and elliptical apertures.

Researchers found that the laryngeal jet also influences the flow field in the tracheobronchial (TB) region. Xi et al. [186] found that the secondary motion in the daughter branches were stronger when computed with the standard TB model compared to the laryngeal-TB model. Moreover, a laryngeal jet is predicted using the laryngeal-TB model which includes the larynx. Lin et al. [53] found that the turbulence induced by the laryngeal jet can significantly affect the flow patterns as well as tracheal wall stress. They also found, neglecting the oropharynx, the larynx generated different flow structures including velocity parabola in the trachea, and turbulence was negligible.

In addition to concentrating on the laryngeal jet, researchers recently started to pay more attentions to other flow structures in this region. Secondary flows, which is the flow at the plan vertical to the main flow direction, in the form of multi-vortex structures behavior in the context of double bifurcation model were studied by Leong et al. [189] through numerical simulation and experimental visualization. It was found that secondary vorticity is amplified through the vortex line stretching due to the secondary flow within the daughter tube. Ball et al. [190] used the RANS $k - \omega$ model to conduct high-resolution turbulence modeling of airflow in an idealized human extra-thoracic airway, and the flow structure was analyzed through iso-surface plots of the negative second eigenvalue of symmetry square of velocity gradient tensor [191]. It was observed that the recirculation bubble formed anterior to the epiglottis. The laryngeal jet impinging on the anterior wall of the trachea causes circumferential flow resulting in repeating secondary vortices. Lin et al. [53] applied a proper orthogonal decomposition [192] technique to study the vortices in an upper human airway based on CT scans. The analysis revealed Taylor-Görtler-like [53, 193] vortical structures, which is the secondary flow that appears in the boundary of concave wall [193], residing in the supra-glottis and the sub-glottis, and counter-rotating vortices appear in the main-stem bronchi. Moreover, these vortical structures are related to the regions of local maximum coherent turbulence. Even though the laryngeal jet and secondary vortices have been studied extensively as discussed above, few investigations concern the time-dependent motion of the flow structure.

In addition to the study of flow field in the oral airways, the flow field has been investigated in the nasal airway as well. Keyhani et al. [194] and Subramaniam et al. [195] modeled a steady laminar airflow pattern in the nasal cavity and compared their results with the experimental data by Hahn et al. [196] and the streamlines of the airflow were given in numerical investigation of Horschler et al. [197]. Recently, more details on the local airflow structures was presented in the narrow and complex flow by Shi et al. [114] and [164]. The typical nasal flow has been introduced by Kleinstreuer et al. [9]. The main feature of flow field in the nasal cavity include:

1) the majority of flow going through the middle-to-low portion of the main passage way between the middle and inferior meatuses;

2) two high speed regions locating under the middle and inferior meatuses [114];

3) small amount of flow reaching the narrow olfactory region and the upper part of the middle and inferior regions;

4) strong secondary flow existing in the middle part of the nasal cavities due to local geometric complexity and the change of flow direction in the vestibule.

Moreover, it was found that the flow in the nasal cavity is influenced by other factors including inflow conditions [114], airway geometry and the size, and orientation of the internal nasal valve [198], which decides the gas velocity direction at the inlet plane. The influence of nasal airway can be revealed from the different geometries available in the literature. However, the CFD techniques used including geometry generation, grid generation, and physical models and numerical methods to solve governing equations are different as well and therefore it is more difficult to identify the geometry influence. Until now, there is no specific investigation on nasal geometric influences reported [9].

2.3.1.2 Properties of the Particle Transport and Deposition

As mentioned above, the micro-particle and nanoparticle transport are two different physical processes. So, there are different regulations governing the particle-deposition. Usually, there are three main mechanisms of micro-particle deposition in the respiratory system: inertial impaction, gravitational sedimentation and diffusion [6, 7]. And nanoparticle deposition is mainly regulated by Brownian diffusion [95] and inertial effect can not be neglected for ultrafine particles [54].

Inertial impaction has dominant effect on larger and fast-moving particles, which is controlled by impaction parameter. The inertial impaction of particle is decided by the air inspiration flow rate Q, particle diameter d_p, and particle density ρ_p and it can be expressed with the impaction parameter (IP) [7]:

$$\mathrm{IP} = \rho_p Q d_p^2. \tag{2.1}$$

Thus, the larger of IP means the larger of particle inertial impaction [7]. Gravitational settling is a function of particle size, particle density and time, with the rate of settling proportional to particle size and particle density [199]. Diffusion takes main action for the ultrafine particles in high concentration gradient region [200]. These mechanisms take effect as aerosol particles are inhaled orally or through the nose. Particles larger than 10 µm are filtered in the nose and/or oropharynx, most likely by inertial impaction; particles of 5 - 10 µm generally reach the proximal generations of the lower respiratory tract, and particles of 1 - 5 µm reach the lung periphery, seen in Fig. 2.4 [45].

The particle deposition can be identified with terms of deposition fraction (DF), deposition

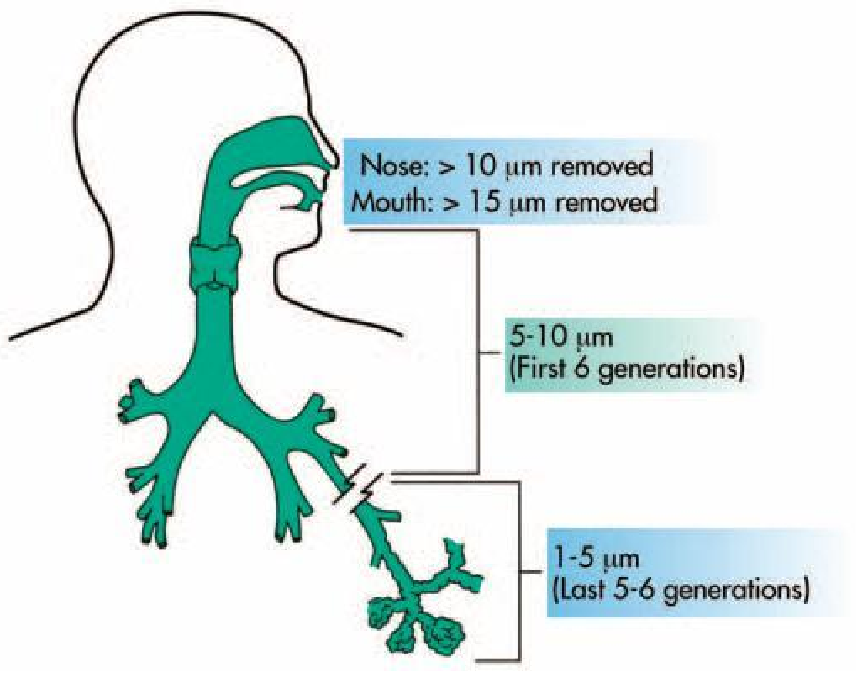

Fig. 2.4: A simplified view of the particle deposition location related to the size [45].

efficiency (DE) and deposition enhance factor (DEF) in a specific respiratory region such as oral airway, nasal cavity and different tracheobronchial branches defined in [59]. DE is defined as ratio of the particle deposition number to the total injected particle number. DF is ratio of the particle deposition number to particle entering into this region. DEF is a parameter to depict the local particle deposition pattern. It is is defined as the ratio of local to average deposition densities. The deposition densities are computed as the number of deposited particles in a surface area divided by the size of that surface area [59]In the past decades, micro-particle transport and deposition have been extensively studied by a lot of researchers in the oral airways [48–50, 58, 59, 64, 70, 71, 86, 89, 200–204]. The main features of micro-particle deposition efficiency is that the particle deposition increases with particle size since the particle inertia increases with particle size. The increasing inspiration flow rates will also enhance the particle deposition due to the impaction parameter increase and large turbulent dispersion.

Besides the total deposition fraction, the regional deposition fraction is another parameter to evaluate the particle deposition. It is well-known that the micron particle deposition during inhalation in the oral airways mainly results from impaction, secondary flow convection, and turbulent dispersion [59]. Hence, they mainly deposit in the stagnation points and sudden geometry change region of cross-sectional area or surface profile [59, 86]. But the results are very different between idealized mouth-throat based on cast and image-based upper airway. For example, in the image-based geometrical model of upper airway [21, 46], it is found that most particles deposit in the mouth-larynx region and few particles can reach the larynx and trachea, but there is higher particle deposition in the trachea in the simplified mouth-throat based on cast [59, 86]. These differences mainly come from the geometric complexity. More realistic model based on medical scans is more complex and it produces more barriers leading to the particle impacting on the wall of the oral-pharynx region.

Other than total and regional particle deposition, local particle deposition pattern is another important parameter for the assessment of particle deposition influence on the health [59, 205, 206]. As particles mainly deposit at stagnation points, more particles may concentrate on the tongue portion, the outer bend of the pharynx/larynx, and the regions close to glottis. Particle can also dwell on the tracheal tube due to the turbulent dispersion and secondary flows. Hence, maximum DEF may appear in this region. Zhang et al. [59] studied the DEF of particles ranging from 1 µm to 10 µm under the inspiration flow rate of 15 L/min, 30 L/min and 60 L/min in the oral airway. Two obvious peaks of DEF can be observed in the condition of $Q_{in} = 30$ L/ min, $d_p = 7$ µm and $Q_{in} = 15$ L/ min, $d_p = 10$ µm. It is also found that the maximum DEF at the higher inspiration rate of 60 L/min is lower than those at the lower flow rates of 30 L/min and 15 L/min. They attributed it to the strong turbulent dispersion and broader distribution of deposited particles under the higher inspiration flow rate [59].

The particle trajectories have been discussed in the work [86] as well to demonstrate the effects of airflow and Stokes numbers. Different particle trajectories were observed in their work and some particles are seen to be entrained by the recirculation flow. Particles at close initial positions were observed to have different properties, such as exiting the mouth-throat model or depositing on the surface. They attributed it to two factors of inhomogeneity of flow field and randomness of turbulence. The same particle in the same initial injection position displays different trajectories in different Stokes number. In the summary, the turbulence has minor effect on the particle trajectory at high Stokes number, and in contrast, has high effect on particle trajectories at smaller Stokes number, which is observed by experiment [207] and other numerical simulations [73, 165] as well.

To target aerosol drug at special site of the human lung, the released locations were studied by Zhang et al. [208] in an oral airway connected with a symmetric triple-bifurcation model. Particle distribution in two different released points at the inlet plane was simulated under the inspiration flow rate of 8 L/min and spherical particle of 7 µm. It is found that the profile of particle distributions at one cross section in trachea fit well with the experimental results [7, 208]. The targeted drug delivery can be implemented by specifying inlet positions of aerosols that deposit on different targeted sites. The specific initial particle deposition are determined via backtracking, which is decided by the relationship between the final and initial positions [7]. Thus, most aerosols will deposit in the desired lung regions, which can be seen from the second cases with four circles located in an orbital path [7, 208].

Most of the investigations have adopted mono-disperse particles in the oral airway, but recently Longest et al. [47, 165] adopted poly-disperse particles. In their studies, they adopted the poly-disperse particle distribution from the laser fraction for the ambient particles. Particles are injected with the same particle number for each class and the final mass deposition results were scaled to reflect the experimentally determined initial poly-disperse size distribution [47]. The poly-disperse particle deposition efficiency from the numerical simulation is fit with the experimental measurement [47].

In comparison with the investigation of micro-particle transport and deposition, there are relatively few investigations of nanoparticle deposition in human respiratory system, mainly due to the difficulty to generate nanoparticles for the experimental measurements and accurate prediction with numerical methods [7, 9]. The regional deposition fraction to evaluate nanoparticle deposition can be determined according to Fick's law [84] as:

$$DF_{region} \;=\; \sum_{i=1}^{n}\left[-A_i\left(\tilde{D}+\frac{\nu}{\sigma_Y}\frac{\partial Y}{\partial n}\right)|_i\right]/(Q_{in}Y_{in}), \tag{2.2}$$

where DF_{region} is particle deposition fraction; Y is the mass fraction; σ_Y is the turbulent Schmidt number; A_i is the area of the local wall cell, i; n is the cell number of wall in one certain region of the airway and $\tilde{D}$ is diffusion coefficient of nanoparticles. In a series of publications, Cheng et al. [51, 209–212] measured ultrafine particles ranging from 3.6 nm to 150 nm transferred and deposited in the upper airways, among others. It is also studied by the numerical simulations in the work [59, 84, 164, 213]. With these experimental and numerical data, it is probable to build empirical equations to predict particle depositions summarized in [61]. Contrary to micro-particle deposition, with the particle size increasing, the particle deposition decreases for nanoparticles because the diffusive capacity is reduced.

The nanoparticle deposition pattern on the wall becomes more uniform with the increasing particle diameter, which can be attributed to significantly decreasing diffusivity and more uniformly distributed concentration field in the tubes for larger nanoparticles [84]. Similar to the particle size, the higher the inhalation flow rate is, the lower the deposition of nanoparticles would be. But in comparison with particle size, the inspiration flow rate has a minor effect on nanoparticle deposition [59].

With the development of nasal drug delivery [12, 214–217] including the targeted position of nasal cavity and deep site of lung through nasal airway, investigations have been made in the nasal airways [79, 114, 116, 198, 218, 219] including the micron particles and nanoparticles. Similar to oral airway, micro-particle deposition in nasal airway during inhalation are mainly regulated by inertial impaction, secondary flow convection, and turbulent dispersion. Under combined functions of these factors forementioned, the hot spots may appear in the nasal airways. Shi et al. [116] found there were three major hot spots (high DEF location mentioned above) in the nasal airways, i.e. the first one in the nasal valve, the second one on the top of meatus wall or middle turbinate, and the last one near the nasopharynx. Moreover, since the cross-sectional area of the passages of nasal cavity is narrow and the Reynolds number is low resprestively, the wall roughness of replica and nasal hairs may significantly affect the *in vitro* and *in vivo* of large micro-particles deposition in nasal cavities [116]. Different from micro-particles in the oral airway, the inertial deposition in the nasal cavity may be simply a function of only Stokes number [9, 61] and without Reynolds number. This may result from the fact the Reynolds number in the nasal cavity is much lower than in the mouth-throat. Earlier research have found that the axial flow can indicate the particle concentration for micro-particles with a low impact parameter, whereas secondary flow may help particles to move into the meatus regions. Although the particles with higher inertia can be driven out more from the flow streamlines, the flow region with larger velocity still carries more particles, in particular, in the main passage way beneath the middle meatus.

Similar to nanoparticle deposition in the oral airway, the nanoparticle deposition in the nasal cavity is governed by diffusion as well and therefore the particle deposition efficiency decreases with the particle size increasing. Local nanoparticle deposition pattern in the nasal airways was studied by Shi et al. [114] and Xi et al. [220]. It was observed by them that the majority of particle deposition happens in the anterior part of the nasal cavity due to the high diffusivity, in particular, for particle with the diameter of 1 nm. In contrast, smaller deposition flux occurs in meatus regions because most particles can not reach the deeper regions of the meatuses. High DEF values can be seen around the nasal valve region due to the locally narrowing airway. Most of the 1 nm particles pass through the middle-to-low main passageway under the convection of the main air flow portion. Specially, a high particle concentration is seen in the main passage way below the middle meatus. Some nanoparticles may enter the meatuses due to both diffusion and secondary flow effects. Furthermore, a larger portion of particles can go through the olfactory when the flow rate increases. For larger particle with size of 5 nm, the distribution of particle deposition fluxes are a bit more uniform because the particle concentrations are distributed somehow more evenly in the airways. Even so, hot spots are basically located in the same region and thus the nasal valve region and middle-meatus zones experience the highest DEF values. In addition, it was also found that the modeling methodologies and solvers may influence the prediction of particle deposition [114] produced the different prediction of flow fields.

2.3.2 Airflow and Particle Transport in the Intrathoracic Region

The property of airflow in the intrathoracic region is very important for understanding the aerosol drug particle pattern and toxic particle dispersion. In this section, the flow field and micron and nano particle motion in the tracheobronchial airways and alveolar region will be presented.

2.3.2.1 Properties of the Airflow

Research has been developed from the first generation to more generations of tracheobronchial airways since the flow field in the first generation largely influence the subsequent flow in the subsequent bifurcations [123, 221]. Turbulence intensity [137, 222], secondary flow [20, 223] and reversed flow [157] are considered in these research during inspiration and expiration phases [9, 20].

Turbulence level was found to decay in the trachea. But the severe geometric transition from parent branch to daughter branch may induce new unsteadiness in the daughter tubes [137]. It was extensively reported that turbulence intensity is enhanced around the flow dividers due to the contraction of the top and bottom surface in the carinal ridges [9] because the contraction may increase the Reynolds number. These enhancements of flow instabilities may help turbulence occur in trachea to propagate to a few generations, i.e. G6 [137, 222].

Secondary flows appear in the bronchial airways because of the upstream flow properties and the pressure gradient induced by centrifugal force [9]. The magnitudes and structures of the secondary flow are determined by several factors including the flow direction, Dean number , Reynolds number, geometric features, axial location with respect to the carinal ridge and Womersley number for oscillatory flows [9, 20, 122, 223, 224]. The Dean number is a dimensionless number in study of flow in curved pipes and channels, which is used to evaluate the secondary flows. For flow in a pipe or tube, Dean number, De, is defined as [225]:

$$De = \frac{\rho V D}{\mu}\left(\frac{D}{2R}\right)^{1/2} \tag{2.3}$$

where, ρ is the density of the fluid; μ is the dynamic viscosity; V is the axial velocity scale; D is the diameter, R is the radius of curvature of the path of the channel. The Womersley number, α, can be defined as [226]:

$$\alpha = R\left(\frac{\rho\omega}{\mu}\right)^{\frac{1}{2}} \tag{2.4}$$

where, R is an appropriate length scale; ω is the angular frequency of the oscillations; and ρ and μ are density and dynamic viscosity of the fluid respectively. The Womersley number results from the solution of the linearized Navier-Stokes equations for oscillatory flow in a tube [226]. It expresses the ratio of the transient or oscillatory inertia force to the shear force. The intensity of secondary flows, which can be expressed as the ratio of the mean secondary velocity, the velocity on the plane vertical to the main flow direction, to the amplitude of the mean axial velocity, may not be larger than 20% in the conducting act [20, 223]. In general, secondary flow still exists in the generations from G10 - G13 [163, 223] and the flow may fully develop after generation G12 with decreased Reynolds number. Double or quadruple secondary vortices [122, 123, 149] can appear in different generations of branches. The four-vortex secondary flows appearance was recognized to vortex line extension upstream from the second bifurcation in the work of Leong et al. [189]. The quadruple vortices were also observed to merge into two vortices in the subsequent branches [123]. In addition, secondary vortices have not been observed in some short bronchi in the CT-based lung model due to the length limitation of flow development [55].

The air flows in the bifurcations have very different properties between inspiration and expiration phase [9, 20]. Different from flow splitting at flow dividers in the inspiratory flow, two flow streams meet in parent tube and it may produce M-shape velocity profiles near flow dividers [9] in the expiratory flow. The flow merging may influence the secondary vortices in the parent tube. Two pairs of helical vortices can be generated by the converging flow streams from parent tubes [20, 118, 223]. During expiratory phase, the secondary flow pattern is much more important due to its influence on particle transport. In contrast to inspiration flow, the inlet flow rate has less influence on the flow pattern in the expiratory flow [223].

The Reynolds number is much smaller in the alveolar region, which is less than 1 [9]. Even in this low Reynolds number, the flow field is still very complex due to the complex geometry features and the rhythmic contraction and expansion of the alveoli [9]. The flow in the alveoli is typically depicted by Poiseuille-like profiles in the lumenal flow accompanying with recirculation flow [116]. The recirculation zones are observed in each alveoli by experimental or numerical methods [146, 158, 221] as well. The patterns of flow streamlines are sensitive to the ratio of the alveolar flow to the ductal flow [151] and profiles of the alveoli and the ratio of cavity volume to duct volume. Karl et al. [157] found one or two recirculation regions appearing in the cavity depending on the different ratios of cavity volume to duct volume and the depth to the width of the cavity through numerical simulation and experimental observation of the flow field via particle image velocimetry (PIV). In addition, the flow in the alveoli shows chaotic behavior as well [155, 156] and it produces convective mixing.

Nonetheless, most of these findings are based on the rigid model. However, the alveolar flow patterns exhibit different features under rhythmic lung expansion and contraction motion in contrast to the case of a rigid alveoli [227]. It is found that the wall expansion induces radial flow in the proximal corner of alveoli and it wraps around the recirculation region, which largely influences the features of the flow patterns in the alveolus. Generally, it is still a great challenge to understand the properties of flow in realistic alveoli considering the physiologically fluid structure interactions.

2.3.2.2 Properties of Particle Transport and Deposition

Particle deposition in the TB airways has been found to be contributed to the occurrence of asthma attacks [228] and bronchogenic carcinomas [229, 230]. Aerosol drug deposition in the TB region can reduce drug delivered into pulmonary region [18, 231]. In contrast, some aerosol drug are targeted to TB region, such as bronchodilator and corticosteroids, to treat TB airway asthma [232, 233]. A series of research has been developed to study the particle transport and deposition in the lung with experimental and numerical methods from one to several bifurcations of the TB trees [13, 14, 20, 54, 66, 67, 87, 122, 124, 127, 128, 147, 149, 162, 206, 215, 234–247].

These studies have emphasized the significant influence of upstream flow [70, 248], cartilaginous rings [14, 249], heterogeneous outflow [250], the use of triple bifurcation models [123], transient flow [20], asymmetric branching [128, 232] and models with obstruction or asthma [232, 251–253]. All of these factors affect actual particle deposition in the lung.

The investigations have confirmed that the location of bifurcation airways and airway geometry features, i.e. asymmetry, non-planar, obstruction may influence particle deposition in the bronchial airways [20, 26, 72, 125, 131, 147]. It is also found that micron particles tend to accumulate around the carinal ridges and to form “hot spots” (high DEF) because of the impaction and secondary flows, which is observed in the experimental [229, 254] and numerical modeling [20, 59, 206, 235, 255]. These “hot spots” increase the possibility of local pathological changes in the lung such as the formation of lung tumors [206].

Recently, the micro-particle transport has been studied in a 16th generation by Zhang et al. It is found that the micron particle deposition is still mainly controlled by particle inertia [72] in the large airways. The micron particle deposition caused by impaction in the small airways may decease with the reduction of flow rates, but the deposition caused by sedimentation probably increase with more residence time [72]. In the large airways such as G1 - G3 of bifurcations, micro-particles mainly deposit in the location around the carinal ridges. In contrast, at medium or small airways, i.e. G7 - G9 and G13 - G15, particle deposition pattern changes to some extent due to the effect of sedimentation. Some particles can be diverted to other places than carinal ridges, which leads to decline in the maximum DEF values. Moreover, in addition to the “hot spots” in the carinal ridges, the airway surface perpendicular to the gravity direction can become high-deposition region.

In the alveolar region, particle deposition in respiratory zones has also been investigated in the past decades based on simplified alveolar ducts, alveolar sacs, and single alveoli [9, 146, 150, 154, 155, 159, 256, 257]. It is found that micro-particle deposition is regulated primarily by gravitational sedimentation in the alveolar regions [9, 258]. Thus, the micron particle deposition pattern is non-uniform on the alveolar walls. In addition, the particle deposition in the alveolar region is also affected significantly by the orientation and presence of bifurcation zones [9, 146]. It is also found that it may influence the particle deposition efficiency and site when the alveolar wall expands and contracts rhythmically [256]. Hence, fluid-structure interaction analysis is important for micro-particle transport in deformable alveolus, considering that tissue forces also influence the movement of the wall [150].

Up to now, as author's best knowledge, there are few studies developed for numerical investigations considering vapor or ultrafine particles transport and deposition in the alveolar region. But, in the reality, large amount of inhaled vapors may appear in the alveolar region [9]. Moreover, the low surface tension, which is generated by the surfactant membrane in the alveolar region, increases the possibilities of these nanoparticles transferring through the liquid wall layer [259]. Thus the vapor and ultrafine particles deposition in the alveolar region are enhanced in line with therapeutic or toxic effects [9].

3. Governing Equations and Models

In this chapter, the equations and models used in the Euler-Lagrangian method with one-way and two-way coupling are presented.

Since the gas velocity in the human upper airway is very low relative to the sound velocity in the ambient environment, it assumes that the airflow is incompressible and three-dimensional incompressible equations are adopted. As it is discussed in the section 2.2.2 that one of the challenge in this field is to predict the laminar-transitional-turbulent flow in the complex respiratory tract. It has shown in the section 2.2.2 that LES and RANS/SST $k - \omega$ are suitable for the numerical simulation of the gas phase in the human upper airway. Therefore they are adopted in the present work and introduced in this section.

For the particle phase, it is assumed that the particle are solid ball and they donot interact with each other. One-way or two-way coupling is adopted depending on whether the drug dose from inhaler in the clinical treatment is considered. Only the drag force and Brownian force are adopted because the ratio of particle density to gas density is quite large. More details on the exerted force model are discussed in sections 3.5 and 3.6.

3.1 3D Instantaneous Navier-Stokes Equations

In the present work, two different coupling ways are adopted to couple the gas phase and dispersed particle phase. The first is simplest one-way coupling, which considers the particles traveling in the gas field without influencing the gas phase [166]. In this case, three dimensional incompressible Navier-Stokes (N-S) equations are used [85] without any additional terms. Another method is the two-way coupling method, which not only considers the influence of gas phase on the particle phase, but also considers the influence of particle phase on the gas phase through momentum source [260]. The governing equations of gas phase are shown as follows [260]:

Continuity Equation

$$\frac{\partial(U_j)}{\partial x_j} = 0, \tag{3.1}$$

Momentum Equation

$$\frac{\partial(U_i)}{\partial t} = -\frac{\partial}{\partial x_j}[U_i U_j] - \frac{\partial}{\partial x_i}\left[\frac{p}{\rho}\right] + \frac{\partial}{\partial x_j}\left[\nu\left(\frac{\partial U_i}{\partial x_j} + \frac{\partial U_j}{\partial x_i}\right)\right] + S_{p,i}. \tag{3.2}$$

The source term S_p is generated by the particle-fluid interactions. Its value is defined related to the coupling way. S_p is equal to 0 when one-way coupling is adopted or only the gas phase is studied. In the two-way coupling, it is equal to the amount of the force exerted by a particle on a unit volume of fluid ∇V, which is given as the change in particle momentum during the period of particle interaction with fluid. The expression of S_p [260] is given as follows:

$$S_{p,i} \;=\; \begin{cases} 0 & : \text{ one} - \text{way coupling} \\ \sum_{\alpha=1}^{N}[\frac{m_p}{\nabla V}\frac{(U_{p,i})_{t_{out}}-(U_{p,i})_{t_{in}}}{t_{out}-t_{in}}]_{\alpha} & : \text{ two} - \text{way coupling.} \end{cases} \tag{3.3}$$

After calculating the particle movement during an Eulerian time step, the source term generated by the particles is evaluated with the Eq. 3.3 and the fluid velocity is updated with gas phase governing equations.

3.2 Reynolds Averaged Navier-Stokes Equations

When the flow is turbulent, a physical variable can be divided in two components, a mean (time-averaged) component and a fluctuating component [10], such as

$$U_i \;=\; \bar{U}_i + u^{'}, \tag{3.4}$$

$$p_i \;=\; \bar{p}_i + p^{'}, \tag{3.5}$$

the symbol of bar, -, represents the time-averaged part and the prime, ′, represents the fluctuating part. Above manipulation is referred to Reynolds decomposition. By taking these decompositions into the instantaneous equations and average the instantaneous gas equations, the Reynolds Averaged Navier-Stokes equations [10] are generated as follows:

$$\frac{\partial(\bar{U}_j)}{\partial x_j} \;=\; 0, \tag{3.6}$$

$$\frac{\partial(U_i)}{\partial t} \;=\; -\frac{\partial}{\partial x_j}[U_iU_j] - \frac{\partial}{\partial x_i}\left[\frac{p}{\rho}\right] + \frac{\partial}{\partial x_j}\left[\nu\left(\frac{\partial U_i}{\partial x_j} + \frac{\partial U_j}{\partial x_i}\right)\right] - \frac{\partial}{\partial x_j}(\overline{u_i^{'}u_j^{'}}). \tag{3.7}$$

A new term $\overline{u_i^{'}u_j^{'}}$ is produced in the Eq. 3.13 and it is called as Reynolds stress tensor. Reynolds stress tensor represents the correlation between fluctuating velocities and all of effects of the turbulent fluid motion on the mean flow are lumped into the single term via the averaging manipulation [10] as presented in the section 2.2.2. The RANS equations are not closed because of Reynolds stress tensor [171]. There are two different ways to close the RANS equations and they are eddy viscosity models and Reynolds stress models [171, 261]. In the present work, the eddy viscosity model of $k - \omega$ is adopted and it will be presented in detail in section 3.4.1.

3.3 Large Eddy Simulation

As mentioned, LES is used to model the turbulence due to its capability to capture the properties of laminar-transitional-turbulent flow. Both of the Smargorinsky subgrid scale model [262] and dynamic Smagorinsky subgrid scale model are adopted. In the present work, Smagorinsky model is used in modeling both of gas phase and particle phase, whereas the dynamic Smagorinsky subgrid scale model is only used in modeling the gas phase.

If filtered variance is depicted [85] as:

$$\widetilde{\phi}(x,y,z) \;=\; \frac{1}{\Delta x \cdot \Delta y \cdot \Delta z}\int_{x-\frac{1}{2}\Delta x}^{x+\frac{1}{2}\Delta x}\int_{y-\frac{1}{2}\Delta y}^{y+\frac{1}{2}\Delta y}\int_{z-\frac{1}{2}\Delta z}^{z+\frac{1}{2}\Delta z}\phi(\xi,\eta,\varphi,t)d\xi d\eta d\varphi. \tag{3.8}$$

After the filtering operation, the volume-averaged three-dimensional N-S equations will be:

$$\frac{\partial(\widetilde{U}_j)}{\partial x_j} \;=\; 0, \tag{3.9}$$

$$\frac{\partial(\widetilde{U}_i)}{\partial t} \;=\; -\frac{\partial}{\partial x_j}[\widetilde{U}_i\widetilde{U}_j] - \frac{\partial}{\partial x_i}\left[\frac{\widetilde{p}}{\rho}\right] + \frac{\partial}{\partial x_j}\left[\nu\left(\frac{\partial\widetilde{U}_i}{\partial x_j} + \frac{\partial\widetilde{U}_j}{\partial x_i}\right) + T_{ij}\right] + \widetilde{S}_{p,i}, \tag{3.10}$$

where

$$\widetilde{S}_{p,i} \;=\; \begin{cases} 0 & : \text{ one} - \text{way coupling} \\ \sum_{\alpha=1}^{N}\left[\frac{m_p}{\nabla V}\frac{(\widetilde{U}_{p,i})_{t_{out}}-(\widetilde{U}_{p,i})_{t_{in}}}{t_{out}-t_{in}}\right]_\alpha & : \text{ two} - \text{way coupling.} \end{cases} \tag{3.11}$$

Here, T_{ij} is sub-grid scale tensor and its expression is as follows:

$$T_{ij} \;=\; \widetilde{U_iU_j} - \widetilde{U}_i\widetilde{U}_j. \tag{3.12}$$

3.4 Eddy viscosity Models

From the RANS equations and filtered N-S equations, it be can seen that the unsolved turbulent terms of Reynolds stress tensor and subgrid stress tensor are produced. These terms are required to be modeled. In present work, eddy viscosity models are adopted for both of the RANS and LES. Eddy viscosity models are based on an artificial eddy viscosity approach, where the effects of turbulence are lumped into a turbulent viscosity. The main difference of the eddy viscosity approach in RANS and LES is the former to model the Reynold stress tensor and the latter to model the subgrid scale stress tensor [171]. Shear stress transport (SST) $k - \omega$ model [174, 178] for RANS equations and Smagorinsky subgird scale model [262] and dynamic Smagorinsky subgrid scale model [263, 264] for LES are presented in the sub-sections.

3.4.1 Shear Stress Transport $k - \omega$ Model

In 1887, Boussinesq first proposed relating the turbulence stresses to the mean flow to close the system of equations. With the Boussinesq assumption [10, 265], the Reynolds stress tensor can be written as:

$$\overline{u_i^{\prime}u_j^{\prime}} \;=\; -\nu_t\left(\frac{\partial\bar{U}_i}{\partial x_j} + \frac{\partial\bar{U}_j}{\partial x_i}\right) + \frac{2}{3}\delta_{ij}k, \tag{3.13}$$

where $k = \frac{1}{2}\overline{u_i^{\prime}u_i^{\prime}}$ is the turbulent kinetic energy.

There are different kinds of eddy viscosity models depending on the way to close the eddy viscosity. Among them, two equation eddy models are popularly used since they can predict the turbulent flow without any prior knowledge of turbulent structures. The shear-stress-transport (SST) $k - \omega$ model, which is created by Menter [174], is a blend of a $k - \omega$ model and $k - \epsilon$ model. $k - \omega$ model is used simulate the flow near wall, and $k - \epsilon$ is used in regions far from the wall. The shear-stress-transport (SST) $k - \omega$ model is quite robust and it can predict the flow near the boundary and the recirculation flow accurately, which is suitable for the present work.

In the SST $k - \omega$ model, the eddy viscosity [174, 178, 261, 265] are defined by the expression of k and ω, as:

$$\nu_t = \frac{a_1 k}{\max(a_1 \omega, SF_2)}. \tag{3.14}$$

where k is the turbulence kinetic energy; ω is dissipation per unit turbulence kinetic energy; a_1 is a constant; S is the shear-strain tensor and F_2 is the blending function [174]. The definitions of S and F_2 are addressed later. In the SST $k - \omega$ model [174],
Turbulence kinetic energy equation is:

$$\frac{\partial k}{\partial t} + U_j \frac{\partial k}{\partial x_j} = P_k - \beta^* k \omega + \frac{\partial}{\partial x_j}\left[(\nu + \sigma_k \nu_T)\frac{\partial k}{\partial x_j}\right]. \tag{3.15}$$

Specific dissipation rate equation is:

$$\frac{\partial \omega}{\partial t} + U_j \frac{\partial \omega}{\partial x_j} = \alpha S^2 - \beta \omega^2 + \frac{\partial}{\partial x_j}\left[(\nu + \sigma_\omega \nu_T)\frac{\partial \omega}{\partial x_j}\right] + 2(1 - F_1)\sigma_{\omega 2}\frac{1}{\omega}\frac{\partial k}{\partial x_i}\frac{\partial \omega}{\partial x_i}. \tag{3.16}$$

The production term of Eq. 3.15 is:

$$P_k = \min\left(\tau_{ij}\frac{\partial U_i}{\partial x_j}, 10\beta^* k\omega\right). \tag{3.17}$$

The cross-diffusion term of Eq. 3.16 is:

$$CD_{k\omega} = \max\left(2\rho\sigma_{\omega 2}\frac{1}{\omega}\frac{\partial k}{\partial x_i}\frac{\partial \omega}{\partial x_i}, 10^{-10}\right). \tag{3.18}$$

The blending equation in Eq. 3.16 is:

$$F_1 = \tanh\left\{\left\{\min\left[\max\left(\frac{2\sqrt{k}}{\beta^* \omega y}, \frac{500\nu}{y^2\omega}\right), \frac{4\sigma_{\omega 2} k}{CD_{k\omega} y^2}\right]\right\}^4\right\}. \tag{3.19}$$

The blending equation in Eq. 3.14 is:

$$F_2 = \tanh\left[\left[\max\left(\frac{2\sqrt{k}}{\beta^* \omega y}, \frac{500\nu}{y^2\omega}\right)\right]^2\right]. \tag{3.20}$$

The shear-stress strain in Eq. 3.14 is:

$$S = \frac{\partial \mathbf{U}}{\partial y}. \tag{3.21}$$

In these equations and expressions, y is the distance to the wall and ν is the dynamic viscosity and ρ is gas density and τ_{ij} is Reynolds stress tensor [174].

Tab. 3.1: Constants of the shear-stress transport (SST) $k - \omega$ model [174].

α_1	α_2	β_1	β_2	β^*	σ_{k1}	σ_{k2}	$\sigma_{\omega 1}$	$\sigma_{\omega 2}$
$\frac{5}{9}$	0.44	$\frac{3}{40}$	0.0828	$\frac{9}{100}$	0.85	1	0.5	0.856

The constants (α, β, etc.) in these equations are defined as [174]:

$$\phi = \phi_1 F_1 + \phi_2(1 - F_1), \tag{3.22}$$

where ϕ_1 represents constant with the subscript 1 and ϕ_2 represents constant with the subscript 2. Then, the constant ϕ can be computed with the constants in the Tab. 3.1.

3.4.2 Smargorinsky Subgrid Scale Model

In the Smargorinsky sub-grid scale model [262], the eddy-viscosity assumption, namely Boussinesq's hypothesis is adopted to model the sub-grid tensor as in section 3.4.1 as:

$$T_{ij} = 2\nu_t \widetilde{S_{ij}} + \frac{1}{3} T_{kk}\delta_{ij}, \; i, j, k = 1, 2, 3, . \tag{3.23}$$

$$\overline{S_{ij}} = \frac{1}{2}\left(\frac{\partial \widetilde{U}_i}{\partial x_j} + \frac{\partial \widetilde{U}_j}{\partial x_i}\right), i, j = 1, 2, 3, \tag{3.24}$$

$$\nu_t = L_s^2 |\widetilde{S}|, \tag{3.25}$$

$$L_s = C_s \Delta, \tag{3.26}$$

$$|\widetilde{S}| = (2\widetilde{S_{ij}S_{ij}})^{1/2}, \tag{3.27}$$

$$\Delta = (\Delta x \Delta y \Delta z)^{1/3}. \tag{3.28}$$

S_{ij} is the strain rate tensor; $\overline{S_{ij}}$ is the filtered strain rate tensor; ν_t is eddy viscosity; L_s is the subgrid length scale; the Smagorinsky constant C_s is 0.167; Δ is filtered scale, Δx, Δy and Δz is the length of computational cell in x, y and z directions.

Finally, the 3-D equations can be written in following format:

continuity Equation

$$\frac{\partial(\widetilde{U}_j)}{\partial x_j} = 0, \tag{3.29}$$

momentum Equation

$$\frac{\partial(\widetilde{U}_i)}{\partial t} = -\frac{\partial}{\partial x_j}[\widetilde{U}_i\widetilde{U}_j] - \frac{\partial}{\partial x_i}\left[\frac{\widetilde{p}}{\rho}\right] + \frac{\partial}{\partial x_j}\left[(\nu + \nu_t)\left(\frac{\partial \widetilde{U}_i}{\partial x_j} + \frac{\partial \widetilde{U}_j}{\partial x_i}\right)\right] + \widetilde{S}_{p,i}. \tag{3.30}$$

It should be noted that the length scale for sub-grid scale stress tensor in Eq. 3.26 is not correct when the flow is close to the wall because it will lead to a non-zero eddy viscosity at the wall [10], which is contrary to the fact that the eddy viscosity should be zero where there is no turbulence. In order to fix this situation, Moin et al. [266] adopted a Van Driest damping function to specify the length scale as:

$$L_s \; = \; C_s\Delta\left[1 - e^{\left(\frac{y^+}{A^+}\right)}\right], \tag{3.31}$$

where $y^+ \; = \; \frac{u_\tau d}{\nu}$ is the non-dimensional distance to the wall and u_τ is the wall shear stress velocity, d is the distance to the nearest wall and $A^+ \; = \; 25$ is the Van Driest constant [10].

3.4.3 Dynamic Smagorinsky Subgrid Scale Model

The dynamic Smagorinsky sub-grid model is adapted based on Smagorinsky model by Germano et al. [263, 264]. The dynamic model allows the Smagorinsky constant C_s to vary in space and time [267]. C_s is computed locally at each time step based on two filtering of the flow variables, which are denoted by superscript r and superscript t. These filters are the grid filter and the test filter, respectively, and the test filter width, is assumed to be larger than the grid filter width because it is filtered again on the airflow field.

After, the Navier-Stokes equations are filtered in LES, the sub-grid stress is given by

$$T_{ij} \; = \; (U_iU_j)^r - U_i^rU_j^r. \tag{3.32}$$

Filtering again with the test filter results in a similar set of equations, but with a different subgrid-scale stress term as [263]:

$$\tau_{ij} \; = \; (U_iU_j)^{rt} - U_i^{rt}U_j^{rt}, \tag{3.33}$$

where the superscript rt indicates grid filtering followed by test filtering. The two sub-grid scale stress terms are related by the Germano identity [263, 264]:

$$L_{ij} \; = \; \tau_{ij} - T_{ij}^t, \tag{3.34}$$

where

$$L_{ij} \; = \; (U_i^rU_j^r)^t - U_i^{rt}U_j^{rt} \tag{3.35}$$

is the resolved turbulent stress [263]. The Germano identity is used to calculate dynamic local values for C_s by applying the Smagorinsky model to both τ_{ij} and T_{ij}. [263]. The anisotropic part of L_{ij} is represented as [263, 264]:

$$L_{ij} - \delta_{ij}L_{kk}/3 \; = \; -2C_sM_{ij}, \tag{3.36}$$

where

$$M_{ij} \; = \; (\Delta^t)^2|S^{rt}|S_{ij}^r)^{rt} - (\Delta^r)^2\left(|S^r|S_{ij}^r\right)^t. \tag{3.37}$$

C_s can be calculated as:

$$C_s^2 \; = \; -\frac{1}{2}\frac{L_{kl}S_{kl}^r}{M_{mm}S_{mm}^r}. \tag{3.38}$$

3.5 Lagrangian Equations for Particle Phase

In this section, the governing equations of particle phase are discussed as well as the forces exerted on the particle [268].

The Lagrangian equations are adopted to depict the particle movement. One particle P can be presented by the position of its center $\mathbf{X}_p$, its diameter d_p, velocity $\mathbf{U}_p$ and density ρ_p. The mass of one particle can be calculated as:

$$m_p = \frac{1}{6}\rho_p \pi d_p^3. \tag{3.39}$$

In the Lagrangian method, the positon of each particle $\mathbf{X}_p$ is calculated from the equation

$$\frac{d\mathbf{X}_p}{dt} = \mathbf{U}_p. \tag{3.40}$$

To determine the particle trajectory, the velocity of particle should be evaluated. The motion of particle is controlled by Newton's equation as follows:

$$\frac{d\mathbf{U}_p}{dt} = \sum \mathbf{F}, \tag{3.41}$$

where $\sum \mathbf{F}$ is the force exerted on the particle per unit mass, and it usually consists of drag force, gravitational force, Magnus force, Saffman force, Basst force, virtual force and Brownian force [268]. Drag force is produced by the particle inertia; Magnus force is produced by whirlpool of fluid around the spinning object, which is a force perpendicular to the line of motion; Staffman force is produced by the shear layer; Basset force term and virtual force are generated by the acceleration of the particle to the fluid and Brownian force is generated by the Brownian motion of the particles [268]. In the assumption of particle rotation being small enough in comparison with particle translation, the Magnus force is neglected; the Saffman force is ignored since the velocity gradient is not very big; the Basset force and virtual-mass force are excluded due to large ratio of particle density to flow density. In addition, Brownian force is ignored in the case of micro-particles because of low diffusion, but there is enough diffusion to influence the trajectory of sub-micron particles so that it is considered in the case of sub-micron particle. As analyzed above, the force can be reduced to two terms of drag force $\mathbf{F}_D$ and gravity force $\mathbf{g}$ in the case of micro-particle and three terms of drag force $\mathbf{F}_D$, gravitational force $\mathbf{g}$ and Brownian force $\mathbf{F}_B$ in the case of sub-micron particle as follows:

$$\mathbf{F} = \begin{cases} \mathbf{F}_D + \mathbf{g} & : \text{ micron particle} \\ \mathbf{F}_D + \mathbf{g} + \mathbf{F}_B. & : \text{ sub} - \text{micron particle.} \end{cases} \tag{3.42}$$

3.6 Laws of Exerted Forces

Depending on which drag model is used, the formulations of $\mathbf{F}_D$ and $\mathbf{F}_B$ are different. In present work [46],

$$\mathbf{F}_D = \frac{18\mu}{\rho_p d_p^2}\frac{C_D \mathrm{Re}_p}{24}(\mathbf{U} - \mathbf{U}_p). \tag{3.43}$$

Here, $\mathbf{U}$ is velocity of the gas phase, $\mathbf{U}_p$ is the velocity of particle, μ is the dynamic viscosity of the air, ρ is the density of air flow, ρ_p is the density of the particle, d_p is the particle diameter and T_p is the particle temperature. Re_p is the relative Reynolds number and it is defined as [46]:

$$\mathrm{Re}_p = \frac{\rho_p d_p |\mathbf{U} - \mathbf{U}_p|}{\mu}. \tag{3.44}$$

The factor C_D depends on the relative Reynolds number Re_p [67]:

$$C_D = \begin{cases} \frac{24}{\mathrm{Re}_p} & : \ \mathrm{Re}_p < 0.5 \\ \frac{24}{\mathrm{Re}_p}\left(1 + 0.179\sqrt{\mathrm{Re}_p} + 0.013\mathrm{Re}_p\right) & : \ 0.5 < \mathrm{Re}_p < 6000 \end{cases} \tag{3.45}$$

For the sub-micron particles, the drag force [67] is defined as

$$\mathbf{F}_D = \frac{18\mu}{\rho_p d_p^2 C_c}(\mathbf{U} - \mathbf{U}_p), \tag{3.46}$$

Where Cunningham correction factor C_c [67]is calculated using the expression:

$$C_c = 1 + \frac{2\lambda}{d_p}(1.257 + 0.4e^{(-1.1\frac{d_p}{2\lambda})}) \tag{3.47}$$

and λ is the mean free path of the air molecule. The Brownian force is given as:

$$F_{b_i} = \zeta_i \sqrt{\frac{\pi S_o}{\Delta t}}. \tag{3.48}$$

ζ_i are generated by zero-mean, unit-variance-independent Gaussian random function and the Brownian force should be calculated at each time step [67]:

$$S_0 = \frac{216\nu k_B T}{\pi^2 \rho d_p^5 \left(\frac{\rho_p}{\rho}\right)^2 C_c}, \tag{3.49}$$

where T is the absolute temperature of the air flow, ν is the kinematic viscosity of gas, and k_B is the Boltzmann constant.

4. Numerical Methods and Solvers

In this chapter, the numerical methods to solve the governing equations of gas phase and particle phase are explained. As the thesis adopts the OpenFOAM as a platform, at first, the numerical methods to solve N-S equations are introduced. Afterwards, the numerical methods for solving the particle motion are presented. Based on the numerical methods, the solvers used to solve the 3D N-S equations and Lagrangian equations have been constructed on the basis of solvers in OpenFOAM 1.5 of "oodles" [184] and "icoLagrangianFoam" [269].

4.1 Solving N-S Equations in OpenFOAM

To solve these equations, the open source software platform of OpenFOAM 1.5 [184] is adopted. It is a free and open source software of the commercial company OpenCFD Ltd [184]. It is very popular among CFD researchers because it is powerful to solve complex flow field with finite volume method involving turbulence, chemical reactions and heat transfer and is convenient to extend since its source code is available. It is built with a set of efficient C++ modules. Based on these modules, libraries, solvers and utilities are constructed. Libraries is mainly used to create tool boxes accessible to the solvers and utilities; solvers are used to solve engineering mechanics; utilities are used to conduct pre-processing and post-processing. It ranges from mesh conversion to simple data manipulation and visualization. More information on the programming and case setting up can be referred from the "User Guide" and "Programmer Guide" of OpenFOAM 1.5 [184].

The standard solver of "oodles" in OpenFOAM 1.5 is adopted as the basis of the new solver, which will be introduced in detail in the section 4.3, therefore the numerical methods to solve the 3D N-S in the thesis are the same as the methods in "oodles". In the solver, the pressure-implicit split-operator (PISO) is used to solve equations for velocity and pressure due to its ability to solve transient problems. The user must specify the number of correctors in the PISO dictionary by the "nCorrectors" keyword. Different numerical schemes for interpolating the spatial and temporal terms such as gradient term, divergence term, Laplacian terms, flux terms and the first time derivative term are available in the OpenFOAM, which should be set up in the file of "fvSchmemes" [184]. More information on setting up the numerical schemes and the mathematical expression can be found in the "User Guide" and "Programmer Guide" of OpenFOAM 1.5 [184]. In addition, the solver of "turbFoam" in openFOAM 1.5 is also adopted to solve the RANS SST $k - \omega$ model. More details on the solver can be found in [184].

4.2 Modeling Particle Motion

As discussed by Ge [166] that the implicit scheme is very robust and accurate to track the particle motion. In this thesis, the particle motion is also carried out with implicit method [184].

These equations are solved using the implicit method as follows: In the case of micro-particles [260]:

$$\mathbf{U}_p^{n+1} = \frac{\mathbf{U}_p^n + \mathbf{U}\frac{\Delta t}{\tau_p} + \mathrm{g}\Delta t}{1 + \frac{\Delta t}{\tau_p}}. \tag{4.1}$$

In the case of sub-micron particles:

$$\mathbf{U}_p^{n+1} = \frac{\mathbf{U}_p^n + \mathbf{U}\frac{\Delta t}{\tau_p} + (\mathrm{g} + \mathbf{F}_B)\Delta t}{1 + \frac{\Delta t}{\tau_p}}, \tag{4.2}$$

where τ_p is particle relaxation time and it is defined as:

$$\tau_p = \frac{4}{3}\frac{\rho_p d_p}{\rho C_D \left|\mathbf{U}_p - \mathbf{U}\right|} \tag{4.3}$$

and the particle position is carried out using the following equation:

$$\mathbf{X}_p^{n+1} = \mathbf{X}_p^n + \mathbf{U}_p^n \Delta t. \tag{4.4}$$

4.3 Solvers

In the scope of the governing equations and physical models, the "icoLagrangianFoam" and "oodles" are adopted. The solver of "icoLagrangianFoam" is designed to solve the solid particle in the laminar flow. It has basic injection models to inject particles in the flow field and basic functions to solve the Lagrangian equations. These functions can be taken as the basic frame of the required solver in the present problem. However, it is far enough to fulfill the requirement of the project in the injection model, in the drag model and in the boundary conditions for particles. There are also errors during output of the particle data and paralleled computation. At the same time, the module to simulate the turbulence is also missing. But, the oodles solver can manipulate turbulence with LES. So, these solvers were chosen as a basis to construct new solvers named oodLFoam, oodLFoamct, oodLFoamp and oodLFoampct, which are used to solve different kinds of problems. Other Utilities are built on the solvers which make sure that the post-processing program is compatible with the results.

At first, the code of "oodles" is copied to the folder of /OpenFOAM/usr-1.5/applications/ with the new name of "oodLFoam". The file of "oodles.C" is given a new name of "oodLagrangianFoam.C" and all the files in the folder of "icoLagrangianFoam" other than the files in the sub-folder of "Make" and "icoLangrangianFoam.C" are moved into the new folder. The name of new solver is defined in the file of "files" in the sub-folder of "Make". The necessary "lib" related to particles has to be added in the file of "Options" in the folder of

"Make" as well. The link to other libs related to particle mption should be included in the file of "oodles.C" and the sentence to call the member function of particle motion. Two new variables are induced to decide computing gas phase or particle phase such as "computeFlowfield" and "computeParticle". After these manipulations, the solver can be compiled using the command of "wmake", which is used in OpenFOAM to compile new lib and solvers. After these manipulations, a new solver is built, which can solve the gas phase with LES and evolve particles with Lagrangian method. It should be mentioned that the injection method in the "oodLFoam" is particular for the current geometry and it only solves micro-particles without considering particle interactions and the influence of particle on the gas phase.

Other solvers are constructed based on "oodLFoam". "oodLFoamp" is built for the polydispersed particles. The diameter of particles ranges from sub-micron meter to hundred micrometer. There are mainly two different revisions including the injection method and update method of particle properties. In this solver, the particles are injected one by one class, which has the same diameter. And as the case in the "oodLFoam", the particle injection position is randomly distributed at the inlet plane and the particle velocity is the same. In addition, the drag model of sub-micron particles and Brownian force is considered. To study the particle motion in the geometry of CT scans, two solvers named "oodLFoamct" and "oodLFoampct" are constructed. The main difference between them is that the injection method is different since the inlet plane of the mouth-throat model based on CT scans is not vertical anymore.

4.4 Flow Chart of Numerical Scheme

In this section, it presents the numerical procedure from the generation of geometrical models to the post-process of numerical results, which may make it easy to understand the present work because many softwares are adopted and they are related to many file formats.

As show in Fig. 4.1, the geometrical models are constructed at first. There are two different ways to produce the geometrical models for two kinds of configurations. The first one is the simplified geometrical models such as constricted tube and the cast-based mouth-throat model, which are generated with the surface module of the Ansys ICEM-CFD 11.0 [183]. In the case of constricted tube, it is depicted by a cosine function (c.f. section 5.1.1), the coordinates of points to depict the configuration can be generated by the surface module of Ansys ICEM-CFD 11.0 directly Ansys ICEM-CFD 11.0 [183]. In contrast, in the case of the cast-based mouth-throat, the configuration is more complicated. The coordinates of cross section-sectional positions and radius value of cross sections of the cast-based mouth-throat models are picked out from the figures from the literature [89] with the format of ".png" and saved in a text file of ".dat" as shown in Fig. 4.1. These points are manually imported in Ansys ICEM-CFD 11.0 [183] and then the surface of the cast-based mouth-throat model with the format of ".tin" is generated in the Ansys ICEM-CFD 11.0 [183].

Another kind of the geometrical models based on CT scans, i.e. CT-based mouth-throat and CT-based nasal cavity, are very complex, thus it has to adopt the specific software to

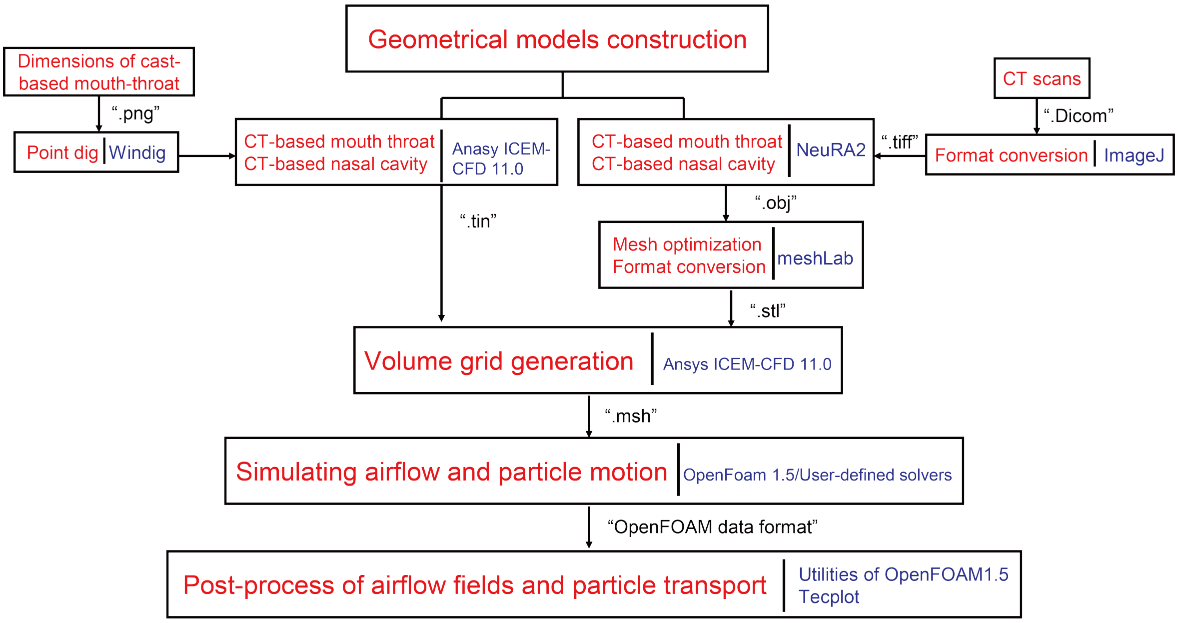

Fig. 4.1: Schematic of the work chart of the numerical procedure.

generate the surface grid.In this case, the CT scans from the surgeon with the format of ".Dicom" is imported into ImageJ [270] at first seen in Fig. 4.1, and they are transferred to a image file with file format of ".tiff", which includes all of the CT scans. Then, the ".tiff" is imported into NeuRA2 seen in Fig. 4.1. The image undergoes process of reparation to delete the artifact, closure of the focused structure (e.g. mouth-throat and nasal cavity), segmentation to separate the focused structure, mesh generation to produce the surface grid and mesh optimization to smooth the surface. The surface mesh with the format of ".obj" is exported and the surface has to be further smoothed in the meshLab [271] seen in Fig. 4.1. Finally, the geometrical models based on CT scans are exported out from meshLab [271] with the format of ".stl" and imported into Ansys ICEM-CFD 11.0 [183].

The volume grids are generated using Ansys ICEM-CFD 11.0 [183]. Hexagonal grids are adopted for the constricted tube and cast-based mouth-throat, and the tetrahedral grids are used for the CT-based mouth-throat and CT-based mouth-throat. The volume grids with the format of ".msh" are exported out and imported into the OpenFOAM 1.5 [184] seen in Fig. 4.1. Airflow in the constricted tube, and airflow and mono-disperse and poly-disperse particle transport in the cast-based mouth-throat, the airflow in the cast-based mouth-throat considering the unsteady inspiration flow rate, airflow and particle transport in the CT-based mouth-throat, and airflow in the CT-based nasal cavity are simulated using the user-defined solvers based on OpenFOAM 1.5 [184], which are presented in section 4.3, as shown in Fig. 4.1. The numerical results are transferred to the file format of Tecplot [272] using the utilities of OpenFOAM 1.5 [184] seen in Fig. 4.1. The contour plots of the airflow fields and the particle deposition and transport are exported from Tecplot [272].

5. Numerical Results and Discussion

In this chapter, the numerical results are presented. At first, the airflow in the constricted tube is discussed to evaluate the methodology. Then, the airflow field in the mouth-throat based on cast are presented including steady and unsteady flow fields, as well as the micro-particle transport and deposition. In addition, the poly-disperse particles are simulated as well in the cast-based mouth-throat using one-way and two-way coupling methods. Moreover, the unsteady inspiration flow rate has been implemented in simulating the airflow field in the cast-based mouth-throat to discuss the influence of unsteady inspiration pattern on the properties of airflow field. To investigate the influence of geometrical models of the upper airway on the airflow field and particle transport and deposition, a more realistic mouth-throat based on CT scans has been constructed, and the airflow field and particle deposition have been simulated in the CT-based mouth-throat model and results are compared with the case of the cast-based mouth-throat model. At the same time, the airflow field in a nasal cavity based on CT scans is addressed as well to set the initial basis for the further study.

5.1 Airflow Field in the Constricted Tube

In the year of 1983, Ahmed et al. [273] studied the transitional flow field in an axi-symmetric constricted tube with 75% reduction through experimental method, and then the case was studied through numerical simulations by several researchers [46, 86]. These numerical simulations are mainly to evaluate the physical models through comparison of numerical flow field with the experimental results because the flow field in mouth-throat also transits from the laminar to turbulent as the flow field in the constricted tube and the geometry is rather simple with a simple boundary, which qualifies this setting for evaluation of the present method. In this section, the transitional flow field in the constricted tube is simulated with LES. The results have been discussed and compared with the experimental [273] and numerical [46, 86] data to evaluate the present methodology.

5.1.1 Configuration and Grid Generation

An axi-symmetric constricted tube with an area reduction of 75% is depicted by a cosine function [86] as follows:

$$r = \begin{cases} R - \frac{R}{2}\cos\left(\frac{\pi z}{R}\right) & : \quad |z| \leq D \\ R & : \quad |z| > D. \end{cases} \tag{5.1}$$

Where, r is the radial coordinate; z is the axial coordinate; R is radius of the inlet plane; and

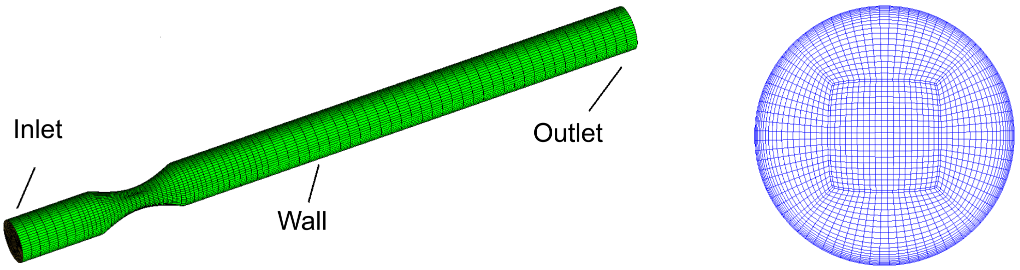

Fig. 5.1: Grid on the peripheral surface (left) and grid on the inlet surface (right) of the constricted tube.

D is the diameter of the inlet plane. The diameter D adopted in the simulation is 2 inches and the distance in axial direction is from -2 D to 12 D, which is expected to reduce the influence of boundary conditions. The geometry is generated using software Ansys ICEM-CFD 11.0 [183] as shown in Fig. 5.1. At first, the points are generated manually and functional method in the geometry generation module of Ansys ICEM-CFD 11.0. Afterwards, the curves are generated with these points and the surface is generated with the curves. More details can be found in the user manual of Ansys ICEM-CFD 11.0 [183].The grids are generated with Ansys ICEM-CFD 11.0 as well and hexagonal grids are used. In the center of the constricted tube, H-Grid seen in Fig. 5.1 is adopted and in the outer part, the O-grid is adopted to prove good grid qualities.

5.1.2 Computational Conditions

The Reynolds number at the inlet plane is 2,000 and the dynamic viscosity is 1.2 10^{-4}. The boundary conditions is set as follows:

(1) Inlet:

$$V_n = 0.473 \ \pm \ 2\% \ (4\%) \ \text{m/s}; \ \text{Re} \ = \ 2,000; \ \frac{\partial P}{\partial n} \ = \ 0; \tag{5.2}$$

(2) Outlet:

$$\frac{\partial \mathbf{V}}{\partial n} \ = \ 0; \ P \ = \ 0 \ \text{Pa (relative to the ambient pressure)}; \tag{5.3}$$

(3) Wall

$$\mathbf{V} \ = \ 0 \ \text{m/s}; \ \frac{\partial P}{\partial n} \ = \ 0. \tag{5.4}$$

To evaluate the influence of the turbulent fluctuation on the flow field, 2 and 4% velocity fluctuations have been adopted and are compared later. It assumes that the air in the configuration is static in the beginning. Thus, the velocity is 0 m/s and pressure is 0 Pa relative to the environmental pressure.

5.1.3 Grid Evaluation

Five different sets of grids with 292,581, 580,545, 1,043,955, 2,032,800 and 2,731,820 grid nodes are used to evaluate the grid node number. The grid evaluation aims to make sure

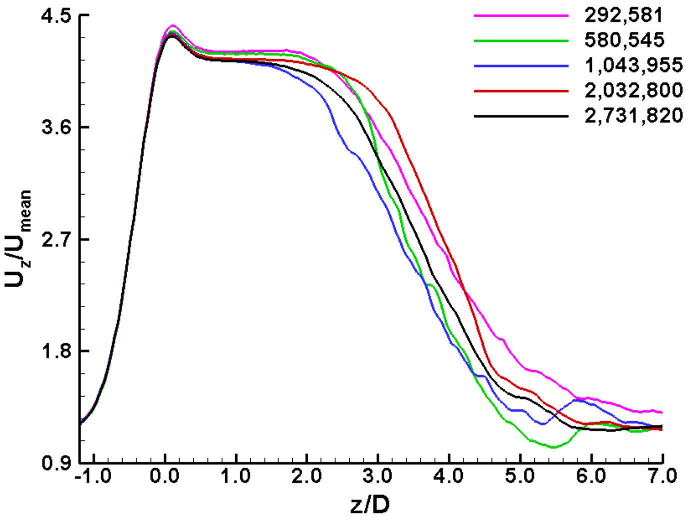

Fig. 5.2: Axial velocity profile at the centerline corresponding to different grid nodes.

that the physical result from numerical simulation is independent of the number of grid nodes. The velocity profile along the centerline for different gird nodes are shown in Fig. 5.2. It is seen that the results from the four sets of grids with the 292,581, 580,545, 1,043,955, 2,032,800 and 2,731,820 grid nodes oscillate in the two sides of the result from the final grid with the 2,731,820 grid nodes in the transitional flow region and have minor discrepancy. Thus, the gas field is independent of the number of grid nodes when last set grid is adopted. The final grid with the 2,731,820 grid nodes is suitable for numerical simulation of the flow field in the constricted tube.

5.1.4 Velocity Profiles

The normalized axial velocity at the centerline and at different cross sections are shown in Figs. 5.3 and 5.4, respectively. In these figures, the velocity is normalized by the mean velocity at the inlet plane, $\mathbf{U}_{mean}$, and the distance in the axial direction is normalized by the tube diameter, D, and in the radial direction with the radius, R, of the tube.

From Fig. 5.3, it can be seen that the present result fits well with the experimental result as well as the numerical result. Moreover, it shows that a variation of the initial velocity fluctuation hardly affects the computed results, which can be seen from the figure. Thus, 2% velocity fluctuation will be adopted in the present work. From experimental data [273], it is known that the axial flow velocity increases due to area reduction, and it does not change significantly until the location around $z = 2\ D$.

After this relatively steady period, the velocity deceases quickly because the flow transits from laminar to turbulent coupled with large-scale lateral momentum transfer. In addition, it is described that the flow transition occurs in the region $1 < z/D < 4$ [273]. The comparison of the velocity at the centerline shown in Fig. 5.3 displays that the present result fits well with the experimental [273] and numerical [86] results; in particular, in the transitional regime,

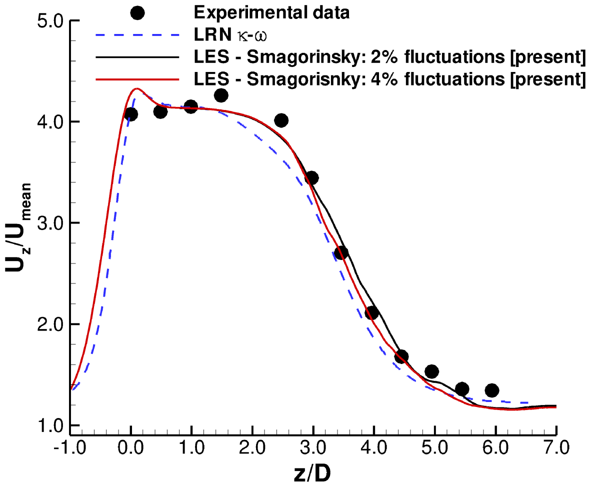

Fig. 5.3: Comparison of the computed centerline velocity with measurements [273] and numerical results [86] for the constricted tube.

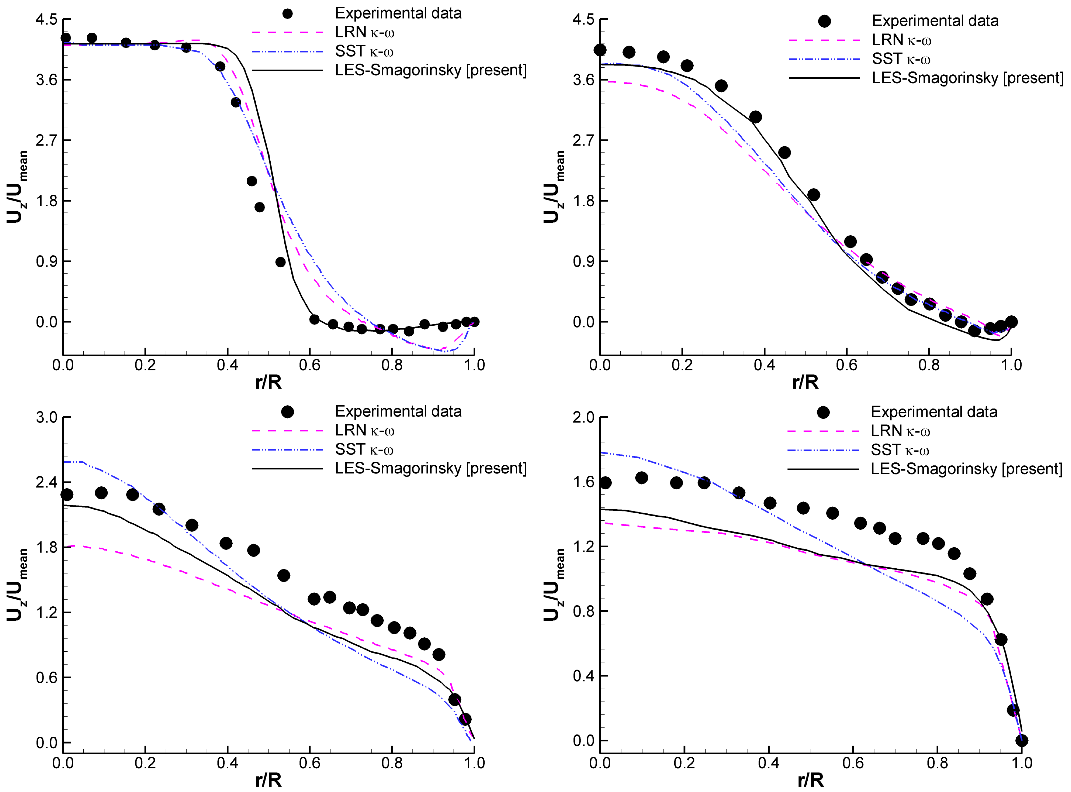

Fig. 5.4: Comparison of normalized axial velocity at different sections downstream of the glottis with experimental data [273] and numerical results of LRN $k - \omega$ model [86] and SST $k - \omega$ model [46] at $z = D$ (top left), $z = 2.5\ D$ (top right), $z = 4D$ (bottom left), and $z = 5D$ (bottom right).

it performs better than the RANS $k - \omega$ model of Zhang et al. [86]. Detailed comparison of the velocity profile has been performed at different cross-sections. From the Fig. 5.4, it can be seen that the numerical simulations can resolve the evolution of shear layer and recirculation zone. However, the present numerical simulations clearly predict the tendency and the results are much closer to the experimental data [273]. It is seen that the present numerical simulations improve the prediction of the velocity profile in the shear layer region at $z = D$ in Fig. 5.4 (top left), and near the center at $z = 2.5\ D$ (top right). At positions $z = 4\ D$ in Fig. 5.4 (bottom left) and at $z = 5\ D$ (bottom right), the general performance of all models is lower than before, the present result is closest to the experimental result and the principal shape is captured. At position $z = 5\ D$, the velocity profile becomes more blunt and the present result is close to and slightly better than the numerical results of Zhang et al. [86] and of Jayaraju et al. [46]. It should be emphasized that the discrepancies between experimental and numerical results may also be due to the experimental uncertainty in the region where the velocity varies quickly [56].

5.1.5 Summary

A constricted tube is constructed using the geometry module in the Ansys ICEM-CFD 11.0 [183] and the grids are generated with the commercial software as well. The velocity at the centerline and the velocity profiles at different cross sections have been compared with the experimental and numerical data from literature [46, 86, 90, 273]. The comparison shows that the present numerical method improves the description of the flow field in the constricted tube, in particular, in the transition regime. Moreover, the comparison of numerical results from different numerical models and experimental results show that the present methodology adequately predicts the flow field transiting from laminar to turbulent. This work sets the basis for the further simulation of the flow field in the idealized mouth-throat model based on cast, the realistic mouth-throat model based on CT scans, and the nasal cavity based on the CT scans.

5.2 Airflow Field and Particle Transport in the Cast-Based Mouth-Throat

As it is introduced in the chapter 2 that many investigations have been conducted on the flow field in the upper airways, some questions still need to be answered such as the properties of secondary flows, recirculated flow zone and laryngeal jet in the steady and unsteady gas fields; and the properties of particle transport and deposition, in particular the interaction between the unsteady flow structure and the particle dispersion and transport.

In this section, the work on the airflow and micro-particle motion is presented in detail. In the beginning, the geometry construction of mouth-throat model in sub-section as well as the grid generation are introduced. Afterwards, the computational conditions will be introduced to develop the numerical simulations. The numerical results of airflow field at different inspiration flow rates as well as the mono-disperse micro-particle deposition and transport are presented. Moreover, the numerical results from the poly-disperse particle size distribution are discussed as well in this section.

5.2.1 Geometry Construction and Grid Generation

As discussed in the chapter 2 that Cheng et al. [48] first reported a mouth-throat model in 1999, which is based on cast. Based on this Cheng's model, a circular simplified oral airway is constructed by Zhang et al. [86] to study the filtering function of mouth-throat. The geometrical model shown in Fig. 5.5 [20] is built based on the key diameter and length scale values of the oral cavity, pharynx, larynx, and trachea of the geometrical model reported by Cheng et al. [48]. More details of these two geometrical models can be found in section 2.1.2.

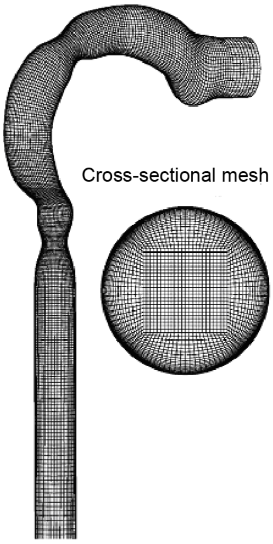

Fig. 5.5: Simplified model of mouth-throat built by Zhang et al. [86].

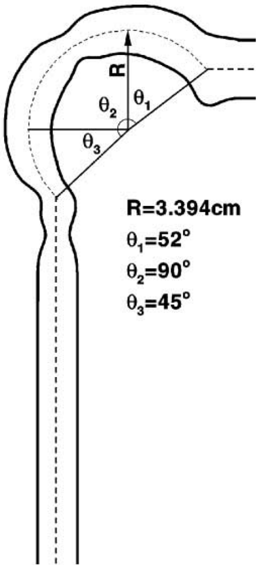

Fig. 5.6: The profile of the centerline of mouth-throat [89].

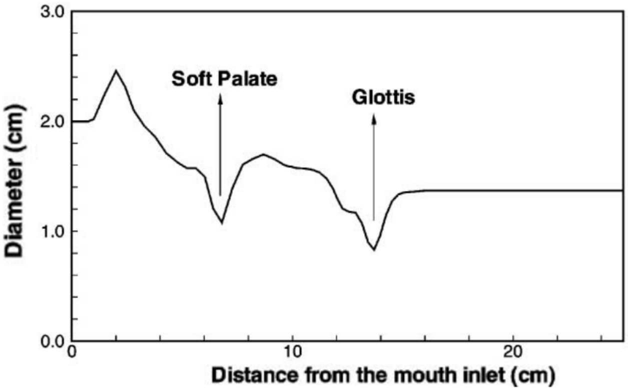

Fig. 5.7: Variations of cross-sectional diameter along the centerline [89].

Although other simplified mouth-throat models mentioned in the Chapter 2 are reported by other researchers as well, there are more detailed dimension information on the geometry such as the diameter of different cross sections and the profile of the centerline. So, this mouth-throat model is chosen as the basis.

The coordinates of points at the centerline shown in Fig. 5.6 and the diameter variation along the oral airway from mouth to trachea shown in Fig. 5.7 are taken from [89]. Together with the cross section is circular, the information is enough to construct the idealized mouth-throat. The data file of the points coordinate is taken from the figures by WinDig [274]. The circles at different cross sections and surfaces are generated based on these points using the geometry module of Ansys ICEM-CFD 11.0. From the comparison of Figs. 5.5 and 5.8 (left), it is easy to find that there are minor difference between the mouth-throat model built by Zhang et al. [86] and the present geometircal model in the location of soft palate and glottis.

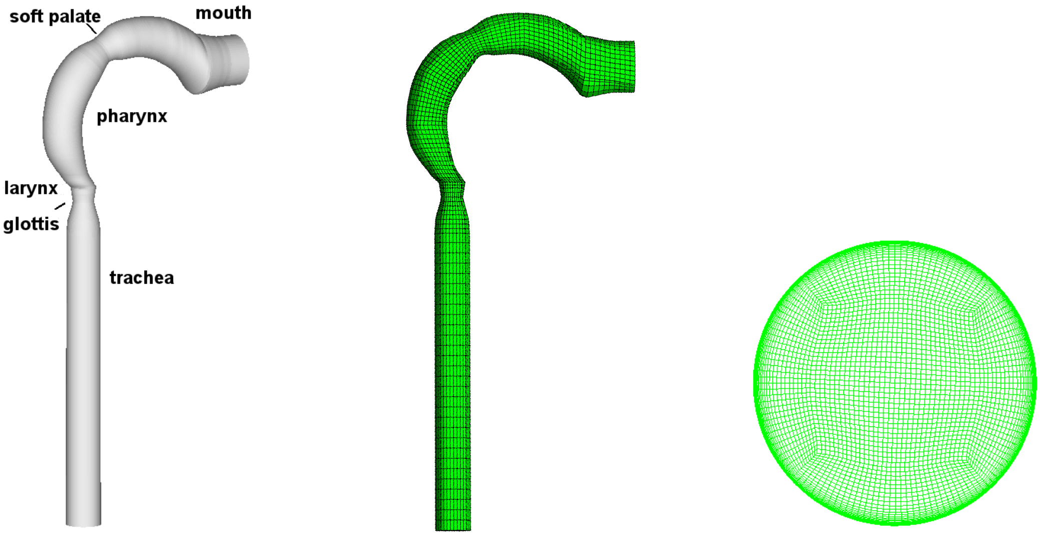

Fig. 5.8: Configuration (left), grid on the wall (center) and at the inlet plane (right) of the present mouth-throat.

The change of surface curvature is much more sudden in the present mouth-throat model than mouth-throat model built by Zhang et al. [86] due to the surface sensitivity to the error of data and different ways to generate the lines and surface.

In the same way that is used in the constricted tube, the grids of mouth-throat based on cast are generated with Ansys ICEM-CFD 11.0 as well and hexagonal grids are used. In the center of the geometry, H-Grid is adopted and in the outer part, the O-grid is adopted as shown in Fig. 5.8 (center and right).

5.2.2 Computational Conditions

The gas transport in the geometry is assumed to be the air at the room temperature. Then, the physical conditions of the gas are as follows:

$$\rho_g \;=\; 1.21 \text{ kg/m}^3;\ \mathrm{T_g} \;=\; 293.15 \text{ K};\ \nu \;=\; 14.9\ 10^{-6} \text{ m}^2\text{/s}. \tag{5.5}$$

Although the respiratory pattern is transitional in the realistic situation including inspiratory and expiratory phase, at present, most of the investigations concentrate on the inspiration phase and assume that the inspiration flow rate is steady. There are three different inspiration flow rates of 15, 30 and 60 L/min corresponding to breathing at rest, normal breathing and intensive breathing in exercise adopted in the present work. The boundary condition corresponding to inspiration flow rate of 30 L/min is as follows:

(1) Inlet:

$$V_n \;=\; 1.592 \;\pm\; 2\% \text{ m/s};\ \mathrm{Re} \;=\; 2,120;\ \frac{\partial P}{\partial n} \;=\; 0; \tag{5.6}$$

(2) Outlet:

$$\frac{\partial \mathbf{V}}{\partial n} \;=\; 0;\ P \;=\; 0 \text{ Pa (relative to the ambient pressure)}; \tag{5.7}$$

(3) Wall

$$\mathbf{V} \;=\; 0 \text{ m/s};\ \frac{\partial P}{\partial n} \;=\; 0. \tag{5.8}$$

It is assumed that the air in the configuration is static in the beginning. Thus, the velocity is 0 m/s and pressure is 0 Pa relative to the environmental pressure. The boundary conditions in the other two cases can be given according to this case.

The computations are carried out in the cluster of bwGrid Cluster at Heidelberg University. A simulation takes around 2 weeks with 56 processors for the flow field in the case of flow inspiration rate of 30 L/min for 1,276,500 grid nodes.

5.2.3 Grid Evaluation

To make the physical result from the numerical simulation independent of the number of grid nodes, the velocity profile at the centerline from different gird nodes are compared, which are shown in Figs. 5.9. The number of grid nodes has been evaluated at the inspiration flow rates of 30 L/min and 60 L/min. 101,443, 453,132, 932,052, 1,276,500, and 1,864,500 grid nodes are adopted to evaluate the influence of grid nodes on the numerical results at the inspiration

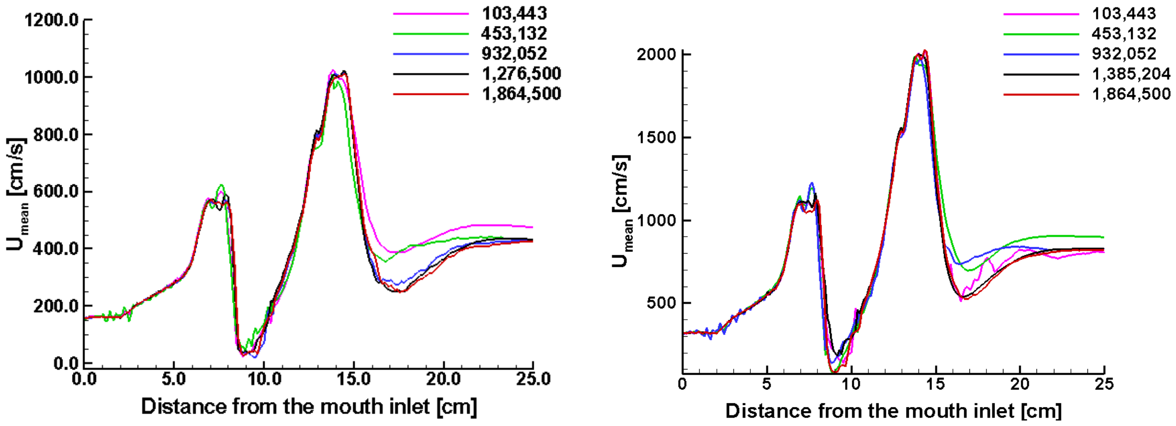

Fig. 5.9: The time-averaged velocity profile along the centerline of the cast-based mouth-throat corresponding to different sets of grids at the inspiration flow rate of 30 L/min (left) and 60 L/min (right).

flow rate of 30 L/min, and 101,443, 453,132, 932,052, 1,385,204 and 1,864,500 grid nodes are used at 60 L/min.

From the Fig. 5.9, it can be seen that with the number of grid nodes increasing, the discrepancy among different computations has decreased and there are minor differences between the computations from last two sets of grid nodes. From the comparison for different sets of grid nodes, it can be seen that the final grid is suitable enough for the numerical modeling and the results do not change for the grid nodes of 1,276,500 at inspiration flow rate of 30 L/min and for the grid nodes of 1,385,204 at inspiration rate of 60 L/min. Hence, the flow fields are given on the grid nodes of 1,276,500 at inspiration flow rate of 15 L/min and 30 L/min and grid nodes of 1,385,204 at inspiration rate of 60 L/min. Micro-particle transport is simulated on these two sets of grids as well.

5.2.4 Properties of Airflow Fields

In this section, the mean velocity fields includes the flow structures at different cross sections of mouth-throat, the vortex structures and the laryngeal jet in the three-dimensional space, and the unsteady flow field at different cross sections of the mouth-throat are presented.

5.2.4.1 Mean Velocity Fields

In this sub-section, the mean airflow fields in the simplified mouth-throat are presented and discussed in detail to uncover the properties of the steady flow field. They are gained by averaging the entire gas field in the time direction during enough time-length. The flow fields are simulated using LES/Smagorinsky sub-grid scale model, LES/Smagrorinsky sub-grid scale and dynamic Smagrorinsky sub-grid scale [262] model and RANS/SST $k - \omega$. The mean velocity fields are shown in Figs. 5.10 and 5.11.

It displays in Fig. 5.10 that the averaged velocity contour and streamline (left-hand side of Fig. 5.10) and the axial velocity contour and secondary velocity streamlines at different cross sections (right-hand side of Fig. 5.10) at inspiration flow rate of 30 L/min using LES/Smagorinsky sub-grid model. These cross sections include positions corresponding to the location of oral cavity, pharynx, glottis, as well as one, three and six diameters of the trachea downstream the glottis in Fig. 5.10. Positions A - F denote the posterior side, and A' - F' the anterior side. It should remind readers that the velocity contours and streamlines will be shown at the cross sections in all other cases at same positions because the positions of the cross-sections will not be mentioned in the later sections to avoid the unnecessary repetition.

From the velocity streamline at the mid-plane, it can be seen that the numerical simulation captures the main properties of flow field in the oral airway, including the skewed velocity profile in the oral cavity and pharynx due to centrifugal forces, and flow separation in the lower portion of mouth, in the pharynx region after the soft palate, and downstream of glottis. The asymmetric laryngeal jet extends from the glottis. There is a small recirculation zone in the posterior side of pharynx and the laryngeal jet is impinging on the anterior wall of trachea, and in contrast to the numerical simulation of Zhang et al. [86] in a similar geometry, it is not impinging on the wall. This is probably due to the different geometrical shape in the glottal region.

Secondary vortices are interesting as well to researchers since these may have an effect on the particle deposition [86]. There is a pair of counter vortices at the section of A - A', which

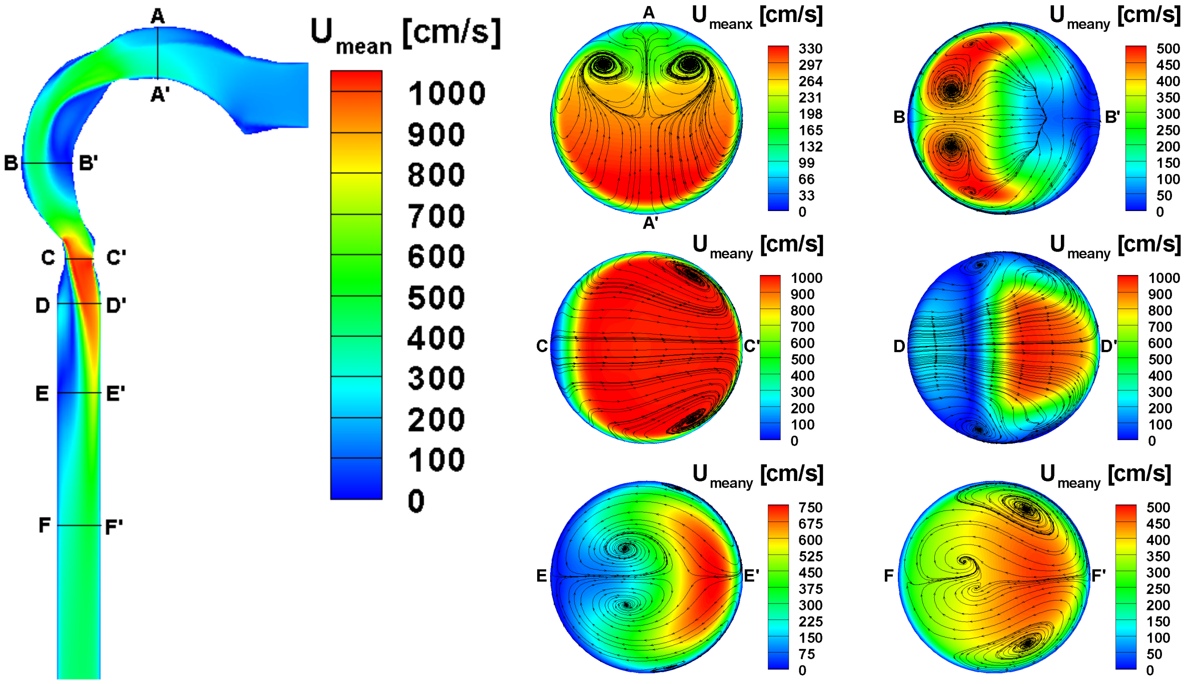

Fig. 5.10: Time-averaged velocity contour and streamlines at the mid-plane (left), and time-averaged axial velocity and secondary streamlines at different cross-sections (right) at inspiration flow rate of 30 L/min with LES/Smagorinsky model.

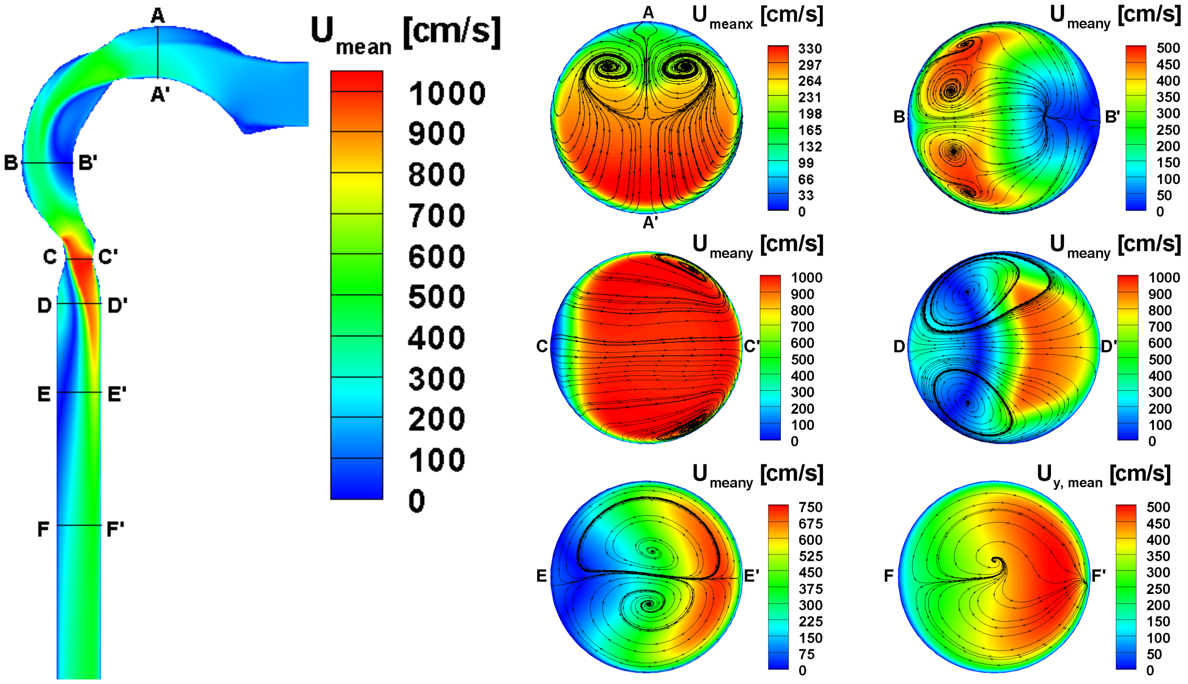

Fig. 5.11: Time-averaged velocity contour and streamlines at the mid-plane (left), and time-averaged axial velocity and secondary streamlines at different cross-sections (right) at the inspiration flow rate of 30 L/min using RANS/SST $k - \omega$.

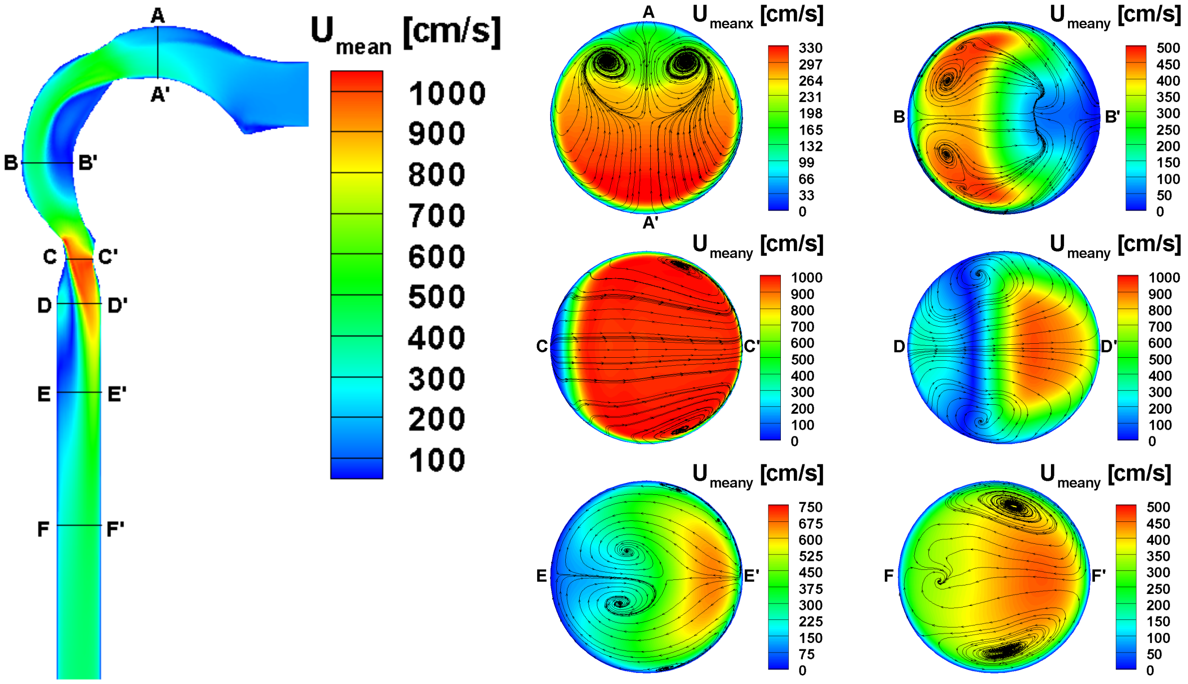

Fig. 5.12: Time-averaged velocity contour and streamlines at the mid-plane (left), and time-averaged axial velocity and secondary streamlines at different cross-sections (right) at the inspiration flow rate of 30 L/min using LES/dynamic Smagorinksy model.

is produced because of the pressure gradient. At section B - B', the flow field becomes more complex coupled with the appearance of a recirculation zone. Moreover, there are two large counter-rotating vortices and another pair of smaller vortices residing at this section. In the glottis at section C - C', where the laryngeal jet has appeared, the axial velocity becomes prominent and distributes evenly, which induces weak secondary vortices. In addition, at this section, the secondary vortices turn to the anterior side. At section D - D' , where the recirculation zone has appeared and which is at the downstream of laryngeal jet, the highest axial velocity is close to the wall and the vortices appear in the interface of the laryngeal jet and the separation zone. At the section E - E' , which is in the tail of laryngeal jet, the laryngeal jet becomes weak and the axial velocity profile distribution becomes even. The length scale of vortices has increased, and it is located at the interface of recirculation zone and laryngeal jet. From the axial velocity and secondary vortices distribution, it can be summarized that the flow field is very sensitive to the geometrical change, in particular, in locations with large curvature. The secondary vortices are related with the laryngeal jet and they tend to appear in the boundary of recirculation zone and laryngeal jet. When the flow goes into F - F' section, the laryngeal jet disappears. Two large vortices locate near the wall and one pair of smaller vortices distributes in the center of the geometry.

To identify the influence of the turbulence model on the properties, the flow field at 30 L/min is simulated as well used the RANS/SST $k-\omega$ model and LES/dynamic Smagorinsky model. The averaged velocity contour and streamline (left-hand side) and the axial velocity contour and secondary velocity streamlines at different cross sections (right-hand side) are shown in Figs. 5.11 and 5.12 respectively. The properties of the flow fields using two methods are similar to the result from LES/Smagorinsky model. For instance, the recirculation flow zone, the profile of laryngeal jet and the secondary vortices can be seen in the same position using these methods. The main difference is the distribution of secondary vortices. In particular, secondary vortices resulting from RANS/SST $k - \omega$ model display distinct different properties with other two cases, which can be seen from the vortices at B - B', D - D', E - E' and F - F' cross sections in Fig. 5.11 such as the length-scale and profile of the vortices. In particular, at D - D' and E - E' cross sections, the length-scales of the vortices from RANS/SST $k - \omega$ model are much larger than other two cases. In addition, there is only one pair of secondary vortices at E - E' cross section from RANS/SST $k - \omega$ model, whereas there are two pairs of the secondary vortices at this cross section from Smagorinsky model and dynamic Smagorinsky model. At the same time, the small secondary vortices at F - F' cross section display different features from these different turbulent models since the turbulence is much complex at this cross section. From these comparison, it is found that LES/Smagorinsky model is more suitable for simulating the flow field in the mouth-throat model rather than RANS/SST $k - \omega$ model. Therefore, all of simulations of the flow fields are conducted using LES/Smagorinsky model in other cases.

In the case of inspiration flow rate of 15 L/min, the Reynolds number decreases and it is only 1,060 at the inlet plane. Correspondingly, the Dean number decreases from the definition of Dean number (c.f. Eq. 2.3). The flow in the mouth-throat model has the similar changing

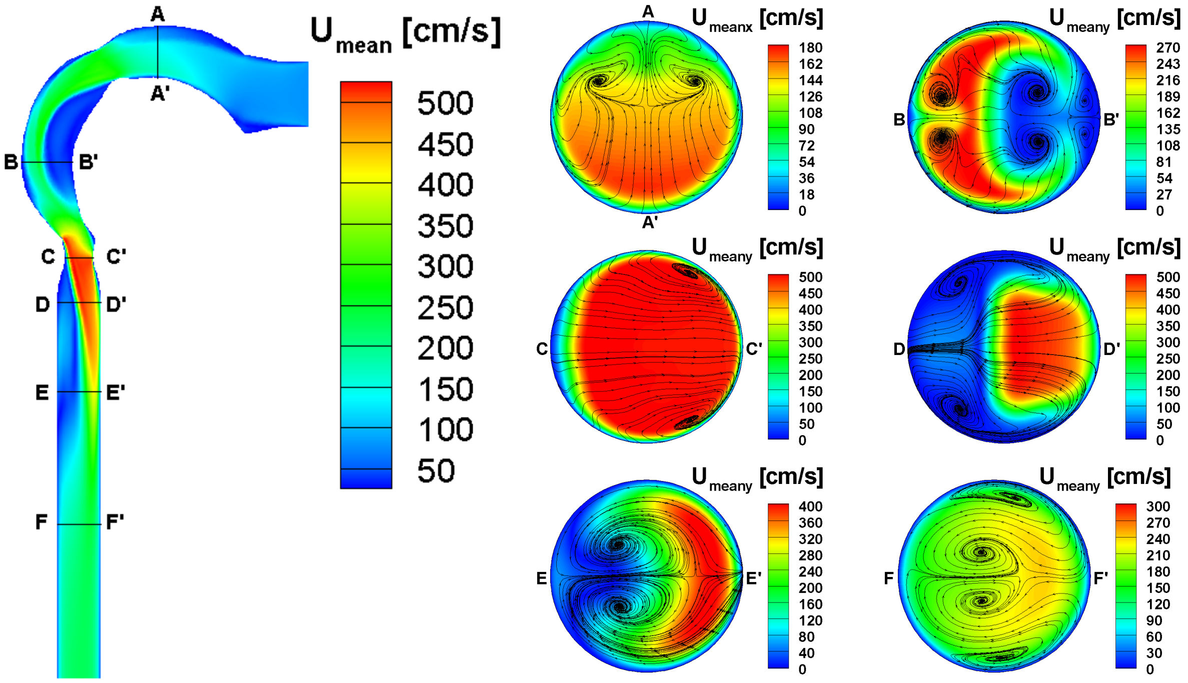

Fig. 5.13: Time-averaged velocity contour and streamlines at the mid-plane (left), and time-averaged axial velocity and secondary streamlines at different cross-sections (right) at the inspiration flow rate of 15 L/min.

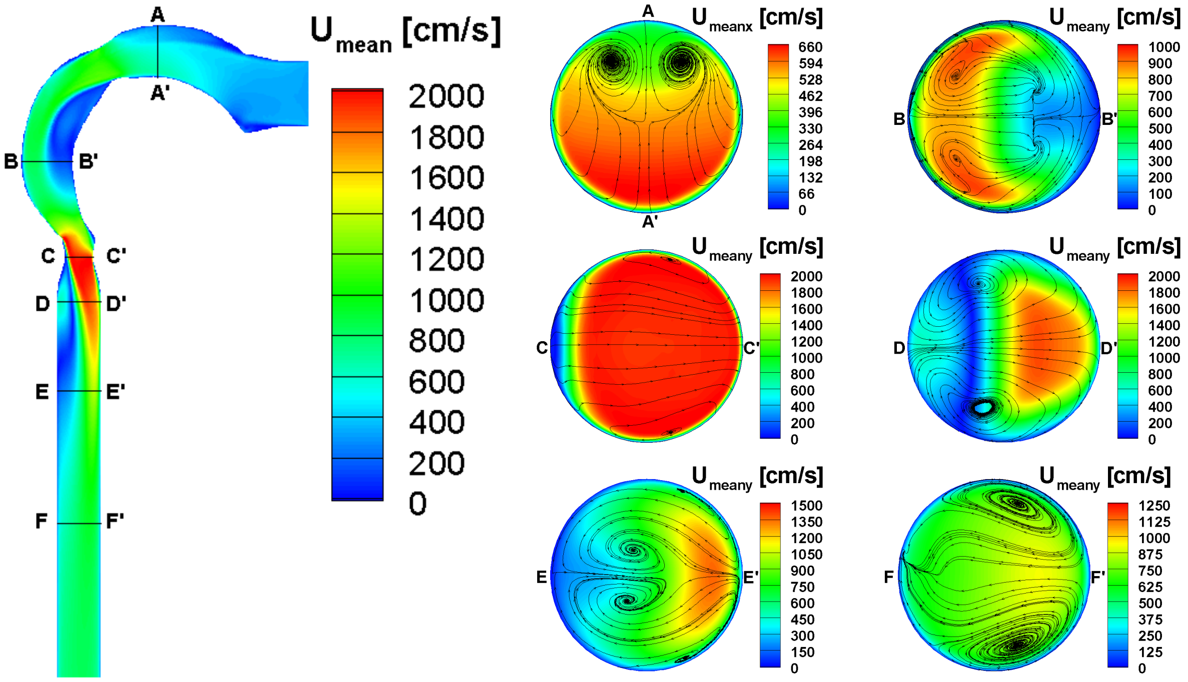

Fig. 5.14: Time-averaged velocity contour and streamlines at the mid-plane (left), and time-averaged axial velocity and secondary streamlines at different cross-sections (right) at the inspiration flow rate of 60 L/min.

tendency such as the velocity skews, the recirculation zone in the mouth cavity, pharynx and trachea, and laryngeal jet. The velocity magnitude in this case is smaller than in the case of 30 L/min and it is almost half of the value at inspiration rate of the 30 L/min.

The main difference between the two cases of 15 and 30 L/min is the distribution of secondary vortices and the profile of laryngeal jet. At the A - A' cross section, the scale of secondary vortices is smaller, and positions of the vortices are lower. At B - B' cross section, there are three pairs of counter-rotating vortices. One pair is in the main flow zone and another two pairs are in the recirculation zone. The lower Reynolds number means that low turbulence appears in the recirculation zone, which helps the vortices to develop. There is no distinct difference for secondary vortices at the location of glottis. The distinct differences for the secondary vortices and axial velocity contour are seen again in the trachea seen at D - D' cross section. The reversed flow region is much larger in this case. The secondary vortices locate in the reversed flow region. It is the same situation at the E - E' cross section. Moreover, the laryngeal jet in this region is more concave than in the case of 30 L/min, and the laryngeal jet is narrower. At the F - F' cross section, in comparison of the case at 30 L/min, the length scale of the secondary vortices are almost same. Due to smaller turbulent intensity, the secondary vortices in the central part of the geometry have more chance to develop.

As the same situation in the cases of 15 and 30 L/min, the inspiration flow rate of 60 L/min has similar basic flow structure such as the recirculation zone, laryngeal jet and secondary vortices. But, at A - A' cross section, the secondary vortices are larger and the positions are upper than the case of 30 L/min. At B - B' cross section, the recirculation zone is smaller and only one pair of vortices are seen in comparison with two pairs seen in the case of 30 L/min and three pairs of vortices seen in the case of 15 L/min. The fewer vortices in the case of 60 L/min may result from the high turbulent intensity, which allows more mixing between the main flow zone and recirculation zone and thus suppresses the recirculation zone. In addition, from E - E' cross section, it can be seen that the recirculation zone is much smaller than the cases of 30 L/min and 15 L/min. At the same time, the mixing zone is much larger in this location. The larger mixing zone may come from the high interaction between the recirculation zone and laryngeal jet under the high turbulence. At the cross section F - F', one pair of larger vortices is seen in the boundary layer since high turbulence appears in this region and the turbulence also eliminates the pressure so that no vortices are seen in the center of the geometry anymore.

In summary, the flow field in mouth-throat model based on cast is very complex including the recirculation zone and laryngeal jet. The flow structures are similar for the three different inspiration flow rates. And the main differences are the distribution of secondary vortices distribution, laryngeal jets and recirculation zones. To further investigate the flow structure, laryngeal jet and the vortex field in the three-dimensional 3D space other than at cross-sections are discussed.

5.2.4.2 Airflow Structures in the 3D Space

To observe the laryngeal jets in detail, the iso-surfaces of velocity at 15, 30 and 60 L/min are shown in Fig. 5.15. It can be seen that the laryngeal jet is larger and more concave at the inspiration of 15 L/min than the laryngeal jet in other two cases, and the laryngeal jet is shortest at the inspiration flow rate of 60 L/min. The length of the laryngeal jets at the 15, 30 and 60 L/min is 9.72, 9.52 and 8.85 cm. At the larger inspiration rate, the pressure drop between two sides of the glottis is larger. Thus, impingement of the laryngeal jet is higher and more concentrated.

Although, in last section, only the secondary vortices are discussed to identify the properties of the vortex field, in fact, the vortices are quite three-dimensional dynamics. It is necessary to discuss the vortex field in three dimensional space. Two ways have been adopted to depict the vortex. One way is to use the utility "Q", which is called Q-criteria [275, 276] in the OpenFOAM 1.5 [184] to capture the vortex. Q can be defined as follows [275, 276]:

$$Q = \frac{1}{2}[|\mathbf{\Omega}|^2 - |\mathbf{S}|^2] \tag{5.9}$$

$$\mathbf{S} = \frac{1}{2}[\nabla\mathbf{V} + (\nabla\mathbf{V})^T] \tag{5.10}$$

$$\mathbf{\Omega} = \frac{1}{2}[\nabla\mathbf{V} - (\nabla\mathbf{V})^T] \tag{5.11}$$

$$\nabla\mathbf{V} \;=\; \frac{\partial U_i}{\partial x_j} \tag{5.12}$$

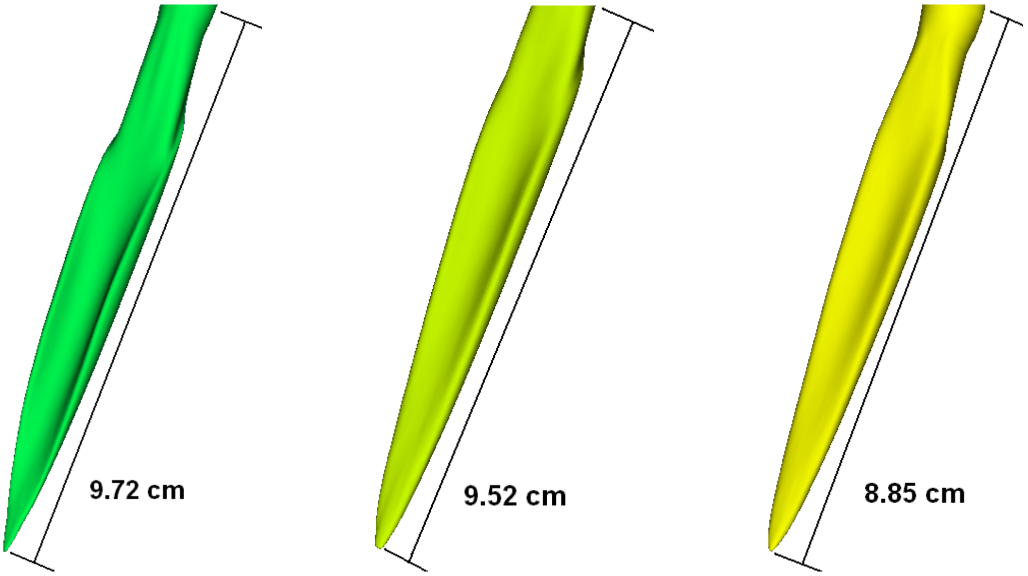

Fig. 5.15: Laryngeal jet at the inspiration flow rate of 15 (left), 30 (center) and 60 L/min (right) with velocity iso-surface of 230, 450 and 900 m/s respectively.

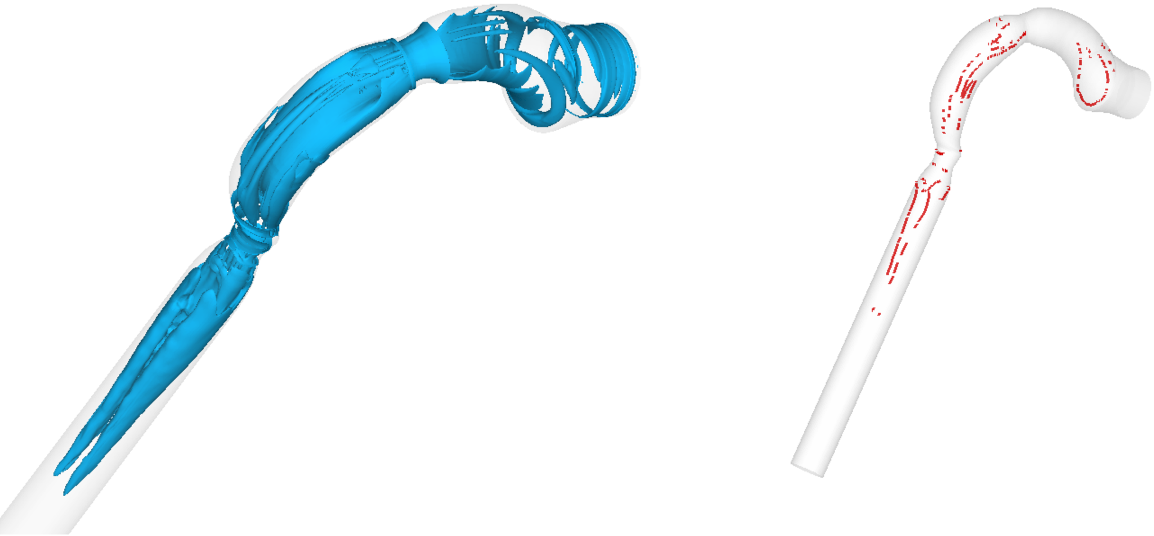

Fig. 5.16: Three dimensional vortices in the cast-based mouth-throat in the mean flow field at the inspiration flow rate of 15 L/min with Q-criteria [275] (left) and Tecplot [277] (right) from different angles of observation.

Where, $\nabla \mathbf{V}$ is the velocity gradient; $(\nabla \mathbf{V})^T$ is the transposition of the velocity gradient; $\mathbf{S}$ is the rate-of-strain tensor of velocity gradient, $\mathbf{\Omega}$ is the vorticity tensor of velocity gradient and Q is the second invariant of the velocity gradient tensor, $\nabla \mathbf{V}$. when $Q > 0$, it indicates vortex. Another way is to use the function of the "vortex core" in the Tecplot [272, 277] to capture the vortex core [277]. More detailed information on these vortex identification methods can be found in [184, 276, 277]. It is found that any one of these methods cannot demonstrate the vortex completely. The feature "vortex core" in Tecplot can capture the vortices totally, but at the same time, it also includes the shear layer near the wall boundary, the shear layer between the recirculation zone and main zone, the shear layer between recirculation zone and laryngeal jet. On one hand, these shear layers make the vortices not so prominent and make the vortices not easy to be seen. The second way can capture the core of vortices precisely, but it cannot provide suitable depict of the vortices structures. Thus, it is suitable to adopt these methods to demonstrate the vortex structure with help of the comparison of the vortex structure.

In this section, the three-dimensional vortex structures are addressed. It can be seen that the stream-wise vortex structures exist in the oral airway, pharynx, larynx and trachea as shown in Fig. 5.16 to 5.18. For instance, at inspiration flow rate of 15 L/min, a hairpin vortex appears in the oral cavity. It appears in the tip of the tongue and extends to the soft palate, seen in Fig. 5.16. The hairpin like vortices also appear in other two inspiration flow rates of 30 and 60 L/min seen in Figs. 5.17 - 5.18. The main difference among the hairpin vortices in these cases is the distance between the legs. It is much further at low inspiration flow rate than the high inspiration flow rate. And at higher inspiration rate, the legs of the vortex can extend to the larynx. In addition, stream-wise counter-rotating vortices are seen in the

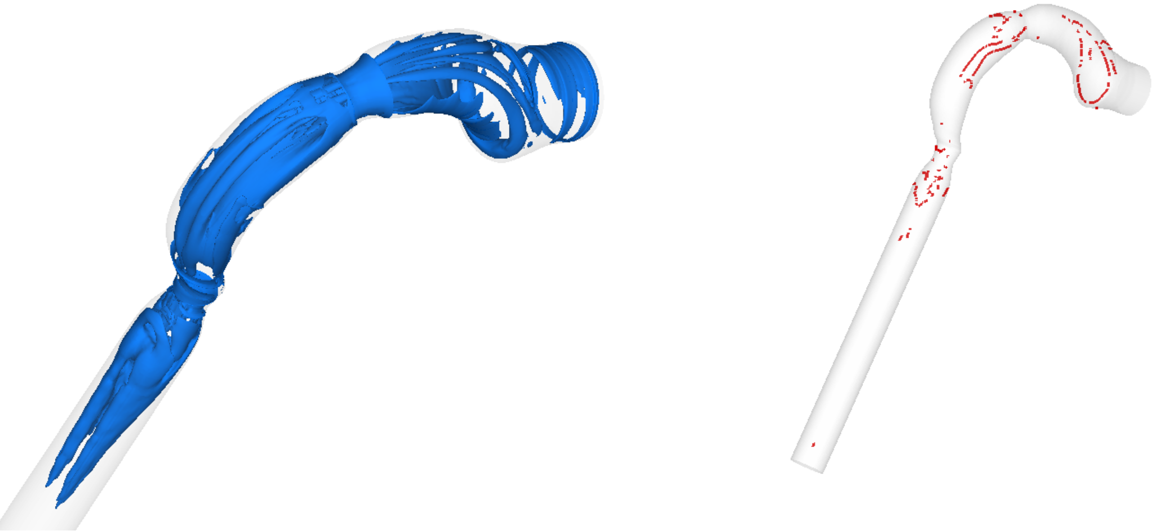

Fig. 5.17: Three dimensional vortices in the cast-based mouth-throat in the mean flow field at the inspiration flow rate of 30 L/min with Q-criteria [275] (left) and Tecplot [277] (right) from different angles of observation.

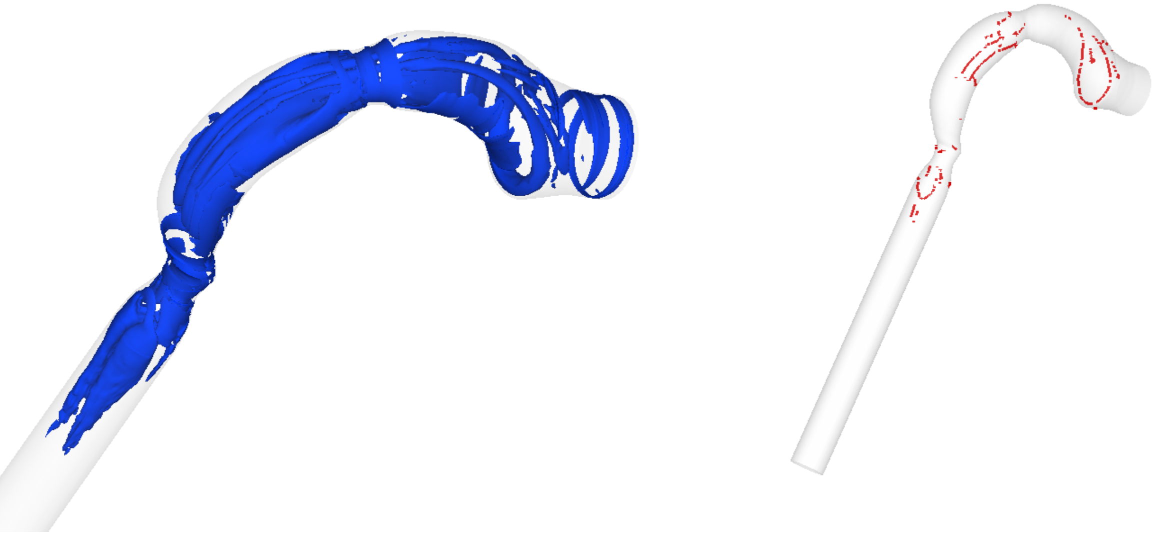

Fig. 5.18: Three dimensional vortices in the cast-based mouth-throat in the mean flow field at the inspiration flow rate of 60 L/min with Q-criteria [275] (left) and Tecplot [277] (right) from different angles of observation.

upper portion of the oral cavity, seen in Fig. 5.16 (left), 5.17 (left) and 5.18 (left).

When airflow enters into pharynx, another pair of counter-rotating vortices appear in the main flow zone seen in Fig. 5.16 (left), 5.17 (left) and 5.18 (left) and extend to the glottis. Moreover, two pairs of counter-rotating vortices are seen in the Fig. 5.16 (right) at 15 L/min in the recirculation flow zone of pharynx and one pair at 30 and 60 L/min in Fig. 5.17 (right) and 5.18 (right). The vortices after the glottis are much more complex than other locations. The hairpin like vortices can be seen from Fig. 5.16 (right), 5.17 (right) and 5.18 (right). Moreover, counter-rotating vortices can be seen as well from these figures. It also can be seen that with the increase of the inspiration flow rate, the length scale of vortices in the trachea decrease.

In summary, the counter-rotating vortices stream-wisely distribute in different regions of the flow fields. The hairpin vortices mainly appear in the mouth cavity and trachea. The length of the vortices is related to the inspiration flow rate. With the increase of the inspiration rate, the length of vortices decreases in the trachea.

5.2.4.3 Unsteady Airflow Fields

To further understand the properties of the flow field in the simplified geometry, the unsteady velocity field is discussed in this section. For the flow field at the inspiration flow rate of 30 L/min, a typical instantaneous velocity contour at the mid-plane (left-hand side) and the axial velocity contour and secondary velocity streamlines (right-hand side) at the same cross-sections as Fig. 5.10 are shown in Fig. 5.19 at time $t = 0.471$ s, which includes the trypical flow strucures of the unsteady airflow field.

The unsteady flow field is significantly different from the mean flow field show in Fig. 5.10. From the typical instantaneous velocity field at the mid-plane in Fig. 5.19, it is found that the instantaneous velocity field maintains almost the same profile in the mouth cavity as the time-averaged flow field. A close look at cross-section A - A' in Fig. 5.19, it shows that the instantaneous axial velocity profile and secondary streamlines remain almost the same as the averaged flow field. These observations indicate that the flow field in the mouth cavity is mainly laminar.

When the flow field enters into the pharynx, unsteadiness occurs at the boundary of recirculation zone and main flow zone as shown in Fig. 5.19 (left-hand side). Compared with the average flow field, no counter-rotating vortices are seen in the instantaneous flow field at B - B' cross-section. Moreover, there are no counter-rotating secondary vortices in flow field at all sections other than cross-section A - A' due to the unsteadiness of the flow field. However, there are large length-scale vortices in the main flow zone at B - B' cross-section as shown in Fig. 5.19, near the location of counter-rotating vortices in the mean flow field displayed at B - B' cross-section in Fig. 5.10. Apart from these large-scale vortices in the main flow zone, there are secondary vortices at different length scales. They reside in the main flow region, in the mixing zone, and in the recirculation region. At section C - C', the laryngeal jet dominates, and the geometry is constricted at the glottis causing the axial velocity to increase, c.f. C - C' section in Fig. 5.19 and 5.10. In contrast to the vortices at the B - B' section shown in Fig. 5.19, not many secondary vortices are seen at section C - C' in Fig. 5.19 . When the airflow enters into section D - D' (Fig. 5.19), the laryngeal jet still dominates the flow and a recirculation zone has developed. There are smaller length-scale vortices in the main flow region, in the recirculation flow zone and in the wall shear layer of

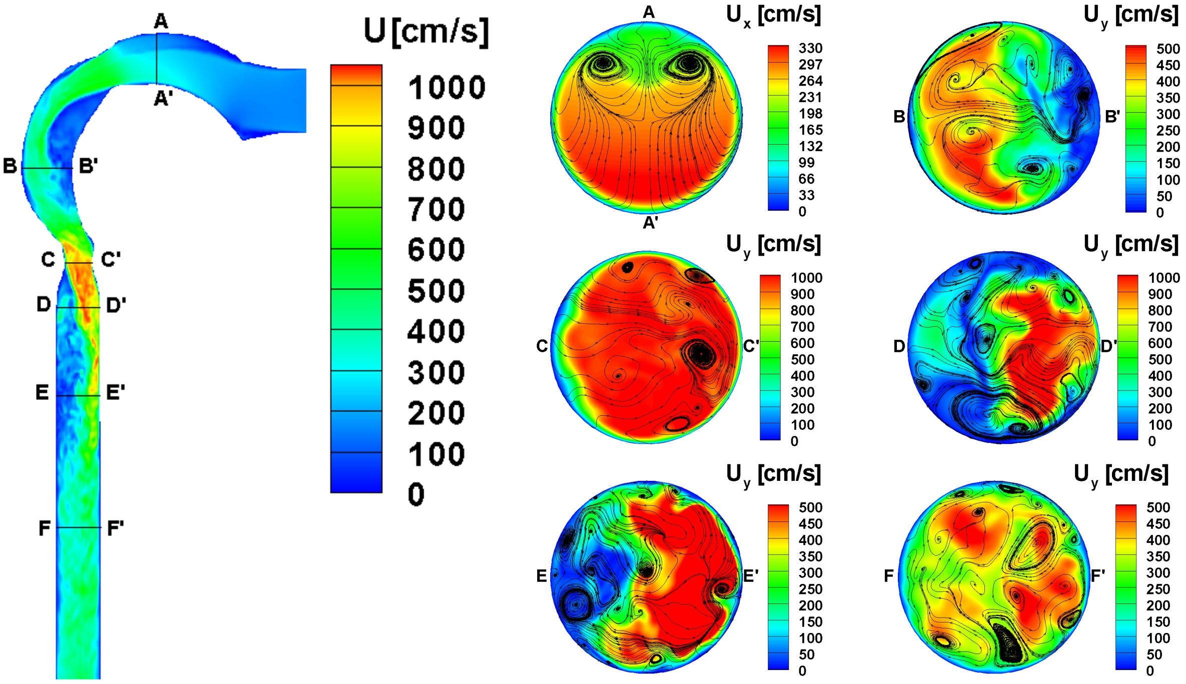

Fig. 5.19: Instantaneous velocity contour at mid-plane (left), and axial velocity contour and secondary streams at cross-sections (right) at time 0.471 s in the cast-based mouth-throat at inspiration flow rate of 30 L/min.

the laryngeal jet as well as in the separation zone. When the airflow enters into section E - E', which is located at the tail of laryngeal jet (c.f. Figs. 5.10 and 5.19), the recirculation zone does not directly touch the laryngeal jet, and the interface between the recirculation zone and the laryngeal jet becomes concave. Moreover, secondary vortices of different length-scales are seen to reside in the recirculation zone, the mixing zone, and in the wall shear layer. It is very interesting to find that there are more relatively smaller vortices in this section, particularly in the wall shear layer, since they may greatly affect particle transport in this region, which is discussed in section 5.2.5. In the F - F' section, the axial velocity contour profile becomes irregular and the secondary vortices distributes all over the cross-section.

In comparison with the flow field at inspiration flow rate of 30 L/min, instantaneous flow field at inspiration flow rate of the 15 L/min displays laminar features in more regions of the cast-based mouth-throat model due to the lower Reynolds number and it also shows significant different properties as compared to the time-averaged flow field seen in Fig. 5.13. From the typical instantaneous velocity field at the mid-plane in Fig. 5.20, it is found that the instantaneous velocity field maintains almost the same profile in the mouth cavity as the time-averaged flow field as well in the case of 15 L/min. A close look at cross-section A - A' in Fig. 5.20, it can be seen that the instantaneous axial velocity profile and secondary streamlines keep almost the same as the averaged flow field seen in Fig. 5.13. These observations indicate that the flow field in the mouth cavity is mainly laminar as well.

As the air goes further into the pharynx, unsteadiness occurs at the boundary of recir-

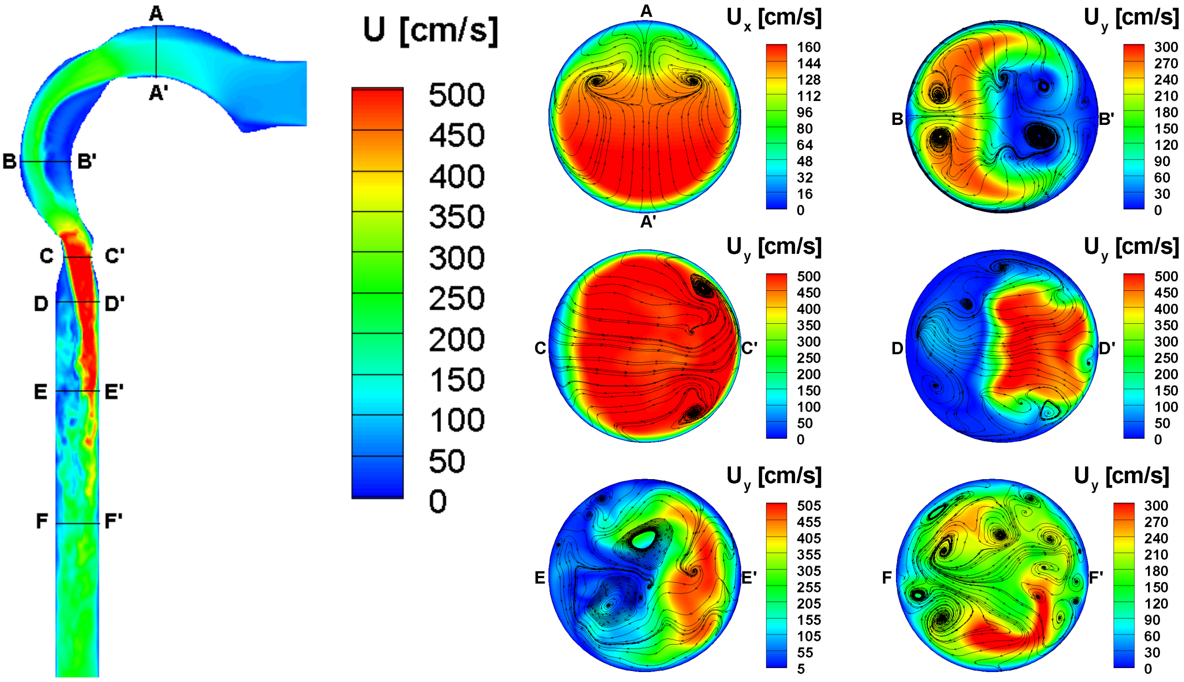

Fig. 5.20: Instantaneous velocity contour at mid-plane (left), and axial velocity contour and secondary streams at cross-sections (right) at time 1.018 10^{-4} s in the cast-based mouth-throat at inspiration flow rate of 15 L/min.

culation zone and main flow zone as shown in Fig. 5.20 (left-hand side). Compared with the average flow field, a pair of counter-rotating vortices can still be seen in the main flow zone in the instantaneous flow field seen at B - B' cross-section. Although, the unsteadiness damages the counter-rotating vortices in the recirculation zone, it can be still seen that the vortices with the large length-scale in the corresponding position of counter-rotating vortices in the mean flow field. These properties show that the laminar flow at B - B' cross section is still prominent, which means that laminar flow occurs not only in the mouth cavity but also in larynx cavity. At the same time, the vortices at B - B' cross section for 15 L/min are not as many as for 30 L/min seen in Fig. 5.19, which means that the unsteadiness in the interface of the recirculation zone and main flow zone is not large enough to produce new vortices at this time. At section C - C', the laryngeal jet dominates as in the time-averaged flow field. Although, two vortices are seen in this time step in corresponding position where two counter-rotating secondary vortices are shown in the averaged flow field, they are much deformed. Moreover, another smaller secondary vortex is seen. When the airflow enters into section D - D' (Fig. 5.20), the laryngeal jet still dominates the flow and a recirculation zone has developed as in the time-averaged flow field. Different scale vortices are seen in the recirculation flow zone and in the boundary of laryngeal jet. When the airflow enters into section E - E', the laryngeal jet still dominates the flow field, but the mixing in the laryngeal jet and the recirculation enhancement is seen from the laryngeal jet boundary shown in the Fig. 5.20. Moreover, secondary vortices are seen in the jet flow region, the interface of the laryngeal

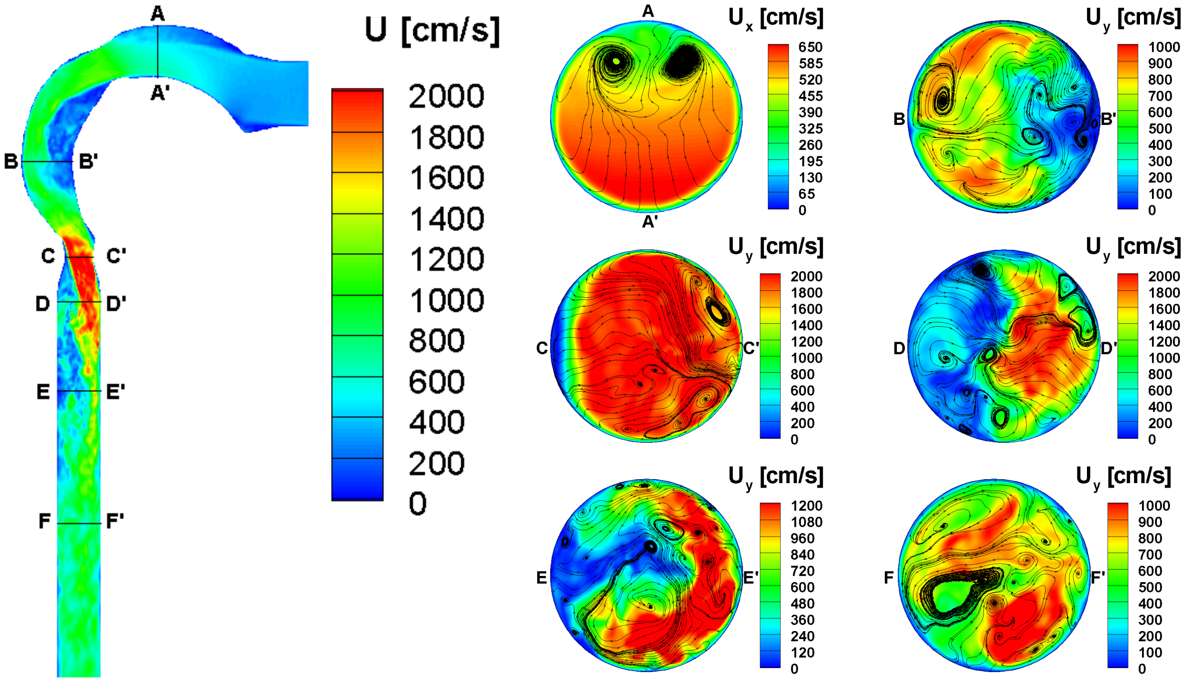

Fig. 5.21: Instantaneous velocity contour at mid-plane (left), and axial velocity contour and secondary streams at cross-sections (right) at time 1.97 10^{-4} s in the cast-based mouth-throat at inspiration flow rate of 60 L/min.

jet and recirculation zone, the recirculation flow zone and the boundary layer of the wall. After the E - E' section, the laryngeal jet deforms and breaks up. When flow goes further to the F - F' section, the turbulence has developed totally and axial velocity contour profile becomes irregular and the secondary vortices distribute all over the cross-section as same as the situation at inspiration flow rate of 30 L/min. And smaller scale secondary vortices have been seen in the boundary layer of the wall.

In comparison with the inspiration flow rate of 30 L/min and 15 L/min, flow field at inspiration flow rate of the 60 L/min are more turbulent due to the higher Reynolds number. The instantaneous flow field is shown in the Fig. 5.21 at the same cross sections as the way in other two cases. Different from other two cases, the unsteadiness appears in the mouth cavity seen in the left-hand of Fig. 5.21. Taking a close look at the velocity contour plot and the secondary streamlines, the axial velocity profile is different from the mean flow field shown in Fig. 5.14. Although there are still counter-rotating vortices, the position and profile of the vortex at right side is distinctly different from vortices in the time-averaged flow field. This unsteadiness induces the turbulent flow evolving in the downstream. The axial velocity and secondary vortices distribution at the other cross sections are similar to the case of inspiration flow rate of the 30 L/min. But, more vortices are seen in the higher Reynolds number at the inspiration rate of 60 L/min.

5.2.5 Monodisperse and Polydipserse Particle Deposition and Dispersion

The particle deposition and dispersion are discussed in this section. The attention is paid to the total particle deposition efficiency, local particle deposition efficiency and the particle deposition pattern on the wall of the geometry as well as the relationship between the release particle positions and the particle trajectories. Moreover, the particle dispersion and transport will be discussed. In addition, the poly-disperse particle distribution, which is measured from dry power inhaler (DPI), and the injection mass of particles, which considers drug dose at per actuation of DPI in the clinical treatment, are adopted along with the parcel method.

5.2.5.1 Mono-Disperse Particle Motion

The mono-disperse micro-particle deposition and transport are studied in the idealized mouth-throat at first. The particles are injected simultaneously with the air randomly at the inlet plane, which have the same velocity as the air flow. The particle position is controlled by the Gauss uniform distribution. The injected particle number was evaluated by Zhang et al. [20] from 1,000 to 10,000. The deposition efficiency does not change with the particle number for 10,000. So, in present work, the injected particle number is set to 10,000. It is assumed that the particle deposition occurs if the distance of the particle center to the wall is less than half of the particle diameter in all cases. The particle density is 1,000 kg/m^3. Three diameters d_p = 2, 5, and 10 µm are studied at three different steady inspiration flow rates with 15, 30, and 60 L/min respectively, therefore 9 cases are computed totally.

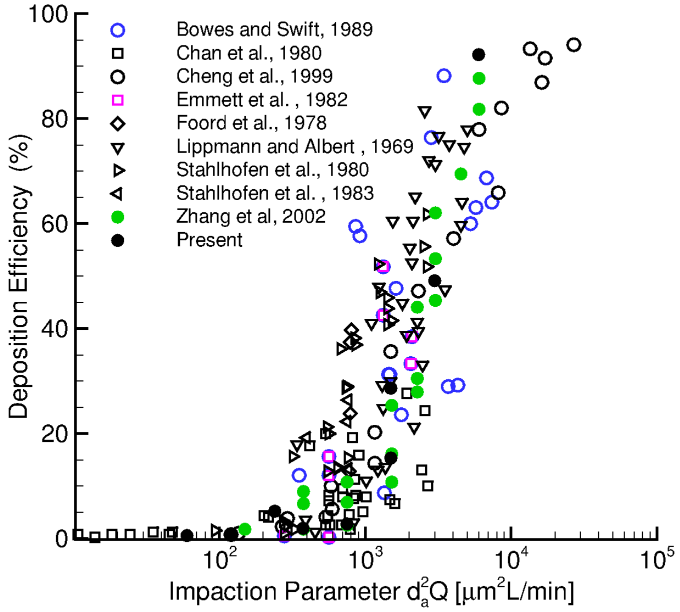

Fig. 5.22: Comparison of total particle deposition in the cast-based mouth-throat with experimental (the open symbols) [48, 248, 278–283] and numerical (solid symbols) [86] data.

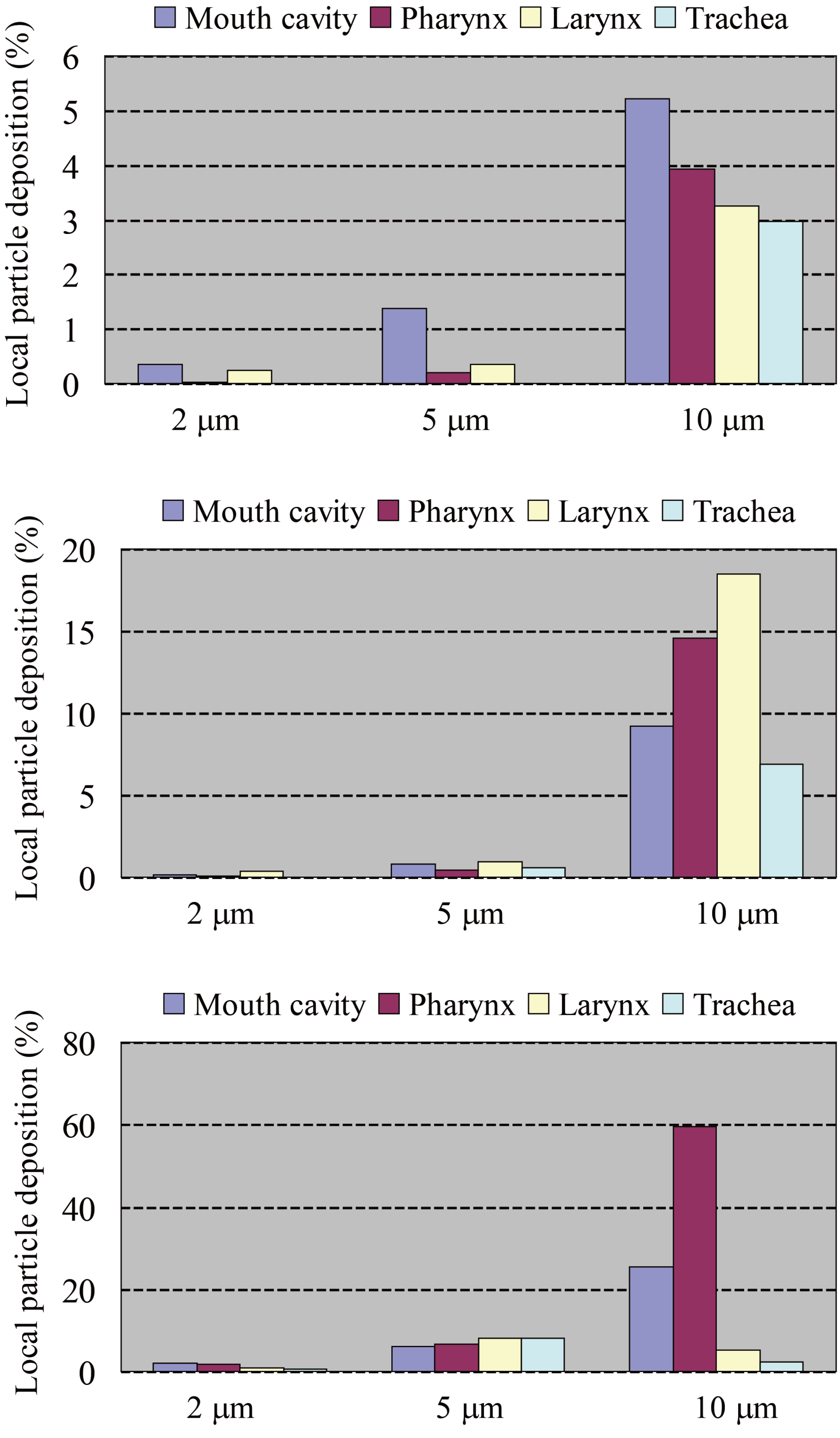

Fig. 5.23: Regional particle deposition efficiency in mouth cavity, pharynx, larynx and trachea of the cast-based mouth-throat for particles of 2, 5 and 10 µm at inspiration flow rate of 15 (top), 30(middle) and 60 (bottom) L/min.

Particle Deposition Efficiency A comparison of the present particle deposition efficiency with vivo measurements and other numerical results is a way to evaluate the idealized mouth-throat model [86]. The comparison of the particle deposition efficiency as a function of impaction parameter, $\rho_p Q d_p^2$, for the present numerical simulations on the final grid with other numerical and experimental results is shown in Fig. 5.22 [48, 86, 248, 278–283]. For the particle inertia, impaction is the main mechanism for the micro-size particle deposition in the oral airway and the particle deposition efficiency increases with increasing impaction parameter. It can be seen that the present results are close to the numerical results from the literature [86]. Moreover, they fit well with the medium trend of the experimental data [48, 248, 278–280, 282, 283], and thus the numerical results are representative values of particle deposition in the human oral airway. Thus, the methodology including the idealized mouth-throat model is suitable to be implemented in the study of particle deposition in the human oral airway.

To identify the particle deposition pattern in different regions and to study the particle size influence on different inspiration flow rates, the particles with 2 µm, 5 µm and 10 µm under different inspiration flow rates corresponding to 15, 30 and 60 L/min are shown in Figs. 5.23 (top, middle and bottom) respectively. At inspiration flow rate of $Q = 15$ L/min, the particles have lower impaction parameter, in particular, for the particle with the size 2 and 5 µm. There is no particle deposition in the trachea at this inspiration flow rate for particles with 2 and 5 µm. And particle deposition mainly occurs in the mouth cavity and larynx for particle size of 2 and 5 µm. At particles with 10 µm, particle deposition occurs in the tracheal region. Moreover, the particles depositing in the region of pharynx are more in number than the particles depositing in the region of larynx. Due to the particle size increasing significantly, the particle inertia increases largely, so that more particles impact on the laryngeal wall. And the particle deposition in the trachea may be resulted from the increase of the particle inertia, the recirculated flow and the turbulent dispersion. When the inspiration flow rate increases to 30 L/min, for the particle with 2 µm is still low, but particle deposition occurs in tracheal region for the particles with 5 and 10 µm. It is also found that at this inspiration flow rate, more particles deposit in the larynx than in the mouth cavity since higher inspiration flow rate makes particle stay in the mouth cavity shorter and it also increases particle inertia so that particle is easier to deposit in the larynx. And at this inspiration flow rate, the largest particle deposition efficiency appears in the larynx. When the flow increases to 60 L/min, the particle with 2 µm deposits in the trachea as well. For the particles of 5 µm, the particle deposition efficiency is almost same in the region of mouth cavity, pharynx, larynx and trachea as in the case of 30 L/min. For the particles of 10 µm, the largest ratio of particle deposition efficiency happens in the region of pharynx. In comparison with the particles of 5 µm, the particles with 10 µm deposition in trachea is lower since most of the particles have deposited in the mouth to larynx so that few particle go into trachea.

Particle Deposition Pattern on the Wall To investigate the particle deposition pattern on the wall of the geometry, the particle deposition positions are shown in Figs. 5.24 - 5.26.

At inspiration flow rate of 15 L/min, particles of 2 µm seen in Fig. 5.24 (left) mainly deposit on the bottom portion of the mouth cavity, the anterior side of the pharynx and the glottis. For particles of 5 µm seen in Fig. 5.24 (center), more particles deposit at the bottom of mouth cavity, posterior side of the soft palate and the upper portion of the glottis. For the particles of 10 µm seen in Fig. 5.24 (right), the particles have great inertia, and more particles deposit in the geometry. The increase of particle deposition in the mouth cavity is mainly at the bottom portion of the mouth cavity, the increase in the pharynx mainly appears in the recirculation flow zone and the posterior side of the upper portion of the glottis and in the recirculation flow zone of trachea. These deposition patterns indicate that the recirculation zone has great influence on the particle deposition and the particles mainly impact on the wall of the larynx.

At inspiration flow rate of 30 L/min, for the particles of 2 µm seen in Fig. 5.25 (left), they mainly deposit at the bottom portion of the mouth cavity, the anterior side of the pharynx and the glottis. But in this case, the particle distribution on the bottom portion of mouth cavity and the upper portion of the glottis is much more dispersed. For particles of 5 µm seen in Fig. 5.25 (center), more particles deposit in the mouth cavity and anterior side of the soft palate, but it is much dispersed as well as on the lateral sides of the upper portion of the glottis. The particles are also seen to deposit on the lateral sides of the trachea, which donnot dwell in the recirculation flow zone and the impinging side of the laryngeal jet. For the particles of 10 µm seen in Fig. 5.25 (right), the particles have great inertia and more particles deposit in the geometry. The increase of particle deposition in the mouth cavity is mainly at the bottom portion of the mouth cavity and also in the portion of soft palate; the increase in the pharynx mainly appears in the recirculation flow zone and the posterior side of the upper portion of the glottis; the increase in the larynx mainly occurs in the glottis and the increase in the trachea mainly appear in the anterior and the lateral sides of the trachea, which means that the laryngeal jet and the recirculation flow influences the particle deposition for larger particles at this inspiration flow rate significantly.

Fig. 5.24: Particle deposition pattern on the wall of cast-based mouth-throat at inspiration flow rate of 15 L/min for particle of 2 (left), 5 (center), and 10 (right) µm.

Fig. 5.25: Particle deposition pattern on the wall of cast-based mouth-throat at inspiration flow rate of 30 L/min for particle of 2 (left), 5 (center), and 10 (right) µm.

Fig. 5.26: Particle deposition pattern on the wall of cast-based mouth-throat at inspiration flow rate of 60 L/min for particle of 2 (left), 5 (center), and 10 (right) µm.

At inspiration flow rate of 60 L/min, for the particles of 2 µm seen in Fig. 5.26 (left), the particle deposition is more influenced by the turbulence. In addition, few particles deposit in the frontier part of the mouth cavity because of the larger flow velocity, and more particles deposit at the end of the soft palate due to the particle impaction. More particles deposit in the posterior part of the larynx because of the particle impaction. Particle deposition in the larynx mainly appears in the anterior part under the portion of the glottis. Particle deposition distributes uniformly in the trachea because of the recirculation zone and the turbulence influence. For particles of 5 µm seen in Fig. 5.26 (center), more particles deposit in the geometry. More particle deposition in the mouth cavity appears in front portion of the mouth cavity. More particle deposition appears in the recirculation zone of the pharynx. The particle deposition in the upper portion of the glottis and anterior side of the glottis. The particle deposition in the trachea increases significantly and the increase may result from the increase in the combined function of impaction and the turbulence. For the particles of

10 µm seen in Fig. 5.26 (right), the particles have great inertia, and most of the particles cannot go through the mouth-throat model. The increase of particle deposition in the mouth cavity is not only resulted from the position of soft palate but also the frontier part of the bottom portion of the mouth cavity.

The particle deposition in the pharynx mainly increases due to the particle impaction on the posterior side of the pharynx. The particle deposition in the larynx mainly increases from the particle impaction on the anterior side. The particle deposition in the trachea mainly dwell in the anterior side, which means that the laryngeal jet increases the possibility of the larger particle deposition in the trachea. Although turbulence has low influence on so large particle's deposition, some particles can be still seen on the posterior side of the trachea.

Initial Particle Position In this section, the particle initial positions are identified to build the relationship between the particle transport, dispersion and deposition, and initial particle position. In Figs. 5.27 - 5.35, the release particle positions at the inlet plane for the particle deposition in different regions of the mouth-throat model and particle going through the mouth-throat model are displayed. In these figures, the green solid circles present the release positions of particles which pass through the mouth-throat model and go into deep site of the lung and the red solid circles indicate the release positions of particles depositing on the wall of mouth cavity; the blue solid circles indicate the release positions of particles depositing on the wall of the pharynx, and the cyan solid circles indicate the release positions of particles depositing on the wall of larynx, and the black solid circles indicate the release positions of particles depositing on the wall of trachea.

From these figures, it can be seen that the particle deposition on the wall mainly concentrates in the region close to the wall and the vortex regions in the top portion of the geometry, where the vortices appear at inlet plane seen in Fig. 5.16. Depending on the particle size, inspiration flow rate and the initial position, these particles may deposit on the wall and go through the mouth-throat model. For instance, at inspiration flow rate of 15 L/min, the particles with 2 µm have lower particle deposition in the geometry. The particles depositing in the mouth cavity are mainly released in the boundary of the inlet plane, where most of them are released at the bottom of the inlet plane and some of them are released at the upper and lateral portions of the inlet plane seen in Fig. 5.27. From the figure, it can also be seen that the particles depositing in the pharynx are released at the bottom and lateral portion of the mouth-throat model. It is very interesting to know that the particles depositing in the larynx are released in the positions close to the vortex as seen in the Fig. 5.16. When the particle size increases to 5 µm seen in Fig. 5.28, the particle deposition in different regions of mouth cavity, pharynx, larynx and trachea increases respectively. The particle deposition in the mouth cavity mainly increases due to the particles released at the bottom portion of the mouth-throat model. The particle deposition in the pharynx mainly results from the particles released in the lateral portions. The particle deposition in the larynx mainly increases from the particle released in the vortex region. When the particle size increases to 10 µm seen in Fig. 5.29, the particles also deposit in the region of trachea. In this case, most of the depositing particles are released at the upper portion of the inlet plane. In addition, more particles released in the vortex region of the inlet plane have the most contribution to the increase of particle deposition in the pharynx and larynx. The increase in the particle deposition on the wall of the mouth cavity is mainly resulted from the bottom portion of the inlet plane.

When inspiration flow rate is increased to 30 L/min, there are still few particles of size 2 μm depositing in the mouth-throat model. The majority of particles depositing in the mouth cavity are released at the boundary of the inlet plane, where most of them are released at the bottom of the inlet plane and some of them are released at the upper and lateral portions of the inlet plane seen in Fig. 5.30. In comparison with the case of 2 μm particles at inspiration flow rate of 15 L/min, released positions of these particles are further away from the wall. From the figure, it also can be seen that the particles depositing in the pharynx and larynx are mainly released in the vortex region, where the vortices appear at inlet plane seen in Fig. 5.17. When the particle size is increased to 5 μm seen in Fig. 5.31, the particle deposition in different regions of oral cavity, pharynx, larynx and trachea increases respectively. The particle deposition in the mouth cavity mainly increases due to the particles released at the bottom portion of the geometry. The increase of particle deposition in the pharynx mainly results from the particles released in the vortex region. The increase of particle deposition in the larynx is mainly due to the particle released in the vortex region as in the case of the inspiration flow rate 15 L/min and particle size of 5 μm. Particle deposition also happens in the trachea. It looks like that the particles are randomly distributed at the inlet plane, but few of these depositing particles are released in the location close to the middle plane. When the particle size increases to 10 μm seen in Fig. 5.32, increase of particle deposition in the mouth cavity is mainly from the bottom portion and lateral portion of inlet plane close to the wall. More particles deposit in the pharynx and larynx. These particles are mainly released in the extension of the vortex region. Majority of the particles depositing in the trachea are released at the lateral portions of the inlet plane. Few particles close to the middle line in the vertical direction deposit in the geometry and most of them can go through the mouth-throat model.

When inspiration flow rate is increased to 60 L/min, the particles of 2 μm depositing in the mouth cavity mainly are released in the boundary of the inlet plane as well. Most of them are released at the lateral portion of the inlet plane while some of them are at bottom portion of the inlet plane, and few particles are in the upper portion and other regions as seen in Fig. 5.33, contrary to the case of 2 μm particles at inspiration flow rate of 15 and 30 L/min, where most of depositing particles are released at the bottom portion of the inlet plane. From Fig. 5.33, it also can be seen that the majority of particles depositing in the pharynx are released in the vortex region, where the vortices appear at inlet plane seen in Fig. 5.18, as in the case of inspiration flow rate of 30 L/min. In comparison with the case of 15 L/min and 30 L/min, the particles depositing in the larynx randomly distribute at the inlet plane. At this inspiration flow rate, the 2 μm particles have enough inertia to deposit in the trachea and these particles randomly distribute at the inlet plane. When the particle

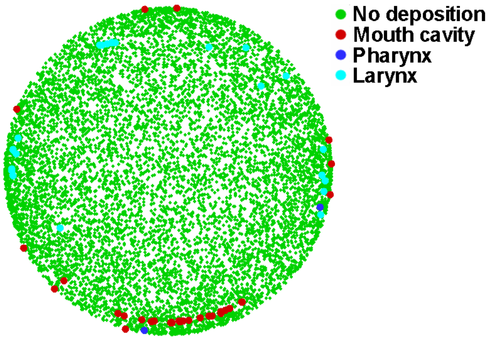

Fig. 5.27: Release positions of 2 μm particles exiting and depositing the mouth-throat model for 15 L/min.

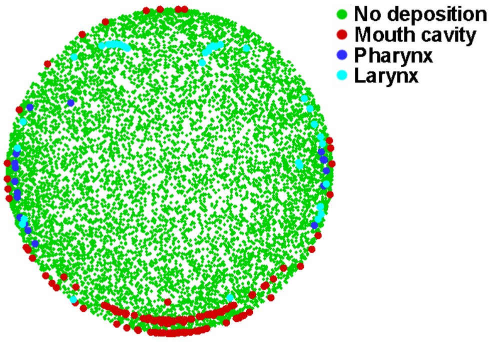

Fig. 5.28: Release positions of 5 μm particles exiting and depositing the mouth-throat model for 15 L/min.

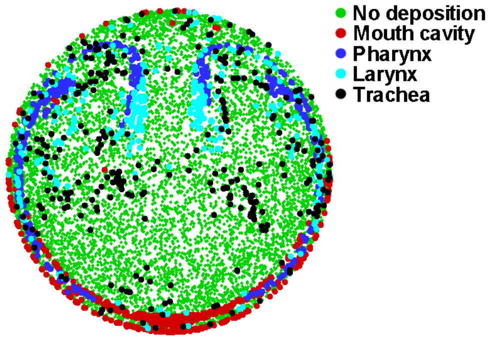

Fig. 5.29: Release positions of 10 μm particles exiting and depositing the mouth-throat model for 15 L/min.

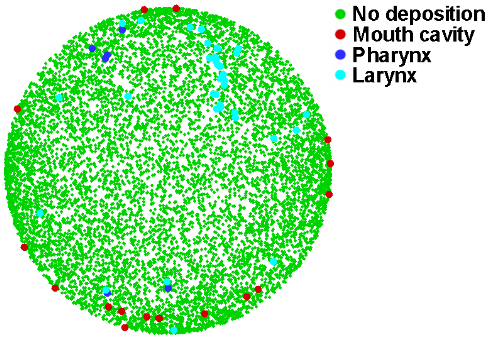

Fig. 5.30: Release positions of 2 μm particles exiting and depositing the mouth-throat model for 30 L/min.

size is increased to 5 μm, the particle deposition in different regions increases significantly seen in Fig. 5.34. The particle deposition in the mouth cavity mainly increases due to the particles released at the bottom portion of the mouth-throat model. The increase of particles deposition in the pharynx mainly results from the particles released in the vortex region and the region close to the wall. But the initial positions of particles, which deposit in the pharynx, are much dispersed. Although the released positions of particles depositing in the pharynx still concentrate in the vortex region, these particles dwell in other regions broadly. Particles depositing in the trachea distribute at the whole inlet plane. When the particle size is increased to 10 μm, increase of particle deposition in the mouth cavity is mainly from the lateral portions and bottom portion of the inlet plane close to the wall, in particular, the upper side of the lateral portions seen in Fig. 5.35. The released positions of particles depositing in the pharynx take over the remaining region of the inlet plane. The particle deposition in the larynx and trachea mainly occurs in the upper portion and the region close to the middle line in the vertical direction.

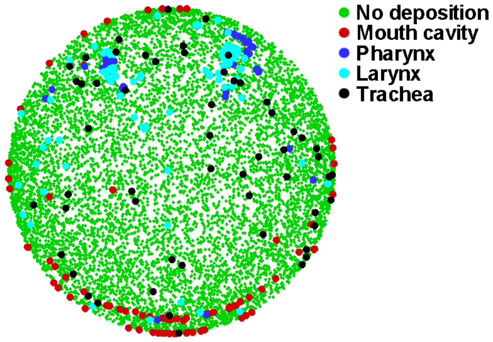

Fig. 5.31: Release positions of 5 µm particles exiting and depositing the mouth-throat model for 30 L/min.

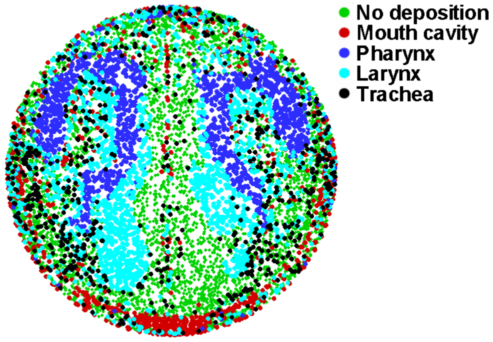

Fig. 5.32: Release positions of 10 µm particles exiting and depositing the mouth-throat model for 30 L/min.

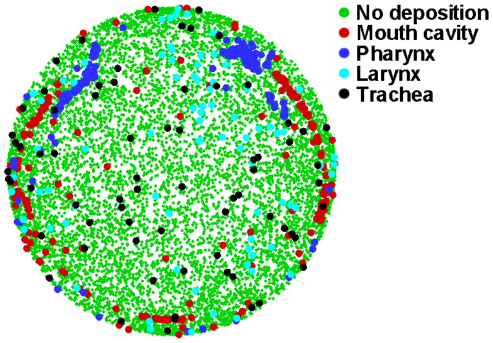

Fig. 5.33: Release positions of 2 µm particles exiting and depositing the mouth-throat model for 60 L/min.

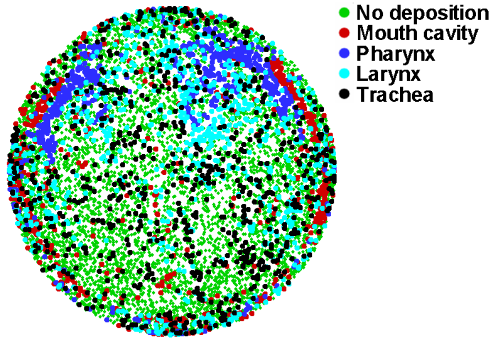

Fig. 5.34: Release positions of 5 µm particles exiting and depositing the mouth-throat model for 60 L/min.

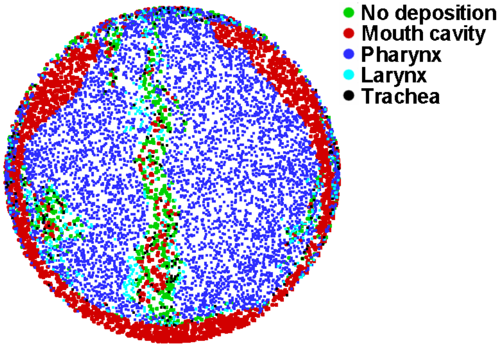

Fig. 5.35: Release positions of 10 µm particles exiting and depositing the mouth-throat model for 60 L/min.

Particle Trajectories To visualize trajectories of individual particles is one way to demonstrate the particle transport, and the influence of particle size and air flow on the particle dispersion and deposition. In the present work, particles at five different positions have been selected for each case. The coordinate of these positions are position 0 at (0.0, 0.0, 0.0) m; position 1 at (0,0.008,0) m; position 2 at (0.0,0.0,-0.008) m; position 3 at (0.0,0.008,0.0) m and position 4 at (0.0,-0.008,0.0) m. At each position, 4 different particles are located in a small circle centered at each position with a radius of 1.0 10^{-4} m. Figs. 5.46 - 5.80 show all of the selected particle trajectories for inspiration flow rates of 15, 30 and 60 L/min and 2, 5 and 10 μm particles respectively. In these figures, particle No. 1 is indicated with the red line; No. 2 with the green line; No. 3 with the blue line and No. 4 with the cyan line.

At the inspiration flow rate of 15 L/min, for the 2 μm particles at location of position 0 (c.f. 5.36), all of the particles go through the mouth-throat model. All of these particles mainly follow the laminar flow in the mouth cavity. The particle dispersion appears in the middle of pharynx. The dispersion of these particles enlarges at the bottom of pharynx. After the particle dispersion appears, these particles have different fates. At position 1, the particles disperse in the pharynx as well seen in Fig. 5.37. The second particle (green line) disperses largely and has very different trajectory from other particles, and the first and second particle are entrained by the vortex in the trachea significantly. At position 2, all of particles go through the mouth-throat model as well. These particles conduct approximate linear motion, which donot conduct any oscillated motion seen in Fig. 5.38. The dominant difference is that the first and fourth particle disperses significantly in the trachea. At position 3, the particle dispersion mainly appears in the trachea as well seen in Fig. 5.39. At position 4, the particle dispersed as much as at position 3 in the trachea as shown in Fig. 5.40. Moreover, it can also be seen that the first particle conducts helix motion with small amplitude. From Figs. 5.36 -

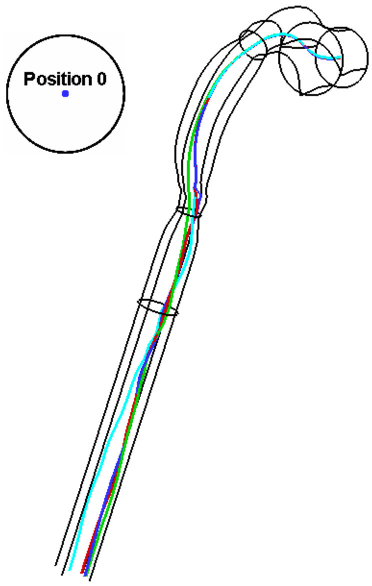

Fig. 5.36: Trajectories of 2 μm particles at position 0 at the inspiration flow rate of 15 L/min.

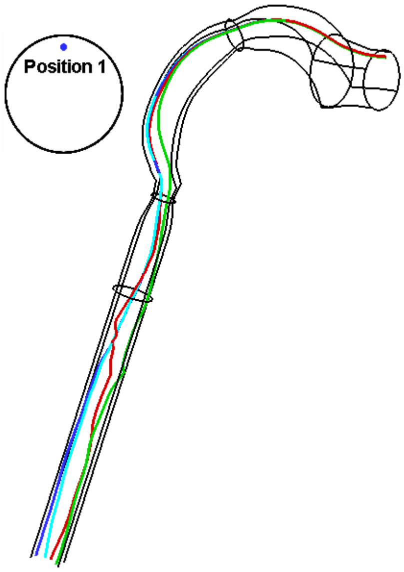

Fig. 5.37: Trajectories of 2 μm particles at position 1 at the inspiration flow rate of 15 L/min.

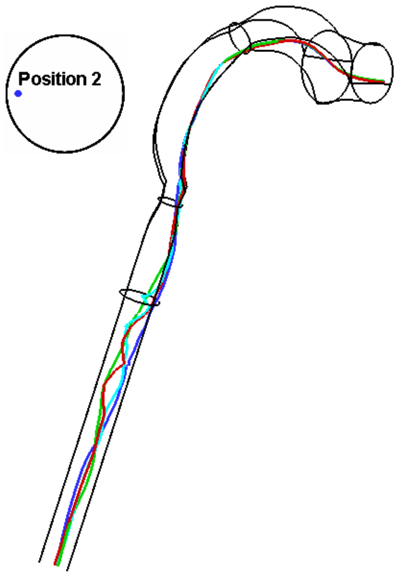

Fig. 5.38: Trajectories of 2 μm particles at position 2 at the inspiration flow rate of 15 L/min.

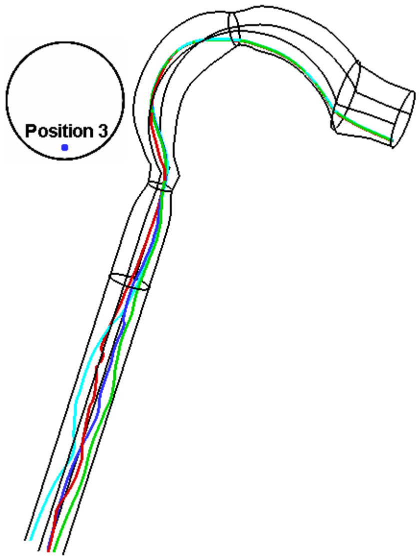

Fig. 5.39: Trajectories of 2 μm particles at position 3 at the inspiration flow rate of 15 L/min.

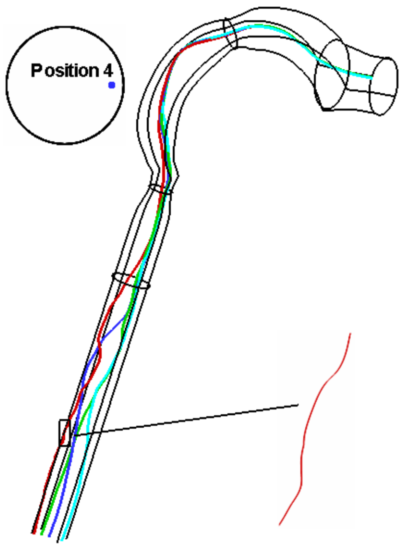

Fig. 5.40: Trajectories of 2 μm particles at position 4 at the inspiration flow rate of 15 L/min.

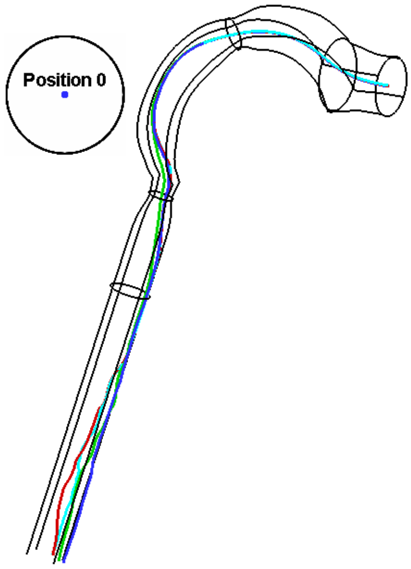

Fig. 5.41: Trajectories of 5 μm particles at position 0 at the inspiration flow rate of 15 L/min.

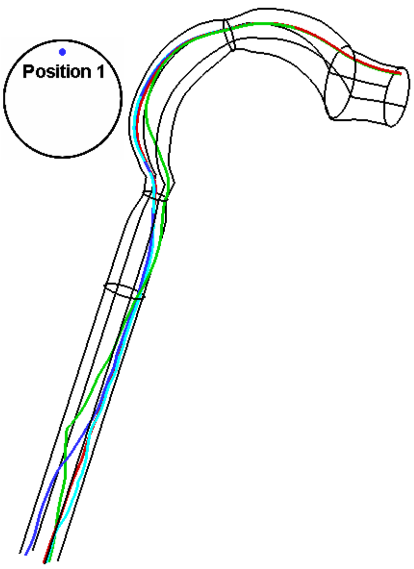

Fig. 5.42: Trajectories of 5 µm particles at position 1 at the inspiration flow rate of 15 L/min.

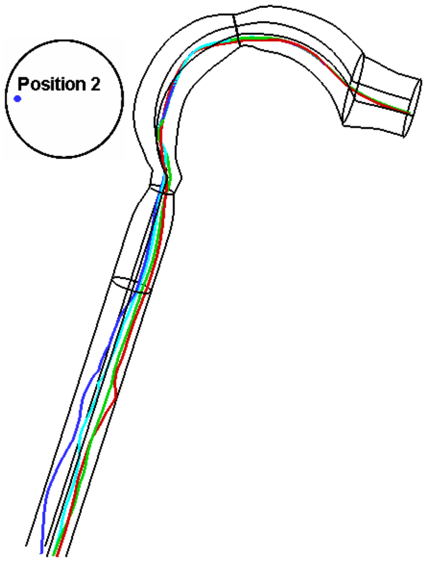

Fig. 5.43: Trajectories of 5 µm particles at position 2 at the inspiration flow rate of 15 L/min.

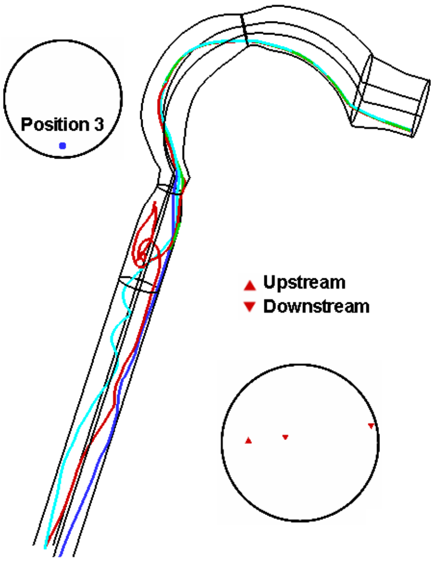

Fig. 5.44: Trajectories of 5 µm particles at position 3 at the inspiration flow rate of 15 L/min.

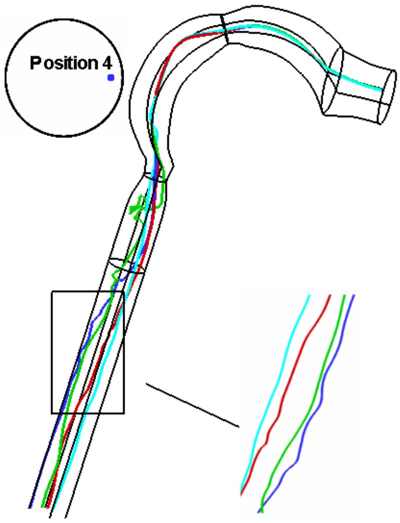

Fig. 5.45: Trajectories of 5 µm particles at position 4 at the inspiration flow rate of 15 L/min.

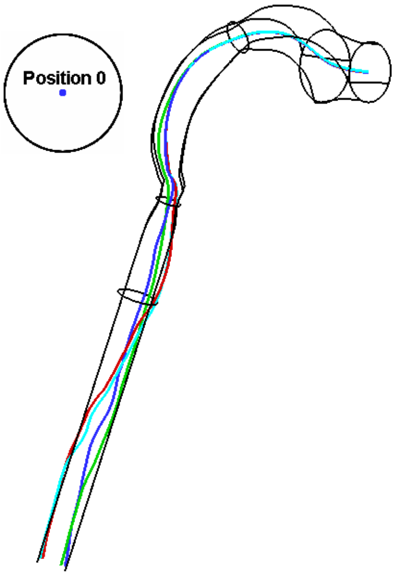

Fig. 5.46: Trajectories of 10 µm particles at position 0 at the inspiration flow rate of 15 L/min.

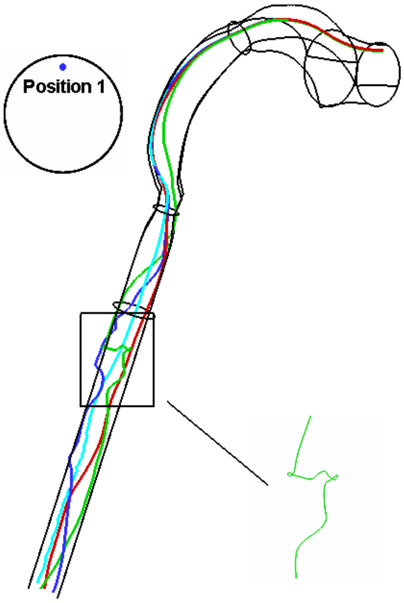

Fig. 5.47: Trajectories of 10 µm particles at position 1 at the inspiration flow rate of 15 L/min.

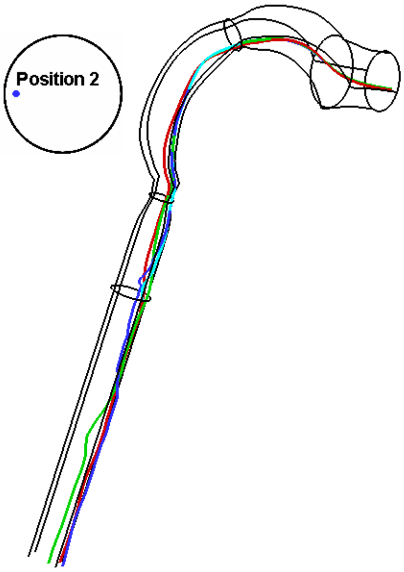

Fig. 5.48: Trajectories of 10 µm particles at position 2 at the inspiration flow rate of 15 L/min.

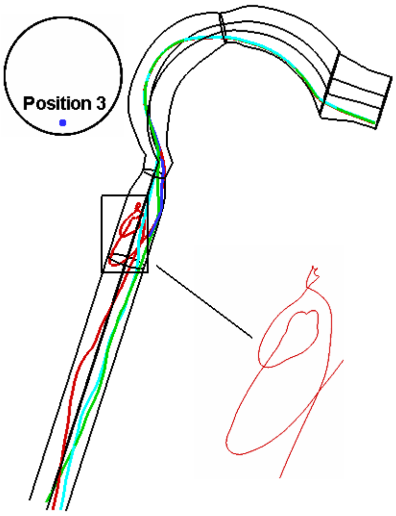

Fig. 5.49: Trajectories of 10 µm particles at position 3 at the inspiration flow rate of 15 L/min.

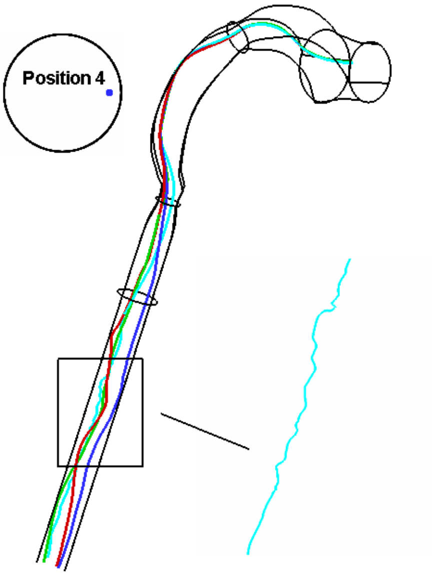

Fig. 5.50: Trajectories of 10 µm particles at position 4 at the inspiration flow rate of 15 L/min.

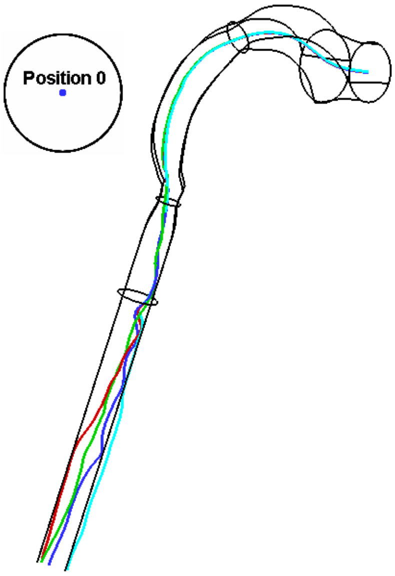

Fig. 5.51: Trajectories of 2 µm particles at position 0 at the inspiration flow rate of 30 L/min.

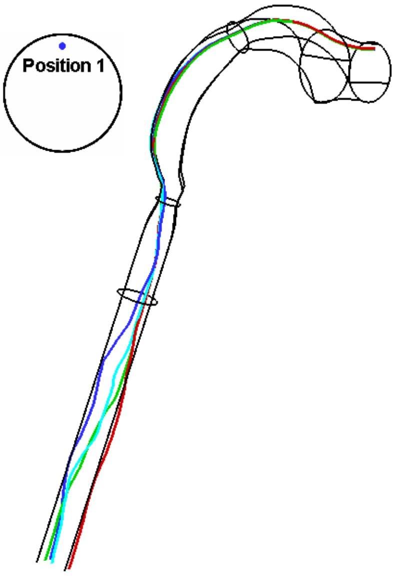

Fig. 5.52: Trajectories of 2 µm particles at position 1 at the inspiration flow rate of 30 L/min.

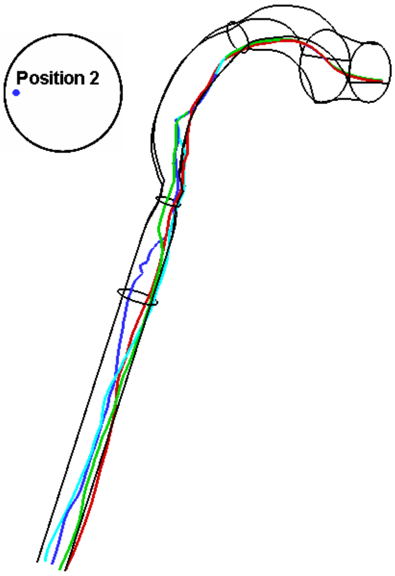

Fig. 5.53: Trajectories of 2 µm particles at position 2 at the inspiration flow rate of 30 L/min.

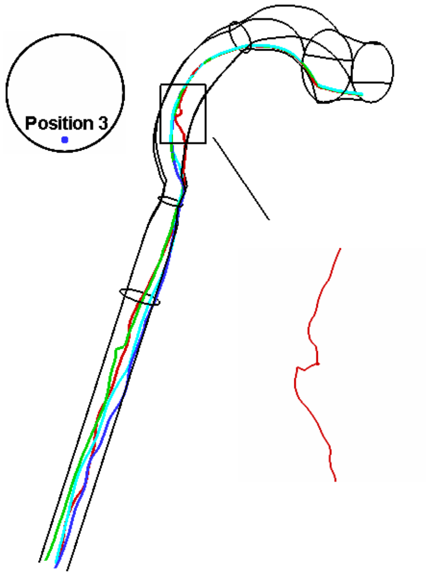

Fig. 5.54: Trajectories of 2 µm particles at position 3 at the inspiration flow rate of 30 L/min.

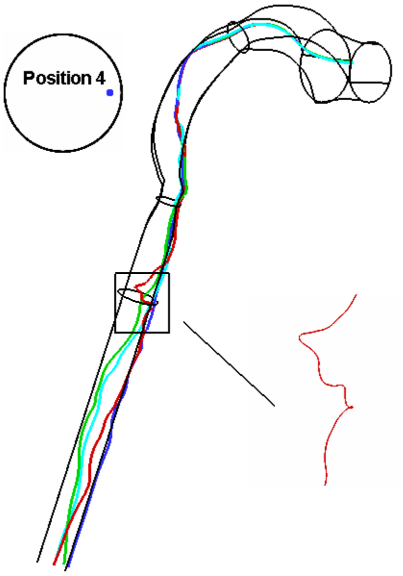

Fig. 5.55: Trajectories of 2 µm particles at position 4 at the inspiration flow rate of 30 L/min.

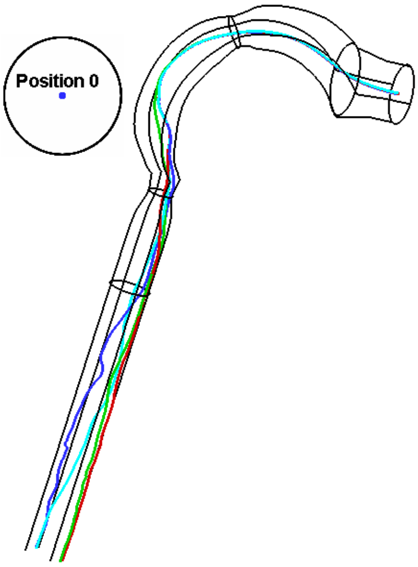

Fig. 5.56: Trajectories of 5 µm particles at position 0 at the inspiration flow rate of 30 L/min.

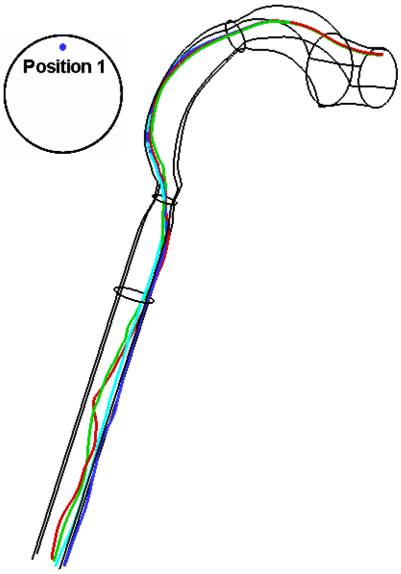

Fig. 5.57: Trajectories of 5 µm particles at position 1 at the inspiration flow rate of 30 L/min.

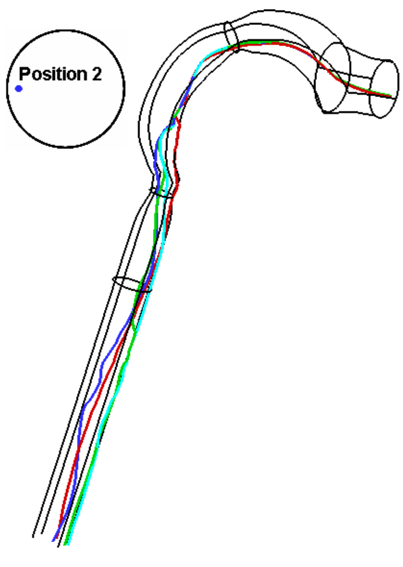

Fig. 5.58: Trajectories of 5 µm particles at position 2 at the inspiration flow rate of 30 L/min.

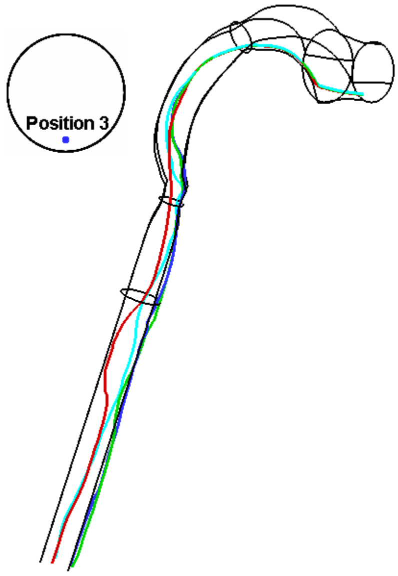

Fig. 5.59: Trajectories of 5 µm particles at position 3 at the inspiration flow rate of 30 L/min.

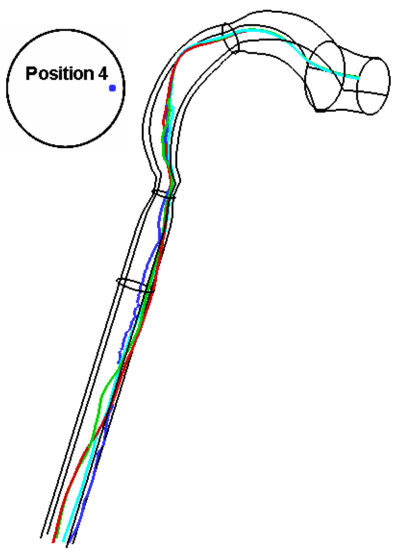

Fig. 5.60: Trajectories of 5 µm particles at position 4 at the inspiration flow rate of 30 L/min.

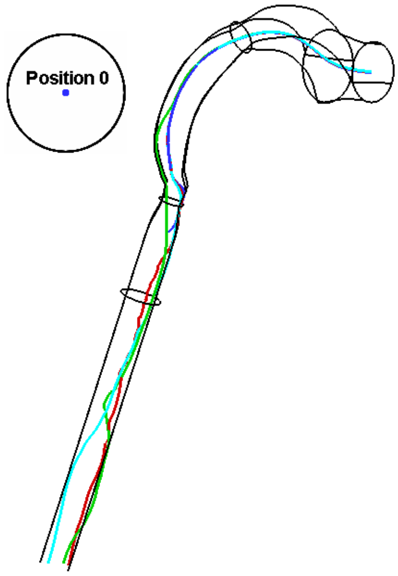

Fig. 5.61: Trajectories of 10 µm particles at position 0 at the inspiration flow rate of 30 L/min.

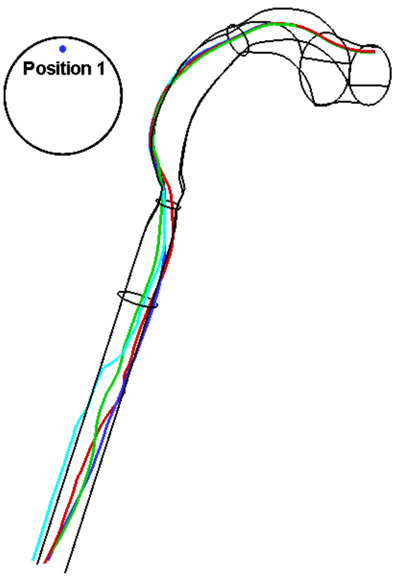

Fig. 5.62: Trajectories of 10 µm particles at position 1 at the inspiration flow rate of 30 L/min.

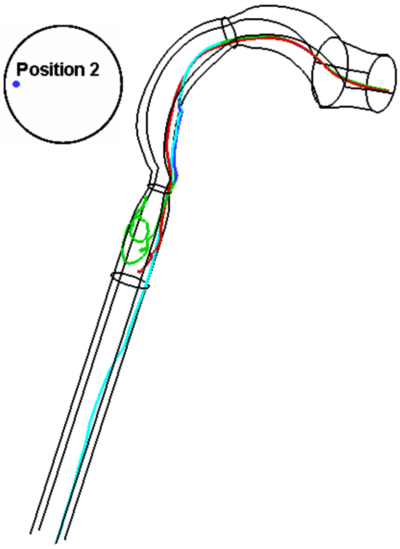

Fig. 5.63: Trajectories of 10 µm particles at position 2 at the inspiration flow rate of 30 L/min.

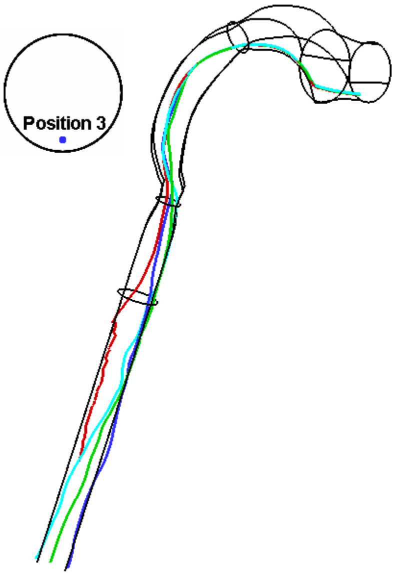

Fig. 5.64: Trajectories of 10 µm particles at position 3 at the inspiration flow rate of 30 L/min.

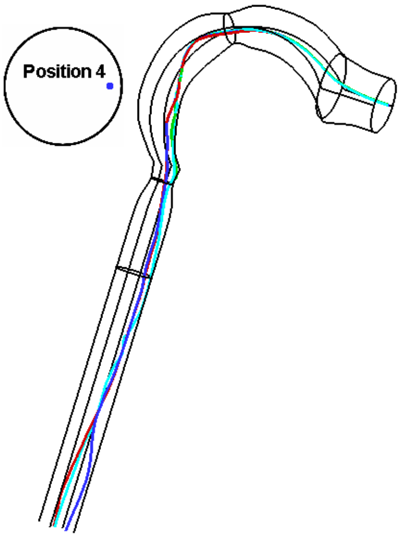

Fig. 5.65: Trajectories of 10 µm particles at position 4 at the inspiration flow rate of 30 L/min.

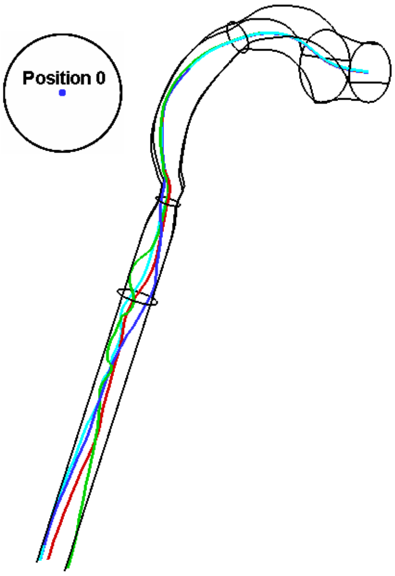

Fig. 5.66: Trajectories of 2 μm particles at position 0 at the inspiration flow rate of 60 L/min.

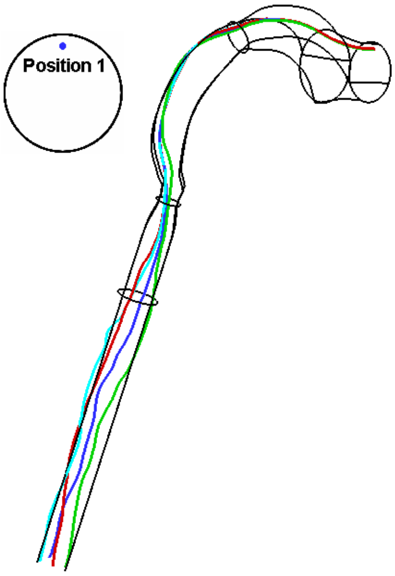

Fig. 5.67: Trajectories of 2 μm particles at position 1 at the inspiration flow rate of 60 L/min.

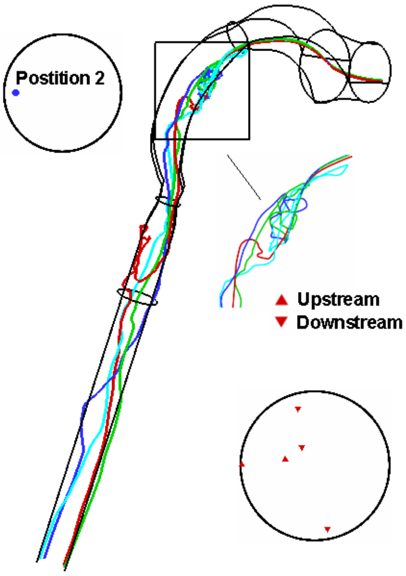

Fig. 5.68: Trajectories of 2 μm particles at position 2 at the inspiration flow rate of 60 L/min.

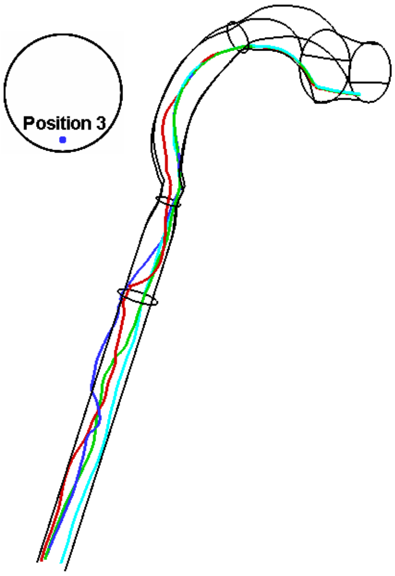

Fig. 5.69: Trajectories of 2 μm particles at position 3 at the inspiration flow rate of 60 L/min.

5.40, it can be found that although the initial positions of particles are very close, they can exhibit different trajectories due to the inhomogeneity, the randomness of the turbulence and the effects of large flow structure.

At the inspiration flow rate of 15 L/min, the 5 μm particles have more inertia in comparison with the 2 μm particles and they may exhibit less dispersion. The particles at these five different positions disperse less in the pharynx than the case of the inspiration flow rate of 15 L/min and particles of 2 μm, which display explicitly at the bottom of pharynx. In the trachea, the particles at position 0, 1 and 2 exhibit distinct dispersion at the end of the laryngeal jet seen in Figs. 5.41 - 5.43. At position 3, the second particle (the green line) cannot go through the mouth-throat model and stays on the wall. The particle follows the flow and impacts the tracheal wall which is taken by the laryngeal jet. The first particle (red line) shows complex trajectory in the recirculation zone of the trachea as seen in Fig. 5.44. This kind of the complex motion makes the particle dwell more in the geometry, which will increase the chance of the particle deposition on the wall of the trachea. At position 4, the second particle (the green line) also has recirculated motion in the recirculation zone in the trachea as shown in Fig. 5.45. In addition to the complex recirculated motion, the first and third particle are seen to undergo helix motion with different amplitudes and frequencies in the trachea as well.

At the inspiration flow rate of 15 L/min, for particles of 10 μm, particles at positions 0 and 2 have no particular dispersion as seen in Figs. 5.46 and 5.48. The second particle (green line) at position 1 conducts very distinct transverse motion in the trachea (c.f. Fig. 5.47), which is entrained by the vortex. In addition, the second, the third and the fourth particle is much less dispersed in the pharynx due to larger inertia. The first particle (red line) at position 3 conducts much more recirculated flow in the recirculation zone as shown in Fig. 5.49. At position 4, the fourth particle conducts the complex curve motion in the trachea which can be seen from the amplitude and frequency seen in Fig. 5.50.

At the inspiration flow rate of 30 L/min, for the 2 μm particles, the particle dispersion at each position mainly appears in the trachea because the flow is faster. The particles at position 0 carry out a short transverse motion in the trachea and they have totally different trajectories after the motion as seen in Fig. 5.51. The particles do not undergo complex motions at position 1 after dispersion as shown in Fig. 5.52. The first, second and third particles at position 2 conduct the transverse motion in the pharynx, which may be induced by the vortex in the recirculation zone of pharynx as shown in Fig. 5.52. The fist particle (red line) at position 3 is also seen to conduct transverse motion seen in Fig. 5.54. At position 4, the first particle (red line) conducts transverse motion in the trachea seen in Fig. 5.55.

At the inspiration flow rate of 30 L/min, for the 5 μm particles, the particles perform less recirculated motion at position 0, 1, 3 and 4 seen in Figs. 5.56, 5.57, 5.59 and 5.60. The particles at position 2 seen in Fig. 5.58 are entrained by the vortex in the pharynx.

At the inspiration flow rate of 30 L/min, for the 10 μm particles, there are more particles depositing on the wall. The first particle at position 0 conducts curve motion in the trachea seen in Fig. 5.61. The third particle at position 0 impacts on the wall of trachea seen in

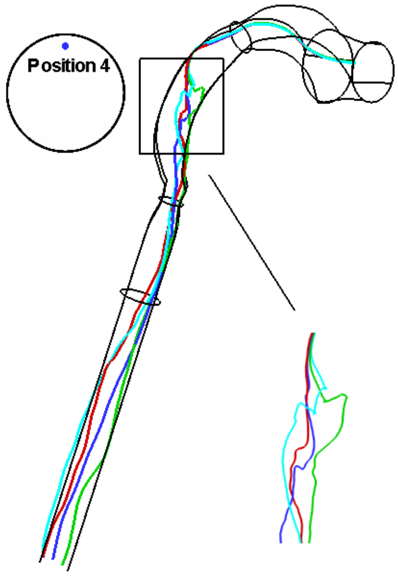

Fig. 5.70: Trajectories of 2 µm particles at position 4 at the inspiration flow rate of 60 L/min.

Fig. 5.71: Trajectories of 5 µm particles at position 0 at the inspiration flow rate of 60 L/min.

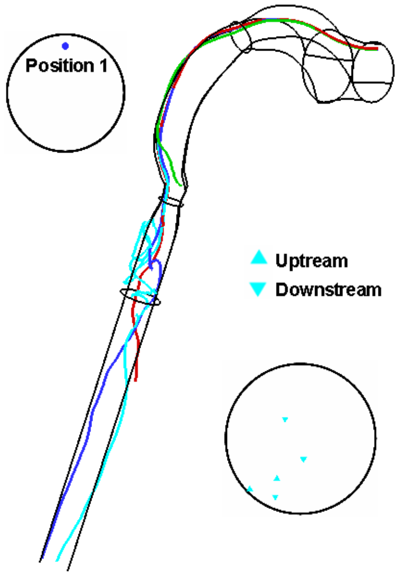

Fig. 5.72: Trajectories of 5 µm particles at position 1 at the inspiration flow rate of 60 L/min.

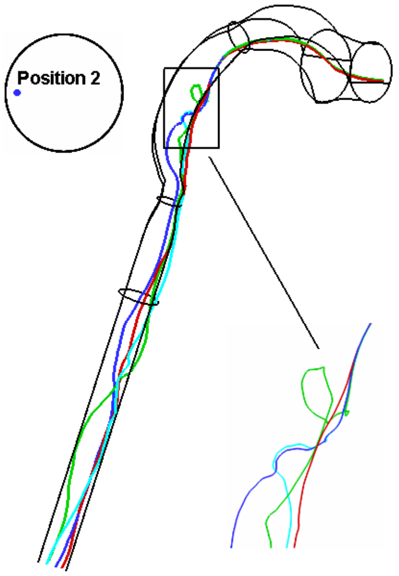

Fig. 5.73: Trajectories of 5 µm particles at position 2 at the inspiration flow rate of 60 L/min.

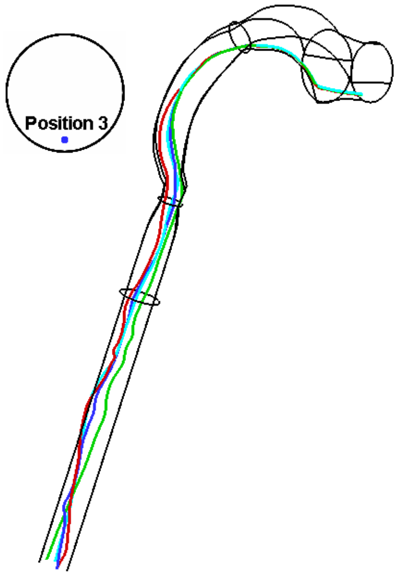

Fig. 5.74: Trajectories of 5 μm particles at position 3 at the inspiration flow rate of 60 L/min.

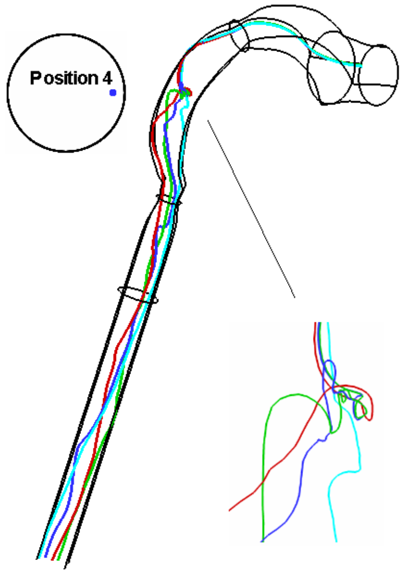

Fig. 5.75: Trajectories of 5 μm particles at position 4 at the inspiration flow rate of 60 L/min.

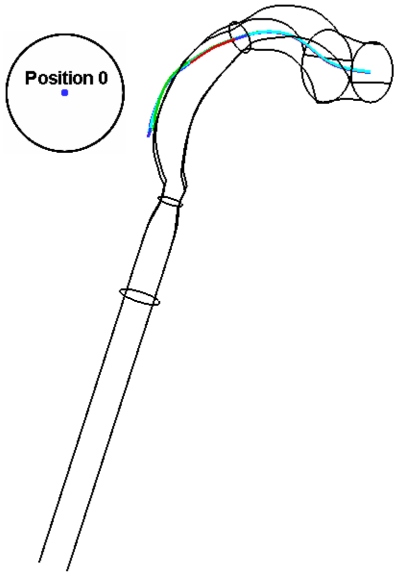

Fig. 5.76: Trajectories of 10 μm particles at position 0 at the inspiration flow rate of 60 L/min.

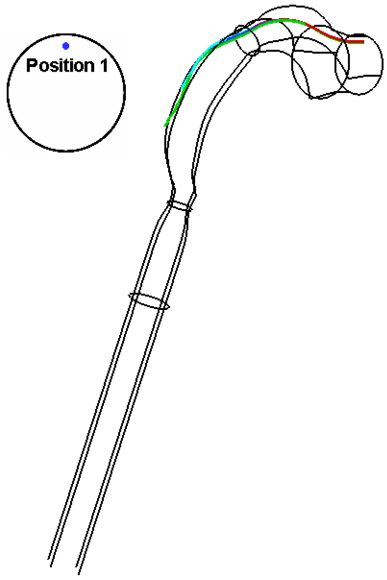

Fig. 5.77: Trajectories of 10 μm particles at position 1 at the inspiration flow rate of 60 L/min.

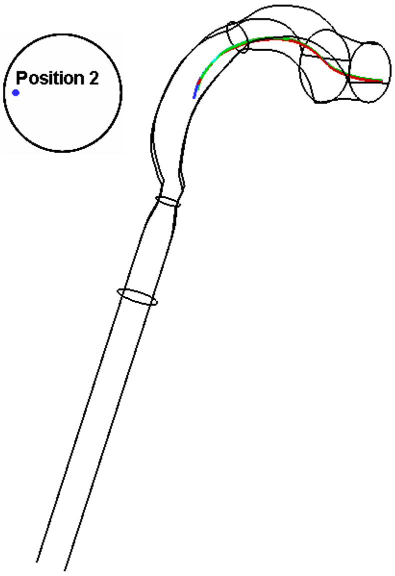

Fig. 5.78: Trajectories of 10 μm particles at position 2 at the inspiration flow rate of 60 L/min.

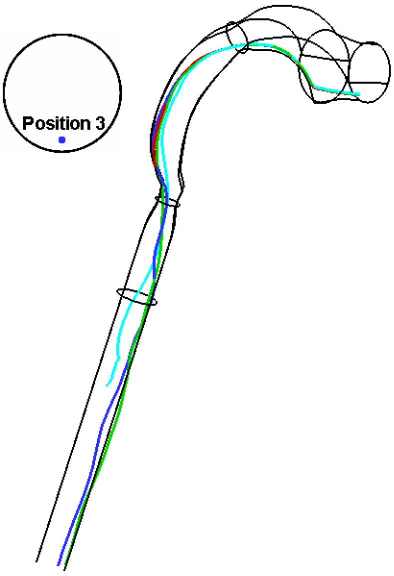

Fig. 5.79: Trajectories of 10 μm particles at position 3 at the inspiration flow rate of 60 L/min.

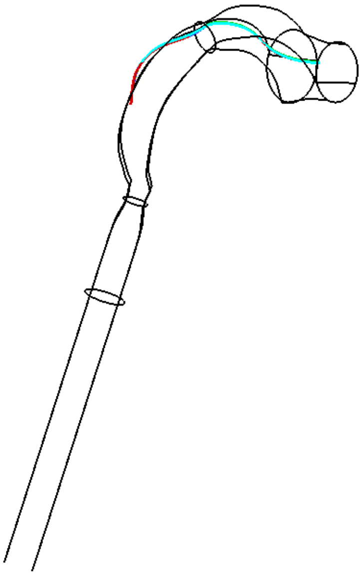

Fig. 5.80: Trajectories of 10 μm particles at position 4 at the inspiration flow rate of 60 L/min.

Fig. 5.61. Particles at position 1 seen in Fig. 5.62 go into the trachea following the laryngeal jet and they are not distinctly entrained by the vortex. There are more particles depositing in the geometry for particles at position 2 seen in Fig. 5.63. The first particle (red line) at this position deposits on the tracheal wall. The second particle at this position (green line) conducts very complex motion in the trachea and it deposits on the wall. The third particle at this position (blue line) deposits in the larynx region. The first particle (red line) at position 3 seen in Fig. 5.64 is entrained by the turbulence in the trachea explicitly. The first (red line) and third particle (blue line) at position 4 have similar trajectories from pharynx seen in Fig. 5.65. The second (green line) and fourth particle (cyan line) at this position has similar trajectories, but the second particle cannot go through the mouth-throat model and deposits on the wall of larynx. At the same time. The particles with larger diameter perform helix motion with smaller amplitude, which can be seen from the first particle at positions 0 and 3 as shown in Figs. 5.61 and 5.64.

At the inspiration flow rate of 60 L/min, for the 2 µm particles, at position 0, all particles keep almost the same trajectories in the mouth cavity and pharynx. The second particle (green line) is entrained by the vortex explicitly in the trachea seen in Fig. 5.66. The particles at position 1 keep almost the same trajectories until they go into the trachea and there are no distinct phenomena entrained by turbulence seen in Fig. 5.67. The particles at position 2 conduct very complex motions seen in Fig. 5.68, because the intensity of the turbulence is very high. For example, all of the particles conduct very complex motion in the recirculation zone of pharynx and the first particle (red line) conduct curve motion in the recirculation zone of trachea as well. Particles at position 3 disperse in the pharynx seen in Fig. 5.69. All of the particles at position 4 are entrained by the vortex in the pharynx and then they disperse (c.f. Fig. 5.70).

At the inspiration flow rate of 60 L/min, for the 5 µm particles, at position 0, the second particle (green line) and the third particle (blue line) are entrained by the vortices in the trachea seen in Fig. 5.66. The fourth particle conducts complex motion in the recirculated zone. At position 1, not all of the particles can go out of the geometry seen in Fig. 5.72. The first particle (read line) at this position deposits on the wall of trachea. The second particle deposits in the larynx. The third particle (blue line) at this position is entrained by the turbulence. The fourth particle conducts complex motion in the recirculation zone of the trachea. At position 2, particles disperse in the pharynx, which are entrained by vortex which can be seen from the curved motion in the pharynx in Fig. 5.73. The particles at position 3 have distinct entrained motion in the pharynx and trachea as shown in Fig. 5.74. The particles at position 4 are entrained in the pharynx by the vortex in the pharynx seen in Fig. 5.75.

At the inspiration flow rate of 60 L/min, for the 10 µm particles, most of the particles deposit on the wall and they have no chance to be influenced by the turbulence and recirculation zone. The particles at position 0, 1, 2 and 4 impact on the wall in the pharynx directly seen in Figs. 5.76, 5.77, 5.78 and 5.80. At position 3, the first particle (red line) deposits on the wall of larynx and the fourth particle (cyan line) deposits on the wall of trachea as shown in Fig. 5.79. Other two particles can go out of the geometry.

In summary, the trajectories of the particles are related to the particle's release position, particle size and inspiration flow rate. The vortex dynamics in the recirculation zones in the pharynx and trachea can entrain the particle dispersion. The particles conduct different trajectories after the dispersion. The particles can conduct different kinds of complex motions such as the helix motion, recirculated motion and curved motion with different amplitudes. The particles released at the lateral portions of the inlet plane are inclined to carry out complex motions such as the recirculated motion. In addition, particles are easier to be entrained by the airflow at high inspiration rate and the particles with smaller particle diameter.

5.2.5.2 Polydisperse Particle Deposition

In reality, the particle size distribution from the aerosol drug device is poly-disperse distribution, but most of the research assume the particle is mono-disperse. In this section, the influence of poly-disperse particle distribution on the particle deposition in the cast-based mouth throat is discussed.

The poly-disperse particle distribution is examined by the group of Prof. Urbanetz (Research Center Pharmaceutical Engineering GmbH, Graz, Austria) from dry power inhaler (DPI). The relationship of the particle mass fraction and particle diameter is shown in Fig. 5.81 [284]. The particle diameter ranges from 0.35 to 23.5 µm. The mass median diameter is 1.79 µm and Sauter mean diameter is 1.38 µm. The particle density is 1,000 kg/m^3 and the particle velocity is set to be same as the inspiration flow velocity of 1.592 m/s in the present work.

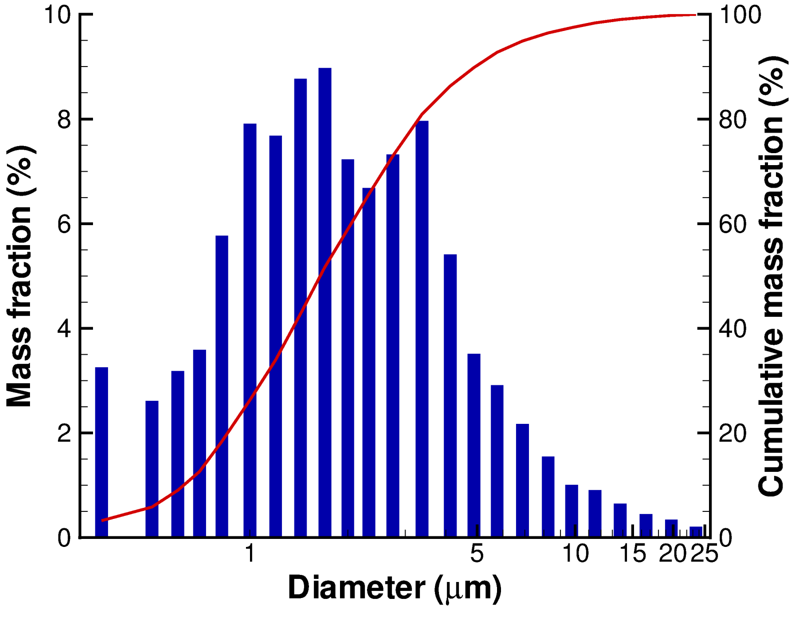

Fig. 5.81: Relationship between the initial poly-disperse particle diameter distribution and mass fraction.

Tab. 5.1: Particle deposition in the cast-based mouth-throat at different modeling conditions.

Particle distribution	mono-disperse	mono-disperse	mono-disperse	poly-disperse	poly-disperse
Particle size	1.38 µm	1.79 µm	1.38 µm	Fig. 5.81	Fig. 5.81
Injection drug dose			200 µg	200 µg	200 µg
Coupling method	one-way	one-way	two-way	one-way	two-way
Particle/parcel number	10,000	10,000	10,000	24,000	10,000
Particle deposition	0.45%	0.49%	0.51%	7.6%	6.37%

There are two different ways to compute the particle motion for the poly-disperse particle at the present work. The first method is one-way coupling. In this method, 1,000 particles of each class are injected simultaneously with the air randomly at the inlet plane and 24,000 particles are injected totally. The particle deposition efficiency is computed by multiplying the mass fraction and the ratio of depositing particle to the injected particle at each class.

Another way is the two-way coupling. In this method, the injection for one actuation injection is considered in the present work, which is 200 µg for the drug of "salbutamolsulfat" from MDI (metered dose inhaler) [29]. 10,000 parcels are injected at the same time at the inlet plane. Each parcel has the same mass and the parcel number distribution for each class is proportional to the mass fraction. The velocity is same as the inspiration flow velocity and they distribute randomly and uniformly at the inlet plane. The particle position is controlled by Gauss uniform distribution. The particle density is 1,000 kg/m^3.

The injection process can be written as following equations:

$$m_{parcel} = \frac{m_{in}}{N_p} \tag{5.13}$$

$$N_{pi} = \frac{m_{in} f_i}{m_p} = N_p f_i \tag{5.14}$$

Where N_p is the total parcel number, N_{pi} is parcel number corresponding to the i^{th} class , m_{in} is the injection mass at one one actuation, m_p is the mass of one parcel, f_i is mass fraction corresponding to the i^{th} class. In the computation, the injection mass is set to $m_{in} = 200$ µg and injection parcel number is set to $N_p = 10,000$.

In addition to poly-disperse particles, mono-disperse particles with Sauter diameter of 1.38 µm are used as well together with the realistic injection drug dose of 200 µg. The two-way coupling is adopted as well. The injection method is same as mentioned above. The main difference is that the particles have the same diameter.

The particle deposition efficiencies at different modeling conditions considering different particle distribution pattern, particle size, coupling ways and injection doses are shown in Tab. 5.1. The total particle deposition efficiency is 7.6% using the one-way coupling considering realistic poly-disperse particle distribution, whereas it is 6.37% using two-way coupling considering realistic poly-disperse particle distribution. Both of these results are much higher than the particle deposition efficiency from the mass medium diameter, Sauter mean diameter and realistic injection dose with two-coupling way seen in Tab. 5.1. It can be seen that the particle deposition from poly-disperse particle deposition is much higher than the particle deposition in other cases, which indicates that the particle distribution is very important in the particle deposition. The Sauter mean diameter and mass medium diameter are not suitable in the numerical simulation for particle deposition. For the more realistic simulation, it is important to use the poly-disperse particle distribution initially.

The poly-disperse particle deposition on the surface is shown in Fig. 5.82 using one-way coupling. From the figure, it can be seen that the large particles deposit in the mouth cavity, in the posterior side of the pharynx and in the glottis. The smaller particles are seen to deposit in the mouth cavity, the anterior side of the pharynx and the trachea. The particle deposition efficiencies in different regions are shown in Fig. 5.83. From the figure, it can be seen that the particles dominantly deposit in the pharynx, but particle deposition in other region has the equal level. To identify the contribution of each particle class to the particle deposition in the geometry and in different regions, the relationship between the particle deposition efficiency and particle diameter in the mouth cavity, pharynx, larynx and trachea is shown in Fig. 5.84.

It is found that particles in the initial size range of 1 - 5 µm have little contribution to the particle deposition displayed in Fig. 5.84, although the major part of injected mass consists of these particles, c.f. Fig. 5.81. The total mass fractions of particles in the size ranges 0.35 - 1 µm, 1 - 5 µm, and 5 - 23.5 µm are 26.3%, 63.5%, and 10.2% respectively, whereas the corresponding particle deposition efficiencies are 3.1%, 0.4%, and 4.1%. It is found that the

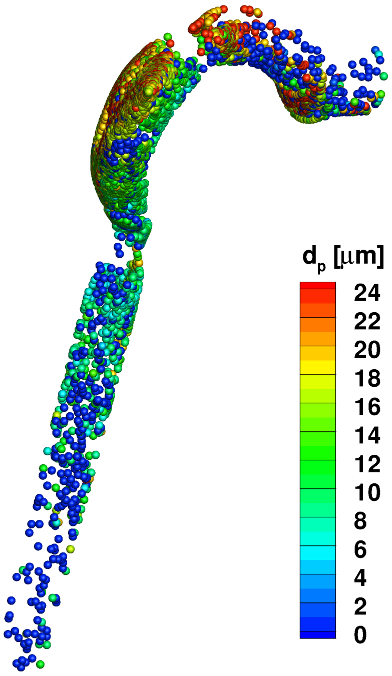

Fig. 5.82: Poly-disperse particle deposition on the surface of the cast-based mouth-throat using one-way coupling.

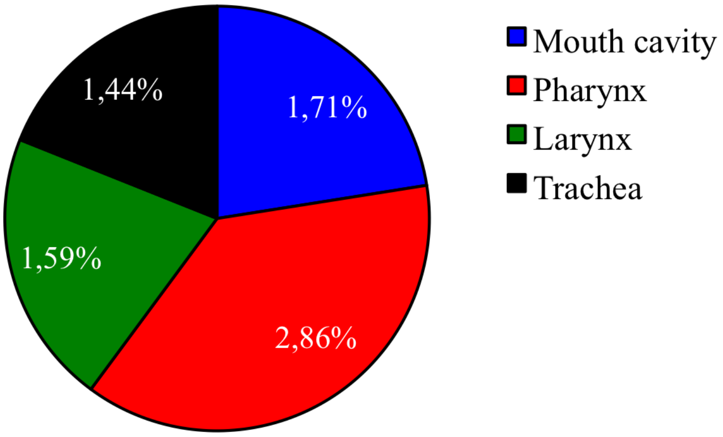

Fig. 5.83: Poly-disperse particle deposition deposition in different regions of the cast-based mouth-throat using one-way coupling.

particles larger than 5 µm mainly deposit in the pharynx and larynx, whereas the particles less than 1 µm may deposit in different regions of the mouth throat other than the pharynx.

The total particle deposition efficiency is 6.37% using two-way coupling together with the parcel method in comparison with 7.6% using one-way coupling. The comparison of the results from these two different methods is shown in Fig. 5.85. From the figure, it can be seen that the main difference for two different methods results from in the size range of sub-micron particles. The sub-micron particle deposition is much lower for using two-way coupling than using one-way coupling. In addition, for the particles ranging from 1 to 5 µm, deposition is higher using one-way coupling than two-way coupling method. For instance, contribution of

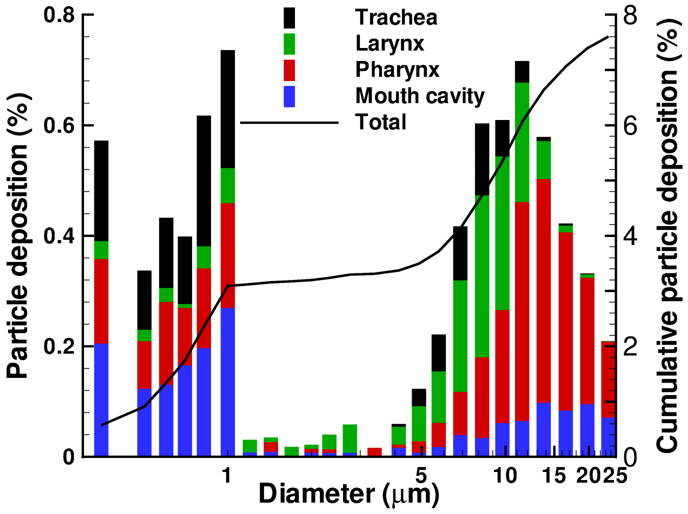

Fig. 5.84: Contribution of each class to particle deposition in different regions of the cast-based mouth-throat using one-way coupling.

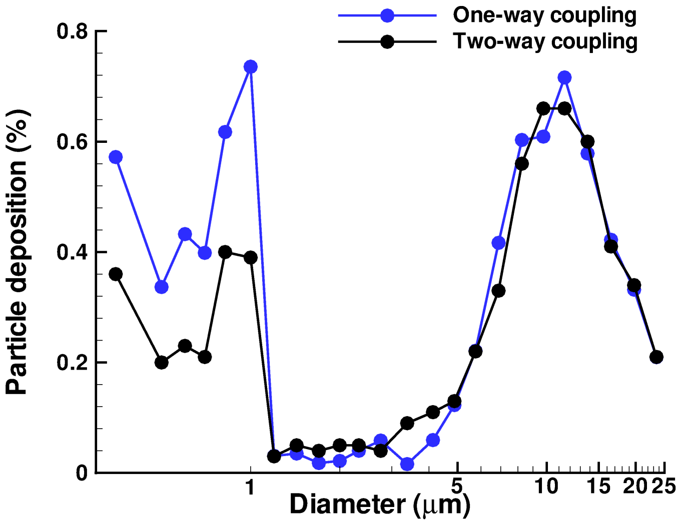

Fig. 5.85: The comparison of contribution of each class on the total particle deposition efficiency in the cast-based mouth-throat using two different coupling ways.

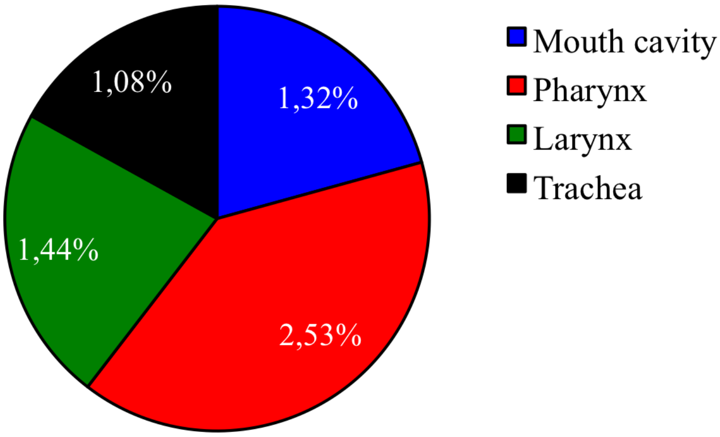

Fig. 5.86: Poly-disperse particle deposition deposition in different regions of the cast-based mouth-throat using two-way coupling.

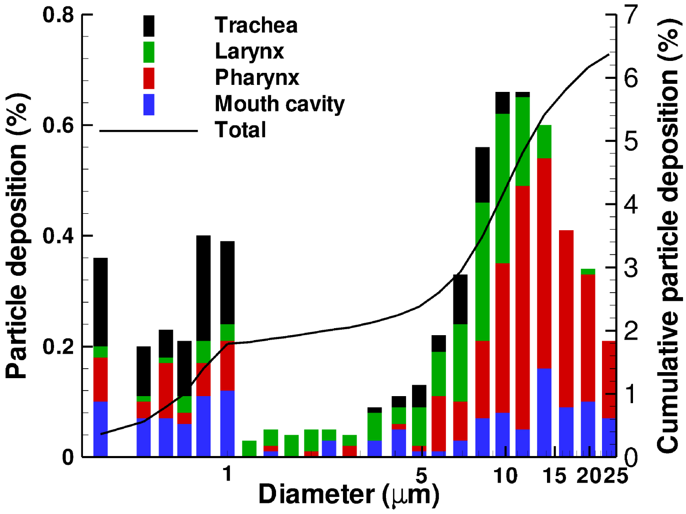

Fig. 5.87: Contribution of each class to particle deposition in different regions of the cast-based mouth-throat using two-way coupling.

particles in the range of 0.35 - 1 μm, 1 - 5 μm, and 5 - 23.5 μm are 1.79%, 0.59%, and 3.99% correspondingly. Moreover, the particle deposition in different regions of the mouth-throat is higher using one-way coupling than two-way coupling from the comparison of Figs. 5.83 and 5.86.

At the same time, the contribution of particle size to the particle deposition in different regions of the mouth-throat is different as well. This contribution to the particle deposition in different regions of the mouth-throat using two-way coupling is shown in Fig. 5.87. From the figure, it can be seen that few particles of size less than 1 μm deposit in the larynx as compared to particles depositing in the mouth cavity, pharynx and trachea. But, more particles ranging from 1 to 5 μm deposit in the larynx and pharynx. No particles in this range deposit in the trachea. When the particle diameter is larger than 5 μm, the particles are filtered gradually from the mouth cavity. For instance, the maximum particle deposition appears in the mouth cavity and pharynx for particle size larger than 15 μm and no particles deposit in the larynx and trachea, when the particle diameter is larger than 15 μm. The particle deposition in the larynx and trachea is mainly contributed by the particles ranging from 5 to 15 μm. From Fig. 5.84, it can also be seen that particle sizes of maximum contribution to particle deposition in the mouth cavity, pharynx, larynx and trachea are 13.75, 11.5, 9.75 and 8.2 μm respectively.

In summary, the particle size distribution greatly influences particle deposition in the human upper airway and it is very important to use the poly-disperse particle pattern in the numerical study. From the comparison of the one-way and two-way coupling, it can be seen that the difference is mainly induced by the sub-micron particles. It is necessary to use two-way coupling for the numeral modeling of poly-disperse particle distribution, which considers the realistic drug dose. It is also suggested to make the particle distribution in the range of 1 to 5 μm for the drug formation as much as possible since the particles in other size ranges can contribute greatly to the particle deposition in the oral airway even they take less ratio of the mass fractions.

5.2.6 Summary

In this work, an idealized mouth-throat model was constructed based on the cast from literature [48, 89] using Ansys ICEM-CFD 11.0. The flow field in the mouth-throat model was simulated considering three different inspiration flow rates of 15, 30 and 60 L/min. The mean and unsteady flow field were simulated and compared. The main flow features were seen in the mean flow field in the idealized mouth-throat including a skewed velocity profile, flow separation after the sudden geometric change at the soft palate and glottis, and the laryngeal jet. In addition, a small recirculation zone is seen in the posterior side of the pharynx and the laryngeal jet is impinging on the anterior side of trachea, which indicates that the flow field is very sensitive to the geometric profile, in particular, in locations with large curvatures. The laryngeal jet profile influences the axial velocity profile, and it changes with the location of laryngeal jet.

Other than the mean flow field, the unsteady flow fields have been studied in this project as well. It is found that secondary vortices at very different length scales exist in the flow field. It is found that after the flow has entered into the pharynx, it becomes unsteady and involves turbulent structures. In contrast to the averaged flow field, no counter-rotating vortices are seen in the instantaneous flow fields at the same location in the pharynx at inspiration flow rate of 30 L/min, but large-scale secondary vortices exist in the main flow zone in the pharynx. Behind the pharynx, no counter-rotating vortices are seen in all instantaneous flow fields. Depending upon the axial location, secondary vortices occur in the separation zone, the mixing zone, the main flow zone, and the wall shear layer of the separation zone and the laryngeal jet. Vortices appearing in the wall shear layer have small scales, whereas those in the mixing zone tend to be at larger scales. The laryngeal jet is highly unsteady and it breaks up at the tail. The break up may cause the momentum to redistribute and enhance the turbulence intensity further downstream. The highly unsteady recirculation zone resides at the posterior side downstream the glottis, and it strongly affects the flow structure towards the laryngeal jet. The mixing pattern changes with the profile of the laryngeal jet, and its interface becomes concave at the tail. It can be seen that the separation zone, the laryngeal jet, and the secondary vortices are closely interrelated.

It is found that the flow structures have relationship with the inspiration flow rates. For example, in the mean flow field, the laryngeal jets becomes more concentrated with the increasing inspiration flow rate. The recirculation zone after glottis reduces as the inspiration flow rate increases. Moreover, there are three pairs of vortices in the pharynx at the inspiration flow rate of 15 L/min, two pairs of the vortices at the inspiration flow rate of 30 L/min, and one pair of vortices at the inspiration flow rate of 60 L/min. The length scale of the vortices in trachea becomes smaller as the inspiration flow rate increases. Similarly, the length-scale of vortices in the three-dimensional space also becomes smaller as the inspiration flow rate increases.

For the unsteady flow field, the flow field becomes more turbulent because of the increasing Reynolds number induced by increasing the inspiration flow. It can be seen that the unsteadiness appears further from the inlet for the lower inspiration flow rate. For instance, the counter-rotating vortices still can be seen in the pharynx which means that the laminar flow is still prevalent in the pharynx, but no counter-rotating vortices are seen at other two inspiration rates. At high inspiration flow rate of 60 L/min, the unsteadiness appears even in the mouth cavity. Moreover, few secondary vortices are seen at the low inspiration flow rate.

In addition to the flow field, the mono-disperse particles have been tracked as well in this section. Three sizes of particles have been tracked at three different inspiration flow rates. Thus, 9 cases are studied. The total particle deposition efficiencies in the cast-based mouth-throat are compared with the experimental and numerical data from the literature. It is found that the present results are close to the numerical results from the literature. Moreover, they fit well with the medium trend of the experimental data. Thus, the methodology including the idealized mouth-throat model is suitable to be implemented in the study of particle deposition in the human oral airway. Moreover, the particle deposition efficiency in different regions, the particle deposition pattern on the surface, the particle fates are related to the initial particle distribution at the inlet plane and the particle trajectories has been studied.

The investigations show that regional particle deposition, the particle deposition pattern and the particle fates depend on initial particle distribution at the inlet plane, the particle size and inspiration flow rate. The turbulence and recirculation flow are found to have great influence on the particle trajectories. Therefore, they may affect the particle deposition. Desponding on the particle size and the inspiration flow rate, the particles tend to deposit on the bottom of the mouth cavity, the tip of soft palate, the recirculation zone and the posterior side of the pharynx, the glottis and the lateral as well as anterior sides of trachea. The particles near the vertical symmetrical line about the inlet plane have more chances to go through the mouth-throat model. The particles close to the upper portion of the inlet plane tend to deposit in the mouth cavity and the particles in the vortex region tend to deposit in the pharynx and larynx region. In addition, the investigation of the particles' trajectories shows that the particles are entrained by the recirculation zone and the turbulence. The particles are seen to conduct the curve motion and recirculated motion. Moreover, the particles in very close initial positions may have different fates such as going through the geometry, depositing on the surface or undergoing complex motions.

In addition to simulating the mono-disperse particle motion, the poly-disperse particles are simulated as well to study the influence of particle size distribution on the particle deposition. One-way and two-way coupling have been implemented without or with considering the realistic injection drug dose. It is found that poly-disperse particle distribution has great influence on the particle deposition efficiency and it is more reasonable to adopt the poly-disperse particle distribution in the numerical simulations. The particle deposition efficiency is higher using one-way coupling method and it is mainly in the size range of less than 1 μm since the sub-micron particles have more relationship with the gas diffusion. It is suggested to adopt the two-way coupling in the numerical simulations. It is also found that the particles less than 1 μm and larger than 5 μm have main contributions to the particle deposition.

5.3 Airflow Field in the Cast-Based Mouth-Throat Under Unsteady Inspiration Flow Rate

One of the main factors to influence the particle deposition in the human respiratory system is the inspiration flow rate. Commonly, the flow rate at the inlet plane is set to uniform and set to the value corresponding to the light, normal and heavy breathing. But the realistic inspiration pattern is periodic, so that it is necessary to study the unsteady inspiration flow rate pattern influences on the flow field.

In this section, the flow field considering the inspiration flow rate under an unsteady respiratory flow rate of normal breathing for light activity will be simulated in the cast-based mouth-throat.

5.3.1 Computational Conditions

In this work, a typical inspiration flow pattern, which is considered to represent the normal breathing for light activity is shown in Fig. 5.88 [84] and the properties of the inspiration flow at the mouth inlet plane is listed in Table 5.2. Due to focus on the inspiration phase, the expiratory phase between inspiratory cycles is replaced with an intermittent zero-flow period as it has been handled in the work of Zhang et al. [84]. The flow field has been simulated for five periods with the solver of "oodLFoam" and the flow fields at five different time steps will be discussed. Two time steps are chosen at the accelerating phase, one at the peek and other two at the decelerating phase as shown in Fig. 5.88.

As in the section 5.2, the gas transport in the mouth-throat model is assumed to be air at the room temperature. Then, the physical conditions of the gas are as follows:

$$\rho_g = 1.21\ \mathrm{kg/m^3};\ \mathrm{T_g} = 273.15\ \mathrm{K};\ \nu = 14.9\ 10^{-6}\ \mathrm{m^2/s}. \qquad (5.15)$$

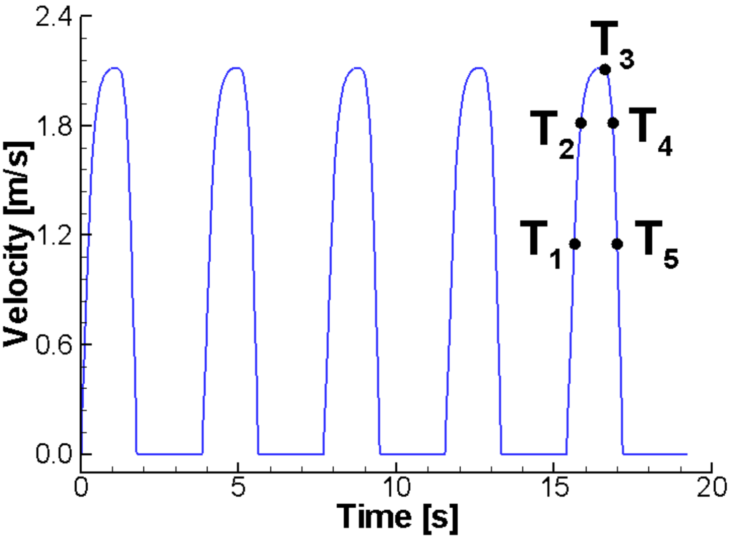

Fig. 5.88: The inspiration flow velocity wave and the five time steps.

Tab. 5.2: Physical properties of the representative inhalation wave form [84].

Physical parameters	Tidal volume (ml)	Time ratio of inspiratory phase (t_{in}/t_{total})	Breathing frequency (cycle/min)	Peak Reynolds number at inlet plane
Light activity	907	0.46	15.5	8,920

The boundary conditions are as follows:

(1) Inlet:

$$\frac{\partial P}{\partial n} = 0; \tag{5.16}$$

(2) Outlet:

$$\frac{\partial \mathbf{V}}{\partial n} = 0; \; P = 0 \text{ Pa (relative to the ambient pressure)}; \tag{5.17}$$

(3) Wall:

$$\mathbf{V} = 0 \text{ m/s}; \; \frac{\partial P}{\partial n} = 0. \tag{5.18}$$

It should be mentioned that the velocity at the inlet is not set to be uniform anymore, but adopted the data shown in Fig. 5.88. It assumes that the air in the configuration is static in the beginning so that the velocity is 0 m/s and pressure is 0 Pa relative to the ambient pressure initially. The numerical simulation is carried out in grid of 1,276,500 grid nodes.

5.3.2 The properties of Airflow Fields

As mentioned above, the airflow field at five different time steps are shown in Figs. 5.89 - 5.93. These flow fields include all of the typical flow features during the cycle which benefits the discussion.

At the time $t = \mathrm{T}_1$, the velocity is at the increasing phase. The flow at this time level displays more laminar seen in Fig. 5.89. At this time level, the velocity magnitude is low relative to the airflow field at other times. As the numerical results from this mouth-throat model under steady inspiration flow rate, the flow recirculation zones are observed in the mouth cavity near the tongue, in the pharynx cavity and in the trachea after the vocal folder, which may be produced from the strong change of cross-sectional areas. A laryngeal jet is observed as well in the trachea. The most obvious different features are observed for the secondary flow patterns.

At A - A' cross section, the flow field displays very obvious laminar properties and there are no counter-rotating vortices seen at this cross section due to insufficient pressure gradient. In contrast, the counter-rotating vortices are observed at other time steps at this cross section. When the flow goes further into the pharynx seen from the section B - B', two pairs of vortices are seen in the recirculation zone and no counter-rotating flow structures are seen in the main flow zone. In the position of glottis seen in C - C' cross section, the laryngeal jet takes dominant effect; the axial velocity distribution becomes uniform and a pair of smaller counter-rotating vortices appear in the front side of the cross-section. When the flow goes further downstream, a pair of larger counter-rotating vortices are observed in the recirculation zone and a pair of smaller vortices seen in the interface of the laryngeal jet and the recirculation zone seen at the D - D' cross section. Three pairs of secondary vortices are seen at E - E' cross section. In addition, the interaction between the recirculation zone and the laryngeal jet becomes intensive seen from the interface between these two flow zones. At the same time, two secondary vortices located in the mixing zone and the length scale of secondary vortices in the recirculation zone becomes smaller. After E - E' cross section, the laryngeal jet becomes unsteady and the interaction between the recirculation zone and the laryngeal jet increases as it can be observed from the velocity contour at the mid-plane of Fig. 5.89. When the flow reaches F - F' section, the maximum axial velocity has shifted to the left side due to the breakage of the laryngeal jet, but three pairs of secondary vortices can still be observed at this section. Although the unsteady motion as well as the interaction between the recirculation zone and the laryngeal jet at this time level of $t = \mathrm{T}_1$, the flow field still shows laminar properties since the counter-rotating vortices are observed at different cross-sections.

At the time level $t = \mathrm{T}_2$, the inlet flow velocity increases as displayed in the Fig. 5.90 and the Reynolds number in the mouth-throat increases as well, so that the flow may transit from laminar to turbulent and it leads to different profile of the flow field. The difference between the time level $t = \mathrm{T}_1$ and $t = \mathrm{T}_2$ is that flow field at this time level is more turbulent. In the mouth cavity, a pair of counter-rotating vortices are observed at A - A' section seen in Fig. 5.90 at this time level, since there is enough centrifugal pressure gradient. At the B - B' cross section, large vortices appear in the main flow zone and more interaction occurs between the main flow zone and the recirculation zone, the smaller vortices appear in the mixing flow zone and recirculation zone. But no counter-rotating vortices appear in this section, which means turbulence has started. After the pharynx, there is no counter-rotating secondary vortices seen in the mouth-throat at this time level. At the glottis, vortices with different length-scale are observed at this cross section and they mainly distribute on the anterior side of the mouth-throat model. At D - D' cross section, the profile of the axial velocity contour is irregular, which means that the laryngeal jet profile is irregular. And smaller secondary vortices are observed in the laryngeal jet zone and the laryngeal jet boundary. At E - E' and F - F' cross sections, the turbulence has significantly developed and the secondary vortices with different length scale distribute everywhere in the mouth-throat at this time level. Moreover, after E - E' cross section, the laryngeal jet becomes more unsteady compared with the case at time $t = \mathrm{T}_1$.

At time $t = \mathrm{T}_3$, the inspiration flow rate has reached the peak value of inspiration curve and the Reynolds number also reaches the maximum value, and the velocity magnitude in mouth-throat becomes maximum as well seen in Fig. 5.91. The flow field in the mouth cavity is still laminar as other times. The flow field in the pharynx displays turbulent properties coupled with irregular secondary vortices distribution. The main different property is that the main flow zone becomes larger as well as the mixing zone due to higher interaction. At the

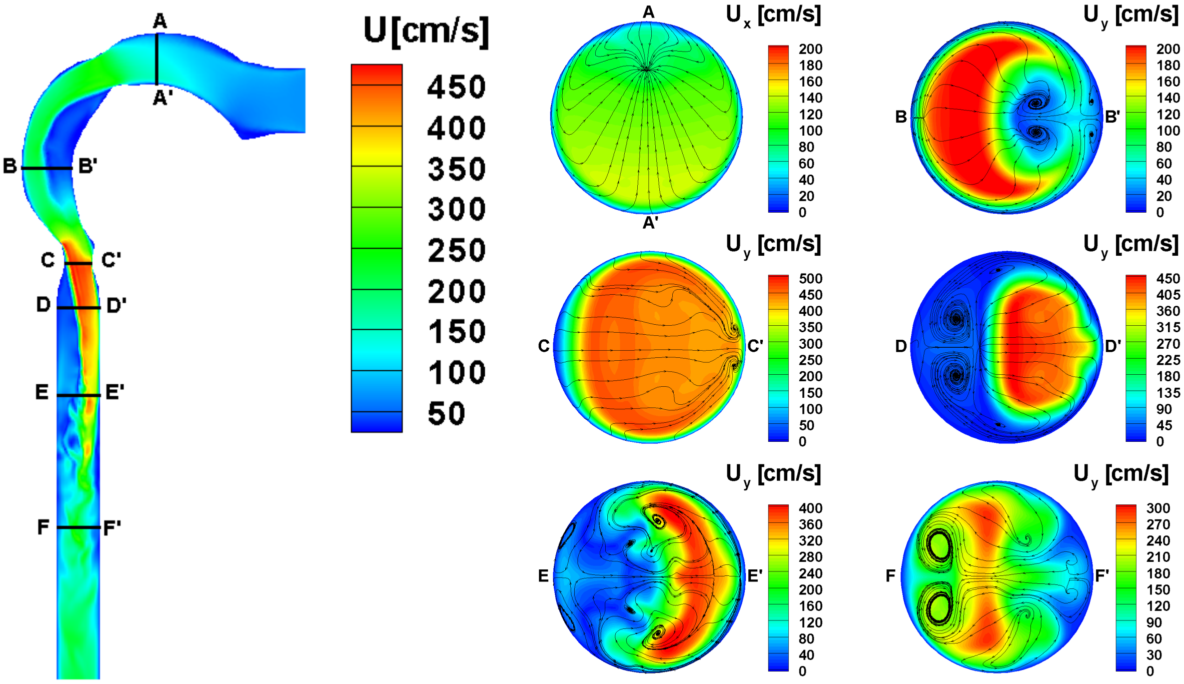

Fig. 5.89: Instantaneous velocity contour at mid-plane (left), and axial velocity contour and secondary streamlines at cross-sections (right) in the cast-based mouth-throat at time $t = \mathrm{T}_1$.

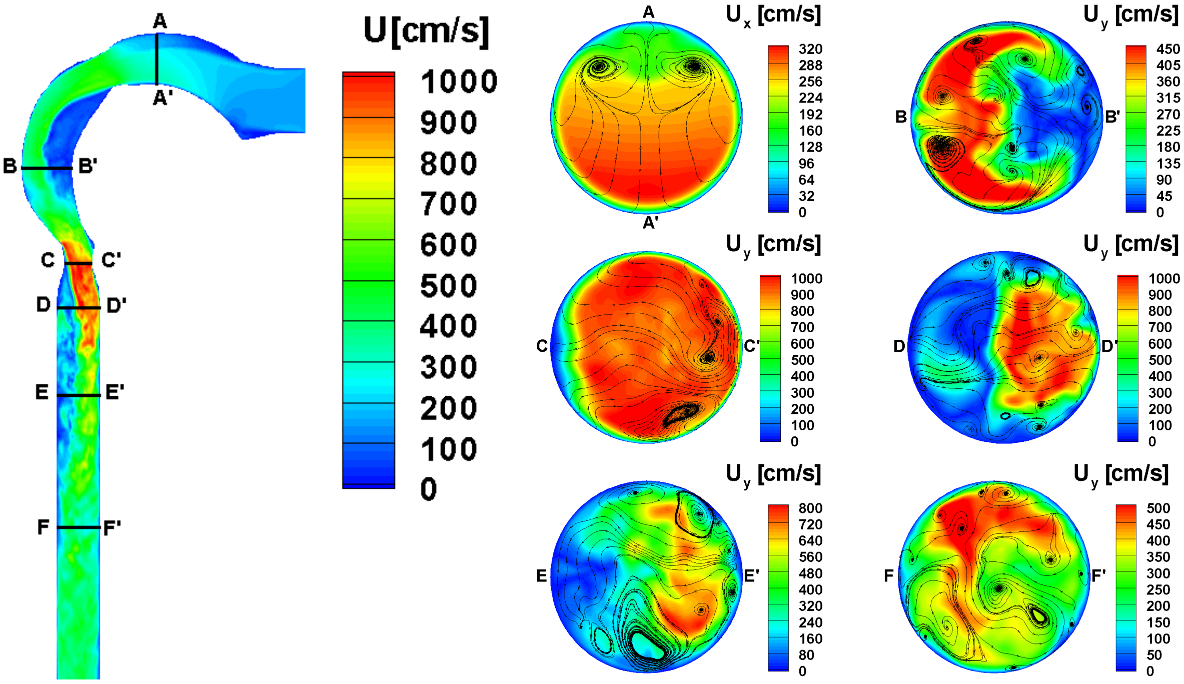

Fig. 5.90: Instantaneous velocity contour at mid-plane (left), and axial velocity contour and secondary streamlines at cross-sections (right) in the cast-based mouth-throat at time $t = \mathrm{T}_2$.

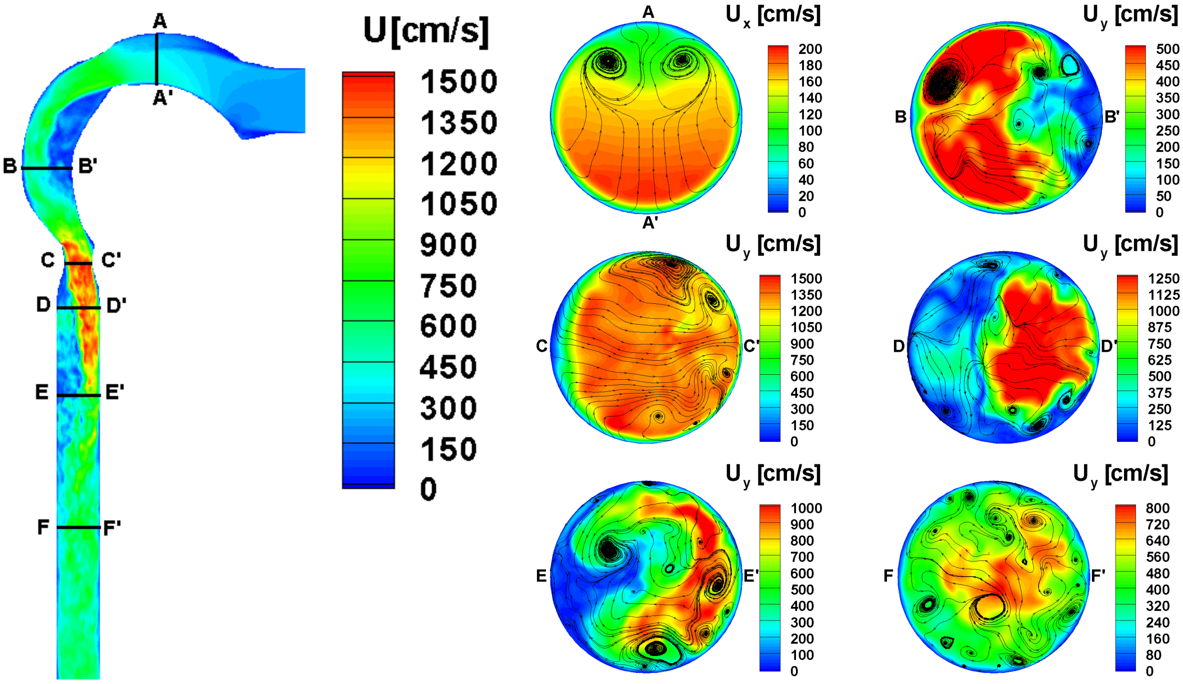

Fig. 5.91: Instantaneous velocity contour at mid-plane (left), and axial velocity contour and secondary streamlines at cross-sections (right) in the cast-based mouth-throat at time $t = \mathrm{T}_3$.

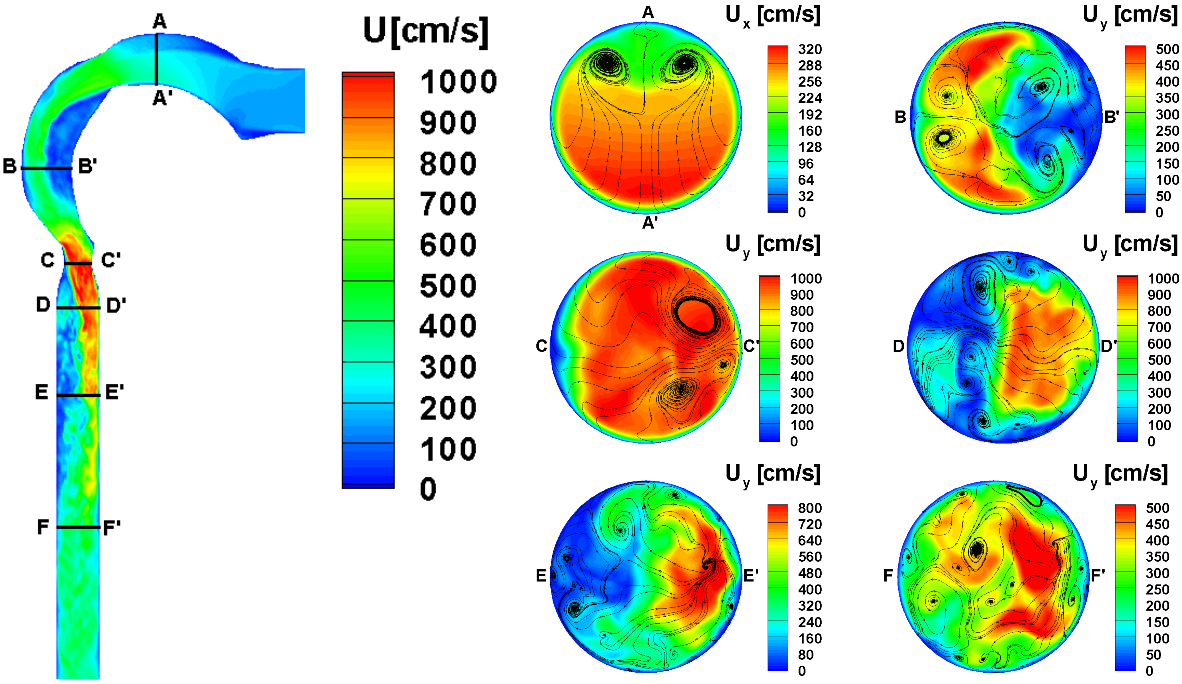

Fig. 5.92: Instantaneous velocity contour at mid-plane (left), and axial velocity contour and secondary streamlines at cross-sections (right) in the cast-based mouth-throat at time $t = \mathrm{T}_4$.

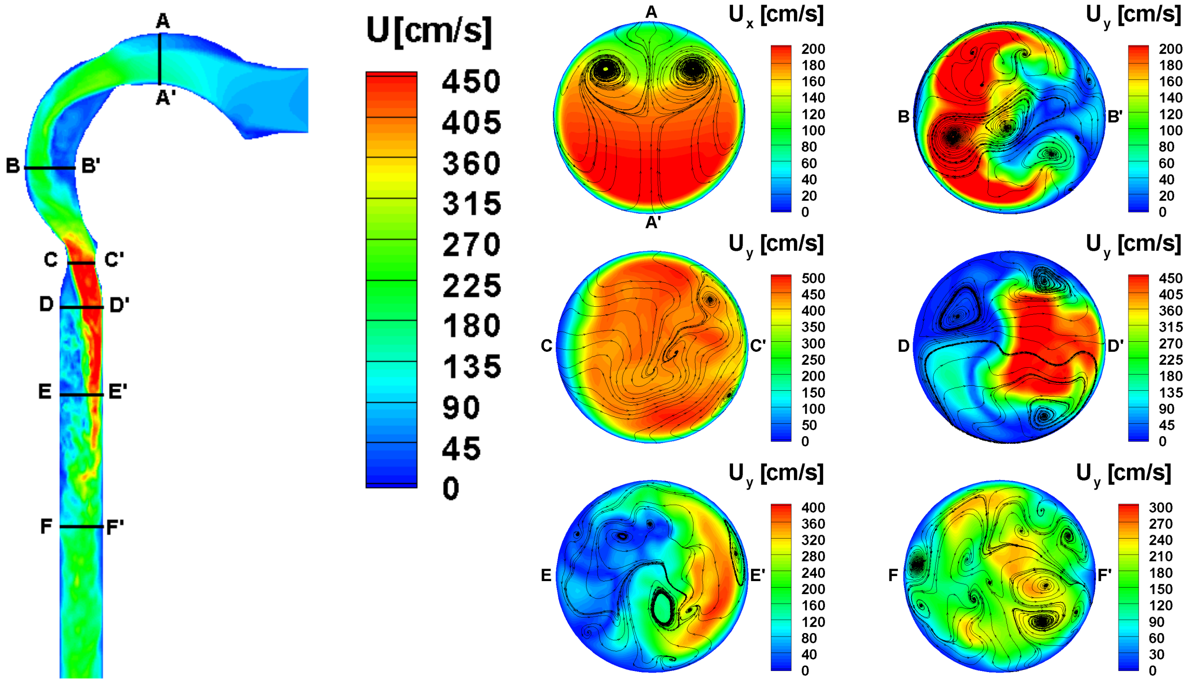

Fig. 5.93: Instantaneous velocity contour at mid-plane (left), and axial velocity contour and secondary streamlines at cross-sections (right) in the cast-based mouth-throat at time $t = \mathrm{T}_5$.

same time, recirculation zone in the pharynx and trachea is much more turbulent as reflected in the velocity contour in the trachea. The recirculation zone in the trachea becomes smaller seen from E - E' cross section and mixing zone becomes larger as well. The laryngeal jet is more unsteady from the profile of the laryngeal jet at E - E' cross section. At F - F' cross section, more secondary vortices with smaller size are observed at all over the cross section which implies more turbulence in the trachea than other times.

After the inlet inspiration flow velocity has reached the peak, it enters into the decreasing phase. At the time $t = \mathrm{T}_4$, the flow has the same Reynolds number with the time $t = \mathrm{T}_2$. But, at this time level, the flow field is in the phase of transiting from turbulent to laminar. With decreasing turbulence, the large counter-rotating vortices are gradually produced in the pharynx seen at the B - B' cross section seen in Fig. 5.92. The axial velocity distribution at the glottis seen from C - C' cross section becomes more uniform as well as the appearance of larger secondary vortices. But in the trachea, the turbulence still domains the flow field, which can be seen from the secondary vortices distribution at the cross sections of D - D', E - E' and F - F'.

At time $t = \mathrm{T}_5$, the inspiration velocity deceases to the first time level as well as Reynolds number. But, different from the flow field at time $t = \mathrm{T}_1$, the flow field at this time level displays more turbulence shown in Fig. 5.93. A pair of counter-rotating secondary vortices are observed in the mouth cavity due to the flow postponing. But there are no other counter-rotating secondary vortices in other regions of the mouth-throat model as at time

$t = \mathrm{T}_1$ displayed in Fig. 5.89. The flow field at this time level is much closer to the flow field at time $t = \mathrm{T}_4$. A pair of large vortices are observed at B - B' cross section as at time level $t = \mathrm{T}_4$. At the same time, the recirculation zone becomes larger. Other than the quantity of vortices at the cross section C - C', the quantity of secondary vortices at other cross sections decreases as well, in particular the secondary vortices distribution at the F - F'cross section, which means the turbulence decreases. But, in comparison with the flow field at $t = \mathrm{T}_1$, the flow field at this time level is much more turbulence. At the same time, the recirculation has become larger.

5.3.3 Summary

The airflow field in the cast-based mouth-throat model has been simulated considering the unsteady inspiration flow mode and neglecting the expiration flow phase. Flow fields at five different times have been discussed including two times at the accelerating phase, one at the peek point and two at the decelerating phase. It exhibits a extinct process that the flow transits from laminar to turbulent and the flow transits from turbulent to laminar flow. At the low inspiration flow rate, the laminar flow is prevalent in the mouth-throat model. Even in the trachea where the turbulence takes a predominant level usually, the counter-rotating vortices can be observed. Few secondary vortices are observed in the mouth-throat model. With the inspiration flow rate increasing, the Reynolds number increases and the unsteadiness appear after flow goes into the pharynx. The counter-rotating vortices disappear and the unsteady vortices appear in the main flow zone, recirculation zone after the soft palate and the glottis, the mixing zone, boundary of the laryngeal jet, boundary of wall and the laryngeal jet region depending on the time and location. After the peek, the inspiration flow rate decreases as well as the Reynolds number, which leads to the flow transiting from turbulent to laminar gradually. The large vortices re-appear in the main flow zone in the pharynx. When the inspiration flow rate decreases to the value at the first time. Although the flow rate is not so turbulent as the last two times of T_3 and T_4 , the flow still keeps obvious properties of the turbulence, which can be seen from the secondary vortices because of the lingering effect of the flow.

5.4 Airflow Field and Particle Transport in the CT-Based Mouth-Throat

As discussed in the chapter 2, investigations have shown that the geometric features have great influence on the features of airflow and the particle deposition and dispersion, and numerical modeling of flow field and particle motion in the more realistic geometry based on CT scans has been developed recently [9, 46, 53]. In this section, a new mouth-throat model is constructed based on CT scans. The flow field and mono-disperse particles are simulated with the solver "oodLFoamct". The properties of the airflow field and the particle deposition are discussed.

5.4.1 Model Preparation and Grid Generation

Four different sets of CT scans are provided by Medical School in the University of Heidelberg. Among them, one is chosen with few artifact, mouth open and glottis open seen in Figs. 5.94 and 5.95. As aforementioned in the section 4.4, these CT scans are imported into ImageJ and they are converted from the file format of "Dicom" to format of ".tiff" as presented in section 4.4 because NeuRA2 [78] can only operate this kind of file format.

After that, the image should be repaired because some of them still have artifact and the geometry has to be closed manually seen in the Fig. 5.96 to separate the structure of mouth-throat out. In addition, for the same purpose, the operation of "cut plane" is used to create a close zone which is required for segmentation. After the reparation, this focused structure is segmented and the interesting part is taken out seen in Fig. 5.97. As the same process presented in section 4.4 to generate the geometrical model based on CT scans, the surface grid is generated with the format of ".stil".

Two points should be mentioned here. One is that it is very important to choose right scale parameter when the surface grid or configuration is exported from NeuRA2. Second is that it is better to set the direction in meshLab [271] to make the configuration in front view, which will take convenience in the post-process of airflow fields.

Fig. 5.94: A sample of CT scans on the right view.

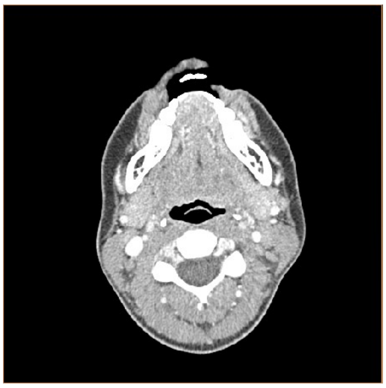

Fig. 5.95: The second sample of CT scans on the top view.

Fig. 5.96: The second sample of CT scans on the top view after respiration.

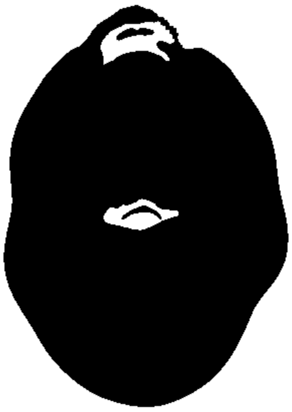

Fig. 5.97: The second sample of CT scans on the top view after segmentation.

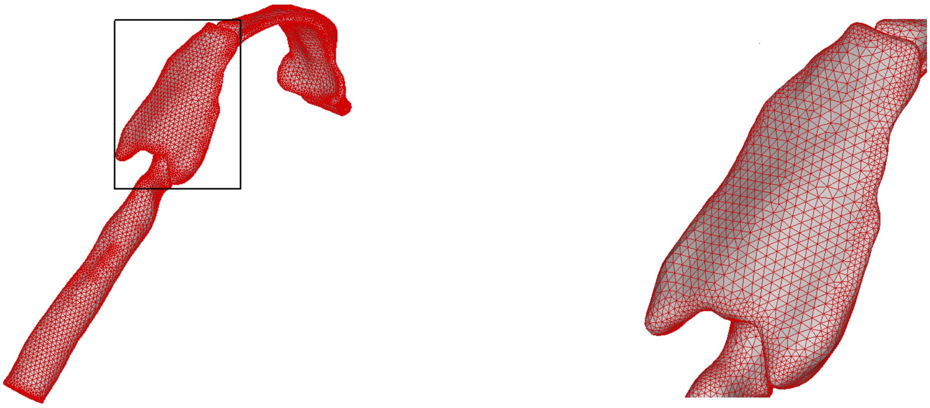

Fig. 5.98: The grid on the surface (left) and the zoom out of the pharynx part (right) of mouth-throat based on CT scans.

The inlet plane of the configuration has the same angle with the lips, and the outlet plane is normal to the trachea seen in Fig. 5.98 (left), which is much more consistent with the realistic situation. From the zoom out part (Fig. 5.98 (right)), it can be seen that the angle of the triangle on the surface is not sharp which is helpful to generate volume mesh with high quality. Moreover, the triangle distribution is related to the contour of the configuration. More grid nodes distribute on the region where the profile changes acutely, which can make sure that the reconstructed geometrical model is more close to the realistic situation. The computational grid is generated with Ansys ICEM-CFD 11.0 as well. The tetrahedral grid is used and 21,452 grid nodes are adopted in the present study.

5.4.2 Computational Conditions

The gas transported in the geometry is assumed to be the air at the room temperature. Then, the physical condition of the gas is as follows:

$$\rho_g = 1.21\ \mathrm{kg/m^3};\ \mathrm{T_g} \ = \ 273.15\ \mathrm{k};\ \nu \ = \ 14.9\ 10^{-6}\ \mathrm{m^2/s} \tag{5.19}$$

As the same way in the mouth-throat model based on cast, in this section, steady inspiration flow rate is adopted. The inspiration flow rate at normal breathing rate of 30 L/min is adopted. The boundary condition corresponding to inspiration flow rate of 30 L/min is as follows:

(1) Inlet:

$$V_n \;=\; 7.423\; \pm 2\%\ \text{m/s};\ \text{Re} \;=\; 5{,}011;\ \frac{\partial P}{\partial n} \;=\; 0; \tag{5.20}$$

(2) Outlet:

$$\frac{\partial \mathbf{V}}{\partial n} \;=\; 0;\ P \;=\; 0\ \text{Pa (relative to the ambient pressure)}; \tag{5.21}$$

(3) Wall:

$$\mathbf{V} \;=\; 0\ \text{m/s};\ \frac{\partial P}{\partial n} \;=\; 0. \tag{5.22}$$

It assumes that the air in the configuration is static in the beginning, then the velocity is 0 m/s and pressure is 0 Pa. The boundary conditions in another two cases can be given according to this case.

In addition to flow field, the micron particles deposition and transport are studied in the mouth-throat based on cast. The particles are injected simultaneously with the air randomly at the inlet plane, which has the same velocity as the air flow. The particle position is controlled by the uniform Gauss distribution. As it is conducted in the idealized mouth-throat, the injected particle number is set to 10,000 here. It is assumed that the particle deposition occurs if the distance of the particle center to the wall is less than half the particle diameter as well. The particle density is 1,000 kg/m^3. Three diameters $d_p = 2$, 5, and 10 µm are studied at the steady inspiration flow rates of 30 L/min.

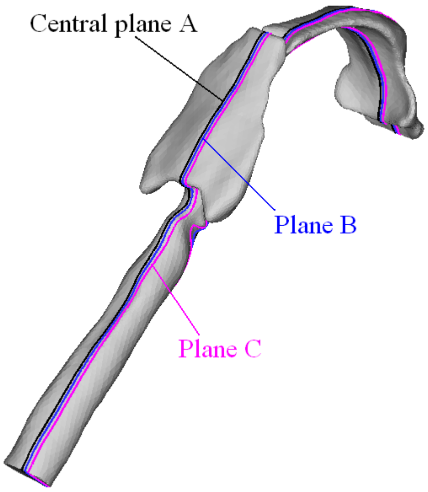

Fig. 5.99: The positions of each cut planes at the CT-based mouth-throat.

5.4.3 Properties of Airflow Field

To study the properties of the flow field in the mouth-throat model based on CT scans, the velocity contour and streamlines at three different cut planes are presented including the mean and instant flow field. The positions of these cut plans are shown in Fig. 5.99. The central plane A is the cut plane at the middle of the geometry and the distance among these positions is 1 mm.

The mean velocity contour and streamlines at the central plane of the configuration are shown in Fig. 5.100. After the flow entering into the mouth-throat, the air flow velocity decreases at first due to the enlargement of the cross section. The velocity in the end of soft palate is enhanced significantly due to the configuration constriction and maximum velocity appears in this region, which is different with the case of simplified geometry in which the maximum velocity occurs in the location of glottis. The flow field cannot develop sufficiently due to the narrow passage to the pharynx and the structure of the pharynx cavity. The flow field is blocked in the pharynx cavity and a high velocity region is shaped, which leads to few flow going further into larynx and trachea. At the same time, a reversed flow region appears in the upper side of the pharynx and a vortex is created in the lower portion of the pharynx. In the glottis, the velocity increases again due to the configuration constriction, but the velocity is not as large as the region in the upper portion of the pharynx. Moreover, there is no laryngeal jet and reversed flow after glottis in present simulation, which was seen in the simplified geometry and in the numerical simulation in a CT scans model by Jayaraju et al. [46].

The velocity at plane B seen in Fig. 5.101 has almost similar properties of the velocity

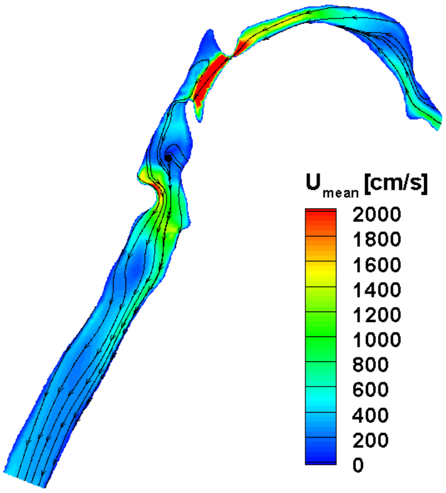

Fig. 5.100: The time-averaged velocity contour and streamlines at the central plane A of the CT-based mouth-throat.

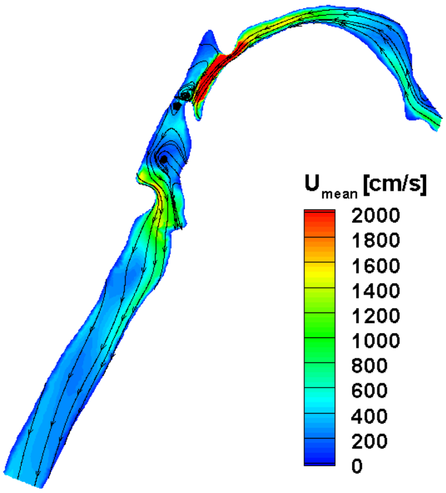

Fig. 5.101: The time-averaged velocity contour and streamlines at the cut plane B of the CT-based mouth-throat.

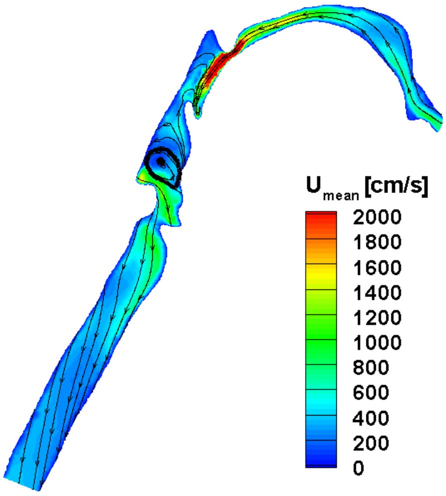

Fig. 5.102: The time-averaged velocity contour and streamlines at the cut plane C of the CT-based mouth-throat.

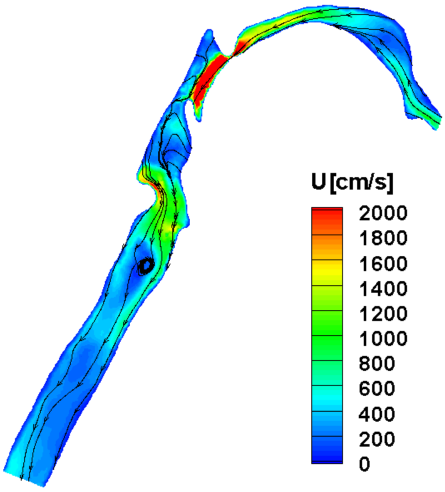

Fig. 5.103: The instant velocity contour and streamlines at the central plane A at time of 1.92228 s.

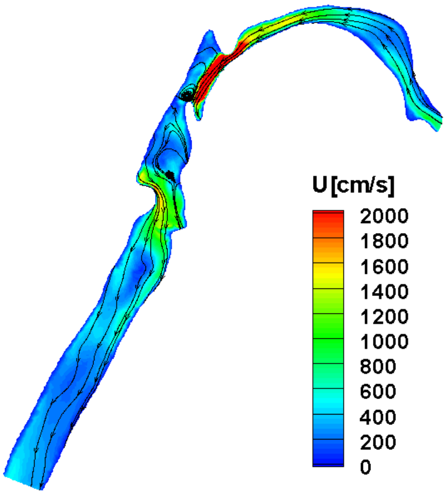

Fig. 5.104: The instant velocity contour and streamlines at the cut plane B of the CT-based mouth-throat at time of 1.92228 s.

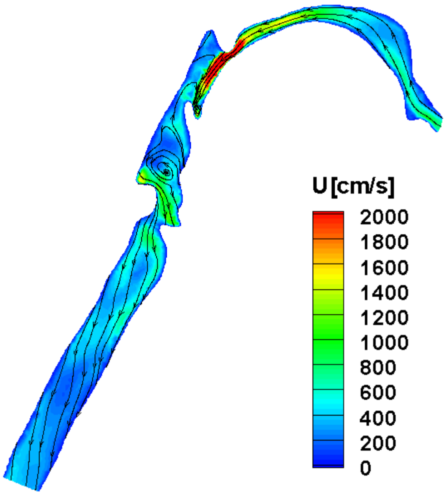

Fig. 5.105: The instant velocity contour and streamlines at the cut plane C of the CT-based mouth-throat at time of 1.92228 s.

development as the flow at central plane A. The main difference is that there are another two vortices seen in the region near epiglottis. Moreover, the length scale of the vortex in the pharynx cavity is larger at cut plane B than central plane A. At the same time, the vortex is even larger at plane C seen in Fig. 5.102. At the same time, the vortices near the epiglottis seen at the cut plane B is not seen in the cut plane C. Although the constriction at the end of the soft palate limits the flow development, the complexity of the geometry still creates complex vortices in three-dimensional space.

To further understand the properties of flow field in the more realistic mouth-throat based on CT scans, a typical instantaneous flow field at 1.9228 s is shown as well at the central plane A seen in Fig. 5.103, at cut plane B seen in Fig. 5.104 and cut plane C seen in Fig. 5.105. From these figures, it can be observed that the flow has similar features as in the time-averaged flow field at all of these cut planes. The main difference is that a vortex is seen in the trachea in the instant flow field at central plane A shown in Fig. 5.103 in contrast that a vortex appears in pharynx in the time-averaged flow field. Different with the flow field at central plane A, there is no vortex seen in trachea and there is still one vortex observed in the pharynx at cut plane B shown in Fig. 5.104. In comparison with the time-averaged flow field at B cut plane, only one vortex around epiglottis is observed. At cut plane C shown in Fig. 5.105, only one vortex is observed as the case in the time-averaged flow field. It is not hard to see that the main differences between the time-averaged and instantaneous flow field are the vortex distribution and they mainly appear in the region of epiglottis and trachea. In particular, the dynamical motion of the vortex in the trachea may influence the particle deposition for smaller particle in this region.

In summary, the present numerical method improves the understanding the flow field in the upper respiratory system. It shows that the flow field can be very different with the flow field in the simplified geometry due to the different geometrical feature. It may also be different with the flow field in another realistic geometry model since the configurations are still very different. The flow field is very unsteady, in particular, for the vortex in the region of epiglottis and trachea.

5.4.4 Particle Deposition and Dispersion

Particle deposition efficiency is an important parameter to evaluate the particle deposition. In the present simulation, for the particle size of 2 µm, the particle deposition efficiency is 85.05%, for the particle size of 5 µm, it is 99.64% and for the particle size of 10 µm, it is 100%. It can be seen that few particle going through the geometry when the particle diameter is no less than 5 µm, which is different with the result in the simplified model. It mainly comes from the geometrical difference. The particle deposition patterns for particles diameter of 10, 5 and 2 µm are shown in Figs. 5.107, 5.108, and 5.109 respectively. From Fig. 5.107, it can be seen that no particles with 10 µm can go through the pharynx, and most of them deposit before the soft palate, others deposit in the location of the end of soft palate and few deposit in the pharynx cavity. In the case of particle diameter equal to 5 µm, there are more particles to go through the mouth cavity, but they deposit in the pharynx cavity in Fig. 5.108. When the particle size decreases to 2 µm, there are more particles going through the pharynx and reaching the trachea. There are more particles depositing on the wall of pharynx and trachea. The particles not only deposit on the impact side of wall, they also deposit on the sidewall. It may be caused by the vortex in the trachea.

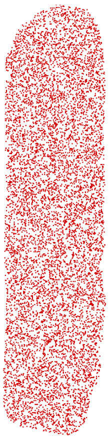

Fig. 5.106: The right view of particle initial distribution pattern at the inlet plane of the CT-based mouth-throat.

Fig. 5.107: The 10 µm particle deposition on the surface of the mouth-throat model of the CT-based mouth-throat.

Fig. 5.108: The 5 µm particle deposition on the surface of the mouth-throat model of the CT-based mouth-throat.

Fig. 5.109: The 2 µm particle deposition on the surface of the mouth-throat model of the CT-based mouth-throat.

In summary, the particle deposition efficiency increases with the particle size due to the increasing particle inertia. The constriction after the soft palate builds the first block for particles going into the deep lung, and the bottom of the pharynx consists of the second barrier for particle motion. And most of particles deposit before they reach the trachea.

5.4.5 Summary

A mouth-throat model has been constructed based on CT scans. The flow field and micro-particle motion were simulated with LES and Lagrangian method, which has been evaluated in a constricted tube and the cast-based mouth-throat model. It has been found that the flow field in the present geometry is very different with the flow field in the simplified mouth-throat such that the maximum velocity appears in the region of the soft palate tip and no laryngeal jet is observed at present simulation.

The velocity is enhanced significantly at the top portion of the pharynx coupled with the recirculation flow in the mean flow field. The vortices have been observed in the pharynx cavity and in the region of epiglottis in the mean flow field and there is a vortex in the trachea as well in the instant flow field. Although the velocity contour is similar in both mean flow field and instant flow field, the flow field has very complex vortex field with high spacial and temporal dynamics.

Particles with 2, 5, 10 μm are tracked separately at the normal inspiration flow rate of 30 L/min. It is found that the few particles with 10 μm go through the mouth-cavity, few particles with 5 μm can reach the trachea. Most of the particles with 10 and 5 μm deposit in the mouth-cavity and pharynx cavity. When the particle size decreases to 2 μm, more particles go through the pharynx and deposit in the trachea, or go further into the pulmonary region. Moreover, the vortex in the trachea may increases the particle deposition in this region.

5.5 Airflow Field in the Nasal Cavity

In the section, it discusses the construction of the nasal cavity based on CT scans, and the numerical simulation in the CT-based nasal cavity. In this section, the airflow field in the nasal cavity model is analyzed and it sets the basis of investigating aerosol drug delivery through nasal cavity.

5.5.1 Geometry Construction and Grid Generation

The method to construct the nasal cavity based on CT scans is almost same as to construct the mouth-throat model based on CT scans using NeuRA2 [78]. But there is much more work to repair the CT scans, which intends to delete the artifact, and to identify the focused part because the anatomical structure of nasal cavity is very complex. The nasal cavity includes three meatuses seen in the Fig. 5.110. In addition, there are so many passages between the sinus and the nasal passage seen in Figs. 5.111 and 5.112 which adds many difficulties to the geometry construction because it takes effort to sperate the nasal cavity from the sinuses. It is very important to make comparison from different observation angles such as the front, left and top side view during the process of the geometry construction.

A nasal airway is constructed shown in Fig. 5.113, which is built from a different set of CT scans from the set used to construct the mouth-throat model because this set of CT scans has high quality in the part of nasal cavity. This geometry of nasal cavity with ".stl" format is imported into Ansys ICEM-CFD 11.0 to generate the grid. Two tubes are added to the nostrils and a tube is added to the nasopharynx shown in Fig. 5.114 to decrease the influence of inlet and outlet boundary conditions. The tetrahedral grid is adopted due to the complexity of the geometry.

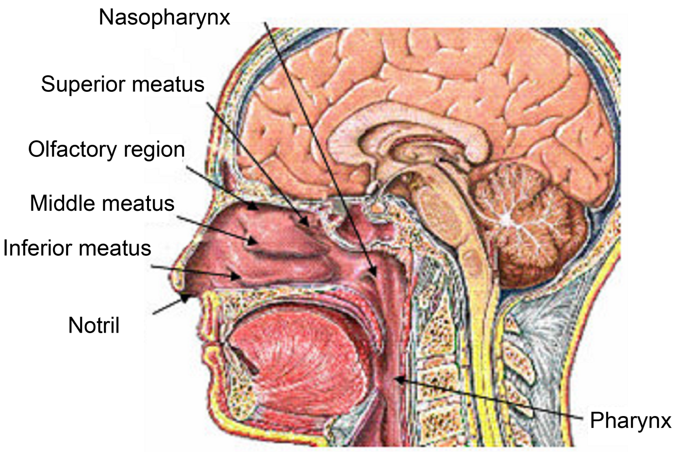

Fig. 5.110: The anatomical view of the nasal cavity.

Fig. 5.111: A sample CT scan of the nasal cavity from the left view.

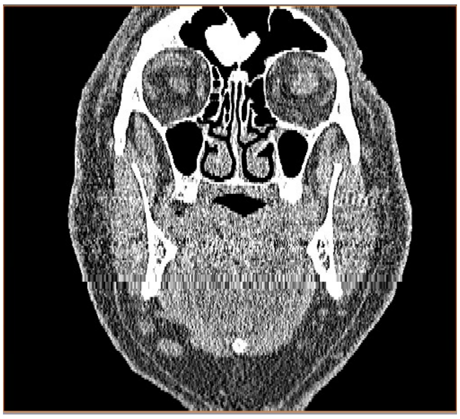

Fig. 5.112: A sample CT scan of the nasal cavity from the top view.

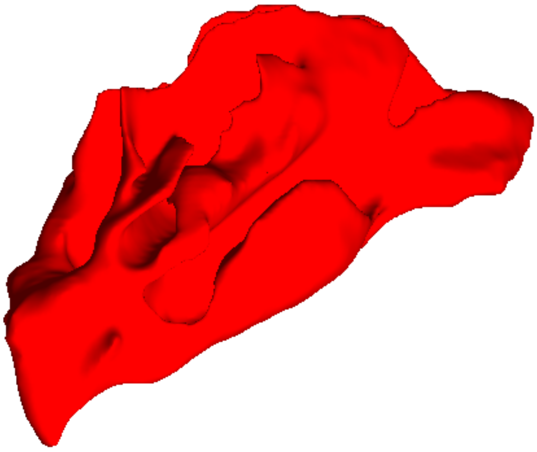

Fig. 5.113: The 3D view of reconstructed nasal cavity based on CT scans.

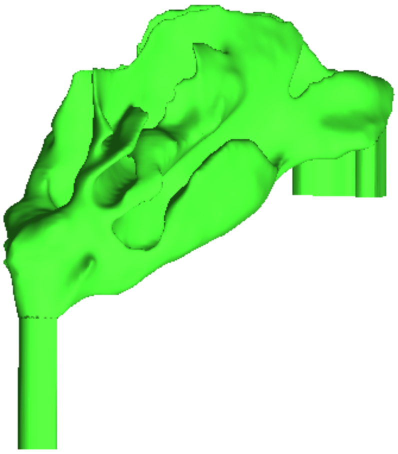

Fig. 5.114: The final geometry of nasal cavity used to generate the grid.

5.5.2 Computational Conditions

The gas transport in the geometry is assumed to be air at room temperature. Then, the physical condition of the gas is as follows:

$$\rho_g = 1.21 \text{ kg/m}^3; \; \mathrm{T_g} = 293.15 \text{ K}; \; \nu = 14.9\ 10^{-6} \text{ m}^2/\text{s}. \tag{5.23}$$

At present, only one case is simulated and the inspiration flow rate at the rest breathing of 7.5 L/min is considered. The boundary conditions corresponding to inspiration flow rate of 7.5 L/min are as follows:

(1) Inlet:

$$V_n = 1.448 \pm 2\% \text{ m/s}; \; \mathrm{Re} = 897; \; \frac{\partial P}{\partial \mathrm{n}} = 0; \tag{5.24}$$

(2) Outlet:

$$\frac{\partial \mathbf{V}}{\partial n} = 0; \; P = 0 \text{ Pa (relative to the ambient pressure)}; \tag{5.25}$$

(3) Wall:

$$\mathbf{V} = 0; \ \frac{\partial P}{\partial n} = 0. \tag{5.26}$$

It assumes that the air in the configuration is static in the beginning so that the velocity is 0 m/s and pressure is 0 Pa relative to the ambient pressure initially. The numerical simulation is carried out in grid of 207,180 grid nodes.

5.5.3 Properties of Mean Airflow Field

In this section, the time-averaged flow field in the nasal cavity is presented. The pressure on the surface is shown in Fig. 5.115. The pressure on the surface of the nostril is maximum because the air has a impinging effect at this position. After the position, the pressure decreases gradually to the nasopharynx region. The velocity field at successive cross sections are shown in Fig. 5.116. From the Fig. 5.116, it can be seen that the velocity field in the nasal cavity is non-uniform. The maximum velocity appears in the nasal valve region and

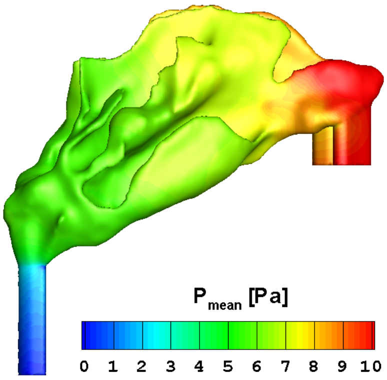

Fig. 5.115: The pressure distribution on the surface of the nasal cavity.

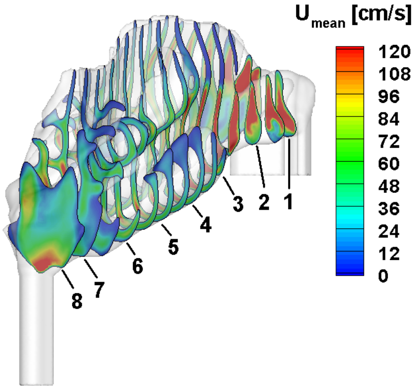

Fig. 5.116: The velocity contours at successive sections with $\triangle = 1$ cm.

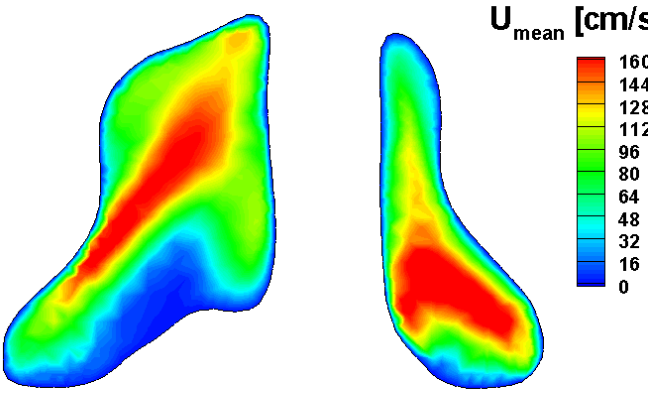

Fig. 5.117: Velocity contour at the cross-section 1 of the nasal cavity.

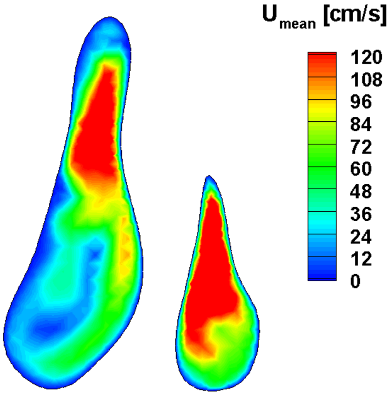

Fig. 5.118: Velocity contour at the cross-section 2 of the nasal cavity.

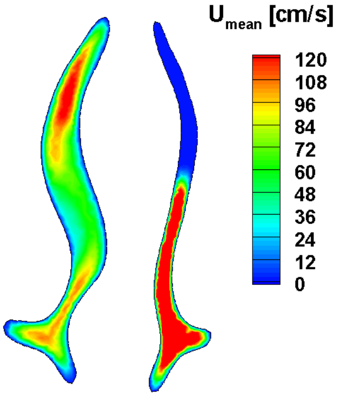

Fig. 5.119: Velocity contour at the cross-section 3 of the nasal cavity.

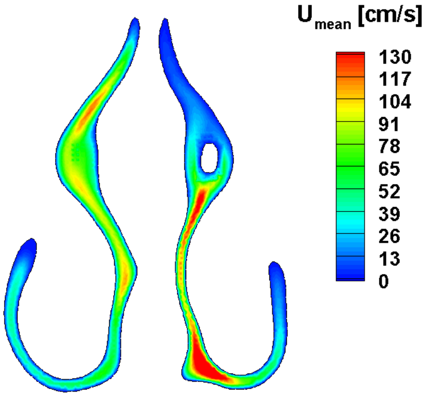

Fig. 5.120: Velocity contour at the cross-section 4 of the nasal cavity.

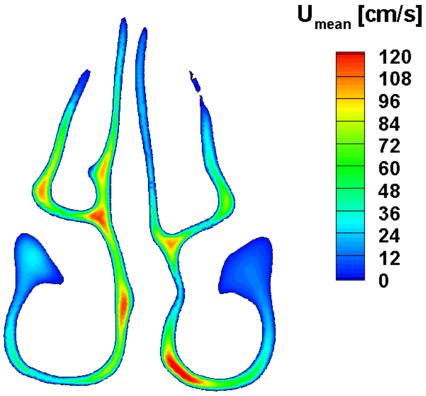

Fig. 5.121: Velocity contour at the cross-section 5 of the nasal cavity.

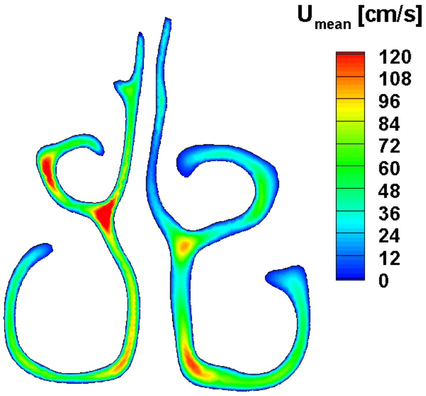

Fig. 5.122: Velocity contour at the cross-section 6 of the nasal cavity.

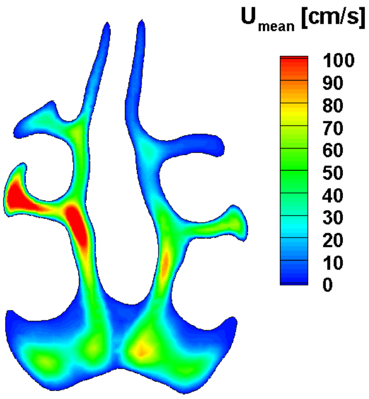

Fig. 5.123: Velocity contour at the cross-section 7 of the nasal cavity.

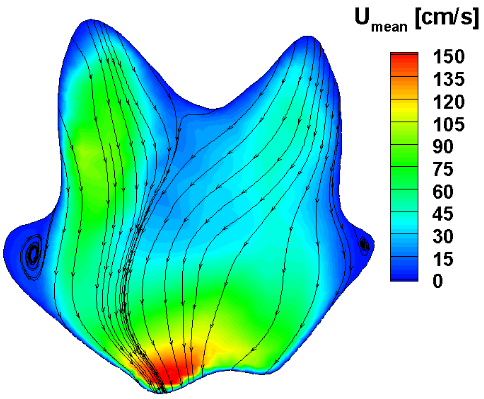

Fig. 5.124: Velocity contour at the cross-section 8 of the nasal cavity.

little air reaches the olfactory region and tips of the meatuses, which is reported to protect the smelling cell [26].

To further study the properties of the velocity field, the velocity contours at different cross sections located at different positions are shown in Figs. 5.117 - 5.124. The airflow field at the cross section 1 and 2 seen in Figs. 5.117 and 5.118 are very concentrated. The majority of air goes through the upper portion of cross section 1 and 2. The maximum velocity region appears at cross section 1 seen in Fig. 5.117. The flow mainly goes through the nasal passage in the inferior region at cross section 3 seen in Fig. 5.119. Little air can reach the narrow region of the nasal passage (the upper region of the right passage). But the flow still can go further through the wide passage in this region (the upper region of the left passage). From the position of cross section 4 seen in Fig. 5.120, the flow gradually goes into the meatus region. The flow mainly goes through the region in middle passage seen in Figs. 5.120 - 5.123. Little airflow can get the tip of inferior meatus at cross sections 5 - 7 as shown in Figs. 5.120 - 5.123. The middle meatus is important passage for air to go through as reflected in Figs. 5.122 and 5.123, but it is still hard for air to reach the tip of the narrow region of the middle meatus seen in Fig. 5.122. In the comparison of middle meatus, little air can enter into superior meatus and the olfactory region. At the position of cross section 8, the flow has begun to go out of the nasal cavity seen in Fig. 5.124 and the maximum velocity region locates at the bottom of the cross section. The secondary streamlines at this cross section show the air flowing into the outlet as well seen in Fig. 5.124. Two vortices are observed in the lateral sides of the nasopharynx region which are entrained by the small cavities in the lateral sides.

5.5.4 Summary

In this section, a nasal cavity is built based on the CT scans. The airflow field is simulated in the nasal cavity model, which paves way to study the air flow field and particle dispersion and deposition in the nasal cavity towards the investigation of aerosol drug delivery through nasal airway. At first, a nasal cavity model is constructed based on the CT scans using NeuRA2. The method of constructing the geometry is almost same as the way of constructing the mouth-throat based on CT scans. The main difference is that much effort is needed in this case to segment the nasal cavity. The flow field is simulated using "oodLFoam" in the nasal cavity at rest condition. The time-averaged velocity field has been discussed in different cross sections. It is observed that few air can reach the tips of meatuses and the olfactory region. The flow goes through the nasal cavity mainly through the main air passage. In addition, the vortices are observed in the nasopharynx region.

6. Conclusions and Perspectives

In this thesis, the airflow field and particle motion have been simulated in the human upper respiratory system with LES and Lagrangian equations. The numerical simulations have been carried out in four different geometrical models. The geometry models are built based on human cast from literature [89] and the CT scans using NeuRA2 [78]. The grids are generated with Ansys ICEM-CFD 11.0 [183]. The airflow field is simulated with LES coupling with Smagorinsky sub-grid scale model [262]. The particle is simulated with Lagrangian tracking model in the scope of one-way and two-way coupling. User-defined solvers are created based on the platform of OpenFOAM 1.5 [184] which can solve the airflow field using LES and solve the mono-disperse or the poly-disperse particle motion using Lagrangian equations with one-way/two-way coupling. The numerical simulations have been performed with these solvers.

First, the airflow field in the constricted tube has been simulated to study the laminar-transitional-turbulent flow and to evaluate the capability of the present methodology on simulating the laminar-transitional-turbulent flow which is prevalent in the human upper respiratory system. In comparison of the velocity at the center line of the constricted tube and the velocity profile on different cross sections with the experimental result and the numerical results from RANS/LRN $k - \omega$ model [86] and RANS/SST $k - \omega$ model [46], it is demonstrated that the present methodology has the capability to predict the transitional flow in the constricted tube and it even improves the prediction of the transitional region of the airflow field. Thus, it sets the basis for further studies of the airflow field in the human upper respiratory system.

A mouth-throat model is constructed based on the human cast from the literature [48, 86]. The grids are generated using Ansys ICEM-CFD 11.0. The airflow field and particle motion have been simulated in the cast-based mouth-throat model. The gas fields are simulated at three different inspiration flow rates of 15, 30 and 60 L/min. The time-averaged and unsteady airflow fields have been investigated. The numerical simulation has captured the main flow features including a skewed velocity profile, flow separation after the sudden geometric change at the soft palate and glottis, and the laryngeal jet. Both the length scale and location of secondary vortices change with the location of laryngeal jet, and it trends to distribute at the interface of separation zone and laryngeal jet. In addition, the secondary vortices distribution and laryngeal jet have relationship with the inspiration flow rate as well. For instance, the secondary vortices distribute in the pharynx and the trachea and the laryngeal jet becomes more concentrate with the inspiration flow rate increasing. Three dimensional vortices are observed in the cast-based mouth-throat model. The observation of the unsteady flow field shows that after the airflow has entered into the pharynx, the airflow field becomes unsteady and involves turbulent structures at 30 and 60 L/min. In contrast to the averaged airflow field, no counter-rotating vortices are seen in instantaneous airflow fields. Depending upon the axial location and time, secondary vortices occur in the separation zone, the mixing zone, the main flow zone and the wall shear layer of the separation zone and the laryngeal jet. Vortices appearing in the wall shear layer have small scales, whereas those in the mixing zone tend to be at larger scales. The laryngeal jet is highly unsteady and it breaks up at the tail.

The mono-disperse particle motion has been simulated in the mouth-throat based on cast as well. The investigation has been developed considering three different size of particles including 2, 5 and 10 μm at three different inspiration flow rates of 15, 30 and 60 L/min. The particle deposition efficiency, the particle deposition pattern on the surface, the relationship between the final particle positions and released particle positions at the inlet palate, and the particle trajectories have been studied. The particle deposition efficiency has been compared with the experimental and numerical results. It shows the present methodology has sufficient capability to predict the particle motion in the mouth-throat. The investigation of the regional particle deposition, the final paritcle positions related to the release particle positions, the particle deposition pattern on the wall of the cast-based mouth-throat and particle trajectories has related to the particle size, inspiration flow rate and initial particle position. The turbulence and recirculated flow have been found to have great influence on the particle trajectories and then it may affect the particle deposition.

In addition to the mono-disperse particle, the poly-disperse particles have been adopted as well in the present thesis. One-way and two-way coupling have been adopted and they have very close results. The numerical simulations show that the poly-disperse particle distribution have great influence on the particle deposition efficiency and it should be considered in the numerical simulation of particle motion. It is found that the particles larger than 5 μm and less than 1 μm contribute most to the particle deposition efficiency and the large particles are filtered gradually in the cast-based mouth-throat model and the sub-micron particles mainly deposit in the mouth cavity and the trachea.

The investigation is also conducted to study the airflow field in the mouth-throat based on cast under the unsteady inspiration flow rate. The properties of the airflow field show great unsteadiness and they are related to the inspiration flow rate and the accelerating or decelerating phase which they dwell in. At the decelerating phase, for the same inspiration flow rate, it shows more turbulent properties than accelerating phase. In addition, airflow field in the mouth cavity keeps laminar in most regions of the inspiration phase.

Another mouth-throat model, which is more close to the realistic anatomical structures of oral airway, has been constructed based on CT scans in the present work. The airflow field and micron particle motion are studied. The numerical simulation shows that the geometric properties have great influence on the airflow field and particle motion and it is significantly different from the case of the simplified mouth-throat model based on cast. For instance, the maximum flow velocity appears in the entrance of the pharynx and the vortex distribution in the geometry. The airflow field in this case shows great unsteady dynamics such as the vortex distribution. The large particles cannot even pass through the pharynx. Particles with 2 μm can pass through the pharynx. However, they cannot go into the deep site totally due to the filtering function of trachea.

To pave the way for further research, the airflow field in the nasal cavity has been carried out as well. The nasal cavity is constructed based on the CT scans using NeuRA2 [78] as well. The airflow field is simulated in the rest condition of 7.5 L/min. It is observed that little air can reach the tips of meatuses and the olfactory region. The airflow go through the nasal cavity mainly through the main air passage. The vortices are also observed in the nasopharynx region.

Moreover, one of challenge in this field is to build a suitable methodology to simulate the airflow and track the particle motion in the complex human upper airway, which involves the knowledge and techniques from many subjects such as medicine, image-processing, computational fluid dynamics and computer science. It involves the operation of different kinds of softwares such as ImageJ [270], NeuRA2 [78], Ansys ICEM-CFD 11.0 [183], OpenFOAM [184] and Tecplot [272], and different file formats such as “Dicom”, “.tiff”, “.stl” .etc. The patient-specific anatomical structures of the respiratory tract also take the difficulty to gain a standard geometrical model and universal conclusion for all human beings. Thus, the project requires synthesized and systematic capacity to deal with the interdisciplinary problem. One of the main contributions of this thesis is that a new methodology has been found, which can be performed in the bio-mechanical investigations. The methodology includes geometry construction based on medical images such as CT and MRI scans, the numerical simulation of the airflow field and particle motion in the oral airway. The methodology has been proved to be suitable to investigate the aerosol drug delivery in the human respiratory system in the thesis and it can be extended to other fields such as blood flow in the vessel and brain aneurysm.

Although, the project has focused on issues of the airflow field and particle motion in the human upper respiratory system, other investigations can be developed based on the present work in the future. The particle motion may be simulated further in the mouth-throat model under the unsteady inspiration flow rate as well as the particle motion in the nasal cavity. The airflow field in the nasal cavity should be conducted at other inspiration flow rates. In addition, the spray droplets should be considered for some drugs which require a new kind of solver because the present solver only considers the incompressible flow field and the compressible flow field should be used in the case of spray droplet coupled with the droplet evaporation. More research fields such as the transport in the respiratory tract including the extra-thoracic and intrathoracic regions, and blood flows in the vessel, heart and aneurysm can be explored based on the present methodology as well.

Appendix

A. Abbreviations

Abbreviation	Elaboration
2D	Two dimensional
3D	Three-dimensional
CAD	Computer aided design
CFD	Computational fluid dynamics
COPD	Chronic obstructive pulmonary disease
CT	Computed tomography
DE	Deposition efficiency
DES	Detached eddy simulation
DEF	Deposition enhance factor
DF	Deposition fraction
DNS	Direct numerical simulation
DPI	Dry powder inhaler
G	Generation(s)
LBM	Lattice Boltzmann method
LES	Large eddy simulation
LRN	Low Reynolds number
TB	Tracheo-bronchial
IP	Impaction parameter
MDI	Metereddose inhaler
MMD	Mass median diameter
MMAD	Mass median aerodynamic diameter
MRI	Magnetic resonance imaging
MT	Mouth–throat
N–S	Navier–Stokes
PISO	Pressure-implicit split-operator
PIV	particle image velocimetry
RANS	Reynolds averaged Navier–Stokes equations
RNG	Renormalization group
SGS	Subgrid-grid scale
SST	Shear stress transport

B. Nomenclature

Symbol	Unit	Description
A_i	m^2	Area of local cell (i)
A^+		Van Direst constant
C_c		Conningham correction factor
C_D		Drag coefficient
C_s		Smagorinsky constant
D	m	Diameter of constricted tube
d	m	Distance to the wall
d_p	m	Particle diameter
D_e		Dean number
DF_{region}		Regional nano-particle deposition fraction
$\mathbf{F}$	m/s^2	Exerted force on particle
F_1		Blending function
F_2		Blending function
$\mathbf{F}_B$	m/s^2	Brownian force on particle
$\mathbf{F}_D$	m/s^2	Drag force on particle
f_i		Mass fraction
k	m^2/s^2	kinetic turbulent energy
m_{in}	kg	Injection particle mass
m_p	kg	Particle mass
m_{parcel}	kg	Parcel mass
N_P		Parcel number
N_p		Particle number
L_s	m	Turbulent length scalar
L_s	m	Subgrid length
L_{ij}	m^2/s^2	Resolved turbulent stress
P	Pa	Pressure
p	Pa	Pressure
Q_{in}	L/min	Inspiration flow rate
Q	L/min	Inspiration flow rate
Q	$1/s^2$	Second invariant of velocity gradient tensor

R	m	Radius of constricted tube
Re		Reynolds number
Re_p		Particle Reynolds number
$\mathbf{S}$	1/s	Vorticity tensor of velocity gradient
T	K	Gas temperature
T_g	K	Gas emperature
T_p	K	Particle temperature
T_{ij}	m^2/s^2	Sub-grid scale tensor
t	s	Time
t_{out}	s	Droplet-eddy interaction time scalar
t_{in}	s	Time scalar for drag force
$\mathbf{U}$	m/s	Gas Velocity (vector)
U_i	m/s	Velocity
U_j	m/s	Velocity
$\mathbf{U}_p$	m/s	Particle velocity (vector)
V_n	m/s	Gas velocity in the normal direction
V	m/s	Axial velocity
$\mathbf{V}$	m/s	Velocity (vector)
X	m	Coordinate
$\mathbf{X}_p$	m/s	Particle position
Y	m	Coordinate
Y_i		Mass fraction
Z	m	Coordinate
x	m	Coordinate
y	m	Coordinate, the distance to the wall
z	m	Coordinate
ω	1/s	Specific turbulent dissipation
ω	1/s	Angular frequency
$\mathbf{\Omega}$	1/s	Rate-of-strain tensor of velocity gradient
ν	$\mathrm{m/s^2}$	Kinetic viscosity coefficient
ν_t	$\mathrm{m/s^2}$	Turbulent kinetic viscosity coefficient
ρ	$\mathrm{kg/m^3}$	Gas mass density
ρ_g	$\mathrm{kg/m^3}$	Gas mass density
ρ_p	$\mathrm{kg/m^3}$	Particle mass density
λ	m	Mean free path of air molecule
μ	g/(ms)	dynamic viscosity coefficient
ς		Gaussian random number

τ_p	s	Particle relaxation time
τ_{ij}	m^2/s^2	Reynolds stress tensor
σ_Y		Turbulent Schmidt number
ϵ	m^2/s^3	kinetic turbulent dissipation rate
α		Womersley number
ϕ		Constant of SST $k - \omega$ model
ϕ_1		Constant of $k - \epsilon$ model
ϕ_2		Constant of $k - \omega$ model
Δ	m	Filtering length
ΔV	m^3	Cell volume
Δx	m/s	Cell length
Δy	m/s	Cell length
Δz	m/s	Cell length
Δt	s	Time step
$\triangledown \mathbf{V}$	1/s	Velocity gradient
$\tilde{D}$		Diffusion coefficient

Subscripts and Superscripts

Symbol	Quantity
B	Brownian force
D	Drag force
g	Gas phase
i	index
j	index
k	index
m	index
l	index
p	Particle
r	Grid filter
t	Test filter
$\bar{}$	Averaged variable
$\tilde{}$	Filtering variable

Physical Constants

Symbol	Quantity
$k_B = 1.38065 \times 10^{23}$ m$^2 \cdot$ kg $\cdot$ s$^{-2} \cdot$ K	Boltzmann constant
$\mathcal{R} = 8.31451$ J/(mol·K)	Universal gas constant
$g = 9.8$ m/s^2	Gravitational acceleration

C. Acknowledgements

First of all, I would like to sincerely thank Prof. Dr. Eva Gutheil. Her knowledge, experience, physical insight, guidance and encouragement have promoted me to keep working with high efficiency and succeed to complete the project. She is such a considerate and patient supervisor that she serves as a role model for professional excellence and integrity.

I am grateful to Prof. Baumann for reviewing my thesis. It has been a continuous and kind support from him during the whole project, which included valuable feedback on my dissertation, observing surgical operation and discussions on anatomical structure of the respiratory system. I would like to extend my gratitude to PD Dr. Rohde for his help in providing CT scans. I am cordially obliged to Prof. Plinkert for his support and guidance during the process of conducting the project.

Moreover, I would like to express my gratitude to my mentor of Dr. Ge. He helped me to understand the physical model and the method to handle the data.The acknowledgement is also given to Prof. Urbanetz for providing the poly-disperse particle distribution from DPI. In addition, I would like to thank Dr. Jungblut for his precious help in using NeuRA2, which I needed to construct the mouth-throat model. The gratitude is given to Prof. Wittum and Dr. Krömker for their support and cooperation, which allowed me to use NeuRA2.

I thank the Ministry for Education and Research and the Ministry for Science, Research and Arts Baden-Wuerttemberg for allowing me to use bwGrid at Heidelberg University and Karlsruhe Institute of Technology.

I acknowledge German Science Foundation (Deutsche Forschungsgemeinschaft - DFG) for the financial support through the International Graduiertenkolleg (IGK) 710 “Complex processes: Modeling, Simulation and Optimization” and Heidelberg Graduate School “Mathematical and Computational Methods for the Sciences”.

I will always cheer the memories of my colleagues in the group of “Multiphase Flows and Combustion”, including Mr. Cao, Mr. Hu, Mr. Humza, Mr. Gopireddy, Mr. Olguin, Mr. Trunk and Ms. Vogel. Thanks for all of your help and encouragement during past three and half years in the group, in particular for the help from Mr. Humza and Ms. Vogel.

A special debt of gratitude should go to my wife, Jian Guan, my parents and my sister for their love, their continuous encouragement and support. Without them, I could not achieve anything today.

D. Declaration

I hereby declare that this thesis is my own work and effort and that it has not been submitted anywhere for any award. Where other sources of information have been used, they have been referenced and acknowledged.

Signature:

Place and date:

Bibliography

[1] A. H. Mokdad, J. S. Marks, D. F. Stroup, and J. L. Gerberding. Actual causes of death in the united states, 2000. *JAMA-J. Am. Med. Assoc.*, 291:1238–1245, 2004.

[2] T. P. Brunshidle, B. Konowalchuk, I. Nabeel, and J. E. Sullivan. A review of the measurement, emission, particle characteristics and potential human health impacts of ultrafine particles: Characterization of ultrafine particles. Technical Report PubH 5103, University of Minnesota, Minnesota state, United States, 2003.

[3] Health effects of air pollution. Technical Report AQ 07-02, Auckland Regional Council, Auckland, New Zealand, 2007.

[4] Aerosol drug administration. *http://www.enotes.com/nursing-encyclopedia/aerosol-drug-administration.*

[5] A. H. L. Chow, H. H. Y. Tong, P. Chattopadhyay, and B. Y. Shekunov. Particle engineering for pulmonary drug delivery. *Pharm. Res.*, 24:411–437, 2007.

[6] D. R. Hess, T. R. Myers, J. L. Rau, and S. Giordano. A guide to aerosol delivery devices for respiratory therapists. Technical report, American Association for Respiratory Care, TX, United States, 2007.

[7] C. Kleinstreuer, Z. Zhang, and J. F. Donohue. Targeted drug-aerosol delivery in the human respiratory system. *Annu. Rev. Biomed. Eng.*, 10:195–220, 2008.

[8] A. M. Prater. Explanation of the mechanism of breathing. *http://.helium.com/items/1672443-how-breathing-works.*, 2009.

[9] C. Kleinstreuer and Z. Zhang. Airflow and particle transport in the human respiratory system. *Annu. Rev. Fluid Mech.*, 42:301–334, 2010.

[10] S. T. Jayaraju. *Study of the air flow and aerosol transport in human upper airway using LES and DES methodologies.* Phd diss., Vrije Universiteit Brussel, Brussels, Belgium, 2009.

[11] K. H. Cheng and D. L. Swift. Calculation of total deposition fraction of ultrafine aerosols in human extrathoracic and intrathoracic regions. *Aerosol Sci. Technol.*, 22:194–201, 1995.

[12] Y. S. Cheng. Aerosol deposition in the extrathoracic region. *Aerosol Sci. Technol.*, 37:659–671, 2003.

[13] C. Kleinstreuer, Z. Li, and Z. Zhang. Particle deposition in the human tracheobronchial airways due to transient inspiratory flow patterns. *J. Aerosol Sci.*, 38:625–644, 2007.

[14] Y. Zhang and W. H. Finlay. Measurement of the effect of cartilaginous rings on particle deposition in a proximal lung bifurcation model. *Aerosol Sci. Technol.*, 39:394–399, 2005.

[15] S. Antwortet. Explain the breathing mechanism in human beings ? *http://www .blurtit.com/q9997289.html.*

[16] Lungs. *http://www.tutornext.com/lungs/7766.*

[17] G. R. Kevin. Human respiration. *http://www.indiastudychannel.com/resources/ 114979 -Human-respiration.aspx*, 2010.

[18] W. H. Finlay. *The Mechanics of Inhaled Pharmaceutical Aerosols: An Introduction.* London, Academic press, 2001.

[19] Respiration in human beings. *http://www.tutorvista.com/biology/respiration-in-human -beings.*

[20] C. Kleinstreuer and Z. Zhang. Transient airflow structures and particle transport in a sequentially branching lung airway model. *Phys. Fluids*, 14:862–880, 2002.

[21] H. Takano, N. Nishida, M. Itoh, N. Hyo, and Y. Majima. Inhaled particle deposition in unsteady-state respiratory flow at a numerically constructed model of the human larynx. *J. Aerosol Med.*, 19:314–28, 2006.

[22] Particulates. *http://en.wikipedia.org/wiki/Particulates.*

[23] A. Voiland and R. Simmon. Aerosols: tiny particles, big impact. *http://earth observatory.nasa.gov/Features/Aerosols/.*

[24] Terms of environment: glossary, abbreviations and acronyms. *http://www.epa.gov/OC EPAterms/pterms.html.*

[25] C. A. Pope, R. T. Burnett, M. J. Thun, E. E. Calle, D. Krewski, K. Ito, and G. D. Thurston. Lung cancer, cardiopulmonary mortality, and long-term exposure to fine particulate air pollution. *JAMA-J. Am. Med. Assoc.*, 287:1132–1141, 2002.

[26] Z. li. *Airflow and micro-particle transport and deposition in realistic lung airways including the alveolar region.* Phd diss., North Carolina State University, Raleigh, NC, 2007.

[27] C. Kleinstreuer, Z. Zhang, and Z. Li. Modeling airflow and particle transport/deposition in pulmonary airways. *Respir. Physiol. Neurobiol.*, 163:128–38, 2008.

[28] L. B. Lave and E. P. Seskin. An analysis of the association between u.s. mortality and air pollution. *J. Amer. Statist. Assoc.*, 68:284–290, 1973.

[29] N. R. Labiris and M. B. Dolovich. Pulmonary drug delivery. Part II: the role of inhalant delivery devices and drug formulations in therapeutic effectiveness of aerosolized medications. *Br. J. Clin. Pharmacol.*, 56:600–12, 2003.

[30] Frequently asked questions - fine particles ($PM_{2.5}$). *http://matracking.ehs.state.ma.us /Environmental_Data/Air_Quality/Fine_Particles_FAQ.html.*

[31] Health effects of fine particles and smoke. *http://yosemite.epa.gov/R10/airpage.nsf/ webpage/Health+Effects+of+Fine+Particles+and+Smoke.*

[32] J. Green and E. Gommeren. Pharmaceutical aerosols: enhancing the metered dose inhaler. *Drug Delivery Technol.*, 4:1–10, 2004.

[33] S. Shaikh, S. Nazim, A. Shaikh, T. Khan, Md.Zameeruddin, Q. Majaz, and S. Chalikwar. Recent trends in applications of pulmonary drug delivery: a review. *Int. J. Pharm. Res. Dev.*, 2:171–180, 2011.

[34] G. C. Khilnani and A. Banga. Aerosol therapy. *Indian J. Chest Dis. Allied Sci.*, 50:209–220, 2008.

[35] J. L. Rau. The inhalation of drugs: advantages and problems. *Respir. Care*, 50:367–82, 2005.

[36] L. Borgstrom, E. Derom, E. Stahl, E. Wahlin-Boll, and R. Pauwels. The inhalation device influences lung deposition and bronchodilating effect of terbutaline. *Am. J. Respir. Crit. Care Med.*, 153:1636–40, 1996.

[37] Bethesda. Technical Report 97-4051, National Heart, Lung, and Blood Institute, MD, United States, 2007.

[38] S. P. Newman, D. Pavia, and S. W. Clarke. Simple instructions for using pressurized aerosol bronchodilators, 1980.

[39] D. Pavia, M. Thomson, and H. S. Shannon. Aerosol inhalation and depth of deposition in the human lung. the effect of airway obstruction and tidal volume inhaled. *Arch. Environ. Health*, 32:131–7, 1977.

[40] D. Pavia, M. L. Thomson, S. W. Clarke, and H. S. Shannon. Effect of lung function and mode of inhalation on penetration of aerosol into the human lung. *Thorax*, 32:194–7, 1977.

[41] S. P. Newman, G. Woodman, S. W. Clarke, and M. A. Sackner. Effect of inspirease on the deposition of metered-dose aerosols in the human respiratory tract. *Chest*, 89:551–6, 1986.

[42] R. A. Lewis and J. S. Fleming. Fractional deposition from a jet nebulizer: how it differs from a metered dose inhaler. *Br. J. Dis.p Chest*, 79:361–7, 1985.

[43] S. P. Newman, A. Hollingworth, and A. R. Clark. Effect of different modes of inhalation on drug-delivery from a dry powder inhaler. *Int. J. Pharm.*, 102:127–132, 1994.

[44] A. C. Raimondi, J. Schottlender, D. Lombardi, and N. A. Molfino. Treatment of acute severe asthma with inhaled albuterol delivered via jet nebulizer, metered dose inhaler with spacer, or dry powder. *Chest*, 112:24–8, 1997.

[45] J. L. Rau and J. Rau. *Respiratory care pharmacology.* Mosby, St. Louis, 2002.

[46] S. T. Jayaraju, M. Brouns, S. Verbanck, and C. Lacor. Fluid flow and particle deposition analysis in a realistic extrathoracic airway model using unstructured grids. *J. Aerosol Sci.*, 38:494–508, 2007.

[47] P. W. Longest, M. Hindle, S. Das Choudhuri, and J. X. Xi. Comparison of ambient and spray aerosol deposition in a standard induction port and more realistic mouth-throat geometry. *J. Aerosol Sci.*, 39:572–591, 2008.

[48] Y. S. Cheng, Y. Zhou, and B. T. Chen. Particle deposition in a cast of human oral airways. *Aerosol Sci. Technol.*, 31:286–300, 1999.

[49] T. E. Corcoran and N. Chigier. Characterization of the laryngeal jet using phase doppler interferometry. *J. Aerosol Med.*, 13:125–137, 2000.

[50] B. Grgic, W. H. Finlay, and A. F. Heenan. Regional aerosol deposition and flow measurements in an idealized mouth and throat. *J. Aerosol Sci.*, 35:21–32, 2004.

[51] K. H. Cheng, Y. S. Cheng, H. C. Yeh, and D. L. Swift. Deposition of ultrafine aerosols in the head airways during natural breathing and during simulated breath-holding using replicate human upper airway casts. *Aerosol Sci. Technol.*, 23:465–474, 1995.

[52] C. Kleinstreuer, Z. Li, and Z. Zhang. Simulation of airflow fields and microparticle deposition in realistic human lung airway models. Part II: Particle transport and deposition. *Eur. J. Mech. B-Fluid.*, 26:650–668, 2007.

[53] C. L. Lin, M. H. Tawhai, G. McLennan, and E. A. Hoffman. Characteristics of the turbulent laryngeal jet and its effect on airflow in the human intra-thoracic airways. *Respir. Physiol. Neurobiol.*, 157:295–309, 2007.

[54] P. W. Longest and J. X. Xi. Computational investigation of particle inertia effects on submicron aerosol deposition in the respiratory tract. *J. Aerosol Sci.*, 38:111–130, 2007.

[55] Y. Liu and H. Y. Luo. Modeling the bifurcating flow in a CT-scanned human lung airway. *J. Biomech.*, 41:2681–2688, 2008.

[56] X. Y. Luo, J. S. Hinton, T. T. Liew, and K. K. Tan. LES modelling of flow in a simple airway model. *Med. Eng. Phys.*, 26:403–413, 2004.

[57] E. A. Matida, W. H. Finlay, M. Breuer, and C. F. Lange. Improving prediction of aerosol deposition in an idealized mouth using large-eddy simulation. *J. Aerosol Med.*, 19:290–300, 2006.

[58] W. H. Finlay, E. A. Matida, C. F. Lange, and B. Grgic. Improved numerical simulation of aerosol deposition in an idealized mouth-throat. *J. Aerosol Sci.*, 35:1–19, 2004.

[59] C. Kleinstreuer, Z. Zhang, J. F. Donohue, and C. S. Kim. Comparison of micro- and nano-size particle depositions in a human upper airway model. *J. Aerosol Sci.*, 36:211–233, 2005.

[60] W. H. Finlay and A. R. Martin. A general, algebraic equation for predicting total respiratory tract deposition of micrometer-sized aerosol particles in humans. *J. Aerosol Sci.*, 38:246–253, 2007.

[61] W. H. Finlay and A. R. Martin. Recent advances in predictive understanding of respiratory tract deposition. *J. Aerosol Med. Pulm. D.*, 21:189–205, 2008.

[62] J. Heyder, J. Gebhart, G. Rudolf, C. F. Schiller, and W. Stahlhofen. Deposition of particles in the human respiratory tract in the size range 0.005-15 μm. *J. Aerosol Sci.*, 17:811–825, 1986.

[63] Y. S. Cheng, H. C. Yeh, and D. L. Swift. Aerosol deposition in human nasal airway for particles 1 nm to 20 μm - a model study. *Radiat. Prot. Dosim.*, 38:41–47, 1991.

[64] W. Stahlhofen, G. Rudolf, and A. C. James. Inercomparison of experimental regional aerosol deposition data. *J. Aerosol Med.*, 2:285–308, 1989.

[65] W. I. Li, M. Perzl, J. Heyder, R. Langer, J. D. Brain, K. H. Englemeier, R. W. Niven, and D. A. Edwards. Aerodynamics and aerosol particle deaggregation phenomena in model oral-pharyngeal cavities. *J. Aerosol Sci.*, 27:1269–1286, 1996.

[66] G. Yu, Z. Zhang, and R. Lessmann. Computer simulation of the flow field and particle deposition by diffusion in a 3-d human airway bifurcation. *Aerosol Sci. Technol.*, 25:338–352, 1996.

[67] L. Gradon and A. Moskal. Temporary and spatial deposition of aerosol particles in the upper human airways during breathing cycle. *J. Aerosol Sci.*, 33:1525–1539, 2002.

[68] T. Gemci, B. Shortall, G. M. Allen, T. E. Corcoran, and N. Chigier. A CFD study of the throat during aerosol drug delivery using heliox and air. *J. Aerosol Sci.*, 34:1175–1192, 2003.

[69] I. M. Katz and T. B. Martonen. Flow patterns in three-dimensional laryngeal models. *J. Aerosol Med.*, 9:501–511, 1996.

[70] I. M. Katz, B. M. Davis, and T. B. Martonen. A numerical study of particle motion within the human larynx and trachea. *J. Aerosol Sci.*, 30:173–183, 1999.

[71] K. W. Stapleton, E. Guentsch, M. K. Hoskinson, and W. H. Finlay. On the suitability of k-epsilon turbulence modeling for aerosol deposition in the mouth and throat: A comparison with experiment. *J. Aerosol Sci.*, 31:739–749, 2000.

[72] C. Kleinstreuer, Z. Zhang, and C. S. Kim. Comparison of analytical and CFD models with regard to micron particle deposition in a human 16-generation tracheobronchial airway model. *J. Aerosol Sci.*, 40:16–28, 2009.

[73] E. A. Matida, M. Ilie, and W. H. Finlay. Asymmetrical aerosol deposition in an idealized mouth with a DPI mouthpiece inlet. *Aerosol Sci. Technol.*, 42:10–17, 2008.

[74] J. Xi and P. W. Longest. Transport and deposition of micro-aerosols in realistic and simplified models of the oral airway. *Ann. Biomed. Eng.*, 35:560–81, 2007.

[75] Amira. *http://www.amira.com/.*

[76] Mimics. *http://www.materialise.com/mimics.*

[77] Simpleware. *http://www.simpleware.com/.*

[78] D. Jungblut, G. Queisser, and G. Wittum. Inertia based filtering of high resolution images using a gpu cluster. *Comput. Vis. Sci.*, 14:181–186, 2012.

[79] H. Shi, C. Kleinstreuer, and Z. Zhang. Laminar airflow and nanoparticle or vapor deposition in a human nasal cavity model. *J. Biomech. Eng.*, 128:697–706, 2006.

[80] A. Pollard, A. Johnstone, M. Uddin, A. Heenan, and W. H. Finlay. The flow inside an idealised form of the human extra-thoracic airway. *Exp. Fluids*, 37:673–689, 2004.

[81] W. H. Finlay, B. Grgic, P. K. P. Burnell, and A. F. Heenan. In vitro intersubject and intrasubject deposition measurements in realistic mouth-throat geometries. *J. Aerosol Sci.*, 35:1025–1040, 2004.

[82] S. K. Kim and S. K. Chung. Investigation on the respiratory airflow in human airway by PIV. *J. Visual.*, 12:259–266, 2009.

[83] T. Gemci, V. Ponyavin, Y. Chen, H. Chen, and R. Collins. Computational model of airflow in upper 17 generations of human respiratory tract. *J. Biomech.*, 41:2047–54, 2008.

[84] C. Kleinstreuer and Z. Zhang. Airflow structures and nano-particle deposition in a human upper airway model. *J. Comput. Phys.*, 198:178–210, 2004.

[85] J. R. Fan, H. H. Jin, M. J. Zeng, and K. F. Cen. Large eddy simulation of inhaled particle deposition within the human upper respiratory tract. *J. Aerosol Sci.*, 38:257–268, 2007.

[86] Z. Zhang, C. Kleinstreuer, and C. S. Kim. Micro-particle transport and deposition in a human oral airway model. *J. Aerosol Sci.*, 33:1635–1652, 2002.

[87] Z. Zhang, G. Yu, and R. Lessmann. Fluid flow and particle diffusion in the human upper respiratory system. *Aerosol Sci. Technol.*, 28:146–158, 1998.

[88] S. T. Jayaraju, M. Brouns, C. Lacor, B. Belkassem, and S. Verbanck. Large eddy and detached eddy simulations of fluid flow and particle deposition in a human mouth-throat. *J. Aerosol Sci.*, 39:862–875, 2008.

[89] C. Kleinstreuer and Z. Zhang. Laminar-to-turbulent fluid-particle flows in a human airway model. *Int. J. Multiphas. Flow*, 29:271–289, 2003.

[90] Z. Zhang and C. Kleinstreuer. Low-reynolds-number turbulent flows in locally constricted conduits: A comparison study. *AIAA J.*, 41:831–840, 2003.

[91] C. Kleinstreuer and Z. Zhang. Species heat and mass transfer in a human upper airway model. *Int. J. Heat Mass Transfer*, 46:4755–4768, 2003.

[92] Z. Zhang, C. Kleinstreuer, and C. S. Kim. Isotonic and hypertonic saline droplet deposition in a human upper airway model. *J. Aerosol Med.*, 19:184–98, 2006.

[93] Z. Zhang, C. Kleinstreuer, and C. S. Kim. Transport and uptake of MTBE and ethanol vapors in a human upper airway model. *Inhal. Toxicol.*, 18:169–84, 2006.

[94] Z. Zhang, C. Kleinstreuer, and C. S. Kim. Water vapor transport and its effects on the deposition of hygroscopic droplets in a human upper airway model. *Aerosol Sci. Technol.*, 40:1–16, 2006.

[95] C. Kleinstreuer, Z. Zhang, C. S. Kim, and Y. S. Cheng. Vaporizing microdroplet inhalation, transport, and deposition in a human upper airway model. *Aerosol Sci. Technol.*, 38:36–49, 2004.

[96] C. Kleinstreuer, Z. Zhang, and C. S. Kim. Combined inertial and gravitational deposition of microparticles in small model airways of a human respiratory system. *J. Aerosol Sci.*, 38:1047–1061, 2007.

[97] W. H. DeHaan and W. H. Finlay. In vitro monodisperse aerosol deposition in a mouth and throat with six different inhalation devices. *J. Aerosol Med.*, 14:361–367, 2001.

[98] W. H. Finlay, Y. Zhang, and K. Gilbertson. In vivo-in vitro comparison of deposition in three mouth-throat models with qvar (R) and turbuhaler (R) inhalers. *J. Aerosol Med.*, 20:227–235, 2007.

[99] W. H. Finlay and Y. Zhang. Experimental measurements of particle deposition in three proximal lung bifurcation models with an idealized mouth-throat. *J. Aerosol Med.*, 18:460–473, 2005.

[100] W. H. Finlay and W. H. DeHaan. Predicting extrathoracic deposition from dry powder inhalers. *J. Aerosol Sci.*, 35:309–331, 2004.

[101] W. H. Finlay, E. A. Matida, W. H. DeHaan, and C. F. Lange. Simulation of particle deposition in an idealized mouth with different small diameter inlets. *Aerosol Sci. Technol.*, 37:924–932, 2003.

[102] T. Brancatisano, P. W. Collett, and L. A. Engel. Respiratory movements of the vocal cords. *J. Appl. Physiol.*, 54:1269–76, 1983.

[103] A. A. Lowe and J. A. Fleetham. *Two- and three-dimensional analyses of tongue, airway, and soft palate size. In Atlas of the Dizcult Airway.* Mosby Year Book, St. Louis, 1991.

[104] E. K. Pae, A. A. Lowe, K. Sasaki, C. Price, M. Tsuchiya, and J. A. Fleetham. A cephalometric and electromyographic study of upper airway structures in the upright and supine positions. *Am. J. Orthod. Dentofacial Orthop.*, 106:52–9, 1994.

[105] D. O. Rodenstein, G. Dooms, Y. Thomas, G. Liistro, D. C. Stanescu, C. Culee, and G. Aubert-Tulkens. Pharyngeal shape and dimensions in healthy subjects, snorers, and patients with obstructive sleep apnoea. *Thorax*, 45:722–7, 1990.

[106] M. Brouns, S. T. Jayaraju, C. Lacor, J. De Mey, M. Noppen, W. Vincken, and S. Verbanck. Tracheal stenosis: a flow dynamics study. *J. Appl. Physiol.*, 102:1178–1184, 2007.

[107] J. Lin, G. L. Hu, J. R. Fan, and D. Pan. Study on airflow and inhaled particle deposition within realistic human upper respiratory tract. *J. Phys.: Conf. Ser.*, 147:01206, 2009.

[108] A. F. Heenan, W. H. Finlay, B. Grgic, A. Pollard, and P. K. P. Burnell. An investigation of the relationship between the flow field and regional deposition in realistic extra-thoracic airways. *J. Aerosol Sci.*, 35:1013–1023, 2004.

[109] P. W. Scherer, II Hahn, and M. M. Mozell. The biophysics of nasal airflow. *Otolaryngol. Clin. North. Am.*, 22:265–78, 1989.

[110] A. S. Wexler, L. M. Hopkins, J. T. Kelly, and A. K. Prasad. Particle image velocimetry measurements in complex geometries. *Exp. Fluids*, 29:91–95, 2000.

[111] S.K. Kim and Y.R. Son. Particle image velocimetry measurements in nasal airflow. *Trans. KSME B.*, 26:566–569, 2002.

[112] M. Kleven, M. C. Melaaen, M. Reimers, and P. G. Djupesland. Computational modeling of nasal aerodynamics. In 5^{th} *World congress of Biomechanics*, Munich, Germany, Junly 2006.

[113] D. J. Doorly, V. Franke, A. Gambarruto, D. J. Taylor, and R. C. Schroter. Nasal airflow: computational and experimental modeling. In 5^{th} *World congress of Biomechanics*, Munich, Germany, Junly 2006.

[114] C. Kleinstreuer, H. Shi, and Z. Zhang. Dilute suspension flow with nanoparticle deposition in a representative nasal airway model. *Phys. Fluids*, 20, 2008.

[115] E. A. Matida, Y. Liu, J. Gu, and M. R. Johnson. Numerical simulation of aerosol deposition in a 3-d human nasal cavity using RANS, RANS/EIM, and LES. *J. Aerosol Sci.*, 38:683–700, 2007.

[116] C. Kleinstreuer, H. A. Shi, and Z. Zhang. Modeling of inertial particle transport and deposition in human nasal cavities with wall roughness. *J. Aerosol Sci.*, 38:398–419, 2007.

[117] R. C. Schroter and M. F. Sudlow. Flow patterns in models of the human bronchial airways. *Respir. Physiol.*, 7:341–55, 1969.

[118] T. J. Pedley. Pulmonary fluid dynamics. *Annu. Rev. Fluid Mech.*, 9:229–74, 1977.

[119] D. Isabey and H. K. Chang. Steady and unsteady pressure-flow relationships in central airways. *J. Appl. Physiol.*, 51:1338–48, 1981.

[120] B. Snyder and D. E. Olson. Flow development in a model airway bronchus. *J. Fluid Mech.*, 207:379–392, 1989.

[121] Y. Zhao and B. B. Lieber. Steady inspiratory flow in a model symmetric bifurcation. *J. Biomech. Eng.*, 116:488–96, 1994.

[122] J. K. Comer, C. Kleinstreuer, and Z. Zhang. Flow structures and particle deposition patterns in double-bifurcation airway models. part 1. air flow fields. *J. Fluid Mech.*, 435:25–54, 2001.

[123] C. Kleinstreuer, Z. Zhang, and C. S. Kim. Flow structure and particle transport in a triple bifurcation airway model. *Journal of Fluids Engineering-Transactions of the Asme*, 123:320–330, 2001.

[124] Y. Liu, R. M. So, and C. H. Zhang. Modeling the bifurcating flow in a human lung airway. *J. Biomech.*, 35:465–73, 2002.

[125] A. Farkas and I. Balashazy. Simulation of the effect of local obstructions and blockage on airflow and aerosol deposition in central human airways. *J. Aerosol Sci.*, 38:865–884, 2007.

[126] C.S. Kim and A. J.owe91 Iglesias. Deposition of inhaled particles in bifurcating airway models: I. inspiratory deposition. *J. Aerosol. Med.*, 2:1–14, 1989.

[127] I. Balashazy, W. Hofmann, and T. B. Martonen. Inspiratory particle deposition in airway bifurcation models. *J. Aerosol Sci.*, 22:15–30, 1991.

[128] I. Balashazy and W. Hofmann. Deposition of aerosols in asymmetric airway bifurcations. *J. Aerosol Sci.*, 26:273–292, 1995.

[129] Y. Liu, R. M. C. So, and C. H. Zhang. Modeling the bifurcating flow in an asymmetric human lung airway. *J. Biomech.*, 36:951–959, 2003.

[130] Y. Liu, X. L. Yang, and H. Y. Luo. Respiratory flow in obstructed airways. *J. Biomech.*, 39:2743–2751, 2006.

[131] H. Y. Luo, Y. Liu, and X. L. Yang. Particle deposition in obstructed airways. *J. Biomech.*, 40:3096–104, 2007.

[132] E. R. Weibel. *Morphometry of the Human Lung.* Springer Verlag, Berlin-Göttingen-Heidelberg, 1963.

[133] B. Haefeli-Bleuer and E. R. Weibel. Morphometry of the human pulmonary acinus. *Anat. Rec.*, 220:401–14, 1988.

[134] K. Horsfield, G. Dart, D. E. Olson, G. F. Filley, and G. Cumming. Models of the human bronchial tree. *J. Appl. Physiol.*, 31:207–17, 1971.

[135] R. F. Phalen, M. J. Oldham, C. B. Beaucage, T. T. Crocker, and J. D. Mortensen. Postnatal enlargement of human tracheobronchial airways and implications for particle deposition. *Anat. Rec.*, 212:368–80, 1985.

[136] O. G. Raabe, H. C. Yeh, G. M. Schum, and R. F. Phalen. Tracheobronchial geometry: human, dog, rat, hamster. Technical Report LF-53, Lovelace Foundation for Medical Education and Research, Albuquerque, NM, 1976.

[137] C. Kleinstreuer and Z. Zhang. An adjustable triple-bifurcation unit model for air-particle flow simulations in human tracheobronchial airways. *J. Biomech. Eng.*, 131:021007, 2009.

[138] H. Kitaoka, R. Takaki, and B. Suki. A three-dimensional model of the human airway tree. *J. Appl. Physiol.*, 87:2207–17, 1999.

[139] M. Howatson Tawhai, A. J. Pullan, and P. J. Hunter. Generation of an anatomically based three-dimensional model of the conducting airways. *Ann. Biomed. Eng.*, 28:793–802, 2000.

[140] M. H. Tawhai, P. Hunter, J. Tschirren, J. Reinhardt, G. McLennan, and E. A. Hoffman. Ct-based geometry analysis and finite element models of the human and ovine bronchial tree. *J. Appl. Physiol.*, 97:2310–21, 2004.

[141] R. M. Spencer, J. D. Schroeter, and T.B. Martonen. Computer simulations of pulmonary airway structures using data-driven surface modeling techniques. *Comput. Biol. Med.*, 31:499–511.

[142] N. T. Tgavalekos, J. G. Venegas, B. Suki, and K. R. Lutchen. Relation between structure, function, and imaging in a three-dimensional model of the lung. *Ann. Biomed. Eng.*, 31:363–73, 2003.

[143] T. Sera, H. Fujioka, H. Yokota, A. Makinouchi, R. Himeno, R. C. Schroter, and K. Tanishita. Three-dimensional visualization and morphometry of small airways from microfocal x-ray computed tomography. *J. Biomech.*, 36:1587–94, 2003.

[144] A. Schmidt, S. Zidowitz, A. Kriete, T. Denhard, S. Krass, and H. O. Peitgen. A digital reference model of the human bronchial tree. *Comput. Med. Imaging Graph.*, 28:203–11, 2004.

[145] K. S. Burrowes, A. J. Swan, N. J. Warren, and M. H. Tawhai. Towards a virtual lung: multi-scale, multi-physics modelling of the pulmonary system. *Philos. Transact. A Math. Phys. Eng. Sci.*, 366:3247–63, 2008.

[146] B. Ma and K. R. Lutchen. CFD simulation of aerosol deposition in an anatomically based human large-medium airway model. *Ann. Biomed. Eng.*, 37:271–85, 2009.

[147] N. Nowak, P. P. Kakade, and A. V. Annapragada. Computational fluid dynamics simulation of airflow and aerosol deposition in human lungs. *Ann. Biomed. Eng.*, 31:374–90, 2003.

[148] J. R. Cebral and R. M. Summers. Tracheal and central bronchial aerodynamics using virtual bronchoscopy and computational fluid dynamics. *IEEE Trans. Med. Imaging*, 23:1021–33, 2004.

[149] C. van Ertbruggen, C. Hirsch, and M. Paiva. Anatomically based three-dimensional model of airways to simulate flow and particle transport using computational fluid dynamics. *J. Appl. Physiol.*, 98:970–980, 2005.

[150] S. N. Ghadiali and H. L. Dailey. Fluid-structure analysis of microparticle transport in deformable pulmonary alveoli. *J. Aerosol Sci.*, 38:269–288, 2007.

[151] A. Tsuda, F. S. Henry, and J. P. Butler. Chaotic mixing of alveolated duct flow in rhythmically expanding pulmonary acinus. *J. Appl. Physiol.*, 79:1055–63, 1995.

[152] A. Tsuda, F. S. Henry, and J. P. Butler. Gas and aerosol mixing in the acinus. *Respir. Physiol. Neurobiol.*, 163:139–49, 2008.

[153] C. Darquenne. Heterogeneity of aerosol deposition in a two-dimensional model of human alveolated ducts. *J. Aerosol Sci.*, 33:1261–1278, 2002.

[154] C. Darquenne and N. Paiva. Two- and three-dimensional simulations of aerosol transport and deposition in alveolar zone of human lung. *J. Appl. Physiol.*, 80:1401–1414, 1996.

[155] S. Haber and A. Tsuda. A cyclic model for particle motion in the pulmonary acinus. *J. Fluid Mech.*, 567:157–184, 2006.

[156] A. Tsuda, F. S. Henry, and F. E. Laine-Pearson. Hamiltonian chaos in a model alveolus. *J. Biomech. Eng.- T. ASME*, 131, 2009.

[157] A. Karl, F. S. Henry, and A. Tsuda. Low reynolds number viscous flow in an alveolated duct. *J. Biomech. Eng.- T. ASME*, 126:420–429, 2004.

[158] C. van Ertbruggen, P. Corieri, R. Theunissen, M. L. Riethmuller, and C. Darquenne. Validation of CFD predictions of flow in a 3d alveolated bend with experimental data. *J. Biomech.*, 41:399–405, 2008.

[159] C. Darquenne, L. Harrington, and G. K. Prisk. Importance of the bifurcation zone and branch orientation in simulated aerosol deposition in the alveolar zone of the human lung. *J. Aerosol Sci.*, 37:37–62, 2006.

[160] A. Tsuda, J. P. Butler, and J. J. Fredberg. Effects of alveolated duct structure on aerosol kinetics. i. diffusional deposition in the absence of gravity. *J. Appl. Physiol.*, 76:2497–509, 1994.

[161] C. Kleinstreuer, P. W. Longest, and J. R. Buchanan. Efficient computation of micro-particle dynamics including wall effects. *Comput. Fluids*, 33:577–601, 2004.

[162] G. Ahmadi, P. Zamankhan, Z. C. Wang, P. K. Hopke, Y. S. Cheng, W. C. Su, and D. Leonard. Airflow and deposition of nano-particles in a human nasal cavity. *Aerosol Sci. Technol.*, 40:463–476, 2006.

[163] Z. Zhang, C. Kleinstreuer, and C. S. Kim. Airflow and nanoparticle deposition in a 16-generation tracheobronchial airway model. *Ann. Biomed. Eng.*, 36:2095–110, 2008.

[164] P. W. Longest and J. X. Xi. Effects of oral airway geometry characteristics on the diffusional deposition of inhaled nanoparticles. *J. Biomech. Eng.- T. ASME*, 130, 2008.

[165] P. W. Longest, M. Hindle, S. Das Choudhuri, and P. R. Byron. Numerical simulations of capillary aerosol generation: CFD model development and comparisons with experimental data. *Aerosol Sci. Technol.*, 41:952–973, 2007.

[166] H.-W. Ge. *Probability density function modeling of turbulent non-reactive and reactive spray flows.* Phd diss., University of Heidelberg, Heidelberg, 2007.

[167] H.-W. Ge and E. Gutheil. An efficient numerical solution scheme for the computation of the particle velocity in two-phase flows. *Prog. Comput. Fluid Dy.*, 7(8):467–472, 2007.

[168] P. W. Longest and M. J. Oldham. Numerical and experimental deposition of fine respiratory aerosols: Development of a two-phase drift flux model with near-wall velocity corrections. *J. Aerosol Sci.*, 39:48–70, 2008.

[169] A. Pollard, C. G. Ball, and M. Uddin. Mean flow structures inside the human upper airway. *Flow Turbul. Combust.*, 81:155–188, 2008.

[170] D. C. Wilcox. *Turbulence Modeling for CFD.* DCW Industries Inc., La Canada, CA, 1998.

[171] D. C. Wilcox. *Turbulence Modeling for CFD(Third Edition).* DCW Industries Inc., La Canada, CA, 2006.

[172] D. C. Wilcox. Reassessment of the scale-determining equation for advanced turbulence models. *AIAA J.*, 26:1299–1310, 1988.

[173] V. akhot, S. A. Orszag, S. Thangam, T. B. Gatski, and C. G. Speziale. Development of turbulence models for shear flows by a double expansion technique. *Phys. Fluids*, 4:1510–1520, 1992.

[174] F. R. Menter. Zonal two equation $k-\omega$ turbulence models for aerodynamic flows. *AIAA paper*, pages 93–2906, 1993.

[175] W. P. Jones and B. E. Launder. Calculation of low-reynolds-number phenomena with a two-equation model of turbulence. *Int. J. Heat Mass Transfer*, 16:1119–1130, 1973.

[176] A. Radmehr and S. V. Patankar. Computation of boundary layer transition using low-reynolds-number turbulence models. *Numer. Heat Tr. B-Fund.*, 39:525–543, 2001.

[177] Rng k-epsilonmodel. *http://www.cfd-online.com/Wiki/RNG_k-epsilon_model.*

[178] F. R. Menter. 2-equation eddy-viscosity turbulence models for engineering applications. *AIAA J.*, 32:1598–1605, 1994.

[179] Fine/hexa user manual, version 2.1-a. Technical Report 1050, Numeca International, Avenue Franklin Roosevelt, Brussel, Belgium, 2005.

[180] S. B. Pope. *Turbulent Flows.* London, Cambridge University Press, 2001.

[181] M. Strelets. Detached eddy simulation of massively separated flows. *AIAA Paper*, pages 2001–0879, 2001.

[182] A. A. Amsden, P. J. O'Rourke, and T. D. Butler. Kiva-ii: A computer program for chemically reactive flows with sprays. Technical Report UC-96, Los Alamos National Laboratory, May 1989.

[183] Ansys. *http://www.ansys.com/.*

[184] Openfoam. *http://www.openfoam.com/.*

[185] C. Kleinstreuer and Z. Zhang. Targeted drug aerosol deposition analysis for a four-generation lung airway model with hemispherical tumors. *J. Biomech. Eng.*, 125:197–206, 2003.

[186] P. W. Longest, J. X. Xi, and T. B. Martonen. Effects of the laryngeal jet on nano- and microparticle transport and deposition in an approximate model of the upper tracheobronchial airways. *J. Appl. Physiol.*, 104:1761–1777, 2008.

[187] T. E. Corcoran and N. Chigier. Inertial deposition effects: a study of aerosol mechanics in the trachea using laser doppler velocimetry and fluorescent dye. *J. Biomech. Eng.*, 124:629–37, 2002.

[188] M. Brouns, S. Verbanck, and C. Lacor. Influence of glottic aperture on the tracheal flow. *J. Biomech.*, 40:165–72, 2007.

[189] C. H. Wang, F. Y. Leong, and K. A. Smith. Secondary flow behavior in a double bifurcation. *Phys. Fluids*, 21, 2009.

[190] A. Pollard, C. G. Ball, and M. Uddin. High resolution turbulence modelling of airflow in an idealised human extra-thoracic airway. *Comput. Fluids*, 37:943–964, 2008.

[191] J. Jeong and F. Hussain. On the identification of a vortex. *J. Fluid Mech.*, 285:69–94, 1995.

[192] P. Holmes, J. L. Lumley, and G. Berkooz. *Turbulence, coherent structures, dynamical systems and symmetry.* Cambridge University Press, London, 1996.

[193] W. C. Saric. Götler vortices. *Annu. Rev. Fluid Mech.*, 26:379–409, 1994.

[194] K. Keyhani, P. W. Scherer, and M. M. Mozell. Numerical simulation of airflow in the human nasal cavity. *J. Biomech. Eng.*, 117:429–41, 1995.

[195] R. P. Subramaniam, R. B. Richardson, K. T. Morgan, J. S. Kimbell, and R. A. Guilmette. Computational fluid dynamics simulations of inspiratory airflow in the human nose and nasopharynx. *Inhal. Toxicol.*, 10:473–502, 1998.

[196] I. Hahn, P. W. Scherer, and M. M. Mozell. Velocity profiles measured for airflow through a large-scale model of the human nasal cavity. *J. Appl. Physiol.*, 75:2273–87, 1993.

[197] I. Horschler, M. Meinke, and W. Schroder. Numerical simulation of the flow field in a model of the nasal cavity. *Comput. Fluids*, 32:39–45, 2003.

[198] D. J. Doorly, D. J. Taylor, A. M. Gambaruto, R. C. Schroter, and N. Tolley. Nasal architecture: form and flow. *Philos. T. Roy. Soc. A.*, 366:3225–3246, 2008.

[199] W. Stahlhofen, J. Gebhart, and J. Heyder. Experimental determination of the regional deposition of aerosol particles in the human respiratory tract. *Am. Ind. Hyg. Assoc. J.*, 41:385–98a, 1980.

[200] J. Heyder. Deposition of inhaled particles in the human respiratory tract and consequences for regional targeting in respiratory drug delivery. *Proc. Am. Thorac. Soc.*, 1:315–20, 2004.

[201] T. Gemci, T. E. Corcoran, and N. Chigier. A numerical and experimental study of spray dynamics in a simple throat model. *Aerosol Sci. Technol.*, 36:18–38, 2002.

[202] I. M. Katz and T. B. Martonen. Three-dimensional fluid particle trajectories in the human larynx and trachea. *J. Aerosol Med.*, 9:513–520, 1996.

[203] W. I. Li, M. Perzl, G. A. Ferron, R. Batycky, J. Heyder, and D. A. Edwards. The macrotransport properties of aerosol particles in the human oral-pharyngeal region. *J. Aerosol Sci.*, 29:995–1010, 1998.

[204] P. R. Byron. Prediction of drug residence times in regions of the human respiratory tract following aerosol inhalation. *J. Pharm. Sci.*, 75:433–8, 1986.

[205] R. B. Schlesinger and M. Lippmann. Selective particle deposition and bronchogenic carcinoma. *Environ. Res.*, 15:424–31, 1978.

[206] I. Balashazy, W. Hofmann, and T. Heistracher. Local particle deposition patterns may play a key role in the development of lung cancer. *J. Appl. Physiol.*, 94:1719–25, 2003.

[207] R. B. Schlesinger and M. Lippmann. Particle deposition in the trachea: in vivo and in hollow casts. *Thorax*, 31:678–84, 1976.

[208] C. Kleinstreuer, H. Shi, and Z. Zhang. Computational analyses of a pressurized metered dose inhaler and a new drug-aerosol targeting methodology. *J. Aerosol Med.*, 20:294–309, 2007.

[209] K. H. Cheng, Y. S. Cheng, H. C. Yeh, R. A. Guilmette, S. Q. Simpson, Y. H. Yang, and D. L. Swift. In vivo measurements of nasal airway dimensions and ultrafine aerosol deposition in the human nasal and oral airways. *J. Aerosol Sci.*, 27:785–801, 1996.

[210] K. H. Cheng, Y. S. Cheng, H. C. Yeh, and D. L. Swift. Measurements of airway dimensions and calculation of mass transfer characteristics of the human oral passage. *J. Biomech. Eng.- T. ASME*, 119:476–482, 1997.

[211] K. H. Cheng, Y. S. Cheng, H. C. Yeh, and D. L. Swift. An experimental method for measuring aerosol deposition efficiency in the human oral airway. *Am. Ind. Hyg. Assoc. J.*, 58:207–213, 1997.

[212] Y. S. Cheng, Y. Yamada, H. C. Yeh, and D. L. Swift. Diffusional deposition of ultrafine aerosols in a human nasal cast. *J. Aerosol Sci.*, 19:741–751, 1988.

[213] C. Kleinstreuer, H. Shi, Z. Zhang, and C. S. Kim. Nanoparticle transport and deposition in bifurcating tubes with different inlet conditions. *Phys. Fluids*, 16:2199–2213, 2004.

[214] B. Asgharian and S. Anjilvel. A monte-carlo calculation of the deposition efficiency of inhaled particles in lower airways. *J. Aerosol Sci.*, 25:711–721, 1994.

[215] B. A. Wong, J. T. Kelly, B. Asgharian, and J. S. Kimbell. Particle deposition in human nasal airway replicas manufactured by different methods. part i: Inertial regime particles. *Aerosol Sci. Technol.*, 38:1063–1071, 2004.

[216] W. C. Su and Y. S. Cheng. Deposition of fiber in the human nasal airway. *Aerosol Sci. Technol.*, 39:888–901, 2005.

[217] J. Y. Tu, K. Inthavong, Z. F. Tian, H. F. Li, W. Yang, C. L. Xue, and C. G. Li. A numerical study of spray particle deposition in a human nasal cavity. *Aerosol Sci. Technol.*, 40:1034–U3, 2006.

[218] D. J. Doorly, D. J. Taylor, and R. C. Schroter. Mechanics of airflow in the human nasal airways. *Respir. Physiol. Neurobiol.*, 163:100–110, 2008.

[219] J. D. Schroeter, J. S. Kimbell, and B. Asgharian. Analysis of particle deposition in the turbinate and olfactory regions using a human nasal computational fluid dynamics model. *J. Aerosol Med.*, 19:301–313, 2006.

[220] P. W. Longest and J. X. Xi. Numerical predictions of submicrometer aerosol deposition in the nasal cavity using a novel drift flux approach. *Int. J. Heat Mass Transfer*, 51:5562–5577, 2008.

[221] R. Theunissen and M. L. Riethmuller. *Particle image velocimetry in lung bifurcation models. In Particle Image Velocimetry: New Developments and Recent Applications.* Berlin, Springer, 2008.

[222] D. E. Olson, M. F. Sudlow, K. Horsfiel, and G. F. Filley. Convective patterns of flow during inspiration. *Arch. Int. Med.*, 131:51–57, 1973.

[223] F. E. Fresconi and A. K. Prasad. Secondary velocity fields in the conducting airways of the human lung. *J. Biomech. Eng.*, 129:722–32, 2007.

[224] B. B. Lieber and Y. Zhao. Oscillatory flow in a symmetric bifurcation airway model. *Ann. Biomed. Eng.*, 26:821–830, 1998.

[225] S. A. Berger, L. Talbot, and L. S. Yao. Flow in curved pipes. *Ann. Rev. Fluid Mech.*, 15:461–512, 1983.

[226] J. R. Womersley. Method for the calculation of velocity, rate of flow and viscous drag in arteries when the pressure gradient is known. *J. Physiol.*, 127(3):553–563, 1955.

[227] J. Sznitman, F. Heimsch, T. Heimsch, D. Rusch, and T. Rosgen. Three-dimensional convective alveolar flow induced by rhythmic breathing motion of the pulmonary acinus. *J. Biomech. Eng.*, 129:658–65, 2007.

[228] R. J. Pandya, G. Solomon, A. Kinner, and J. R. Balmes. Diesel exhaust and asthma: hypotheses and molecular mechanisms of action. *Environ. Health Perspect.*, 110:103–12, 2002.

[229] T. B. Martonen. *Surrogate experimental models for studying particle deposition in the human respiratory tract: an overview.* Lewis, Chesea, Michigan, 1986.

[230] C. P. Yang, R. P. Gallagher, N. S. Weiss, P. R. Band, D. B. Thomas, and D. A. Russell. Differences in incidence rates of cancers of the respiratory tract by anatomic subsite and histologic type: an etiologic implication. *J. Natl. Cancer Inst.*, 81:1828–31, 1989.

[231] T. B. Martonen. Mathematical model for the selective deposition of inhaled pharmaceuticals. *J. Pharm. Sci.*, 82:1191–9, 1993.

[232] T. Martonen, J. Fleming, J. Schroeter, J. Conway, and D. Hwang. In silico modeling of asthma. *Adv. Drug. Deliv. Rev.*, 55:829–49, 2003.

[233] G. Sbirlea-Apiou, M. Lemaire, I. Katz, J. Conway, J. Fleming, and T. Martonen. Simulation of the regional manifestation of asthma. *J. Pharm. Sci.*, 93:1205–16, 2004.

[234] J. S. Andrade, A. M. Alencar, M. P. Almeida, J. Mendes, S. V. Buldyrev, S. Zapperi, H. E. Stanley, and B. Suki. Asymmetric flow in symmetric branched structures. *Phys. Rev. Lett.*, 81:926–929, 1998.

[235] I. Balashazy and W. Hofmann. Particle deposition in airway bifurcations .1. inspiratory flow. *J. Aerosol Sci.*, 24:745–772, 1993.

[236] I. Balashazy, W. Hofmann, and T. Heistracher. Computation of local enhancement factors for the quantification of particle deposition patterns in airway bifurcations. *J. Aerosol Sci.*, 30:185–203, 1999.

[237] C. S. Kim and D. M. Fisher. Deposition characteristics of aerosol particles in sequentially bifurcating airway models. *Aerosol Sci. Technol.*, 31:198–220, 1999.

[238] R. K. Calay, J. Kurujareon, and A. E. Holdo. Numerical simulation of respiratory flow patterns within human lung. *Respir. Physiol. Neurobiol.*, 130:201–21, 2002.

[239] G. A. Ferron and D. A. Edwards. Numerical simulation of air and particle transport in the human conduction airways. *J. Aerosol. Med.*, 9:303–316, 1996.

[240] Gatlin B., Cuicchi C., Hammersley J., Olson D., Reddy R., and Burnside G. Particle path and wall deposition patterns in laminar flow through a bifurcation. In *Proc. ASME FEDSM*, Vancouver, BC, Canada, June 1997.

[241] J. W. Lee and D. Y. Lee. Dispersion of aerosol bolus during one respiration cycle in a model of lung airways. *J. Aerosol Sci.*, 33:1219–1234, 2002.

[242] J. W. Lee, J. H. Goo, and M. K. Chung. Characteristics of inertial deposition in a double bifurcation. *J. Aerosol. Sci.*, 27:119–138, 1996.

[243] B. Mauroy, M. Filoche, J. S. Andrade, and B. Sapoval. Interplay between geometry and flow distribution in an airway tree. *Phys. Rev. Lett.*, 90, 2003.

[244] Z. Zhang, C. Kleinstreuer, and C. S. Kim. Effects of curved inlet tubes on air flow and particle deposition in bifurcating lung models. *J. Biomech.*, 34:659–69, 2001.

[245] C. Kleinstreuer, Z. Zhang, and C. S. Kim. Cyclic micron-size particle inhalation and deposition in a triple bifurcation lung airway model. *J. Aerosol Sci.*, 33:257–281, 2002.

[246] J. K. Comer, C. Kleinstreuer, S. Hyun, and C. S. Kim. Aerosol transport and deposition in sequentially bifurcating airways. *J. Biomech. Eng.*, 122:152–8, 2000.

[247] W. Hofmann, R. Golser, and I. Balashazy. Inspiratory deposition efficiency of ultrafine particles in a human airway bifurcation model. *Aerosol Sci. Technol.*, 37:988–994, 2003.

[248] T. L. Chan, R. M. Schreck, and M. Lippmann. Effect of the laryngeal jet on particle deposition in the human trachea and upper bronchial airways. *J. Aerosol Sci.*, 11:447–459, 1980.

[249] T. B. Martonen, Y. Yang, and Z. Q. Xue. Influences of cartilaginous rings on tracheobronchial fluid-dynamics. *Inhal. Toxicol.*, 6:185–203, 1994.

[250] Z. Zhang, C. Kleinstreuer, and C. S. Kim. Effects of asymmetric branch flow rates on aerosol deposition in bifurcating airways. *J. Med. Eng. Technol.*, 24:192–202, 2000.

[251] D. C. Chalupa, P. E. Morrow, G. Oberdorster, M. J. Utell, and M. W. Frampton. Ultrafine particle deposition in subjects with asthma. *Environ. Health Perspect.*, 112:879–82, 2004.

[252] C. J. Musante and T. B. Martonen. Computer simulations of particle deposition in the developing human lung. *J. Air Waste Manag. Assoc.*, 50:1426–32, 2000.

[253] P. W. Longest, S. Vinchurkar, and T. Martonen. Transport and deposition of respiratory aerosols in models of childhood asthma. *J. Aerosol Sci.*, 37:1234–1257, 2006.

[254] R. B. Schlesinger, D. E. Bohning, T. L. Chan, and M. Lippmann. Particle deposition in a hollow cast of human tracheobronchial tree. *J. Aerosol Sci.*, 8:429–445, 1977.

[255] Z. Q. Zhang and T. Martonen. Deposition of ultrafine aerosols in human tracheobronchial airways. *Inhal. Toxicol.*, 9:99–110, 1997.

[256] S. Haber, D. Yitzhak, and A. Tsuda. Gravitational deposition in a rhythmically expanding and contracting alveolus. *J. Appl. Physiol.*, 95:657–71, 2003.

[257] I. Balashazy, W. Hofmann, A. Farkas, and B. G. Madas. Three-dimensional model for aerosol transport and deposition in expanding and contracting alveoli. *Inhal. Toxicol.*, 20:611–21, 2008.

[258] C. Kleinstreuer and Z. Li. Airflow analysis in the alveolar region using the lattice-boltzmann method. *Med. Biol. Eng. Comput.*, 49:441–451, 2011.

[259] M. Geiser, H. V. Im, S. Schurch, and P. Gehr. *Structural and interfacial aspects of particle retention.* Marcel Dekker, New York, 2000.

[260] A. Vallier. Tutorial icolagrangianfoam/solidparticle. Technical report, Lund Tekniska Högskola, Lund, Sweden, 2007.

[261] Turbulence modeling resource. *http://turbmodels.larc.nasa.gov/sst.html.*

[262] J. Smagorinsky. General circulation experiments with the primitive equations i. the basic experiment. *Mon. Weather Rev.*, 91:99–164, 1963.

[263] M. Germano, U. Piomelli, P. Moin, and W. H. Cabot. A dynamic subgrid-scale eddy viscosity model. *Phys. Fluids*, 3:1760–1765, 1991.

[264] Dynamic subgrid-scale model. *http://www.cfd-online.com/Wiki/Dynamic_subgrid-scale_model#References.*

[265] SST $k-\omega$ model. *http://www.cfd-online.com/Wiki/SST_k-omega_model.*

[266] P. Moin and J. Kim. Numerical investigation of turbulent channel flow. *J. Fluid Mech.*, 118:341–377, 1982.

[267] D. K. Lilly. A proposed modification of the germano subgrid-scale closure method. *Phys. Fluids*, 4(3):633–635, 1991.

[268] G. M. Faeth. Evaporation and combustion of sprays. *Mon. Weather Rev.*, 9:1–76, 1983.

[269] Openfoamwiki. *www.openfoamwiki.net.*

[270] Imagej. *http://rsbweb.nih.gov/ij/.*

[271] Meshlab. *http://meshlab.sourceforge.net/.*

[272] Tecplot. *http://www.tecplot.com/.*

[273] S. A. Ahmed and D. P. Giddens. Velocity measurements in steady flow through axisymmetric stenoses at moderate reynolds numbers. *J. Biomech.*, 16:505–16, 1983.

[274] D. Lovy. Windig. *http://www.unige.ch/sciences/chifi/cpb/windig.html.*

[275] J. C. R. Hunt, A. Wray, and P. Moin. Eddies, stream, and convergence zones in turbulent fows. Technical Report Report CTR-S88, Center for Turbulence Research, California, USA, 1988.

[276] G. Haller. An objective definition of a vortex. *J. Fluid Mech.*, 525:1–26, 2005.

[277] Fx fluid feature extraction toolkit. *http://raphael.mit.edu/fx/.*

[278] M. Lippmann and R. E. Albert. The effect of particle size on the regional deposition of inhaled aerosols in the human respiratory tract. *Am. Ind. Hyg. Assoc. J.*, 30:257–75, 1969.

[279] N. Foord, A. Black, and M. Walsh. Regional deposition of 2.5-7.5 μm diameter inhaled particles in healthy male non-smokers. *J. Aerosol Sci.*, 9:383–390, 1978.

[280] W. Stahlhofen, J. Gebhart, and J. Heyder. Experimental determination of the regional deposition of aerosol particles in the human respiratory tract. *Am. Ind. Hyg. Assoc. J.*, 41:385–98a, 1980.

[281] W. Stahlhofen, J. Gebhart, J. Heyder, and G. Scheuch. New regional deposition data of the human respiratory tract. *J. Aerosol Sci.*, 14:186–188, 1983.

[282] P. C. Emmett, R. J. Aitken, and W. J. Hannan. Measurements of the total and regional deposition of inhaled particles in the human respiratory tract. *J. Aerosol Sci.*, 13:549–560, 1982.

[283] S. M. Bowes and D. L. Swift. Deposition of inhaled particles in the oral airway during oronasal breathing. *Aerosol Sci. Technol.*, 11:157–167, 1989.

[284] E. M. Littringer, A. Mescher, H. Schroettner, L. A. P. Walzel, and N. A. Urbanetz. The influence of mannitol carrier shape and surface roughness on the performance of dry powder inhalates. *Eur. J. Pharm. Sci.*, 2011. submitted.